ISBN 978-82-471-2415-4 (printed ver.)
ISBN 978-82-471-2416-1 (electronic ver.)
ISSN 1503-8181

Yan-Lin Shao

Doctoral Thesis

Doctoral theses at NTNU, 2010:215

Yan-Lin Shao

Numerical Potential-Flow Studies on Weakly-Nonlinear Wave-Body Interactions with/without Small Forward Speeds

NTNU
Norwegian University of Science and Technology

Doctoral theses at NTNU, 2010:215

NTNU
Norwegian University of
Science and Technology
Thesis for the degree of
doctor philosophiae
Faculty of Engineering Science and Technology
Department of Marine Technology

NTNU

Norwegian University of
Science and Technology

Yan-Lin Shao

Numerical Potential-Flow Studies on Weakly-Nonlinear Wave-Body Interactions with/without Small Forward Speeds

Thesis for the degree of doctor philosophiae

Trondheim, August 2010

Norwegian University of
Science and Technology
Faculty of Engineering Science and Technology
Department of Marine Technology

NTNU
Norwegian University of
Science and Technology

NTNU
Norwegian University of Science and Technology

Thesis for the degree of doctor philosophiae

Faculty of Engineering Science and Technology
Department of Marine Technology

ISBN 978-82-471-2415-4 (printed ver.)
ISBN 978-82-471-2416-1 (electronic ver.)
ISSN 1503-8181

Doctoral Theses at NTNU, 2010:215

Printed by Tapir Uttrykk

Abstract

A two-dimensional Quadratic Boundary Element Method (QBEM) and a three-dimensional cubic Higher-order Boundary Element Method (HOBEM) are developed to study respectively the two-dimensional and three-dimensional weakly-nonlinear wave-body interactions with/without forward speed within potential flow theory of an incompressible liquid.

A direct method based on a triangular polar-coordinate system transformation for the evaluation of the Cauchy Principle Value (CPV) integrals for the diagonal terms of the influence matrix in the 3D HOBEM is presented.

A numerical module based on the Fast Multipole Method (FMM) is developed, which can be used as an option to speed up the present 3D HOBEM solver. Both the operation count and the required memory of a FMM accelerated BEM is asymptotically O(N), where N is the total number of the unknowns. Suggestion on the selection of a proper matrix solver for a specific problem is given.

A new approach based on domain decomposition using body-fixed coordinate system in the inner domain and the inertial reference frame in the outer domain is proposed for the weakly-nonlinear wave-body analysis. Consistent theoretical description of the new method based on second-order theory is presented. The new method does not require any derivatives on the right-hand sides of the body boundary conditions and thus avoid the m_j-like terms and their derivatives. Furthermore, because the body boundary condition is formulated on the instantaneous position of the body, the resulting integral equations are valid for both smooth bodies and bodies with sharp corners. In order to improve the convergence of the second-order forces/moments on a body with sharp corners in the near-field approach, a re-formulation of the quadratic force is suggested. This re-formulation transfers the integrals on the body into the sum of two groups of integrals. The first group contains integrals on body surface with integrands whose singularities are weaker than that of the velocity square. The second group consists of regular integrals on the inner free surface and the control surface in the inner domain.

A two-dimensional third-order numerical wave tank (NWT) is developed. The effect of the Stokes drift in the second-order solution is discussed. A two-time scale approach is proposed as a secularity (solvability) condition in order to avoid unphysical third-order results. The numerical results for the second-order diffraction/radiation of a horizontal semi-submerged circular cylinder are verified by some other analytical and numerical results. Comparisons with the experimental results are also made.

The second-order wave-body interaction with/without the presence of a small forward speed for a three-dimensional floating body is studied by both the traditional method (if applicable) with a formulation in the inertial coordinate system and the new method with a formulation in the body-fixed coordinate system near the body. Both bodies without sharp corners and a truncated vertical circular cylinder with sharp corners are studied. Comparisons between the present numerical results with some

other analytical and numerical results (if any) show good agreement. The influences of a small forward speed on the second-order wave loads on floating bodies are investigated.

The complete third-order wave diffraction of a stationary three-dimensional body is studied by the time-domain HOBEM, which means that the solution contains not only the triple-harmonic effect but also the third-order contribution with fundamental frequencies of the incident waves. Careful convergence studies and alternative way of calculating the force have been made with very satisfactory results.

Acknowledgements

Here, first and foremost I would like to express my sincere gratitude to my supervisor, professor Odd M. Faltinsen, for the great guidance, inspiration and supervision he has shown in helping me complete this research. It has been difficult for me with a background on structural mechanics to start a doctoral study on hydrodynamics. It was his patience and encouragement which helped me make through in every way.

I want to thank all the lecturers for their excellent courses that I have learnt during the first year. These courses laid helpful basis for me on marine hydrodynamics in the later stage of the PhD study. I also appreciate the important guidance provided by Prof. Greco Marilena during this work.

I wish to thank Prof. Torgeir Moan, the director of Centre for Ships and Ocean Structures (CeSOS) where my study was carried out, for his successful creation of a scientific and pleasant environment in CeSOS.

I also wish to thank the help from the staff at CeSOS and the Department of Marine Technology, in particular Sigrid Bakken Wold, Marianne Kjølås and Karelle Gilbert.

It was my pleasure to work with all the other members in CeSOS and the Department of Marine Technology. Special thanks to Kota Ravikiran and Linlin Jiao for the fruitful discussions and talks. I also want to mention Dr. Wei Zhu, Dr. Hui Sun, Dr. Trygve Kristiansen and Dr. David Kristiansen for sharing the experiences from their research and providing valuable references. Csaba Pakozdi and Trygve Kristiansen are acknowledged for their help with the computer set up.

My love and gratitude go to my wife, Huirong, whose endless understanding and support made this work possible. Her sacrifices for our small family during the past several years leave debts I can only hope to repay. I am very grateful to my parents. Without their love, constant support and prayer, I could never have come to this far. Through this work, I also wish to express my love to my dear daughter, Tingting.

Contents

Abstract……i

Acknowledgements……iii

Contents……v

Nomenclature……ix

1 Introduction……1
1.1 Scope and objective……1
1.2 Previous studies…… 2
1.3 Present study …… 9
1.3.1 Outline of the thesis……10
1.3.2 Major contributions of the present study……12

2 Theoretical Description……15
2.1 Introduction……15
2.2 Coordinate systems……16
2.3 The definition of the motions……17
2.4 Formulation of the second-order wave-body problem in the inertial coordinate system……22
2.4.1 General description of the boundary conditions……22
2.4.2 Second-order approximations of the boundary conditions……23
2.4.3 Forces and moments calculation……25
2.5 Formulation of the third-order diffraction problem in the Earth-fixed coordinate system……28
2.5.1 Free-surface conditions……28
2.5.2 Body boundary condition……29
2.5.3 Forces and moments calculation……29
2.6 Formulation of the second-order wave-body problem in the body-fixed coordinate system……30
2.6.1 Free-surface conditions……30
2.6.2 Body boundary condition……33
2.6.3 Forces and moments calculation……33
2.7 Governing equations of unsteady rigid-body motions……35
2.7.1 Rigid-body motion equations in the inertial frame……35
2.7.2 Rigid-body motion equations in the body-fixed frame……38
2.8 Incident wave field……39

3 Basis of the Time-Domain HOBEM in 2D……41
3.1 Boundary integral equation……41
3.2 Quadratic boundary element method……42
3.3 Time marching of the free-surface conditions……45
3.4 Numerical damping zone and active wave absorber……45

3.5 Solution of ϕ_t 47
3.6 Calculation of the higher-order derivatives....49
3.7 Fourier analysis....50

4 Basis of the Time-Domain HOBEM in 3D....51
4.1 Boundary integral equation....51
4.2 HOBEM based on cubic shape functions....52
4.2.1 Shape functions....52
4.2.2 Solid angle and CPV integrals....54
4.3 Time marching of the free-surface conditions....59
4.4 Treatment of ϕ_t -term and the time integration of body motion equations....60
4.5 Low-pass filter on the free surface....62
4.6 Direct calculation of the higher-order derivatives....64
4.7 Types of grid on the free surface....69
4.8 Matrix Solver....69
4.8.1 Why HOBEM? 70
4.8.2 Complexity of BEM solvers....70
4.8.3 Algorithm of FMM....71
4.8.4 Selection of a proper solver....75

5 Use of the Body-Fixed Coordinate System in Weakly-Nonlinear Wave-Body Problems....79
5.1 Comparison of the weakly-nonlinear formulations in inertial and body-fixed coordinate systems....79
5.1.1 Free-surface conditions....79
5.1.2 Body boundary conditions....80
5.2 Domain-decomposition approach using body-fixed coordinate system in the near field 81
5.3 Generation of incident wave field in body-fixed coordinate system....87
5.4 The consistency between body-fixed coordinate system and inertial coordinate system....88

6 Studies on Two-Dimensional Weakly-Nonlinear Problems....93
6.1 The steady-state third-order solution of sloshing in a rectangular tank....93
6.2 Free oscillations and forced oscillations in a rectangular tank....98
6.3 Stokes-drift effect and numerical simulation of the Stokes second-order waves....101
6.4 Secularity condition and numerical simulation of the Stokes third-order waves....107
6.5 Second-order diffraction of a horizontal semi-submerged circular cylinder....112
6.6 Second-order radiation of a horizontal semi-submerged circular cylinder... 118

7 Three-Dimensional Weakly-Nonlinear Problems with Zero Forward Speed 123
7.1 Second-order and third-order wave diffraction on a fixed body....123
7.1.1 Second-order diffraction in monochromatic waves....123
7.1.2 Second-order diffraction in bichromatic waves....133
7.1.3 Third-order diffraction in regular waves....135
7.2 Second-order studies of a body under forced oscillations....142
7.2.1. Linear hydrodynamic coefficients....142
7.2.2. Second-order loads on forced oscillating bodies....144

8 Three-dimensional Weakly-Nonlinear Problems with Small Forward Speeds....155
8.1 Second-order wave diffraction....156
8.2 Second-order wave radiation....162
8.3 Freely-floating body in regular waves....172

9 Summary and future perspectives……**179**
9.1 Summary……...179
9.2 Future perspectives……...183

Appendix……**187**
Appendix A. The double-body basis flow……...187
A.1 The classical double-body basis flow in the inertial coordinate system……187
A.2 The 'double-body' basis flow used in the domain decomposition based method……188
Appendix B. The second-order analytical solution of a circle under forced surging in an infinite fluid……...……...……..……..190
B.1 Solution in the Earth-fixed coordinate system……190
B.2 Solution in the body-fixed coordinate system……191
Appendix C. The second-order analytical solution for sloshing in a two-dimensional rectangular tank under forced surging……192
C.1 Solution in the Earth-fixed coordinate system……192
C.2 Solution in the tank-fixed coordinate system……...198
Appendix D. Elimination of the secular terms in the third-order free-surface conditions……...201
Appendix E. Indirect method for the evaluation of forces and moments due to the ϕ_t-term……203
Appendix F. Alternative formulas for the quadratic forces and moments……...205

References……**209**

Nomenclature

General rules

- The symbols are defined in the text for the first time they appear
- Only the most used symbols are declared here
- The same symbol may have different interpretations in different problems
- The vectors are represented by an arrow above the symbols
- The matrices are represented by bold face characters
- An overdot means time derivative
- A vector with a prime is described in the body-fixed coordinate system

Abbreviations

2D	Two-dimensional
3D	Three-dimensional
BVP	Boundary Value Problem
BIE	Boundary Integral Equation
BEM	Boundary Element Method
CPV	Cauchy Principle Value
COG	Centre of Gravity
FEM	Finite Element Method
FDM	Finite Difference Method
HOBEM	Higher-Order Boundary Element Method
QTF	Quadratic Transfer Function
RAO	Response Amplitude Operator

Subscripts

$b \rightarrow i$	indicates the transformation matrix from body-fixed coordinate system to inertial coordinate system
g	indicates translatory and rotational motions with respect to a coordinate system with origin at the Centre of Gravity
i	i=1, …, 3. The i-th component of a vector
$i \rightarrow b$	indicates the transformation matrix from inertial coordinate system to body-fixed coordinate system
in	indicates variables for incident waves

n	indicates normal derivative
s	indicates variables related to scattered waves
t	indicates time derivative
x,y,z (X,Y,Z)	indicate derivatives along x(X), y(Y) and z(Z) directions, respectively

Superscripts:

(i)	indicates quantities of the *i*-th order (*i*=0, 1, 2, 3)
T	indicates the transpose of the matrix
(2ω)	indicates double-harmonic
+	indicates sum-frequency
-	indicates difference-frequency

Roman symbols:

A	The linear wave amplitude
a_k	k=1,2, 3,4. Coefficients used in Adams-Bashforth-Moulton method
$b^{(m)}$	Forcing term in the m-th order body-boundary conditions formulated in the body-fixed coordinate system
$B^{(m)}$	Forcing term in the m-th order body-boundary conditions formulated in the inertial coordinate system
b_k	k=1,2, 3,4. Coefficients used in Adams-Bashforth-Moulton method
c	The strength of the low-pass filter
C(**x**)	Solid angle coefficient at a position **x**
C_i	Solid angle coefficient at the i-th node P_i
CW	Water line
CW0	Mean water line
d	Draft
$\vec{F}$	Forces vector
$F_1^{(m)}$, $F_2^{(m)}$	Forcing term in the m-th order free-surface conditions formulated in the inertial coordinate system. m=1, 2
$f_1^{(m)}$, $f_2^{(m)}$	Forcing term in the m-th order free-surface conditions formulated in the body-fixed coordinate system. m=1, 2
$\vec{F}_g$	External force vector acting on the body described in OXYZ system.
G	Green function
H_{ik}, A_{ik}	Influence coefficients
$\vec{M}_g$	External moment vector with respect to COG acting on the body
$\vec{g} = -g\vec{K}$	Gravity acceleration vector in the Earth-fixed coordinate system
h	Water depth
I	A 3×3 identity matrix

$\mathbf{I}_B$	Inertia matrix, its elements being the moments and products of inertia of the body
k	Wave number
$\vec{M}$	Moment vector
$\vec{n}$	Normal vector on a surface
N_k	The k-th shape function
NE	Total number of elements
NOD	Total number of nodes
$O_eX_eY_eZ_e$	Earth-fixed coordinate system
$OXYZ$	Inertial coordinate system moving with constant forward speed
$oxyz$	Body-fixed coordinate system
$o_gx_gy_gz_g$	A body-fixed coordinate system with origin at COG
p	Pressure
$\vec{r}$	Position vector
t	Time
T	Linear wave period
R	Radius of an axisymmetric body, e.g. hemisphere, circular cylinder
$\mathbf{R}_{i\to b}$	Transformation matrix from inertial coordinate system to body-fixed coordinate system
$\mathbf{R}_{b\to i}$	Transformation matrix from body-fixed coordinate system to inertial coordinate system
SB	Wetted body surface
SB_0	Mean wetted body surface
S_{bottom}	Sea bottom
SF	Free surface
SF_0	Calm water surface
$\vec{U}$	Forward speed vector in the inertial coordinate system
$\vec{U}'^{(k)}$	The k-th order component of forward speed vector described in the body-fixed coordinate system
$\vec{x}^{(k)}$	k-th order displacement of a point, with its components as $x_1^{(k)}, x_2^{(k)}$ and $x_3^{(k)}$
$\vec{u}^{(k)}$	k-th order displacement of a point, with its components as $u_1^{(k)}, u_2^{(k)}$ and $u_3^{(k)}$
$\vec{U}_B$	Translatory velocity of the body
$s=IEP(e, j)$	A coefficient of the connectivity matrix, which represents the global index of the j-th node of e-th element
L_{offset}	Offset distance in the desingularized BEM. $L_{offset} = l_d \left(D_m\right)^{\beta}$
l_d	A constant coefficient in the definition of L_{offset}
D_m	Size of the mesh which can be approximated by the square root of the area of the local element.
β	A constant coefficient in the definition of L_{offset}

Greek symbols:

ϕ	Velocity potential
ε	Small parameter related to wave steepness and unsteady body motions
δ	Small parameter related to the forward speed/current velocity
$\delta_{i,k}$	Kronecker delta function
η	Total wave elevation
	The local intrinsic coordinates of the 3D boundary element in computational domain
$\overline{\eta}$	$\left(-\overline{\eta}\right)$ denotes the displacement of a point (x,y,0) on the oxy-plane due to the rigid-body motions
$\tilde{\eta}$	Wave elevation observed in the inertial coordinate system OXYZ
$\vec{\xi}$	Translatory motion vector of the origin of OXYZ system, its components being ξ_1, ξ_2 and ξ_3
ξ	Local intrinsic coordinates of the boundary element in computational domain
$\xi_{1,a}$, $\xi_{2,a}$, $\xi_{3,a}$	Amplitude of ξ_1, ξ_2 and ξ_3
$\vec{\alpha}$	The angular motion of the body with respect to the origin of OXYZ system, its components being α_4, α_5 and α_6
$\alpha_{4,a}$, $\alpha_{5,a}$, $\alpha_{6,a}$	Amplitude of α_4, α_5 and α_6
$\vec{\omega}$	Angular velocity vector
ω	Wave frequency; frequencies of the oscillations
ω_0	Fundamental frequency of incident wave without forward speed or current
ω_e	Frequency of encounter
τ	The reduced frequency defined as $\tau=\omega_e U / g$
λ	Linear wave length
	Non-uniformity coefficient in the mesh generation near the sharp corner
ρ	Fluid mass density
$\left\|\mathbf{J}^e\left(\xi\right)\right\|$	Jacobian of the e-th element in 2D HOBEM
$\left\|\mathbf{J}^e\left(\xi,\eta\right)\right\|$	Jacobian of the e-th element in 3D HOBEM
μ_0	Non-dimensional damping coefficient in the numerical damping zone
γ	Empirical coefficient in the damping coefficient of the numerical damping zone
$\vec{\Omega}_B$	Rotational velocity of the body
$\psi_1^{(m)}, \psi_2^{(m)}$	Sub-problems of $\phi_t^{(m)}$ in the modal decomposition method

Special symbols:

∇	Spatial gradient
$\overline{\nabla}$	Spatial gradient in the horizontal plane
ΔS	The fluctuation of the wetted body surface due to of wave elevation
Δt	Time increment in the time-domain simulations

CHAPTER 1

Introduction

1.1. Scope and objective

Nonlinear free-surface body problems can be divided into strongly- and weakly-nonlinear problems. Slamming (e.g. Zhao & Faltinsen (1993) and Zhao et al. (1996)), green water on deck (e.g. Greco, 2001), capsizing of ships (e.g. Kong, 2010) and violent sloshing (e.g. Faltinsen & Timokha, 2009) are examples on strongly nonlinear problems.

A linear solution proportional to the incident wave amplitude is a basis of the weakly-nonlinear wave-body interaction problems for the exterior flow around a ship and an ocean structure. Second-order nonlinear effects according to potential flow theory cause mean, sum- and difference-frequency effects (Faltinsen, 1990). Examples on weakly-nonlinear problems are added resistance of ships, mean wave loads on floating sea structures, slow-drift motions of moored floating structures, resonant vertical sum-frequency loading of Tension Leg Platforms (TLPs).

Super-harmonic ringing loads matter in survival conditions of offshore platforms with natural periods in the range of approximately 3 to 5 seconds (Faltinsen et al., 1995). Higher-order wave effects at an offshore platform can be significant, see for instance Büchmann (2000a), and must be considered in assessing the probability of slamming against the wetdeck. Higher-order springing loads on ships may strongly reduce the fatigue life of ships (see e.g. Storhaug, 2007). Wave-induced extreme hull girder loading causes important nonlinearities in the design wave bending moment amidships (Jensen et al., 2000).

The focus of this study is on the weakly-nonlinear wave-body interaction problems, which means that the strongly-nonlinear problems are out of the scope of this study. The fact that flow separation is neglected in this work implies that the present study is most appropriate for large-volume structures (Faltinsen, 1990). Potential flow theory will be used, by assuming that the water is incompressible and inviscid, and the flow is irrotational. The perturbation scheme will be used throughout the present study. A perturbation scheme makes the frequency-domain analysis possible. Another advantage of using the perturbation scheme is that the computational domain is invariant with time when a time-domain method is followed. Therefore, the influence matrices need only to be set up and

inverted once, and can be used in all the time steps.

Using a perturbation scheme implies that the free-surface elevation is a single-valued function of the lateral coordinates, i.e. we cannot describe the effect of plunging breakers. The water entry of a body with non-vertical wall at the free surface creates a jet flow at the intersection between the body surface and free surface. The latter fact causes that the free surface is not a unique function of the horizontal coordinate. The general problem involves both a water entry and exit phase.

The finite-order theory, e.g. second-order and third-order theory, based on perturbation scheme have been extensively studied in marine hydrodynamics in the last four decades. However, most of the studies are limited to zero Froude number. When the forward speed or current velocity is considered, only the studies on the second-order wave diffraction of a body restrained from unsteady body motions are reported in the literature. However, floating offshore structures experience unsteady body motions that must be accounted for. Recent studies (Storhaug, 2007) on nonlinear ship springing indicate that the second-order velocity potential may be an important excitation source, which is still ignored in the state-of-the-art nonlinear ship hull girder loads analysis. These necessitate the second-order analysis for floating bodies with the presence of forward speed or current effects, which is the objective of this study.

An alternative to the perturbation scheme based method is the fully nonlinear time-domain analysis (see e.g. Ferrant (1998, 2001), Greco (2001), Bai & Eatock Taylor (2007, 2009)). The first-order, second-order and even higher-order results, e.g. the forces, can be obtained by Fourier analysis of the fully-nonlinear results. However, the fully nonlinear analysis is very time-consuming due to the fact that the computational domain changes with time. One has to build up the influence matrices at each time step and solve the matrix equation by a proper matrix solver.

1.2. Previous studies

When a weakly-nonlinear free-surface body problem is theoretically studied, the wave slope and the body motions are assumed asymptotically small. Irrotational flow of an incompressible liquid is considered. A perturbation scheme based on Taylor expansion of the free surface and body boundary condition about the mean position of the free surface and body surface is commonly applied. One can obtain the boundary value problems for any order of the velocity potential by expanding the velocity potential, wave elevation and body motions into perturbation series by Stokes expansion and consistently collecting terms at each order. This section reviews the analytical and numerical studies of the weakly-nonlinear wave-body interactions based on perturbation scheme, which is relevant to the study in this thesis.

Two-dimensional second-order studies, Fr=0.0

Maruo (1960) introduced the well-known formula of the drifting force which enables us to calculate it by the reflected wave amplitude of the linear solutions. Ogilvie (1963) obtained the second-order mean forces on a submerged circular cylinder, which could be achieved without explicitly solving the second-order boundary value problem. Parissis (1966) and Lee (1966) showed independently the complete solutions of the second-order forces on a cylindrical body heaving at the free surface, Lee by the method of multipole expansions, Parissis by the method of integral equations. Potash (1971)

working with the close-fit techniques, extended the studies to sway, heave and roll, including their coupling effects, and to arbitrary section shapes.

Faltinsen (1976) and Faltinsen & Løken (1978) obtained the second-order force through a fictitious radiation potential without solving for the second-order velocity potential. The idea is the same as that of Lighthill (1979) and Molin (1979) for three-dimensional problems. Later, this idea was used by Kyozuka (1980, 1982) and Wu & Eatock Taylor (1989) in solving second-order diffraction/radiation problems of two-dimensional bodies in incident waves. It is understood that this method is a good choice only if one is interested in the integrated force on the body. However, this technique cannot be used for calculating other quantities such as the hydrodynamic pressure, the sectional force and bending moment or the wave elevation due to the second-order effects. These facts necessitate the complete second-order solution with the second-order velocity potential.

In two dimensions, the second-order wave diffraction problem is more complicated than the radiation problems. The difficulty arises from the fact that the reflected waves by the body make partial standing waves with the interaction of the incident waves. Consequently, the forcing term in the second-order free-surface condition does not decay with horizontal distance away from the body on the weather side. Considering that the forcing terms in the inhomogeneous second-order free-surface condition can be regarded as a pressure distribution over the free surface, Miao & Liu (1989) constructed analytically a particular solution for the second-order velocity potential which satisfies the inhomogeneous free-surface condition. The solution was obtained in the frequency domain. A representation for the potential due to an arbitrary pressure distribution available in Wehausen & Laitone (1960) was used in their construction of the particular solution. To this particular solution, one can add a second-harmonic function which satisfies the homogeneous free-surface condition and a radiation condition and is constructed in such a way that the total potential satisfies the condition of no-flow through the body surface. An alternative particular solution was obtained by McIver (1994) based on the theory of analytic functions. Consequently, McIver (1994) was able to get the high-frequency approximations for the second-order results, e.g. the forces on an arbitrary two-dimensional body with vertical wall at the free-surface zone.

A time-domain second-order model based on perturbation scheme was proposed by Isaacson and his associates to study the interactions between the waves and two-dimensional bodies (see e.g. Isaacson & Cheung (1990, 1991), Cheung & Isaacson (1993), Isaacson & Ng (1993a) and Ng & Isaacson (1993)). A constant Boundary Element Method (BEM) was adopted. The Sommerfeld-Orlanski radiation condition (Orlanski, 1976) was used to enforce the first-order and the second-order radiation conditions. Wang & Wu (2008) employed a second-order time-domain method to analyze the resonant oscillation of the liquid confined within two two-dimensional floating bodies. A finite element method (FEM) with quadratic shape functions was used as a numerical tool. The radiation conditions are satisfied through a combination of the damping-zone method and the Sommerfeld-Orlanski equation. A second-order wave tank was developed by Zhang & William (1996, 1999) based on a boundary element method. A novel second-order radiation condition was applied on a vertical control surface at the end of the wave tank.

Two-dimensional third-order studies, Fr=0.0

Third-order numerical wave tank (NWT) has been studied by, for instance Büchmann (1995), Molin & Stassen (1998) and Stassen et al. (1998) by using BEM. According to Molin & Stassen (1998) and

Stassen et al. (1998), the generated third-order waves are not physical if a secularity (solvability) condition is not used. Molin & Stassen (1998) proposed a technique with stretched coordinates in order to obtain a physical third-order solution. It was shown by Stassen et al. (1998) that the phase shift between the measurement and the second-order model can be significantly reduced by adopting the third-order model with the stretching technique of Molin & Stassen (1998).

Three-dimensional second-order studies, Fr=0.0 or Fr≠0.0

For simple geometries, for instance the bottom-mounted vertical circular cylinder and the truncated vertical circular cylinder, it is possible to find the second-order analytical/semi-analytical solutions. Among others, Eatock Taylor & Hung (1987), Chau & Eatock Taylor (1992), Eatock Taylor & Huang (1997) developed the semi-analytical solutions for the second-order diffraction of a bottom-mounted vertical circular cylinder. The semi-analytical solution for the second-order wave diffraction by an array of vertical circular cylinders was developed by e.g. Moubayed & Williams (1995) and Malenica et al. (1999). Huang & Eatock Taylor (1996, 1997) and Chatjigeorgiou & Mavrakos (2007) solved the second-order wave diffraction of a truncated vertical circular cylinder semi-analytically. A semi-analytical solution for the second-order wave diffraction by arrays of elliptical cylinders was obtained by Chatjigeorgiou & Mavrakos (2009).

For a floating body of arbitrary shape, it is not possible to find an analytical solution up to second order. We then have to rely on numerical methods. The numerical analysis for the second-order wave diffraction of three-dimensional bodies in the frequency domain can be found in, for instance Molin (1979), Løken (1986), Scolan (1989), Chau (1989), Kim & Yue (1989, 1990), Chen et al. (1995) and Choi et al. (2001). Isaacson & Cheung (1992) has investigated the second-order wave diffraction problems by means of time-domain boundary element methods. Wang & Wu (2007) studied the second-order diffraction of an array of bottom-mounted vertical circular cylinders by a Finite Element Method (FEM) in the time domain.

The forced oscillations of a free-surface piercing body with no ambient flow have been studied up to second order by e.g. Teng (1995) in the frequency domain and by e.g. Isaacson & Ng (1993b), Bai (2001) and Teng et al.(2002) in the time domain.

When the forward speed or the current effects are considered, only linear semi-analytical (e.g. Malenica et al., 1995) was found in the literature. The presence of the forward speed or the current velocity makes the second-order solution in the frequency domain complicated. It is more straightforward to apply a time-domain approach to study the second-order wave-body problem when the forward speed or the current effect is to be included. However, solving a second-order wave-body interaction problem with even a small forward speed is a non-trivial task, and most of the studies on the second-order wave loads are carried out without considering the forward speed or the current effect. However, it does not mean that the influence of forward speed on the second-order results, e.g. the second-order forces and moments, are not important. Zhao and Faltinsen (1989b) found that the wave drift forces are significantly affected even by a low current speed. Further, the influence on the wave elevation is important. Aanesland et al. (1990) showed experimentally that the presence of a current speed (or quasi-steady slow-drift velocity) has significant influence on the wave elevation around a Tension Leg Platform (TLP). The experimental results were consistent with the linear predictions based on the theoretical model developed by Zhao & Faltinsen (1989b). Skourup et al. (2000) investigated the second-order wave diffraction with the presence of a weak current by using a

time-domain boundary element method (BEM). The numerical results indicate that the second-order loads can be strongly influenced by the current effects. However, to the author's knowledge, for a floating body with forward speed, no study based on consistent second-order theory has been reported. This may partly be due to the numerical difficulties associated with the higher-order derivatives in both the free surface and the body boundary conditions.

Three-dimensional third-order studies, Fr=0.0

The analysis of the third-order problem has also been attempted by some researchers. Malenica & Molin (1995) made a pioneering study of the triple-harmonic part of the third-order diffraction problem for a bottom-mounted vertical circular cylinder. The triple-harmonic part of the third-order diffraction problem for the truncated vertical circular cylinders was investigated by Kinoshita & Bao (2000), who was able to reproduce Malenica & Molin's (1995) results by studying a bottomless truncated cylinder with draft equal to the water depth. Malenica & Molin's (1995) and Kinoshita & Bao's (2000) approaches are analytically based. Faltinsen et al. (1995) obtained an asymptotic solution to the third-order diffraction problem with a long wave length approximation. Teng & Kato (1997) adopted a numerical approach and obtained the triple-harmonic solution of the third-order diffraction problem by solving the integral equations numerically. Without solving the third-order problem explicitly, Markiewicz et al. (1999) obtained the third-order hydrodynamic loads on an oscillating vertical circular cylinder by an indirect method with the assistance of the Green's 2nd identity and an artificial radiation velocity potential. Zhu (1997) studied the third-harmonic diffraction problem by a 3D higher-order panel method. A few approximations have been made in her study in order to simplify the numerical procedure.

Considerations on the calculations of higher-order derivatives in the boundary conditions

One of the difficulties when solving the nonlinear problem, e.g. second-order or third-order problem is how to calculate the second-order or third-order derivatives of the velocity potentials or the wave elevations in the body-boundary and free-surface conditions.

From a numerical point of view, the higher-order derivatives in the free-surface conditions are easier to deal with than that in the body boundary conditions, because the bodies are in general of complex geometries and maybe of high surface-curvatures. Wang & Wu (2007) solved the second-order diffraction problem for an array of cylinders by the Finite Element Method (FEM) in the time domain. They used a curve-fitting technique for the computation of the first-order and the second-order derivatives in the free-surface conditions. With a higher-order Boundary Element Method (BEM), Liu et al. (1995) obtained the first-order and second-order derivatives by means of higher-order shape functions. One can also use a conformal mapping technique from the physical plane to a computational plane with uniform meshes, and thus higher-order Finite Difference Method (FDM) can be applied to calculate the derivatives with high accuracy (see, for instance, Engsig-Karup & Bingham (2009) and Zhu & Faltinsen (2007)). Other possibilities for calculation of the derivatives on the free surface are, for instance, the B-spline based BEM (e.g. Maniar, 1995), the desingularized panel method (e.g. Cao et al., 1991) and the boundary patch method (e.g. Soding, 1993). In principal, all the methods mentioned above can also be used for the direct calculation of the derivatives on the mean body surface.

The second-order derivatives in the body-boundary condition are analogous to the so-called m_j-terms for the linear wave-induced ship motion problem at forward speed (e.g. Ogilvie & Tuck, 1969) and

the linear wave-current-body interaction problem (e.g. Zhao & Faltinsen, 1989a). When a wave-current-body problem is considered, the interaction of the local steady flow and unsteady wave field is taken into account by both the body boundary condition and the free-surface conditions. The so-called m_j-terms in the linear wave-current-body analysis take into account partly the interaction of the local steady flow and the unsteady wave field through the body boundary condition. One should note that the m_j-terms also contain the angle of attack effect due to the ambient steady flow for the unsteady pitch and yaw motions. This effect is always included through the m_j-terms even when the local steady flow effect is neglected. The influence of the m_j-terms was shown by Faltinsen (1974a), who studied numerically the added mass and damping coefficients of the ships by using both the formulas of Ogilvie & Tuck (1969) and Salvesen et al. (1970). The importance of the local steady flow in the forward-speed seakeeping calculation has been revealed by for instance Inglis & Price (1981), Iwashita & Ohkusu (1989), Iwashita & Bertram (1997), Iwashita & Ito (1998), Chen et al. (2000) and Duan & Price (2002). Inglis & Price (1981) and Iwashita & Ohkusu (1989) showed for a submerged prolate spheroid that the added mass and damping coefficients change significantly depending on the inclusion of the local steady flow. Iwashita & Bertram (1997) and Iwashita & Ito (1998) found a clear influence of the local steady flow on the wave pressure near the bow region. It was also mentioned by Chen et al. (2000) that the local steady flow could play a great role in the results of the added mass and damping coefficients, especially for a large Froude number. Duan & Price (2002) found that the local steady flow has significant contribution near the bow and stern regions, even for a submerged slender body. See also the summary of Kim (2005) on the importance of the local steady flow.

There are basically two ways to handle the m_j-terms, i.e. the indirect way and the direct way. The indirect way of treating the m_j-terms is to use Stokes-like theorem. By assuming that the body surface is without sharp corner, the ship hull is wall-sided at the waterline, and the steady wave field can be approximated by the double-body flow, Ogilvie and Tuck (1969) used a modified Stokes theorem (which is referred as Ogilvie-Tuck theorem or Tuck's theorem in the literature) to rewrite the effect of the second-order derivatives in the m_j-term in terms of first-order derivatives in their studies of the forced heave and pitch of a ship of relevance for regular head sea waves. In a second-order radiation problem, Teng et al. (2002) used a similar technique to reduce the second-order derivatives of the velocity potential in the integral equation by one. The cost of doing so in Teng et al.'s (2002) analysis is an additional waterline integral and the evaluation of integrals involving the first-order derivative and the normal derivative of the first-order derivatives of the Green function.

The direct calculation of m_j-terms was early attempted by Zhao and Faltinsen (1989a). Based on the fact that the singularity of the Rankine sources is weakened away from the body surface, they firstly calculated the second-order derivatives on some points offset from the body. The m_j-terms are then obtained through extrapolation. This technique has been shown to be accurate for smooth bodies without sharp corners. Wu (1991) proposed to solve a series of Dirichlet-type problems using the first-order derivatives of velocity potential as the right-hand-side term of the condition on the mean body surface. A similar method was suggested by Chen & Malenica (1998) based on the idea of Wu (1991). There are also successful examples by using a Higher-Order Boundary Element Method (HOBEM) for the calculations of the m_j-terms, see for instance Bingham & Maniar (1996) and Chen et al. (2000).

Considerations on the sharp corners/edges

For many kinds of floating marine structures there are often corners and edges at the intersections of different planes (e.g. the corners of pontoons in some semisubmersibles). Although in reality there may be a small bilge radius at a corner/edge, it is convenient to represent them as sharp corners or edges in a mathematical description of the body surface. However, theoretical and numerical difficulties arise in the linear/nonlinear wave-body interaction analysis with/without forward speed or current effects.

At the sharp corner/edge, it is known that the fluid velocity is singular. Consequently the gradient of the fluid velocity is singular and not integrable. Therefore, the boundary integral equations for a linear wave-body interaction problem with forward speed (or current speed) or a nonlinear wave-body interaction problem are not integrable. This difficulty is not numerical but theoretical. In fact, it is wrong to take Taylor expansion of the body boundary conditions around the sharp corner/edges. In a linear wave-body-current problem, Zhao & Faltinsen (1989b) decomposed the velocity potential into two parts, with the first part satisfying the body boundary condition associated with the m_j-terms, and the second part satisfying the body boundary condition with the m_j-terms excluded. By doing that, they finally obtained an integral equation which is valid for cases with sharp corners. Eatock Taylor & Teng (1993) investigated the effect of corners on the diffraction/radiation forces and wave drift damping. Truncated vertical circular cylinders with the same radius and draft but different corner radii were studied. A small current speed was considered. The Ogilvie-Tuck theorem was applied to avoid direct calculation of the m_j-terms. It was shown by Eatock Taylor & Teng (1993) that the most important hydrodynamic forces and amplitudes of the body motion do not change significantly when the radius of the corner approaches zero. Bai (2001) and Teng et al. (2002) studied the second-order radiation of a truncated vertical circular cylinder in otherwise calm water. A Stokes-like theorem was used to avoid direct calculation of the second-order derivatives in the second-order body boundary condition. Another possible way to handle the theoretical difficulties associated with the sharp corner is that one introduces a local solution consistent with the singular nature of the problem at the corner in the solution of the integral equation.

When the nonlinear wave-body interaction with presence of forward speed/current is studied, the application of the Stokes-like theorems is not straightforward, due to the fact that third-order derivatives of the steady velocity potential are involved in the second-order body boundary conditions. The method proposed by Zhao & Faltinsen (1989b) may in principle be extended to get proper integral equations. However, we then have to divide the velocity potential into several parts since the second-order body boundary condition contains some terms similar to the m_j-terms and terms involving the third-order derivatives. It may also be difficult to find the corresponding artificial velocity potential for all the m_j-like terms.

A numerical difficulty associated with the sharp corners is due to the fact that the normal vectors at the corners/edges are ill-defined. A double-node technique (e.g. Grilli & Svendsen, 1990) is often used in a boundary-element-method solution. Another numerical difficulty is how to get convergent quadratic forces/moments for a body with sharp corners. In theory, the quadratic terms in the Bernoulli's equation are integrable. In reality, the convergence is very slow in the numerical calculations if a near-field method, which directly integrates the pressure on the body surface, is adopted. Zhao & Faltinsen (1989b) showed for a floating truncated vertical circular cylinder the difficulty of the near-field approach to get convergent mean wave forces, especially the vertical mean force. It is also shown that the far-field approach based on momentum and energy relationships is

more robust and efficient. The same problem was re-investigated by Liu et al. (1993) in the frequency domain by the near-field method which resulted in uniform convergence giving a unique result. A Higher-Order BEM (HOBEM) was used. However, their results confirmed neither the near-field nor the far-field results of Zhao & Faltinsen (1989b). A re-investigation of the same problem using a time-domain HOBEM by the near-field method in this thesis (see Chapter 8) will be shown to support the far-field results of Zhao & Faltinsen (1989b). Actually, it has been pointed out by Newman & Lee (2002) and Lee et al. (2002) that the HOBEM is more sensitive to the singularity at the sharp corner in the near-field approach. In order to minimize this problem, they suggested a nonuniform geometric mapping near the corner for the HOBEMs. This idea is similar to the nonuniform spacing of the panels near the corner adopted by Newman & Lee (1992) in the low-order panel method. Unfortunately, the computational results can still be inaccurate especially when the bodies experience large motions.

The momentum analysis based on time-averaging has been shown in the literature to be very accurate and efficient for the calculation of the mean wave forces/moments on a single body. However, the momentum approach is not limited to the mean wave loads analysis. Actually, the momentum analysis can still be powerful for the general purpose of the forces/moments calculations. See for instance Faltinsen (1977), Lee (2007) and Xiang & Faltinsen (2010).

By using the variants of the Stokes's theorem given by Dai (1998), Chen (2004), Dai et al. (2005) and Chen (2007) proposed to use the middle-field formulation, which results in much faster convergence than the original near-field approach in the calculation of nonlinear wave forces. The middle-field formulation rewrites the integral of the pressure on the body surface into the sum of a set of integrals on the free surface as well on an artificial control surface. In principle, the middle-field approach is applicable for not only the mean wave loads but also the sum-frequency and difference-frequency forces/moments. Lee (2007) obtained consistent expressions for the quadratic forces/moments with that of Dai et al. (2005) by using the conservation of momentum.

Considerations on the singularities at the intersection between the free surface and body surface

Zhao & Faltinsen (1988) studied a two-dimensional linear wave-body-current interaction problem in the frequency domain. The bodies studied by them are vertical in the free-surface zone. Two different free-surface conditions with the free-stream flow and the double-body flow as the basis flow respectively have been used in the near field close to the body. It was found that the free-surface condition with double-body basis flow is a much better choice than that with a free-stream basis flow. The reason was that the free-stream basis flow implies a steady flow through the body, while there in reality is a stagnation point at the intersection between the body and the mean free surface. The mathematical consequence of using a free-surface condition with a free-stream basis flow is likely to be singularities at the intersection points.

Isaacson (1977) considered the second-order diffraction theory for a bottom-mounted vertical circular cylinder without current. Taking the radial-derivative of the second-order free-surface condition, Isaacson (1977) found an inconsistency of the body boundary condition and the second-order free-surface condition. He concluded that a nonlinear theory does not exist and one has to rely primarily on the empirical or semi-empirical approach. It was later shown by Hunt & Baddour (1980) that Isaacson's apparent inconsistency follows from a non-analytic property of the solution at the intersection of the body surface and the mean free surface. Hunt & Baddour (1980) concluded that the

inconsistency at the intersection does not invalidate the Stokes's expansion method. Miloh (1980) indicated that Wehausen (1980) has also used a similar argument to refute the Isaacson assertion.

The inconsistency is actually due to the confluence of the boundary conditions at the intersection. For a vertical (wall-sided) intersection, it was shown that the linear potential for horizontal motions has a weak, $r^2\ln(r)$-type singularity, while those for vertical motions or wave diffraction are regular at the intersection point. See e.g. Kravtchenko (1954), Miloh (1980) and Sclavounos (1988). Here r is the distance to the intersection position. For a two-dimensional flow in the vicinity of a body section with the free surface, Sclavounos (1988) showed that leading-order singularity of the second-order velocity potential is $r\ln(r)$. The analysis was made for a wall-sided intersection. Taking the zero-frequency limit of Sclavounos' (1988) analysis, it can be shown that the flow is analytic at the intersection. This is relevant to the double-body basis flow used in this thesis. One should note that the second-order derivatives of the linear velocity potential (e.g. surge radiation potentials) and the first-order derivatives of the second-order velocity potential are integrable. Therefore, the evaluating of the integrals on the computational boundaries in the boundary integral equation (BIE) presents no theoretical difficulties. Alternatively, in order to avoid the direct evaluation of the second-order derivatives at the intersection in the free-surface integral of the BIE, one may use a weak formulation after integrating by parts (see e.g. Chau & Eatock Taylor, 1988).

The applications of the second-order theory based on perturbation scheme to bodies with non-vertical wall in the free-surface zone have also been attempted numerically by, for instance, Papanikolaou & Nowacki (1980), Kim (1989) and Kim & Yue (1989). Papanikolaou & Nowacki (1980) studied the forced oscillations of a two-dimensional triangular section with large positive flare at the waterline. Kim (1989) and Kim & Yue (1989) considered the second-order wave diffraction on a fixed truncated vertical cone. The excitation forces, overturning moments and the wave elevation along the waterline of the cone are presented. It was mentioned in Kim (1989) that the validity of his results for non-vertical intersection cases was established through careful convergence tests.

For a non-vertical intersection case, the validity of the general second-order diffraction/radiation theory seems still to be unknown to the author of this thesis. This needs a dedicated theoretical study of the local behavior of the first-order and the second-order solution in the vicinity of the intersection. For an interior problem, Faltinsen & Timokha (2010a, 2010b) has found the analytical approximate natural sloshing mode in a two-dimensional circular tank and discussed how the singularities are at the intersections of the mean free surface and the body surface for a linear free-surface problem.

1.3. Present study

In the present work, the weakly-nonlinear wave-body interaction problems are solved by using HOBEMs in the time domain. The perturbation scheme is used. A small forward speed or current effect is considered. Numerical codes based on 3-node 2D quadratic BEM and 12-node 3D cubic BEM have been developed for the 2D and 3D studies, respectively. The problem is solved up to second order in wave slope (and/or unsteady body motions) and first order in forward speed. For zero Froude number, the problem is solved to third order in wave steepness. The bodies studied in this thesis are wall-sided at the intersection of the mean free surface and body surface when the body is at

its mean oscillatory position.

1.3.1. Outline of the thesis

Chapter 2 gives the theoretical descriptions. The definitions of body motions in different coordinate systems and their relationships are described. The formulations of the second-order Boundary Value Problem (BVP) in both the inertial coordinate system and the body-fixed coordinate system are presented. A small forward speed effect is included. The formulations are based on a perturbation scheme, which are accurate to second order of the wave slope or the unsteady body motions and first order of the forward speed. The BVP for the third-order diffraction of a fixed body in incident waves is also provided. The rigid-body motion equations in both the inertial and body-fixed reference frame are given.

Chapter 3 describes the basis of the time-domain HOBEM in two dimensions. The discretization of the Boundary Integral Equations (BIEs) by using 3-node quadratic boundary elements is introduced. The evaluation of the influence coefficients is briefly discussed. Other numerical details are also given: the time marching of the free-surface conditions, the mechanisms of the numerical damping zone and the wave absorber, the evaluation of ϕ_t-term in the Bernoulli's equation, calculation of higher-order derivatives in the boundary conditions and the Fourier analysis of the time domain results.

Chapter 4 describes the basis of the time-domain HOBEM in three dimensions. The discretization of the BIEs by using 12-node cubic boundary elements is introduced. Different methods for the evaluation of the solid angle and Cauchy Principle Value (CPV) integrals are presented. Other numerical details include: numerical schemes for the time-evolution of the free-surface conditions, the treatment of ϕ_t-term and the time integration of body motion equations, the low-pass filter applied on the free surface in order to suppress the numerical instabilities, methods of direct calculation of the higher-order derivatives and the selection of the grid types and a proper matrix solver.

In Chapter 5, the advantages and disadvantages of the formulations of BVP in the inertial and body-fixed coordinate systems are discussed. Then we propose a domain decomposition based method taking advantages of the body-fixed coordinate system in the inner domain in order to avoid evaluating the higher-order derivatives in the body boundary condition of the second-order wave-body problem with a small forward speed. The inertial reference frame is used in the outer domain. Taking the HOBEM as an example, the discretized BIEs in the inner and outer domain are shown. In order to demonstrate the consistency between the body-fixed and inertial coordinate system, we have derived analytical (semi-analytical) second-order results for two simple cases, i.e. the forced oscillation of a circle in infinite fluid and the forced oscillation of a 2D rectangular tank with a free surface. The analytical (semi-analytical) results obtained in the body-fixed coordinate system and that in the inertial coordinate system are consistent.

In Chapter 6, with the purpose of verification, studies were carried out in some two-dimensional cases, including: the third-order steady-state solution of a sloshing tank, the free oscillations and forced oscillations in a rectangular tank, reproduction of the Stokes second-order and third-order waves in a Numerical Wave Tank (NWT), and the second-order diffraction and radiation of a horizontal cylinder. All the studied are based on the formulation in the inertial coordinate system. The robustness and accuracy of the numerical methods are demonstrated by the comparisons between the present numerical results and the some other analytical, numerical or experimental results.

In Chapter 7, the numerical methods are verified in three dimensions. Zero Froude number is considered. Both the traditional method based on a formulation in the inertial coordinate system and the new method with a body-fixed coordinate system in the near field are used. The second-order diffraction of a bottom-mounted vertical circular cylinder, a hemisphere and a truncated vertical circular cylinder in monochromatic waves are studied, with good agreement with the other semi-analytical or numerical results. The Quadratic Transfer Functions (QTFs) of the sum-frequency forces and difference-frequency diffraction forces on a bottom-mounted vertical circular cylinder are recovered from the present time-domain results. Third-order wave diffraction of a bottom-mounted vertical circular cylinder is also investigated by the present time-domain HOBEM. The third-order forces on the bottom-mounted vertical circular cylinder contributed by the first-order and second-order velocity potentials are consistent with the semi-analytical results, while differences were observed for the component due to the third-order velocity potential. Careful convergence studies and alternative way of calculating the force have been made with very satisfactory results, indicating that the present results are convergent. Forced oscillations of some floating bodies in otherwise calm water are also investigated. For a vertical circular cylinder with the draft equal to the water depth, the linear hydrodynamic coefficients, e.g. added mass and damping, are obtained from the Fourier analysis of the time-domain results. For an axisymmetric body without sharp corner, the results based on the inertial coordinate-system formulation and that of the body-fixed coordinate system are compared with the purpose of cross-verification. For the forced oscillating of a truncated vertical circular cylinder with sharp corners, our second-order results based on a formulation in the body-fixed coordinate system agrees fairly well with two other studies, in which the second-order derivatives in the body boundary condition are handled by a Stokes-like theorem. Another study by Isaacson & Ng (1993b) calculating the second-order derivatives in the second-order boundary condition gave quite different results.

In Chapter 8, a small forward speed is considered in the second-order wave-body analysis. Only the leading order of the forward speed effect is included, with its higher-order effects neglected. This makes possible for us to use the ‘double-body’ flow as the basis flow. The interactions between the steady flow and the first- and second-order unsteady flows are included in the present model. The second-order wave diffraction on a vertical circular cylinder with draft (d) equal to water depth (h) is studied and compared with some other numerical results. The domain decomposition method from Chapter 5 is used. Sensitivities on the strength of the low-pass filter and the frequency of the application of the filter are studied. The forced oscillations of a vertical circular cylinder with $d=h$ and a truncated vertical circular cylinder are studied up to second order in wave slope or unsteady body motions. The importance of the small forward speed is discussed. For the forced oscillation of an axisymmetric body without any sharp corner, the new method with body-fixed coordinate system gives consistent results with the traditional method with a formulation in the inertial coordinate system. A floating vertical circular cylinder with d=h, free to respond in only surge motion, is studied with different Froude numbers. The Response Amplitude Operators (RAOs) of the surge motions are compared with the semi-analytical results. Then a truncated vertical circular cylinder free to surge and heave in the incident waves is studied. The second-order forces/moments due to the quadratic terms in the Bernoulli’s equation are calculated by a re-formulation based on a formula given by Newman (1977) and another similar formula. The vertical mean wave force near the heave resonance agrees very well with Zhao & Faltinsen’s (1989b) near-field results. The effects of a small forward speed on the horizontal and vertical mean forces are investigated.

1.3.2. Major contributions of the present study

We summarize main contributions of the present work as follows.

- **The direct evaluation of solid angle and CPV terms in the 3D HOBEM**

In the HOBEMs, when the field point is in the same element as the singularity point, a singular integrand is present in the integrals of the influence coefficients. In the present study, the solid angle is calculated according to Montic (1993). A triangular polar-coordinate system transformation proposed by Li et al. (1985) is used to eliminate the singularity when the field point is at a node other than the singularity point. When the field point coincides with the singularity point, a special argument is made in order to make the CPV integral terms exist. Calculating the solid angles and CPV terms directly is more efficient in terms of CPU time compared with the indirect method, which for instance relates the diagonal terms of the influence matrix with the off-diagonal terms.

- **Combination of the 3D cubic HOBEM with the fast multipole method (FMM)**

A numerical module based on the Fast Multipole Method (FMM) is developed, which can be used as an option to speed up the present HOBEM solver. Both the operation count and the required memory of a FMM accelerated BEM is asymptotically O(N), where N is the total number of the unknowns. Suggestion on the selection of a proper matrix solver for a specific problem is given. The FMM accelerated HOBEM will dramatically reduce the required CPU time and memory in the fully nonlinear time domain simulations and the frequency-domain analysis.

- **The second-order and third-order numerical wave tank in two dimensions**

The Stokes second-order and third-order waves are reproduced in a 2D Numerical Wave Tank (NWT) by feeding the velocity profile based on Stokes wave theory on a control surface. It was found that the Stokes drift through the control surface may destroy the second-order result. Therefore, a numerical damping zone which is able to 'drain' water out of the tank is suggested to minimize the effect of the second-order mass transport. It is also found that a secularity (solvability) condition is needed in order to get physical third-order waves in a third-order NWT. A two-time scale approach is proposed to eliminate the secular terms in the free-surface conditions.

- **The complete third-order wave diffraction by time-domain HOBEM**

The complete third-order wave diffraction of a stationary three-dimensional body is studied by a time-domain HOBEM, which means that the solution contains not only the triple-harmonic effect but also the third-order contribution with fundamental frequency of the incident waves. A time-domain third-order diffraction model was mentioned in Sclavounos & Kim (1995), where only the second-order results were shown. However, no published third-order results based on their model were found.

- **A new method based on domain decomposition using body-fixed coordinate system in the inner domain**

Inspired by the work in ship maneuvering and sloshing (Faltinsen & Timokha, 2009), where the body-fixed coordinate systems are commonly applied, a new approach based on domain decomposition using body-fixed coordinate system in the inner domain and the inertial reference frame in the outer domain is proposed. Consistent theoretical description of the new method based on second-order theory is presented. The highlight of this new method is twofold. Firstly, no higher-order derivatives appear in the body boundary conditions and thus the m_j-like terms and their derivatives are

avoided. Secondly, because the body boundary condition is formulated on the instantaneous position of the body, the resulting integral equation is valid for both smooth bodies and bodies with sharp corners. In order to improve the convergence of the second-order forces/moments on a body with sharp corners in the near-field approach, a re-formulation of the quadratic force is presented. This re-formulation transfers the integrals on the body into the sum of two groups of integrals. The first group contains integrals on the body surface with integrands whose singularities are weaker than that of the velocity square. The second group consists of regular integrals on the inner free surface and the control surface in the inner domain.

- **Second-order wave-body analysis with the presence of a small forward speed for a floating body with or without sharp corners**

The second-order wave-body interaction with the presence of a small forward speed for a floating body is studied by both the traditional method with a formulation in the inertial coordinate system and the new method with a formulation in the body-fixed coordinate system. The formulation in the inertial coordinate system is only applicable for a body without sharp corners. The study in the inertial coordinate system may be considered as a generalization of the work by Skourup et al. (2000), who only studied the second-order diffraction problem with small current speed. The new method based on domain decomposition (in Chapter 5) is applicable for bodies with or without sharp corners, and has been applied in the second-order wave loads analysis of truncated vertical circular cylinder with sharp corners.

Parts of the contents and the results have been published in the following papers Shao & Faltinsen (2008, 2010a, 2010b, 2010c), which are listed in the references.

CHAPTER 2

Theoretical Description

2.1 Introduction

When the water is assumed incompressible and inviscid, and the flow is irrotational, the motion of the water can be described by the velocity potential ϕ satisfying the Laplace equation

$$\nabla^2\phi = 0 \qquad \text{in the water domain.} \tag{2.1}$$

The Laplace equation holds no matter an inertial reference frame or an accelerated coordinate system is used.

If the amplitudes of the incident waves, scattered waves, and the body motions relative to the characteristic body dimensions are asymptotically small, we can assume that the velocity potential of the flow and all quantities derivable from the flow may be expanded in a power series with respect to a small parameter ε, which is a measure of the wave slope, the angular body motions and the translatory body motions relative to the characteristic cross-sectional body length in this study. For instance, the velocity potential, wave elevation, the unsteady translatory body motions, the unsteady angular body motions, the forces and moments are expanded respectively as follows

$$\phi = \varepsilon^0\phi^{(0)} + \varepsilon^1\phi^{(1)} + \varepsilon^2\phi^{(2)} + \varepsilon^3\phi^{(3)} \cdots \tag{2.2}$$

$$\eta = \varepsilon^0\eta^{(0)} + \varepsilon^1\eta^{(1)} + \varepsilon^2\eta^{(2)} + \varepsilon^3\eta^{(3)} + \cdots \tag{2.3}$$

$$\vec{\xi} = \varepsilon^1\vec{\xi}^{(1)} + \varepsilon^2\vec{\xi}^{(2)} + \varepsilon^3\vec{\xi}^{(3)} + \cdots \tag{2.4}$$

$$\vec{\alpha} = \varepsilon^1\vec{\alpha}^{(1)} + \varepsilon^2\vec{\alpha}^{(2)} + \varepsilon^3\vec{\alpha}^{(3)} + \cdots \tag{2.5}$$

$$\vec{F} = \varepsilon^0\vec{F}^{(0)} + \varepsilon^1\vec{F}^{(1)} + \varepsilon^2\vec{F}^{(2)} + \varepsilon^3\vec{F}^{(3)} + \cdots \tag{2.6}$$

$$\vec{M} = \varepsilon^0\vec{M}^{(0)} + \varepsilon^1\vec{M}^{(1)} + \varepsilon^2\vec{M}^{(2)} + \varepsilon^3\vec{M}^{(3)} + \cdots . \tag{2.7}$$

Strictly speaking we must require the solution to be analytic which means that the expansion is not valid near a sharp corner with interior angle less than π radians on the body surface. In Eq.(2.2) - Eq.(2.7), the superscript (0) indicates the steady effect, (1) and (2) denote the first-order and

second-order variations, respectively. The zeroth-order terms $\phi^{(0)}$ and $\eta^{(0)}$ are the steady velocity potential and steady wave elevation, which are the consequence of the steady forward speed of the body and/or a steady current.

A two-parameter expansion may at a first-glance seem to be a more appropriate choice for the perturbation expansion, i.e. a perturbation parameter ε as described above and a parameter δ related to the Froude number in case of small Froude numbers $U/\sqrt{gL}$ where U is the steady forward speed and/or current speed. However, one has to solve the linear wave diffraction/radiation problem without a current (or forward speed) and then solve the coupling problem of wave and current (or forward speed). The same applies for the second-order problem. In this study, the one-parameter perturbation expansion is used. Basically, we assume the Froude number to be of O(1) in the series expansion of the flow parameters. However, the boundary value problem may become simpler with a small parameter related to the Froude number. Approximations of the boundary conditions can then be made after the introduction of the one-parameter perturbation expansion into the free-surface and body-boundary conditions. As a result of using the one-parameter perturbation expansion, the mathematical formulation becomes simpler and only one solution is needed at each order.

The assumption of the smallness of the amplitude of the incident wave is violated in extreme wave conditions, in which the wave amplitude and body motions are not small. Another assumption behind the series expansion of Eq.(2.2) - Eq.(2.7) is that the higher-order quantities are much smaller than the low-order ones. This is violated in some cases. One example is the low-frequency lateral translatory and yaw motions in the horizontal plane of a moored ship induced by the low-frequency second-order wave loads. From measurements of low-frequency motions of moored vessels, it is known that in the range of practical wave heights this assumption is in some cases strictly speaking incorrect. See Pinkster (1981). It was pointed out by Faltinsen (1994) that the normal way to calculate the slow-drift motions does not recognize that the second-order motions can affect the linear wave frequency motions. This assumption may also be violated for the large resonant heave, pitch and roll motions for bodies with small waterline area.

The resonant behavior of sloshing can also not be described by the weakly-nonlinear theory adopted in this study. Potential theory without thin free shear layer effects gives zero damping in the sloshing problem. If the weakly-nonlinear assumption which assumes that the liquid motion in tank is of the same order or higher order of the excitation is used, the predicted wave motion at resonance is infinite. In reality it is not infinite because of the viscous damping effect in the tank and the energy transferring between lower and higher modes. The damping sources in the tank are associated with, for instance, the boundary layer on the tank surface, the interior structures and wave breaking. Different ordering of the terms should be used in the analysis of the resonant sloshing. See for instance Faltinsen & Timokha (2009).

2.2 Coordinate systems

As shown in Fig. 2.1, we define four right-handed Cartesian coordinate systems, i.e. $O_eX_eY_eZ_e$, OXYZ, oxyz and $o_gx_gy_gz_g$. $O_eX_eY_eZ_e$ is Earth-fixed with $O_eX_eY_e$-plane on the calm water surface and

the O_eZ_e axis positive upwards. OXYZ is an inertial coordinate system moving with the steady forward speed of the body. The OXY-plane coincides with the $O_eX_eY_e$-plane and the OZ axis parallel to the O_eZ_e axis. oxyz is a body-fixed coordinate system which moves with not only the steady forward speed but also the unsteady rigid-body motions of the body. The oz-axis goes through the center of gravity (COG). When the body is without unsteady motions, oxyz coincides with OXYZ with the origin on the mean free surface. The $o_gx_gy_gz_g$ is an inertial coordinate system with origin located on the COG, with its axis parallel to that of OXYZ. The body is normally assumed to have the oxz-plane as a plane of symmetry.

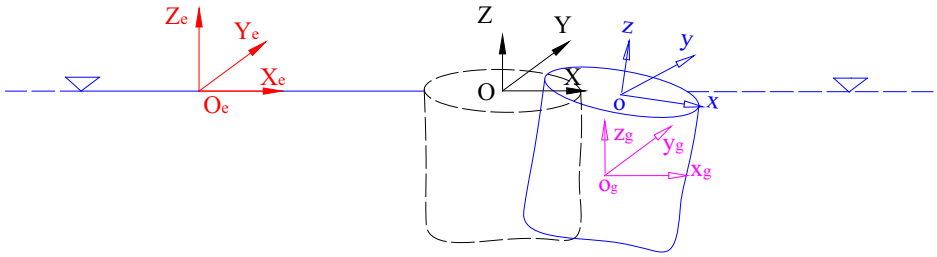

Fig.2.1. Definition of different coordinate systems.

2.3 The definition of the motions

Let us define the translatory motion vector of the origin of oxyz relative to the origin of OXYZ, i.e. $\overrightarrow{Oo}$, be $\vec{\xi}=(\xi_1,\xi_2,\xi_3)$ so that ξ_1 is the surge, ξ_2 is the sway and ξ_3 is the heave. In addition, we define the Euler angles α_4, α_5 and α_6 about the X-, Y- and Z-axis respectively so that α_4 is the roll, α_5 is the pitch and α_6 is the yaw. The centre of the angular motions α_4, α_5 and α_6 is the origin of OXYZ system. Here $\vec{\xi}=(\xi_1,\xi_2,\xi_3)$ and $\vec{\alpha}=(\alpha_4,\alpha_5,\alpha_6)$ are described in the inertial coordinate system OXYZ.

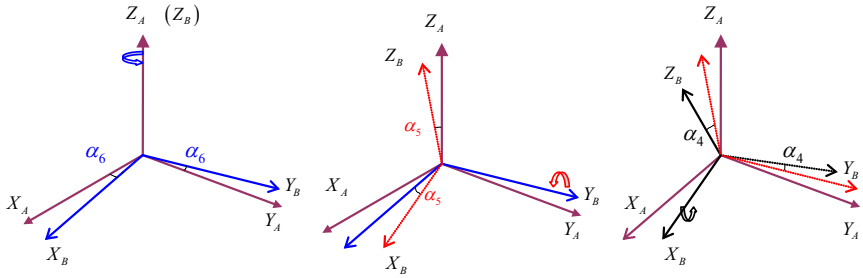

(a) Rotation in yaw (α_6) (b) Rotation in pitch (α_5) (c) Rotation in roll (α_4)

Fig.2.2. The order of the rotation of the Euler angles α_4, α_5 and α_6. The rotations in (b) and (c) are taken respectively with respect to the updated Y_B- and X_B-axis due to the previous rotations.

Similarly, we define $\vec{\xi}_g=(\xi_{1,g},\xi_{2,g},\xi_{3,g})$ as the translatory motion vector of the origin of $o_gx_gy_gz_g$

system relative to the origin of OXYZ. $\xi_{1,g}$ is the surge, $\xi_{2,g}$ is the sway and $\xi_{3,g}$ is the heave. The vector $\vec{\xi}_g$ is defined with respect to OXYZ reference frame. Furthermore, an angular motion vector $\vec{\alpha}_g = \left(\alpha_{4,g}, \alpha_{5,g}, \alpha_{6,g}\right)$ is defined. $\alpha_{4,g}$, $\alpha_{5,g}$ and $\alpha_{6,g}$ are the roll, pitch and yaw angle about the X-, Y- and Z-axis respectively. Here $\alpha_{4,g}$, $\alpha_{5,g}$ and $\alpha_{6,g}$ are defined with respect to COG of the body.

Now consider a point with position vector $\vec{r}_A$ in the $O_A X_A Y_A Z_A$ coordinate system and $\vec{r}_B$ in the $O_B X_B Y_B Z_B$ coordinate system. See Fig. 2.2. $O_A X_A Y_A Z_A$ and $O_B X_B Y_B Z_B$ can be any of the coordinate systems defined in Fig.2.1. $\vec{r}_A$ and $\vec{r}_B$ have the following relationship

$$\vec{r}_B = \overrightarrow{O_B O_A} + \mathbf{R}_{A\to B}\vec{r}_A \quad . \tag{2.8}$$

$\overrightarrow{O_B O_A}$ is the vector from O_B to O_A. $\mathbf{R}_{A\to B}$ is the transformation matrix, which is dependent on the Euler angles and the order of the Euler angles. $\mathbf{R}_{A\to B}$ can be determined as follows. First of all, we let $O_A X_A Y_A Z_A$ and $O_B X_B Y_B Z_B$ coincide. After that, $O_B X_B Y_B Z_B$ is rotated an angle α_6 in yaw about Z_B-axis, then an angle in pitch α_5 about its updated Y_B-axis, and finally an angle α_4 in roll about the updated X_B-axis. See Fig.2.2 as an illustration. With the yaw-pitch-roll Euler angle order, $\mathbf{R}_{A\to B}$ can be expressed as

$$\mathbf{R}_{A\to B} = \mathbf{ABC} = \begin{bmatrix} c_6c_5 & c_6s_5s_4 - s_6c_4 & c_6s_5c_4 + s_6s_4 \\ s_6c_5 & s_6s_5s_4 + c_6c_4 & s_6s_5c_4 - c_6s_4 \\ -s_5 & c_5s_4 & c_5c_4 \end{bmatrix} \tag{2.9}$$

where

$$\mathbf{A} = \begin{bmatrix} c_6 & -s_6 & 0 \\ s_6 & c_6 & 0 \\ 0 & 0 & 1 \end{bmatrix},\ \mathbf{B} = \begin{bmatrix} c_5 & 0 & s_5 \\ 0 & 1 & 0 \\ -c_5 & 0 & c_5 \end{bmatrix},\ \mathbf{C} = \begin{bmatrix} 1 & 0 & 0 \\ 0 & c_4 & -c_4 \\ 0 & c_4 & c_4 \end{bmatrix}. \tag{2.10}$$

Here $s_i = \sin\left(\alpha_i\right)$ and $c_i = \cos\left(\alpha_i\right)$ with i=4, 5, 6.

According to Ogilvie (1983), the transformation matrix $\mathbf{R}_{A\to B}$ can be interpolated in two ways:

Interpretation 1:

It transforms the representation of vector $\vec{r}_A$ in $O_A X_A Y_A Z_A$ system into its representation in $O_B X_B Y_B Z_B$ by $\mathbf{R}_{A\to B}\vec{r}_A$;

Interpretation 2:

It changes a vector $\vec{r}_A$ into another vector $\vec{r}_B$, both in the same reference frame.

Both the interpretations will be used in the later derivations. Note that the product of the transformation matrix $\mathbf{R}_{A\to B}$ and $\mathbf{R}_{B\to A}$ is an identity matrix. That means, if a vector $\vec{r}_A$ has been transformed into another vector by $\mathbf{R}_{B\to A}\vec{r}_A$, one can recover it by using another transformation matrix $\mathbf{R}_{A\to B}$, i.e. $\mathbf{R}_{A\to B}\left(\mathbf{R}_{B\to A}\vec{r}_A\right) = \vec{r}_A$.

If we take $O_A X_A Y_A Z_A$ as the body-fixed reference frame oxyz in Fig.2.1 and $O_B X_B Y_B Z_B$ as the inertial reference frame OXYZ in Fig.2.1, and assume that the Euler angles are small, we have the following approximation of the transformation matrix

$$\mathbf{R}_{b\to i} = I + \mathbf{R}^{(1)}_{b\to i} + \mathbf{R}^{(2)}_{b\to i} + O\left(\varepsilon^3\right) \tag{2.11}$$

where

$$\mathbf{I} = \begin{bmatrix} 1 & 0 & 0 \\ 0 & 1 & 0 \\ 0 & 0 & 1 \end{bmatrix}, \tag{2.12}$$

$$\mathbf{R}^{(1)}_{b\to i} = \begin{bmatrix} 0 & -\alpha_6^{(1)} & \alpha_5^{(1)} \\ \alpha_6^{(1)} & 0 & -\alpha_4^{(1)} \\ -\alpha_5^{(1)} & \alpha_4^{(1)} & 0 \end{bmatrix}, \tag{2.13}$$

$$\mathbf{R}^{(2)}_{b\to i} = \begin{bmatrix} 0 & -\alpha_6^{(2)} & \alpha_5^{(2)} \\ \alpha_6^{(2)} & 0 & -\alpha_4^{(2)} \\ -\alpha_5^{(2)} & \alpha_4^{(2)} & 0 \end{bmatrix} + \begin{bmatrix} -\frac{1}{2}[(\alpha_5^{(1)})^2 + (\alpha_6^{(1)})^2] & \alpha_4^{(1)}\alpha_5^{(1)} & \alpha_4^{(1)}\alpha_6^{(1)} \\ 0 & -\frac{1}{2}[(\alpha_4^{(1)})^2 + (\alpha_6^{(1)})^2] & \alpha_5^{(1)}\alpha_6^{(1)} \\ 0 & 0 & -\frac{1}{2}[(\alpha_4^{(1)})^2 + (\alpha_5^{(1)})^2] \end{bmatrix} \tag{2.14}$$

Here the superscript (1) and (2) indicate the first-order and second-order quantities, respectively. The 'b' in the subscript is the shorthand of the 'body-fixed' and 'i' means 'inertial'. Similarly, the inverse transformation matrix $\mathbf{R}_{i\to b}$ can be approximated as

$$\mathbf{R}_{i\to b} = I + \mathbf{R}^{(1)}_{i\to b} + \mathbf{R}^{(2)}_{i\to b} + O\left(\varepsilon^3\right), \tag{2.15}$$

where

$$\mathbf{R}^{(k)}_{i\to b} = \left[\mathbf{R}^{(k)}_{b\to i}\right]^T \quad , \text{k=1, 2.} \tag{2.16}$$

The superscript '*T*' means the transpose of the matrix.

We will now define some vectors related to the rigid-body motions, gravitational acceleration, forward speed and the normal direction of a point on the body surface. These definitions will be used later in this chapter. Both the descriptions in the inertial coordinate system OXYZ and the body-fixed coordinate system oxyz are given. In order to distinguish the vectors in different coordinate systems, a prime will be used if a vector is described in the body-fixed coordinate system. A vector without a prime shall be considered as a description in the inertial reference frame.

(1) Translatory and angular velocity vectors

The translatory velocity vector $\dot{\vec{\xi}}$ and angular velocity vector $\vec{\omega}$ in the inertial coordinate system OXYZ can be obtained directly by time differentiation. They can be written respectively as

$$\dot{\vec{\xi}} = \dot{\vec{\xi}}^{(1)} + \dot{\vec{\xi}}^{(2)} + O\left(\varepsilon^3\right) \tag{2.17}$$

$$\vec{\omega} = \vec{\omega}^{(1)} + \vec{\omega}^{(2)} + O\left(\varepsilon^3\right) \tag{2.18}$$

with

$$\dot{\vec{\xi}}^{(k)} = \left(\dot{\xi}_1^{(k)}, \dot{\xi}_2^{(k)}, \dot{\xi}_3^{(k)}\right)^T, \text{k=1, 2,} \tag{2.19}$$

$$\vec{\omega}^{(k)} = \left(\dot{\alpha}_4^{(k)}, \dot{\alpha}_5^{(k)}, \dot{\alpha}_6^{(k)}\right)^T, \text{ k=1, 2.} \tag{2.20}$$

Using the *Interpretation 1* of the transformation matrix, we can obtain the representations of the translatory velocity vector $\dot{\vec{\xi}}'$ in oxyz system as

$$\dot{\vec{\xi}}' = \mathbf{R}_{i\to b}\dot{\vec{\xi}} = \dot{\vec{\xi}}'^{(1)} + \dot{\vec{\xi}}'^{(2)} + O\left(\varepsilon^3\right) \tag{2.21}$$

with

$$\dot{\vec{\xi}}'^{(1)} = \dot{\vec{\xi}}^{(1)}, \tag{2.22}$$

$$\dot{\vec{\xi}}'^{(2)} = \dot{\vec{\xi}}^{(2)} + \mathbf{R}_{i\to b}^{(1)}\dot{\vec{\xi}}^{(1)}. \tag{2.23}$$

According to the definition of the Euler angles in Fig.2.2, the angular velocity $\vec{\omega}'$ in the body-fixed coordinate system can be expressed as

$$\vec{\omega}' = \dot{\alpha}_4\vec{e}_1 + \dot{\alpha}_5\vec{e}_2 + \dot{\alpha}_6\vec{e}_3. \tag{2.24}$$

Here $\vec{e}_1$, $\vec{e}_2$ and $\vec{e}_3$ are unit vectors along the X_B-axis in Fig.2.2c, the Y_B-axis in Fig.2.2b and Z_B-axis in Fig.2.2a, respectively. Putting

$$\vec{e}_1 = \begin{bmatrix}1\\0\\0\end{bmatrix},\ \vec{e}_2 = \mathbf{C}^T\begin{bmatrix}0\\1\\0\end{bmatrix},\ \vec{e}_3 = \mathbf{C}^T\mathbf{B}^T\begin{bmatrix}0\\0\\1\end{bmatrix} \tag{2.25}$$

into Eq.(2.24), we have that

$$\vec{\omega}' = \vec{\omega}'^{(1)} + \vec{\omega}'^{(2)} + O\left(\varepsilon^3\right), \tag{2.26}$$

with

$$\vec{\omega}'^{(1)} = \begin{bmatrix}\dot{\alpha}_4^{(1)}\\ \dot{\alpha}_5^{(1)}\\ \dot{\alpha}_6^{(1)}\end{bmatrix},\ \vec{\omega}'^{(2)} = \begin{bmatrix}\dot{\alpha}_4^{(2)} + \dot{\alpha}_6^{(1)}\alpha_5^{(1)}\\ \dot{\alpha}_5^{(2)} - \dot{\alpha}_6^{(1)}\alpha_4^{(1)}\\ \dot{\alpha}_6^{(2)} + \dot{\alpha}_6^{(1)}\alpha_4^{(1)}\end{bmatrix}. \tag{2.27}$$

(2) Displacement and velocity of a point on the body

Using the *Interpretation 2* of $\mathbf{R}_{A\to B}$ described associated with Eq.(2.9), we can express the displacement vector $\vec{x}$ and the velocity vector $\vec{u}$ of a point due to the unsteady rigid-body motions as

$$\vec{x} = \vec{x}^{(1)} + \vec{x}^{(2)} + O\left(\varepsilon^3\right), \tag{2.28}$$

$$\vec{u} = \vec{u}^{(1)} + \vec{u}^{(2)} + O\left(\varepsilon^3\right), \tag{2.29}$$

with

$$\vec{x}^{(k)} = \left(x_1^{(k)}, x_2^{(k)}, x_3^{(k)}\right)^T = \vec{\xi}^{(k)} + \mathbf{R}_{b\to i}^{(k)}\vec{r}', \text{ k=1, 2,} \tag{2.30}$$

$$\vec{u}^{(k)} = \left(u_1^{(k)}, u_2^{(k)}, u_3^{(k)}\right)^T = \dot{\vec{\xi}}^{(k)} + \dot{\mathbf{R}}_{b\to i}^{(k)}\vec{r}', \text{ k=1, 2.} \tag{2.31}$$

The overdots in Eq.(2.31) indicate time differentiation. $\vec{\xi}^{(k)} = \left(\vec{\xi}_1^{(k)}, \vec{\xi}_2^{(k)}, \vec{\xi}_3^{(k)}\right)$ is the k-th order translatory motion vector. $\vec{r}' = \left(x, y, z\right)$ is the position vector of the point in the body-fixed coordinate system. $\vec{x}$ and $\vec{u}$ are vectors described in the inertial coordinate system OXYZ. Their

corresponding representations in the body-fixed coordinate system can be obtained by using the *Interpretation 1* of the transformation matrix

$$\vec{x}' = \mathbf{R}_{i\to b}\vec{x} = \vec{x}'^{(1)} + \vec{x}'^{(2)} + O\left(\varepsilon^3\right), \tag{2.32}$$

$$\vec{u}' = \mathbf{R}_{i\to b}\vec{u} = \vec{u}'^{(1)} + \vec{u}'^{(2)} + O\left(\varepsilon^3\right), \tag{2.33}$$

with

$$\vec{x}'^{(1)} = \vec{x}^{(1)}, \tag{2.34}$$

$$\vec{x}'^{(2)} = \vec{x}^{(2)} + \mathbf{R}^{(1)}_{i\to b}\vec{x}^{(1)}, \tag{2.35}$$

$$\vec{u}'^{(1)} = \vec{u}^{(1)}, \tag{2.36}$$

$$\vec{u}'^{(2)} = \vec{u}^{(2)} + \mathbf{R}^{(1)}_{i\to b}\vec{u}^{(1)}. \tag{2.37}$$

(3) Gravitational acceleration vector

The description of the gravitational acceleration vector $\vec{g} = -g\vec{K}$ in the body-fixed coordinate system oxyz can be approximated as

$$\vec{g}' = \mathbf{R}_{i\to b}\vec{g} = \vec{g}'^{(0)} + \vec{g}'^{(1)} + \vec{g}'^{(2)} + O\left(\varepsilon^3\right), \tag{2.38}$$

with $\vec{g}'^{(0)}$, $\vec{g}'^{(1)}$, $\vec{g}'^{(2)}$ defined respectively as

$$\vec{g}'^{(0)} = -g\begin{bmatrix}0\\0\\1\end{bmatrix}, \quad \vec{g}'^{(1)} = \begin{bmatrix}g_1^{(1)}\\g_2^{(1)}\\g_3^{(1)}\end{bmatrix} = g\begin{bmatrix}\alpha_5^{(1)}\\-\alpha_4^{(1)}\\0\end{bmatrix}, \quad \vec{g}'^{(2)} = \begin{bmatrix}g_1^{(2)}\\g_2^{(2)}\\g_3^{(2)}\end{bmatrix} = \frac{g}{2}\begin{bmatrix}2\alpha_5^{(2)}\\-2\alpha_4^{(2)}\\(\alpha_4^{(1)})^2+(\alpha_5^{(1)})^2\end{bmatrix}. \tag{2.39}$$

$\vec{K}$ is the unit directional vector along the Z-axis of the OXYZ system.

(4) Forward speed vector

In this study, the forward speed is assumed to be always parallel to the X-axis. In the inertial coordinate system OXYZ, the forward vector is $\vec{U}$=$U\vec{I}$ with $\vec{I}$ the unit directional vector along the X-axis. However, when observed in the body-fixed coordinate system, it has components in x-, y- and z-directions due to the angular motions of the body. The forward speed vector in the body-fixed coordinate system $\vec{U}'$ can be obtained by using the *Interpretation 1* of the transformation matrix in Eq.(2.9) as

$$\vec{U}' = \mathbf{R}_{i\to b}\vec{U} = \vec{U}'^{(0)} + \vec{U}'^{(1)} + \vec{U}'^{(2)} + O\left(\varepsilon^3\right), \tag{2.40}$$

where

$$\vec{U}'^{(0)} = U\begin{bmatrix}1\\0\\0\end{bmatrix}, \ \vec{U}'^{(1)} = \begin{bmatrix}U_1'^{(1)}\\U_2'^{(1)}\\U_3'^{(1)}\end{bmatrix} = U\begin{bmatrix}0\\-\alpha_6^{(1)}\\\alpha_5^{(1)}\end{bmatrix}, \ \vec{U}'^{(2)} = \begin{bmatrix}U_1'^{(2)}\\U_2'^{(2)}\\U_3'^{(3)}\end{bmatrix} = U\begin{bmatrix}-\frac{1}{2}[(\alpha_5^{(1)})^2+(\alpha_6^{(1)})^2]\\-\alpha_6^{(2)}+\alpha_4^{(1)}\alpha_5^{(1)}\\\alpha_5^{(2)}+\alpha_4^{(1)}\alpha_6^{(1)}\end{bmatrix}. \tag{2.41}$$

(5) Normal vector on the body surface

The normal vector on the body surface observed in the inertial coordinate system OXYZ can be approximated as

$$\vec{n} = \vec{n}^{(0)} + \vec{n}^{(1)} + \vec{n}^{(2)} + O\left(\varepsilon^3\right), \tag{2.42}$$

with

$$\vec{n}^{(k)} = \mathbf{R}_{b\to i}^{(k)} \vec{n}^{(0)}, \text{ k=1, 2.} \tag{2.43}$$

Here $\vec{n}^{(0)}$ is the normal vector when the body is at rest. It is the same as the normal vector of the body surface described in the body-fixed coordinate system, i.e. $\vec{n}'$. In this study, the normal vector is defined as positive pointing out of the water domain.

2.4 Formulation of the second-order wave-body problem in the inertial coordinate system

The formulation of the second-order wave-body problem in the inertial coordinate system OXYZ (see Fig.2.1) will be presented. A small forward speed is taken into account. We will in this section denote the instantaneous free surface as SF and the body surface as SB, with their mean position as SF_0 and SB_0. The seabed is assumed horizontally along the plane Z=-h.

The governing equation is the Laplace equation as it is stated at the beginning of this chapter. A general description of the free-surface conditions and the body boundary condition is given in Section 2.4.1. In section 2.4.2, we will present the first-order and second-order free-surface conditions together with corresponding body boundary conditions. The formulation is accurate to second order in wave steepness (and the unsteady body motions) and to first order in Froude number.

2.4.1 General description of the boundary conditions

The kinematic free-surface condition states that the fluid particles on the free surface remain on the free surface. Because we are interested in the weakly-nonlinear wave-body problems in this study, the free-surface elevation will be assumed to be a single-valued function of the two horizontal coordinates X and Y in the inertial coordinate system OXYZ. Thus the kinematic free-surface condition takes the following form

$$\left(\frac{\partial}{\partial t} - \vec{U}\cdot\nabla\right)\eta = \phi_Z - \phi_X\eta_X - \phi_Y\eta_Y \quad \text{on Z}=\eta\left(X,Y,t\right), \tag{2.44}$$

where η is the wave elevation. $\vec{U}=\left(U,0,0\right)^T$ is the forward speed vector. The $-\vec{U}\cdot\nabla\eta$ term in Eq.(2.44) is a consequence of applying the Lorentz transformation between (X, Y, Z) in the inertial coordinate system moving with the forward speed and (X_e, Y_e, Z_e) in the Earth-fixed coordinate system (see the definitions of (X, Y, Z) and (X_e, Y_e, Z_e) in Fig.2.1), i.e. $\partial/\partial t = \partial/\partial t - \vec{U}\cdot\nabla$. Eq.(2.44) is not valid when a plunging breaker occurs. The wave elevation of the plunging breaker cannot be described by a single-valued function of the horizontal coordinates. In that case, one needs a formulation which tracks the free surface according to the fluid velocity of the free surface particles. See for instance Greco (2001).

The dynamic free-surface condition follows by imposing the Bernoulli's equation on the free surface and requiring the hydrodynamic pressure to be equal to the atmospheric pressure, i.e.

$$\left(\frac{\partial}{\partial t}-\vec{U}\cdot\nabla\right)\phi+g\eta+\frac{1}{2}\nabla\phi\cdot\nabla\phi=0 \quad \text{on Z=}\eta\left(X,Y,t\right). \tag{2.45}$$

Here g is the acceleration of gravity. The $-\vec{U}\cdot\nabla\phi$ term in Eq.(2.45) is due to the Lorentz transformation between the inertial coordinate system OXYZ and the Earth-fixed coordinate system (X_e, Y_e, Z_e).

The body boundary condition

$$\frac{\partial\phi}{\partial n}=\vec{n}\cdot(\vec{U}+\vec{u}+\vec{\omega}\times\vec{r}\,) \quad \text{on SB} \tag{2.46}$$

ensures that fluid particles cannot penetrate the body surface. Here all the vectors are defined in the inertial coordinate system OXYZ. In this work, the forward speed is assumed positive in the X-direction. Rigid-body motions are assumed with $\vec{u}$ as the unsteady translational velocity of the origin of the body-fixed coordinate system oxyz (see Fig.2.1) and $\vec{\omega}$ as the rotational velocity of the body with respect to the origin of the body-fixed coordinate system oxyz. $\vec{n}$ is the normal vector on the body surface, which is defined positive pointing out of the water domain. $\vec{r}$ is the position vector of a point on the body surface relative to the origin of the body-fixed reference frame oxyz.

2.4.2 Second-order approximations of the boundary conditions

If the amplitudes of the incident waves and the body motions relative to the characteristic body dimensions are asymptotically small, we can Taylor expand the free-surface conditions and body boundary condition about the mean free surface and the mean body position, respectively. Strictly speaking we must require the solution to be analytic which means that the expansion is not valid near a sharp corner with interior angle less than π radians on the body surface.

In Section 2.1, we have presented the series expansions of the velocity potential and the wave elevation. The expansions were made with respect to a perturbation parameter ε related to the wave steepness and the unsteady body motions. No approximation has been made with respect to the forward speed. In order to simplify the analysis, we will only consider a small forward speed.

The leading order of the wave elevation, i.e. $\eta^{(0)}$ in Eq.(2.3), is of $O(U^2)$. This can be understood by putting $\eta^{(0)}$ and $\phi^{(0)}$ into the dynamic free-surface condition (2.45). The $\phi_t^{(0)}$ term is zero because $\phi^{(0)}$ is time-independent. In this work, we only consider a small forward speed. Approximation will be made correct to $O(\delta)$ and $O(\varepsilon^2)$. Here δ is a small parameter related to the Froude number and ε is a parameter measuring the smallness of the wave slope and the unsteady body motions. That means the steady wave elevation $\eta^{(0)}$ is neglected in the following derivations, i.e.

$$\eta=\varepsilon^1\eta^{(1)}+\varepsilon^2\eta^{(2)}+\varepsilon^3\eta^{(3)}+\cdots. \tag{2.47}$$

The steady velocity potential $\phi^{(0)}$ can be determined as the solution of the so-called 'double-body' flow with no steady waves effects included.

Introducing the following series expansions Eq.(2.2) and Eq.(2.47) into Eq.(2.44) and Eq.(2.45),

Taylor expanding Eq.(2.44) and Eq.(2.45) about Z=0 and collecting consistent terms of the same order, we can obtain the free-surface conditions at each order as

$$\frac{\partial \eta_s^{(m)}}{\partial t} = \frac{\partial \phi_s^{(m)}}{\partial Z} + \left(\frac{\partial \phi_{in}^{(m)}}{\partial Z} - \frac{\partial \eta_{in}^{(m)}}{\partial t} \right) + F_1^{(m)} \quad \text{, on Z=0,} \tag{2.48}$$

$$\frac{\partial \phi_s^{(m)}}{\partial t} = -g\eta_s^{(m)} - \left(g\eta_{in}^{(m)} + \frac{\partial \phi_{in}^{(m)}}{\partial t} \right) + F_2^{(m)} \text{, on Z=0,} \tag{2.49}$$

with the forcing terms $F_1^{(m)}$, $F_2^{(m)}$ (m=1, 2) defined as

$$F_1^{(1)} = U\frac{\partial \eta^{(1)}}{\partial X} - \overline{\nabla}\phi^{(0)} \cdot \overline{\nabla}\eta^{(1)} + \eta^{(1)}\frac{\partial^2 \phi^{(0)}}{\partial Z^2}, \tag{2.50}$$

$$F_2^{(1)} = U\frac{\partial \phi^{(1)}}{\partial X} - \nabla\phi^{(0)} \cdot \nabla\phi^{(1)}, \tag{2.51}$$

$$F_1^{(2)} = U\frac{\partial \eta^{(2)}}{\partial X} - \overline{\nabla}\phi^{(0)} \cdot \overline{\nabla}\eta^{(2)} - \overline{\nabla}\phi^{(1)} \cdot \overline{\nabla}\eta^{(1)} + \eta^{(1)}\frac{\partial^2 \phi^{(1)}}{\partial Z^2} + \eta^{(2)}\frac{\partial^2 \phi^{(0)}}{\partial Z^2}, \tag{2.52}$$

$$\begin{aligned} F_2^{(2)} = {} & -\eta^{(1)}\frac{\partial^2 \phi^{(1)}}{\partial Z \partial t} + U\left[\frac{\partial \phi^{(2)}}{\partial X} + \eta^{(1)}\frac{\partial^2 \phi^{(1)}}{\partial X \partial Z} \right] - \frac{1}{2}\nabla\phi^{(1)} \cdot \nabla\phi^{(1)} \\ & -\eta^{(1)}\left[\nabla\left(\frac{\partial \phi^{(0)}}{\partial Z} \right) \cdot \nabla\phi^{(1)} + \nabla\left(\frac{\partial \phi^{(1)}}{\partial Z} \right) \cdot \nabla\phi^{(0)} \right] \end{aligned} . \tag{2.53}$$

The superscript indicates the order of quantity and the subscript means partial differentiation. For instance, $\phi^{(0)}$ is the steady velocity potential, which reflects the effect of the small parameter δ related to the Froude number. In Eq.(2.48) and Eq.(2.49), the subscript 's' and 'in' denote the scattered and incident part of the solution, respectively. The gradient operators ∇ and $\overline{\nabla}$ are defined respectively as

$$\nabla = \vec{I}\frac{\partial}{\partial X} + \vec{J}\frac{\partial}{\partial Y} + \vec{K}\frac{\partial}{\partial Z}, \tag{2.54}$$

$$\overline{\nabla} = \vec{I}\frac{\partial}{\partial X} + \vec{J}\frac{\partial}{\partial Y} \quad . \tag{2.55}$$

$\vec{I}$, $\vec{J}$ and $\vec{K}$ are unit vector along X-, Y- and Z-axis, respectively.

The body boundary conditions at each order follow by the Taylor expansion of the body boundary condition Eq.(2.46)

$$\frac{\partial \phi_s^{(m)}}{\partial n} = B^{(m)} \quad \text{on } SB_0 \tag{2.56}$$

with

$$B^{(1)} = \vec{n}^{(0)} \cdot \left[\vec{u}^{(1)} - \nabla\phi_{in}^{(1)} - \left(\vec{x}^{(1)} \cdot \nabla \right)\nabla\phi^{(0)} \right] + \vec{n}^{(1)} \cdot \left(U\vec{i} - \nabla\phi^{(0)} \right) \quad , \tag{2.57}$$

$$B^{(2)} = \vec{n}^{(0)} \cdot [\vec{u}^{(2)} - \nabla \phi_{in}^{(2)} - \left(\vec{x}^{(1)} \cdot \nabla\right) \nabla \phi^{(1)} - \left(\vec{x}^{(2)} \cdot \nabla\right) \nabla \phi^{(0)} - \frac{1}{2} \left(\vec{x}^{(1)} \cdot \nabla\right)^2 \nabla \phi^{(0)}] + \vec{n}^{(1)} \cdot \left[\vec{u}^{(1)} - \nabla \phi^{(1)} - \left(\vec{x}^{(1)} \cdot \nabla\right) \nabla \phi^{(0)}\right] + \vec{n}^{(2)} \cdot \left[U\vec{i} - \nabla \phi^{(0)}\right] \quad . \tag{2.58}$$

Here $\vec{n}^{(k)}$ (k=0, 1, 2) is the normal vector. $\vec{x}^{(k)}$ and $\vec{u}^{(k)}$ (k=1, 2) are the unsteady displacement and velocity of a point on the body, respectively. See the definitions in Section 2.3.

The double-gradient term in the first-order body boundary condition, i.e. Eq.(2.57), is associated with the so-called m_j-terms in the literature, which was introduced by Ogilvie & Tuck (1969). The second-order body boundary condition, i.e. Eq.(2.58), is more complicated since it involves three double-gradient terms and a triple-gradient term. The double and triple gradient terms in the body boundary conditions represent great numerical difficulties for marine structures with high-curvature surface.

The body boundary conditions in Eq.(2.56) are based on Taylor expansion about the mean body surface. This indicates that the fluid velocity has been assumed to be analytic at the mean body surface. This assumption is violated near the sharp corners. The consequence of applying the body boundary conditions Eq.(2.56) with the forcing terms defined in Eq.(2.57) and Eq.(2.58) in the wave-body analysis with forward speed effect is that the resulting boundary integral equations (BIEs) are not integrable. Why the BIEs are not integrable can be partly understood by a two-dimensional corner flow. See Chapter 5 for the details.

One should note that we have neglected some of the $O(U^2)$ terms in the formulation of the boundary conditions. In order to access for how large forward speed or current velocity the present theory can be applied, one has to consider the parameter $\tau = \omega_e U / g$, which is simply the product of the Froude number and the non-dimensional frequency of encounter. Here U is the forward speed in either the same or the opposite direction as the heading of the incident wave. ω_e is the encounter frequency. In a linear problem, $\omega_e = \omega_0 \pm kU$, where ω_0 is the fundamental frequency of the incident wave. In a second-order problem with regular incident waves, ω_e is interoperated as $2\left(\omega_0 \pm kU\right)$. Theoretically, it is known that important changes happen in the linear body-generated wave systems at τ=0.25. There is no upstream wave system when τ>0.25, while both upstream and downstream wave exist with τ<0.25. It was reported by Zhao & Faltinsen (1988) who used a similar theory correct to $O(\delta)$ and $O(\varepsilon)$ in a two-dimensional linear wave-body-current interaction problem that, the body generated both upstream waves and downstream waves when $\tau > 0.25$. In all the cases studies in this thesis, we have limited ourselves to $\tau < 0.25$.

2.4.3 Forces and moments calculation

Integrating properly the pressure on the instantaneous body surface gives the forces and moments, which may either be defined with respect to the inertial coordinate system OXYZ or the body-fixed coordinate system oxyz (see Fig.2.1). When the forces and moments are defined with respect to OXYZ, they can be expressed respectively as

$$\vec{F} = \iint_{SB} p\vec{n}\, ds, \tag{2.59}$$

$$\vec{M} = \iint_{SB} p\left[\left(\vec{r} - \vec{r}_c\right) \times \vec{n}\right] ds. \tag{2.60}$$

Here p is the pressure on the instantaneous wetted body surface SB(t). $\vec{n}$ is the normal vector on SB(t), which is defined to be positive pointing out of the fluid domain. $\vec{r}=(\mathrm{X}, \mathrm{Y}, \mathrm{Z})$ is the position vector of a point on the body. $\vec{r}_c=(\mathrm{X_c}, \mathrm{Y_c}, \mathrm{Z_c})$ is the position vector of a point, to which the moments are defined with respect. All the vectors in Eq.(2.59) and Eq.(2.60) are defined with respect to OXYZ system.

When the problem is solved with the formulation in the inertial coordinate system, i.e. the free-surface conditions Eq.(2.48), Eq.(2.49) and the body boundary condition Eq.(2.56) are used, the solution, for instance the pressure, is obtained at the mean position of the body surface. The pressure on the instantaneous body surface is then approximated by Taylor expansion about the mean body surface, i.e.

$$p = p^{(0)} + p^{(1)} + p^{(2)} + O\left(\varepsilon^3\right). \tag{2.61}$$

$p^{(0)}$, $p^{(1)}$ and $p^{(2)}$ the hydrostatic, first-order and second-order pressure respectively defined as

$$p^{(0)} = -\rho g Z\,, \tag{2.62}$$

$$p^{(1)} = -\rho\left\{\phi_t^{(1)} - U\phi_X^{(1)} + \nabla\phi^{(0)}\cdot\nabla\phi^{(1)} + g x_3^{(1)}\right\}, \tag{2.63}$$

$$\begin{aligned} p^{(2)} = -\rho\Bigg\{ & \phi_t^{(2)} - U\left(\phi_X^{(2)} + \vec{x}^{(1)}\cdot\nabla\phi_X^{(1)}\right) + \nabla\phi^{(0)}\cdot\nabla\phi^{(2)} + \frac{1}{2}\nabla\phi^{(1)}\cdot\nabla\phi^{(1)} \\ & + \left(\vec{x}^{(1)}\cdot\nabla\right)\left(\phi_t^{(1)} + \nabla\phi^{(0)}\cdot\nabla\phi^{(1)}\right) + g x_3^{(2)}\Bigg\} \end{aligned}. \tag{2.64}$$

Here $x_3^{(1)}$ and $x_3^{(2)}$ are the first-order and second-order rigid-body displacement in Z-direction of a point on the body, respectively. See the definitions in Eq.(2.30).

Applying Eq.(2.61) and Eq.(2.42) in Eq.(2.59) and Eq.(2.60) leads us to the following approximation of $\vec{F}$ and $\vec{M}$

$$\vec{F} = \vec{F}^{(0)} + \vec{F}^{(1)} + \vec{F}^{(2)} + O\left(\varepsilon^3\right), \tag{2.65}$$

$$\vec{M} = \vec{M}^{(0)} + \vec{M}^{(1)} + \vec{M}^{(2)} + O\left(\varepsilon^3\right), \tag{2.66}$$

with

$$\vec{F}^{(0)} = \iint_{SB_0} p^{(0)}\vec{n}^{(0)}\,ds\,, \tag{2.67}$$

$$\vec{F}^{(1)} = \iint_{SB_0}\left[p^{(1)}\vec{n}^{(0)} + p^{(0)}\vec{n}^{(1)}\right]ds\,, \tag{2.68}$$

$$\vec{F}^{(2)} = \iint_{SB_0}\left[p^{(2)}\vec{n}^{(0)} + p^{(1)}\vec{n}^{(1)} + p^{(0)}\vec{n}^{(2)}\right]ds + \int_{CW_0}\frac{1}{2}\rho g\left[\eta^{(1)} - \left(\xi_3^{(1)} + Y\xi_4^{(1)} - X\xi_5^{(1)}\right)\right]^2\vec{n}^{(0)}dl\,, \tag{2.69}$$

$$\vec{M}^{(0)} = \iint_{SB_0} p^{(0)}\left[\left(\vec{r}-\vec{r}_c\right)\times\vec{n}^{(0)}\right]ds\,, \tag{2.70}$$

$$\vec{M}^{(1)} = \iint_{SB_0} p^{(1)}\left[\left(\vec{r}-\vec{r}_c\right)\times\vec{n}^{(0)}\right] + p^{(0)}\left[\left(\vec{r}-\vec{r}_c\right)\times\vec{n}^{(1)}\right]ds\,, \tag{2.71}$$

$$\vec{M}^{(2)} = \iint_{SB_0} \left\{ p^{(2)} \left[(\vec{r} - \vec{r}_c) \times \vec{n}^{(0)} \right] + p^{(1)} \left[(\vec{r} - \vec{r}_c) \times \vec{n}^{(1)} \right] + p^{(0)} \left[(\vec{r} - \vec{r}_c) \times \vec{n}^{(2)} \right] \right\} ds + \int_{CW_0} \frac{1}{2} \rho g \left[\eta^{(1)} - \left(\xi_3^{(1)} + Y \xi_4^{(1)} - X \xi_5^{(1)} \right) \right]^2 \left[(\vec{r} - \vec{r}_c) \times \vec{n}^{(0)} \right] dl \quad . \tag{2.72}$$

Here CW_0 is the mean waterline. The body surface in its static equilibrium position is assumed to be vertical in the free surface zone. The waterline integrals in Eq.(2.69) and Eq.(2.72) are caused by the fluctuation of the wetted body surface due to the relative motion between the wave profile and the body. $\left(\xi_3^{(1)} + Y \xi_4^{(1)} - X \xi_5^{(1)} \right)$ in Eq.(2.69) and Eq.(2.72) is related to the change of vertical position of the intersection between the mean body surface and the mean water surface due to unsteady rigid-body motions. Details of the derivations of the first-order and second-order forces/moments without considering the forward speed (or current) effect can be found, for instance, Standing et al. (1981), Pinkster (1981) and Ogilvie (1983). Faltinsen et al. (1981) included the steady forward speed effect. Our analysis here is similar to their derivations with the steady velocity potential effects included. The derivation of Eq.(2.69) and Eq.(2.72) is lengthy but straightforward, and will not be shown here.

One can alternatively define the forces and moments with respect to the body-fixed reference frame, i.e. oxyz. The results can be obtained by replacing $\vec{r}$ and $\vec{r}_c$ in Eq.(2.67) - Eq.(2.72) by $\vec{r}'$ and $\vec{r}_c'$ respectively, and setting the terms associated with $\vec{n}^{(1)}$ or $\vec{n}^{(2)}$ to be zero. $\vec{r}' = (x, y, z)$ and $\vec{r}_c' = (x_c, y_c, z_c)$ are the position vectors of points described in the body-fixed coordinate system corresponding to $\vec{r}$ and $\vec{r}_c$, respectively.

One should note that the Taylor expansion of the pressure about the mean body surface is only valid if the pressure is analytic near the mean body surface. For body with sharp corners, it is not suggested to use the formulation in the inertial coordinate system for wave-body analysis with presence of forward speed effects.

Using a formulation in the inertial coordinate system, Zhao & Faltinsen (1989b) reported that the two-dimensional added mass coefficients obtained by pressure integration on a body with sharp corner in a current are unphysical. Because the last term in Eq.(2.63), i.e. $-\rho g x_3^{(1)}$, only contributes to the restoring forces, it was not included in the calculation of the added mass coefficients. In Zhao & Faltinsen (1989b), the solution for $\nabla \phi^{(1)}$ was divided into two parts. The first part takes care of the m_j-terms in the linear body boundary condition and it is singular at the sharp corner. The other part is regular, which takes care of the rest of the boundary conditions. Following Zhao & Faltinsen's (1989b) analysis, it can be shown that $\nabla \phi^{(1)}$ is not integrable at the sharp corner, because it includes singular terms of $O(U^2)$. U is a small current speed in Zhao & Faltinsen's (1989b) study. Those singular terms involve the second-order derivatives of the steady velocity potential $\phi^{(0)}$ and therefore are not integrable. In order to get physical results, Zhao & Faltinsen (1989b) has to include an additional term of $O(U^2)$ in the Bernoulli's equation to cancel out the singular part in $\nabla \phi^{(1)}$. See Zhao & Faltinsen (1989b) for the details.

2.5 Formulation of the third-order diffraction problem in the Earth-fixed coordinate system

In Section 2.4.2, we have presented the first-order and second-order approximation of the free-surface and the body boundary conditions formulated in the inertial coordinate system. A small forward speed was taken into account. In this section, the third-order boundary conditions for a diffraction problem will be given. No forward speed or current effect is included. The body is restrained from oscillating in the incident waves. The first- and second-order boundary conditions and the corresponding formulas for forces and moments calculation can be obtained by setting all the terms associated with the forward speed U and steady velocity potential $\phi^{(0)}$ in the corresponding equations in Section 2.4.2 to be zero. In this section, only the third-order free-surface conditions, body boundary condition and formulas for third-order forces and moments will be given. In this case, the Earth-fixed coordinate system $O_eX_eY_eZ_e$, the inertial coordinate system OXYZ and the body-fixed coordinate system oxyz coincide with each other.

2.5.1 Free-surface conditions

The third-order free-surface conditions satisfied at Z=0 are written as

$$\begin{aligned}
&\frac{\partial \eta_s^{(3)}}{\partial t} = \frac{\partial \phi_s^{(3)}}{\partial Z} \\
&+\left(\eta^{(1)}\frac{\partial^2\phi^{(2)}}{\partial Z^2}+\eta^{(2)}\frac{\partial^2\phi^{(1)}}{\partial Z^2}\right)+\frac{1}{2}(\eta^{(1)})^2\frac{\partial^3\phi^{(1)}}{\partial Z^3}-\left(\bar{\nabla}\phi^{(1)}\cdot\bar{\nabla}\eta^{(2)}+\bar{\nabla}\phi^{(2)}\cdot\bar{\nabla}\eta^{(1)}\right)-\eta^{(1)}\bar{\nabla}\eta^{(1)}\cdot\bar{\nabla}\left(\frac{\partial\phi^{(1)}}{\partial Z}\right) \\
&-\left(\eta_{in}^{(1)}\frac{\partial^2\phi_{in}^{(2)}}{\partial Z^2}+\eta_{in}^{(2)}\frac{\partial^2\phi_{in}^{(1)}}{\partial Z^2}\right)-\frac{1}{2}(\eta_{in}^{(1)})^2\frac{\partial^3\phi_{in}^{(1)}}{\partial Z^3}+\left(\bar{\nabla}\phi_{in}^{(1)}\cdot\bar{\nabla}\eta_{in}^{(2)}+\bar{\nabla}\phi_{in}^{(2)}\cdot\bar{\nabla}\eta_{in}^{(1)}\right)+\eta_{in}^{(1)}\bar{\nabla}\eta_{in}^{(1)}\cdot\bar{\nabla}\left(\frac{\partial\phi_{in}^{(1)}}{\partial Z}\right)
\end{aligned} \tag{2.73}$$

and

$$\begin{aligned}
&\frac{\partial\phi_s^{(3)}}{\partial t} = -g\eta_s^{(3)} \\
&-\nabla\phi^{(1)}\cdot\nabla\phi^{(2)}-\eta^{(1)}\nabla\left(\frac{\partial\phi^{(1)}}{\partial Z}\right)\cdot\nabla\phi^{(1)}-\left(\eta^{(1)}\frac{\partial^2\phi^{(2)}}{\partial Z\partial t}+\eta^{(2)}\frac{\partial^2\phi^{(1)}}{\partial Z\partial t}\right)-\frac{1}{2}\left(\eta^{(1)}\right)^2\frac{\partial^3\phi^{(1)}}{\partial Z^2\partial t} \\
&-\nabla\phi_{in}^{(1)}\cdot\nabla\phi_{in}^{(1)}-\eta_{in}^{(1)}\nabla\left(\frac{\partial\phi_{in}^{(1)}}{\partial Z}\right)\cdot\nabla\phi_{in}^{(1)}-\left(\eta_{in}^{(1)}\frac{\partial^2\phi_{in}^{(2)}}{\partial Z\partial t}+\eta_{in}^{(2)}\frac{\partial^2\phi_{in}^{(1)}}{\partial Z\partial t}\right)-\frac{1}{2}\left(\eta_{in}^{(1)}\right)^2\frac{\partial^3\phi_{in}^{(1)}}{\partial Z^2\partial t}.
\end{aligned} \tag{2.74}$$

Here the operators ∇ and $\bar{\nabla}$ are defined in Eq.(2.54) and Eq.(2.55), respectively.

The third-order free-surface conditions in Eq.(2.73) and Eq.(2.74) do not require explicit expressions of the third-order velocity potential and wave elevation of the incident wave. Note that Eq.(2.73) and Eq.(2.74) contains an effect leading to that a secularity condition must be imposed in order to solve the problem. Discussion on the secularity effect will be made in Section 6.4 and Appendix D. The third-order time-domain simulations will be studied in Section 6.4 by using a two-dimensional wave tank. A two-time scales approach presented in Appendix D is used to eliminate the secular terms in a

third-order numerical wave tank (NWT).

2.5.2 Body boundary condition

The third-order body boundary condition for the diffraction of a stationary body takes the following simple form

$$\frac{\partial \phi_s^{(3)}}{\partial n} = -\frac{\partial \phi_{in}^{(3)}}{\partial n} \quad \text{on } SB_0 . \tag{2.75}$$

$\phi_{in}^{(3)}$ is the third-order velocity potential of the incident wave. SB_0 is the mean wetted body surface.

2.5.3 Forces and moments calculation

The third-order force vector is divided into three parts with the first part due to the first-order solution, the second part contributed by the product of the first-order and second-order quantities, and the third part by the third-order velocity potentials, i.e.

$$\vec{F}^{(3)} = \vec{F}_1^{(3)} + \vec{F}_2^{(3)} + \vec{F}_3^{(3)}, \tag{2.76}$$

where

$$\vec{F}_1^{(3)} = -\rho \int_{CW_0} \left[\frac{1}{2} (\eta^{(1)})^2 \phi_{tZ}{}^{(1)} + \frac{1}{2} (\nabla \phi^{(1)} \cdot \nabla \phi^{(1)}) \eta^{(1)} \right] \vec{n}^{(0)} dl \ , \tag{2.77}$$

$$\vec{F}_2^{(3)} = -\rho \iint_{SB_0} \nabla \phi^{(1)} \cdot \nabla \phi^{(2)} \vec{n}^{(0)} \, ds - \rho \int_{CW_0} \eta^{(1)} \phi_t^{(2)} \, \vec{n}^{(0)} dl , \tag{2.78}$$

$$\vec{F}_3^{(3)} = -\rho \iint_{SB_0} \phi_t^{(3)} \vec{n}^{(0)} \, ds . \tag{2.79}$$

Here we have assumed that the body surface in its static equilibrium position is vertical in the free surface zone. The derivation of Eq.(2.77) - Eq.(2.79) is tedious and only the final results are shown here. Basically, one starts with integrating the pressure on the instantaneous wetted body surface. The instantaneous wetted body surface is then considered as the sum of two parts, i.e. $SB_0 + \Delta S$. SB_0 is the mean wetted body surface. ΔS is the fluctuation of the wetted body surface due to of wave elevation. The velocity potential is assumed to be independent on Z-coordinate in the free surface zone. Introducing the Stokes series expansion of the velocity potential and wave elevation and colleting consistently the third-order terms, we can get Eq.(2.77) - Eq.(2.79). Note that $\vec{F}_2^{(3)}$ contains other two integrals along the mean waterline CW_0, i.e. $-\rho \int_{CW_0} \eta^{(2)} \phi_t^{(1)} \, \vec{n}^{(0)} dl$ and $-\rho \int_{CW_0} g \eta^{(1)} \eta^{(2)} \, \vec{n}^{(0)} dl$, which do not show up in Eq.(2.78) because they cancel out with each other. This is obvious if the first-order dynamic free-surface condition, i.e. $\phi_t^{(1)} = -g\eta^{(1)}$, is considered.

Similarly, the third-order moment about the origin of the coordinate system OXYZ can be expressed as

$$\vec{M}^{(3)} = \vec{M}_1^{(3)} + \vec{M}_2^{(3)} + \vec{M}_3^{(3)}, \tag{2.80}$$

where $\vec{M}_1^{(3)}$, $\vec{M}_2^{(3)}$ and $\vec{M}_3^{(3)}$ can be obtained by replacing $\vec{n}^{(0)}$ with $\vec{r} \times \vec{n}^{(0)}$ in Eq.(2.77), Eq.(2.78) and Eq.(2.79), respectively.

2.6 Formulation of the second-order wave-body problem in the body-fixed coordinate system

Inertial coordinate systems are traditionally used in weakly-nonlinear wave-body problems whilst body-fixed coordinate systems are commonly applied in analysis of ship maneuvering and sloshing (Faltinsen & Timokha, 2009). The Laplace equation for the velocity potential still holds in an accelerated coordinate system while the free-surface conditions and body boundary conditions change. A vector with a prime is expressed in the body-fixed coordinate system, i.e. oxyz. Otherwise, it is described in the inertial frame. See Section 2.2 for the definitions of different coordinate systems.

2.6.1 Free-surface conditions

The fully-nonlinear formulation of the free-surface conditions in a non-inertial coordinate system can be found in, for instance Faltinsen &Timokha (2009), as

$$\eta_t = \phi_z - \phi_x\eta_x - \phi_y\eta_y - (\vec{U}' + \dot{\vec{\xi}}' + \vec{\omega}' \times \vec{r}') \cdot (-\eta_x, -\eta_y, 1) \qquad \text{on } z=\eta(x,y,t), \tag{2.81}$$

$$\phi_t = -\frac{1}{2}\nabla\phi \cdot \nabla\phi + (\vec{U}' + \dot{\vec{\xi}}' + \vec{\omega}' \times \vec{r}') \cdot \nabla\phi - U_g \qquad \text{on } z=\eta(x,y,t). \tag{2.82}$$

Here the subscripts x, y, z, and t indicates partial differentiation. $\vec{r}' = (x, y, \eta)$ is the position vector of a point on the free surface. All the vectors are described in the body-fixed coordinate system, i.e. oxyz. The gradients are taken with respect to x, y and z, i.e. $\nabla = \vec{i}\frac{\partial}{\partial x} + \vec{j}\frac{\partial}{\partial y} + \vec{k}\frac{\partial}{\partial z}$.

U_g is the gravity potential. For a point $\vec{r}' = (x, y, \eta)$ on the free surface, U_g can be expressed as

$$U_g = -\vec{g} \cdot \left[\vec{\xi} + \mathbf{R}_{b\to i}\vec{r}' \right], \tag{2.83}$$

where $\vec{g} = -g\vec{K}$. $\vec{\xi} = \xi_1\vec{I} + \xi_2\vec{J} + \xi_3\vec{K}$ is the translatory motion vector of the origin of oxyz relative to the origin of OXYZ. See also the definition in Section 2.3. The second-order approximation of U_g can be obtained by using the second-order approximations of $\mathbf{R}_{b\to i}$ (see Eq.(2.11) - Eq.(2.14)), $\vec{\xi}$ and $\vec{g}$, i.e.

$$U_g = U_g^{(1)} + U_g^{(2)} + O(\varepsilon^3), \tag{2.84}$$

with

$$U_g^{(1)} = g(\eta^{(1)} + \xi_3^{(1)}) - (g_1^{(1)}x + g_2^{(1)}y), \tag{2.85}$$

$$U_g^{(2)} = g(\eta^{(2)} + \xi_3^{(2)}) - (g_1^{(2)}x + g_2^{(2)}y). \tag{2.86}$$

The free-surface elevation observed in the body-fixed coordinate system has two contributions. The first part is due to the rigid-body motions. It can be understood as follows. When the water is calm, i.e. no incoming or scattered waves, the calm water surface has a relative motion observed in the body-fixed reference frame due to the unsteady body motions. The other contribution is associated with the wave motion with the mentioned rigid-body motion effect excluded. Fig.2.3 shows a two-dimensional sketch of the definition of the wave elevation $\tilde{\eta}$ observed in the inertial coordinate

system OXYZ and the wave elevation η observed in the body-fixed coordinate system oxyz. $P(x,\eta)$ is a point on the instantaneous free surface. $(-\bar{\eta})$ is the displacement of a point (x,y,0) on the oxy-plane due to the rigid-body motions. α_5 is the pitch angle of the body. Keeping in mind that the rigid-body motions and the wave elevation are small, we can approximate the relationship between η and $\tilde{\eta}$ as

$$\eta = \bar{\eta} + \tilde{\eta} + O(\varepsilon^3). \tag{2.87}$$

From numerical point of view, it was found to be advantageous to use the decomposition in Eq.(2.87) and to operate with $\tilde{\eta}^{(i)}$ instead of $\eta^{(i)}$ in the free-surface conditions.

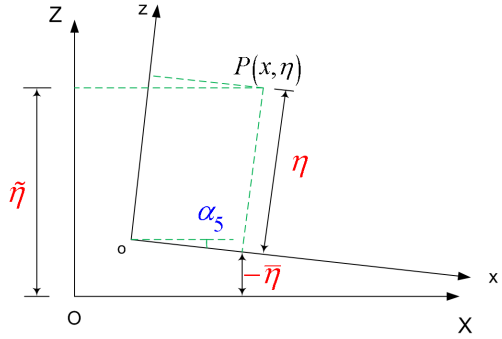

Fig.2.3. Definition of the wave elevations observed in the body-fixed coordinate system oxyz and the inertial coordinate system OXYZ.

Assuming the free-surface elevation η to be asymptotically small, we can similarly as shown in the inertial coordinate system, Taylor expand about the oxy-plane and collect consistent terms at each order. The resulting free-surface conditions can then be written as

$$\tilde{\eta}_t^{(m)} = \phi_z^{(m)} + f_1^{(m)} \quad \text{on z=0,} \tag{2.88}$$

$$\phi_t^{(m)} = -g\tilde{\eta}^{(m)} + f_2^{(m)} \quad \text{on z=0,} \tag{2.89}$$

with the forcing terms $f_1^{(m)}$, $f_2^{(m)}$ (m=1, 2) defined as follows:

$$f_1^{(1)} = \eta^{(1)}\phi_{zz}^{(0)} - (\phi_x^{(0)}\eta_x^{(1)} + \phi_y^{(0)}\eta_y^{(1)}) + U\eta_x^{(1)} - U_3'^{(1)}, \tag{2.90}$$

$$f_2^{(1)} = -\nabla\phi^{(0)}\cdot\nabla\phi^{(1)} + U\phi_x^{(1)} + \left(\vec{\chi}^{(1)} + \vec{U}'^{(1)}\right)\cdot\nabla\phi^{(0)}, \tag{2.91}$$

$$\begin{aligned} f_1^{(2)} = {} & \eta^{(2)}\phi_{zz}^{(0)} + \eta^{(1)}\phi_{zz}^{(1)} - (\phi_x^{(0)}\eta_x^{(2)} + \phi_y^{(0)}\eta_y^{(2)}) - (\phi_x^{(1)}\eta_x^{(1)} + \phi_y^{(1)}\eta_y^{(1)}) \\ & + U\eta_x^{(2)} + (U_1'^{(1)}\eta_x^{(1)} + U_2'^{(1)}\eta_y^{(1)}) - U_3'^{(2)} + (\chi_1^{(1)}\tilde{\eta}_x^{(1)} + \chi_2^{(1)}\tilde{\eta}_y^{(1)}) \end{aligned}, \tag{2.92}$$

$$\begin{aligned} f_2^{(2)} = {} & -\eta^{(1)}\phi_{tz}^{(1)} - \frac{1}{2}\nabla\phi^{(1)}\cdot\nabla\phi^{(1)} - \nabla\phi^{(0)}\cdot\nabla\phi^{(2)} \\ & -\eta^{(1)}(\nabla\phi_z^{(1)}\cdot\nabla\phi^{(0)} + \phi_{zz}^{(0)}\phi_z^{(1)}) + U\phi_x^{(2)} + U\eta^{(1)}\phi_{xz}^{(1)} + \left(\vec{\chi}^{(2)} + \vec{U}'^{(2)}\right)\cdot\nabla\phi^{(0)} \\ & + \left(\vec{\chi}^{(1)} + \vec{U}'^{(1)}\right)\cdot\nabla\phi^{(1)} + \left(\chi_3^{(1)} + U_3'^{(1)}\right)\eta^{(1)}\phi_{zz}^{(0)} \end{aligned}. \tag{2.93}$$

Here $\vec{\chi}^{(1)}$ is the first-order velocity of a point on the free surface due to rigid-body motion, which is defined as

$$\vec{\chi}^{(1)} = \left(\chi_1^{(1)}, \chi_2^{(1)}, \chi_3^{(1)}\right) = (\dot{\xi}_1^{(1)} - y\dot{\alpha}_6^{(1)})\vec{i} + (\dot{\xi}_2^{(1)} + x\dot{\alpha}_6^{(1)})\vec{j} + (\dot{\xi}_3^{(1)} + y\dot{\alpha}_4^{(1)} - x\dot{\alpha}_5^{(1)})\vec{k}\,. \tag{2.94}$$

The forward speed vector $\vec{U}'^{(k)}$(k=1, 2) and its components $U_j'^{(k)}$(k=1, 2; j=1, 2, 3) have been defined in Eq.(2.41).

In the derivation of the forcing terms in Eq.(2.90) - Eq.(2.93), the following equalities have been used in order to simplify the expressions

$$\overline{\eta}_t^{(1)} = -\chi_3^{(1)}, \tag{2.95}$$

$$-g[\overline{\eta}^{(1)} + \xi_3^{(1)}] + g_1'^{(1)}x + g_2'^{(1)}y = 0\,, \tag{2.96}$$

$$\overline{\eta}_t^{(2)} = (\chi_1^{(1)}\overline{\eta}_x^{(1)} + \chi_2^{(1)}\overline{\eta}_y^{(1)}) - \chi_3^{(2)}, \tag{2.97}$$

$$-g[\overline{\eta}^{(2)} + \xi_3^{(2)}] + g_1'^{(2)}x + g_2'^{(2)}y = 0\,. \tag{2.98}$$

$g_1'^{(i)}$, $g_2'^{(i)}$ (i=1, 2) have been defined in Eq.(2.39). The detailed derivation of Eq.(2.90) - Eq.(2.93) is very lengthy and will not be provided here.

Note that the terms associated with the rigid-body motions come into the free-surface conditions formulated in the body-fixed system. These terms disappear in the free-surface conditions of the inertial coordinate system.

By assuming η as small, we have implicitly assumed that both $\overline{\eta}$ and $\tilde{\eta}$ are small and can be written in the form of the Stokes expansions

$$\overline{\eta} = \varepsilon^1\overline{\eta}^{(1)} + \varepsilon^2\overline{\eta}^{(2)} + \cdots\,, \tag{2.99}$$

$$\tilde{\eta} = \varepsilon^1\tilde{\eta}^{(1)} + \varepsilon^2\tilde{\eta}^{(2)} + \cdots, \tag{2.100}$$

with

$$\overline{\eta}^{(i)} = -\left[\xi_3^{(i)} + (-x)\alpha_5^{(i)} + y\alpha_4^{(i)}\right], \text{ i=1, 2.} \tag{2.101}$$

Eq.(2.101) is valid for the yaw-pitch-roll Euler angle order. We note from Eq.(2.101) that the application of Eq.(2.99) is limited by the values of the x- and y-coordinates. It can only be used when x- and y-coordinates are not very large. If the distance between the origin of the coordinate system oxyz to the point (x, y, 0) is too large, the resulting $\overline{\eta}^{(i)}$ (i=1, 2) may become of the same order as the characteristic length of the body, which violates the assumption that η is small. In Chapter 5, we will decompose the whole fluid domain into two parts, namely an inner domain and an outer domain. The body-fixed coordinate system is used in the inner domain and the coordinate system remains inertial in the outer domain. Having a body-fixed coordinate system in the inner domain results in much simpler the body boundary conditions, which will be shown in Section 2.6.2. More discussion on the advantages associated with the simpler body boundary conditions will be given Chapter 5.

$\phi^{(0)}$ in the forcing terms of the free-surface conditions (see Eq.(2.90) - Eq.(2.93)) is the zeroth-order basis flow. More discussion about the relationship between the basis flow in the body-fixed formulation and that in the inertial formulation will be given in Appendix A and Section 5.2.

2.6.2 Body boundary condition

The body boundary condition in the body-fixed coordinate system is

$$\phi_n^{(m)} = b^{(m)}, \text{ m=1, 2, on SB.} \tag{2.102}$$

SB is the body surface at the instantaneous position of the body. Only the mean wetted part of the body surface is used in the formulation. The effect of small variation of the wetted body surface due to the wave elevation and body motion will be handled by the Taylor expansion about the oxy-plane of the body-fixed coordinate system. This is valid as long as the body motion is small relative to the body's cross-dimensional lengths.

The forcing term $b^{(m)}$ (m=1, 2) is defined as

$$b^{(1)} = \vec{n}' \cdot \left(\dot{\vec{\xi}}'^{(1)} + \vec{\omega}'^{(1)} \times \vec{r}' + \vec{U}'^{(1)} \right) , \tag{2.103}$$

$$b^{(2)} = \vec{n}' \cdot \left(\dot{\vec{\xi}}'^{(2)} + \vec{\omega}'^{(2)} \times \vec{r}' + \vec{U}'^{(2)} \right), \tag{2.104}$$

where $\dot{\vec{\xi}}'^{(i)}$ and $\vec{\omega}'^{(i)}$ (i=1, 2) are the translatory and angular velocity vectors of the body expressed in the body-fixed coordinate system. $\vec{U}'^{(k)}$ (k=1, 2) is the steady forward speed vector in the body-fixed coordinate system. $\vec{n}'$ is the normal vector on the body surface. $\vec{r}' = (x, y, z)$ is a position vector of a point on the body surface. See the definitions in Section 2.3.

The body boundary condition is formulated on the instantaneous position of the body surface. The velocity potential ϕ in this section is the absolute velocity potential, which is different from the relative velocity potential. If ϕ were defined as the relative velocity potential, the right-hand-side terms of Eq.(2.102) become zero.

2.6.3 Forces and moments calculation

Pressure integration is used to get the hydrodynamic forces and moments acting on the body. The pressure needed is given by the Bernoulli's equation. However, the Bernoulli's equation is a result of integrating the Euler equations, which are only valid in an inertial system, so we can not directly apply it to an accelerated system. It is important to keep in mind that the $\partial\phi / \partial t$ term in the inertial coordinate system means the time derivative of ϕ for a fixed point with coordinate (X, Y, Z) in the inertial coordinate system. However, in the body-fixed coordinate system we want to operate with the time derivative of ϕ for a fixed point (x, y, z) in the body-fixed system. The relationship between the time derivative in body-fixed system and that in the inertial system can according to Faltinsen & Timokha (2009) be written as

$$\left.\frac{\partial}{\partial t}\right|_{in\ noninertial\ oxyz} = \left.\frac{\partial}{\partial t}\right|_{in\ inertial\ OXYZ} + \vec{v}_b \cdot \nabla , \tag{2.105}$$

where $\vec{v}_b = \dot{\vec{\xi}}' + \vec{\omega}' \times \vec{r}'$ is the velocity at a point (x, y, z) due to rigid-body motions. $\dot{\vec{\xi}}'$ and $\vec{\omega}'$

are the translatory and angular velocity, respectively. See the definition in Section 2.3. ∇ means spatial gradient. Note that Eq.(2.105) has also been used in the derivation of the free-surface conditions in the body-fixed coordinate system, i.e. Eq.(2.88) - Eq.(2.93).

Transforming the time derivative in the inertial coordinate system into the time derivative in the body-fixed reference frame, and integrating the pressure on the body surface, we can express the forces $\vec{F}$ and moments $\vec{M}$ (i=0, 1, 2) in either the inertial coordinate system or body-fixed coordinate system. They can be expressed with respect to the inertial coordinate system respectively as

$$\vec{F} = \vec{F}^{(0)} + \vec{F}^{(1)} + \vec{F}^{(2)} + O\left(\varepsilon^3\right), \tag{2.106}$$

$$\vec{M} = \vec{M}^{(0)} + \vec{M}^{(1)} + \vec{M}^{(2)} + O\left(\varepsilon^3\right). \tag{2.107}$$

with

$$\vec{F}^{(0)} = \iint_{SB} p^{(0)} \vec{n}^{(0)}\, ds\,, \tag{2.108}$$

$$\vec{F}^{(1)} = \iint_{SB} \left[p^{(1)} \vec{n}^{(0)} + p^{(0)} \vec{n}^{(1)} \right] ds\,, \tag{2.109}$$

$$\vec{F}^{(2)} = \iint_{SB} \left[p^{(2)} \vec{n}^{(0)} + p^{(1)} \vec{n}^{(1)} + p^{(0)} \vec{n}^{(2)} \right] ds + \int_{CW_0} \frac{1}{2} \rho g \left(\eta^{(1)}\right)^2 \vec{n}^{(0)} dl\,, \tag{2.110}$$

$$\vec{M}^{(0)} = \iint_{SB} p^{(0)} \left[\left(\vec{r} - \vec{r}_c\right) \times \vec{n}^{(0)} \right] ds\,, \tag{2.111}$$

$$\vec{M}^{(1)} = \iint_{SB} \left\{ p^{(1)} \left[\left(\vec{r} - \vec{r}_c\right) \times \vec{n}^{(0)} \right] + p^{(0)} \left[\left(\vec{r} - \vec{r}_c\right) \times \vec{n}^{(1)} \right] \right\} ds\ , \tag{2.112}$$

$$\begin{aligned} \vec{M}^{(2)} = & \iint_{SB} \left\{ p^{(2)} \left[\left(\vec{r} - \vec{r}_c\right) \times \vec{n}^{(0)} \right] + p^{(1)} \left[\left(\vec{r} - \vec{r}_c\right) \times \vec{n}^{(1)} \right] + p^{(0)} \left[\left(\vec{r} - \vec{r}_c\right) \times \vec{n}^{(2)} \right] \right\} ds \\ & + \int_{CW_0} \frac{1}{2} \rho g \left(\eta^{(1)}\right)^2 \left[\left(\vec{r} - \vec{r}_c\right) \times \vec{n}^{(0)} \right] dl \end{aligned}\,. \tag{2.113}$$

Here CW_0 is the mean waterline. $\vec{r}$ and $\vec{r}_c$ have been defined in the texts associated with Eq.(2.60). The waterline integrals in Eq.(2.110) and Eq.(2.113) are caused by the fluctuation of the wetted body surface due to the relative motion between the wave profile and the body.

Eq.(2.106) - Eq.(2.113) are valid no matter the body has sharp corner or not. This is due to the fact that the solution is obtained at the instantaneous body position when the formulation in the body-fixed coordinate system is used, and that no Taylor expansion about the mean body surface is needed.

The pressure p has been divided into three parts, i.e.

$$p = p^{(0)} + p^{(1)} + p^{(2)} + \cdots \tag{2.114}$$

$p^{(0)}$, $p^{(1)}$ and $p^{(2)}$ are pressure components giving zeroth-order, first-order and second-order contributions to the forces and moments. They are defined respectively as

$$p^{(0)} = -\rho g z\,, \tag{2.115}$$

$$p^{(1)} = -\rho\left\{\phi_t^{(1)} - U\phi_x^{(1)} - \left(\vec{u}'^{(1)} + \vec{U}'^{(1)} - \nabla\phi^{(1)}\right)\cdot\nabla\phi^{(0)} + gx_3^{(1)}\right\}, \tag{2.116}$$

$$p^{(2)} = -\rho\left\{\phi_t^{(2)} - U\phi_x^{(2)} - \left(\vec{u}'^{(1)} + \vec{U}'^{(1)} - \nabla\phi^{(1)}\right)\cdot\nabla\phi^{(1)} - \left(\vec{u}'^{(2)} + \vec{U}'^{(2)} - \nabla\phi^{(2)}\right)\cdot\nabla\phi^{(0)} + \frac{1}{2}\nabla\phi^{(1)}\cdot\nabla\phi^{(1)} + gx_3^{(2)}\right\}. \tag{2.117}$$

$x_3^{(1)}$, $x_3^{(2)}$ and $\vec{u}'^{(1)}$ have been defined in Section 2.3. $p^{(0)}$ is a consequence of the hydrostatic pressure. It is noted that the expression for the pressure $p^{(2)}$ is different from what was given in Section 2.4.3 due to the fact that the Bernoulli's equation takes a different form in an accelerated coordinate system. The time derivatives in Eq.(2.116) and Eq.(2.117) are taken with respect to a fixed point (x, y, z) in the body-fixed coordinate system. One should note that the superscripts (0), (1) and (2) of the pressure do not necessarily indicate the order of magnitude of the pressure itself. Instead, it means that integral of the pressure effect, e.g. forces and moments are of zeroth order, first order and second order, respectively. An example is the pressure at the sharp corner. Within the context of potential theory without flow separation, the $-1/2\rho\nabla\phi^{(1)}\cdot\nabla\phi^{(1)}$ term of $p^{(2)}$ is singular, which means $-1/2\rho\nabla\phi^{(1)}\cdot\nabla\phi^{(1)}$ and thus $p^{(2)}$ is by no means of $O\left(\varepsilon^2\right)$. However, $-1/2\rho\nabla\phi^{(1)}\cdot\nabla\phi^{(1)}$ is integrable at the sharp corner. And its contribution to the forces or the moments is of $O\left(\varepsilon^2\right)$.

Similarly, if we define the forces and moments with respect to oxyz system, the force vector $\vec{F}'$ and moment vector $\vec{M}'$ can be obtained by replacing $\vec{r}$ and $\vec{r}_c$ Eq.(2.108) - Eq.(2.113) by $\vec{r}'$ and $\vec{r}_c'$ respectively, and setting the terms associated with $\vec{n}^{(1)}$ or $\vec{n}^{(2)}$ to be zero. $\vec{r}' = (x, y, z)$ and $\vec{r}_c = (x_c, y_c, z_c)$ are the position vectors of points in the oxyz system corresponding to $\vec{r}$ and $\vec{r}_c$ respectively.

2.7 Governing equations of unsteady rigid-body motions

The detailed derivation of the rigid-body motion equations can be found for instance in Ogilvie (1983), Etkin & Reid (1996) and Faltinsen (2005). In this section, a brief description of the general motion equations without any approximations will be given, followed by their first-order and second-order approximations by assuming that all the unsteady motions are small. The rigid-body motion equations will be presented in both the inertial coordinate system and the body-fixed coordinate system.

The rigid-body motion equations are derived for the motions with respect to the Centre of the Gravity (COG) of the body, which is a moving point observed in the inertial coordinate system OXYZ and the Earth-fixed coordinate system $O_eX_eY_eZ_e$. In this section, a vector with prime is considered as a description in the body-fixed coordinate system, i.e. oxyz, otherwise it is a vector in the inertial reference frame, i.e. OXYZ. See Fig.2.1 for the definitions of the coordinate systems.

2.7.1 Rigid-body motion equations in the inertial frame

The rigid-body motion equations can be derived from the first principles, that is to say, we apply Newton's laws to an element *dm* of the body, and then integrate over all elements. The velocities and

acceleration must of course be relative to an inertial reference frame. The consequence of applying Newton's laws is

$$m\dot{\vec{u}}_g = \vec{F}_g \,. \tag{2.118}$$

Here m is the total mass of the body. $\dot{\vec{u}}_g$ is the translatory acceleration of COG described in the inertial coordinate system (e.g. OXYZ). $\vec{F}_g$ is the external force vector acting on the body described in OXYZ.

Eq.(2.118) relates the external force on the body to the motion of COG. We need also the relation between the external moment and the rotation of the body. It is obtained from a consideration of moment of momentum, which states in the inertial coordinate system that the time derivative of the angular momentum is equal to the external moments acting on the body, i.e.

$$\frac{d}{dt}\left[\iiint \left(\vec{r}-\vec{r}_c\right)\times\vec{u}\; dm\right] = \vec{M}_g \quad . \tag{2.119}$$

Here $\vec{r}=\left(x,y,z\right)$ is the position vector of an arbitrary point on the body relative to the origin of the body-fixed coordinate system oxyz. $\vec{r}_c=\left(x_c,y_c,z_c\right)$ is the COG. $\vec{u}$ denotes the velocity of a point on the body. $\vec{M}_g$ is the external moment vector with respect to COG acting on the body. It can be shown that the vector $\vec{r}$ will be associated with the moments and products of inertia. If the inertial coordinate system is used, the inertias will be time-dependent. Therefore, they become variables in the body-motion equations. This is most undesirable and can be avoided by writing Eq.(2.119) in the body-fixed coordinate system, i.e.

$$\frac{d}{dt}\left[\iiint \mathbf{R}_{b\to i}\left(\left(\vec{r}'-\vec{r}_c'\right)\times\vec{u}'\right)dm\right] = \frac{d}{dt}\left[\mathbf{R}_{b\to i}\iiint\left(\vec{r}'-\vec{r}_c'\right)\times\vec{u}'\; dm\right] = \mathbf{R}_{b\to i}\vec{M}_g{}' \,. \tag{2.120}$$

Here $\vec{r}'$, $\vec{r}_c'$, $\vec{u}'$ and $\vec{M}_g{}'$ are the corresponding descriptions of the vectors of $\vec{r}$, $\vec{r}_c$, $\vec{u}$ and in $\vec{M}_g$ the body-fixed coordinate system, respectively.

Noticing that

$$\iiint\left(\vec{r}'-\vec{r}_c'\right)\times\vec{u}'\; dm = \iiint\left(\vec{r}'-\vec{r}_c'\right)\times\left[\vec{\omega}_g{}'\times\left(\vec{r}'-\vec{r}_c'\right)\right]dm = \mathbf{I}_B\vec{\omega}_g' \tag{2.121}$$

and that, for an arbitrary vector $\vec{s}$, the following equality holds (Etkin & Reid (1996), Appendix A.4)

$$\dot{\mathbf{R}}_{b\to i}\vec{s} = \mathbf{R}_{b\to i}\left(\vec{\omega}_g'\times\vec{s}\right), \tag{2.122}$$

we can rewrite Eq.(2.120) as

$$\mathbf{I}_B\dot{\vec{\omega}}_g' + \vec{\omega}_g'\times\mathbf{I}_B\vec{\omega}_g' = \mathbf{R}_{i\to b}\vec{M}_g \quad . \tag{2.123}$$

Here $\mathbf{I}_B$ is the inertia matrix, its elements being the moments and products of inertia of the body, i.e.

$$\mathbf{I}_B = \begin{bmatrix} I_x & -I_{xy} & -I_{xz} \\ -I_{yx} & I_y & -I_{yz} \\ -I_{zx} & -I_{zy} & I_z \end{bmatrix} \tag{2.124}$$

and

$$
\begin{aligned}
I_x &= \iiint\left[\left(y-y_c\right)^2+\left(z-z_c\right)^2\right]dm; \quad I_{xy}=I_{yx}=\iiint\left(x-x_c\right)\left(y-y_c\right)dm;\\
I_y &= \iiint\left[\left(x-x_c\right)^2+\left(z-z_c\right)^2\right]dm; \quad I_{xz}=I_{zx}=\iiint\left(x-x_c\right)\left(z-z_c\right)dm;\\
I_z &= \iiint\left[\left(x-x_c\right)^2+\left(y-y_c\right)^2\right]dm; \quad I_{yz}=I_{yz}=\iiint\left(y-y_c\right)\left(z-z_c\right)dm.
\end{aligned}
\tag{2.125}
$$

When the oxz-plane is a plane of symmetry, which is the usual assumption, then we have $I_{xy}=I_{yz}=0$ and the only off-diagonal terms are $-I_{xz}$ and $-I_{zx}$. If the direction of the x-axis is so chosen that this product of inertia also vanishes, which is always possible in principle, then the axes are principal axes. See Etkin & Reid (1996). $\vec{\omega}_g'$ is the angular velocity with respect to COG, which is located at $\left(x_c, y_c, z_c\right)$. $\dot{\vec{\omega}}_g'$ is the time differentiation of $\vec{\omega}_g'$. The transformation matrices $\mathbf{R}_{i\to b}$ and $\mathbf{R}_{b\to i}$ have been defined in Section 2.3.

Eq.(2.118) and Eq.(2.123) are exact, which means they are valid for large-amplitude body motions. The force vector $\vec{F}_g$ and moment vector $\vec{M}_g$ include all the external loads effects, such as the gravitational, the buoyancy effects, the hydrodynamic loads and loads from to the mooring lines.

We will now assume that the unsteady rigid-body motions are small and introduce the series expansion of the translatory and angular motions into Eq.(2.118) and Eq.(2.123). The first-order and second-order rigid-body motion equations are

$$
\text{First-order: } \begin{cases} \mathbf{m}\ddot{\vec{\xi}}_g^{(1)} = \vec{F}_g^{(1)} \\ \mathbf{I}_B\dot{\vec{\omega}}_g'^{(1)} = \vec{M}_g^{(1)} \end{cases},
\tag{2.126}
$$

$$
\text{Second-order: } \begin{cases} \mathbf{m}\ddot{\vec{\xi}}_g^{(2)} = \vec{F}_g^{(2)} \\ \mathbf{I}_B\dot{\vec{\omega}}_g'^{(2)} + \vec{\omega}_g'^{(1)}\times\mathbf{I}_B\vec{\omega}_g'^{(1)} = \mathbf{R}_{i\to b}^{(1)}\vec{M}_g^{(1)} + \vec{M}_g^{(2)} \end{cases}.
\tag{2.127}
$$

Here the transformation matrix $\mathbf{R}_{i\to b}^{(1)}$ have been defined in Section 2.3. $\vec{F}_g^{(k)}$ and $\vec{M}_g^{(k)}$ are forces and moments with respect to OXYZ system (see Section 2.4.3). The centre of moments is the structure's instantaneous COG. Note that our definition of the moments is different from that given by Ogilvie (1983), in which the moment centre was chosen to be origin of the inertial coordinate system. Eq.(2.126) and Eq.(2.127) are given for the freely-floating bodies. However, it is straightforward to extend them by adding additional forces and moments terms due to, e.g., the mooring line and DP system. The zeroth-order equations are not shown here. The zeroth-order steady loads effects are important for the equilibrium position of the structure. For a freely-floating body, the zeroth-order buoyancy force, i.e. the hydrostatic pressure integrated on the mean body surface, cancels out each other with the gravity force. And the centre of the buoyancy automatically drops in the same vertical line as COG.

The translatory motion vector of COG, i.e. $\vec{\xi}_g^{(k)}$, is defined as

$$
\vec{\xi}_g^{(k)} = \left(\xi_{g,1}^{(k)}, \xi_{g,2}^{(k)}, \xi_{g,3}^{(k)}\right) \text{ , k=1, 2,}
\tag{2.128}
$$

with $\xi_{g,1}^{(k)}$, $\xi_{g,2}^{(k)}$ and $\xi_{g,3}^{(k)}$ as the components in surge, sway and heave, respectively. The angular

velocity vector $\vec{\omega}_g'^{(k)}$ (k=1, 2) with respect to COG in the body-fixed reference frame can according to Eq.(2.27) be defined as

$$\vec{\omega}_g'^{(1)} = \begin{bmatrix} \dot{\alpha}_{4,g}^{(1)} \\ \dot{\alpha}_{4,g}^{(1)} \\ \dot{\alpha}_{4,g}^{(1)} \end{bmatrix}, \quad \vec{\omega}_g'^{(2)} = \begin{bmatrix} \dot{\alpha}_{4,g}^{(2)} + \dot{\alpha}_{6,g}^{(1)}\alpha_{5,g}^{(1)} \\ \dot{\alpha}_{5,g}^{(2)} - \dot{\alpha}_{6,g}^{(1)}\alpha_{4,g}^{(1)} \\ \dot{\alpha}_{6,g}^{(2)} + \dot{\alpha}_{6,g}^{(1)}\alpha_{4,g}^{(1)} \end{bmatrix}. \tag{2.129}$$

Here $\alpha_{4,g}^{(k)}$, $\alpha_{5,g}^{(k)}$ and $\alpha_{6,g}^{(k)}$ are the Euler angles with respect to COG, respectively. The overhead dots indicate that time differentiation is taken.

Note that, we have in Section 2.3 and Section 2.4 defined $\vec{\xi}^{(k)}$ and $\vec{\alpha}^{(k)}$ with respect to the origin of OXYZ as the translatory and angular motions, respectively. The relationship between the body motion $\vec{\xi}_g^{(k)}$, $\vec{\alpha}_g^{(k)} = \left(\alpha_{4,g}^{(k)}, \alpha_{5,g}^{(k)}, \alpha_{6,g}^{(k)}\right)$ and $\vec{\xi}^{(k)}$, $\vec{\alpha}^{(k)}$ can be obtained by using the transformation matrix in Section 2.3 as

$$\begin{cases} \vec{\xi}^{(k)} = \vec{\xi}_g^{(k)} - \mathbf{R}_{b\to i}^{(k)}\vec{r}_c, k = 1, 2, \\ \vec{\alpha}^{(k)} = \vec{\alpha}_g^{(k)}, k = 1, 2. \end{cases} \tag{2.130}$$

Here $\mathbf{R}_{b\to i}^{(k)}$ (k=1, 2) is the transformation matrix. $\vec{r}_c = \left(x_c, y_c, z_c\right)^T$ is the position vector of COG in the body-fixed reference frame oxyz. In this study, the oxyz system is defined so that oz-axis goes through COG, so that x_c =0 and y_c =0.

The right-hand of the rigid-body motion equations (2.126) and (2.127) includes all the hydrodynamic loads. The fact that the hydrodynamic load contains an instantaneous added-mass term prevents a stable numerical integration in time. Generally numerical stability theory for ordinary differential equations requires that the highest derivatives must be isolated for stability. The numerical instability when solving the motion equations can be avoided by moving all the terms that are explicitly dependent on the body accelerations to the left-hands of Eq.(2.126) and Eq.(2.127). This will be elaborated in details in Section 4.4 of Chapter 4.

2.7.2 Rigid-body motion equations in the body-fixed frame

The motion equations formulated in the inertial coordinate system is commonly used in the ship seakeeping analysis, however, the body-fixed formulation of the motion equations is preferred in the maneuvering analysis of ships.

Similar to what we did in Eq.(2.120), we can rewrite Eq.(2.118) as

$$m\frac{d}{dt}\left(\mathbf{R}_{b\to i}\vec{u}_g'\right) = m\left(\dot{\mathbf{R}}_{b\to i}\vec{u}_g' + \mathbf{R}_{b\to i}\dot{\vec{u}}_g'\right) = \mathbf{R}_{b\to i}\vec{F}_g'. \tag{2.131}$$

Applying Eq.(2.122) in Eq.(2.131) lead us to

$$m\left(\vec{\omega}_g' \times \vec{u}_g' + \dot{\vec{u}}_g'\right) = \vec{F}_g'. \tag{2.132}$$

From Eq.(2.123), we have that

$$\mathbf{I}_B\dot{\vec{\omega}}_g' + \vec{\omega}_g' \times \mathbf{I}_B\vec{\omega}_g' = \vec{M}_g'. \tag{2.133}$$

Eq.(2.132) and Eq.(2.133) serve as the general governing equations for the traslatory and angular motions of the body in body-fixed coordinate system. If the body motions can be assumed small, we can introduce series expansions to the body motions and get the first-order and second-order motions equations similar to Eq.(2.126) and Eq.(2.127).

2.8 Incident wave field

Considering that the incident wave propagates with a heading angle β with respect to the X_e-axis of the Earth-fixed coordinate system defined in Fig.2.1, the first-order, second-order and third-order velocity potential of the regular wave can be written respectively as

$$\phi_{in}^{(1)} = \frac{gA}{\omega}\frac{\cosh\left[k\left(Z_e+h\right)\right]}{\cosh\left(kh\right)}\sin\theta, \tag{2.134}$$

$$\phi_{in}^{(2)} = \frac{3(\alpha^2-1)^2}{8\alpha}\frac{kA^2g}{\omega}\cosh[2k(Z_e+h)]\sin 2\theta, \tag{2.135}$$

$$\phi_{in}^{(3)} = \frac{1}{64}(\alpha^2-1)(\alpha^2+3)(9\alpha^2-13)\frac{A^3k^2g}{\omega}\frac{\cosh[3k(Z_e+h)]}{\cosh 3kh}\sin 3\theta, \tag{2.136}$$

with

$$\theta = k\left(X_e\cos\beta + Y_e\sin\beta\right) - \omega t, \tag{2.137}$$

and

$$\alpha = \coth\left(kh\right). \tag{2.138}$$

Here A is the linear wave amplitude. k is the wave number. h is the water depth. ω is the frequency of the incident wave. The following nonlinear dispersion relationship holds

$$\omega^2 = gk\tanh(kh)\left\{1+k^2A^2\left[\frac{9}{8}\left(\alpha^2-1\right)^2+\alpha^2\right]\right\}. \tag{2.139}$$

The corresponding first-order, second-order and third-order wave elevations are respectively

$$\eta_{in}^{(1)} = A\cos\theta, \tag{2.140}$$

$$\eta_{in}^{(2)} = \frac{1}{4}\alpha(3\alpha^2-1)kA^2\cos 2\theta, \tag{2.141}$$

$$\eta_{in}^{(3)} = \left(1-\frac{3}{8}(\alpha^4-3\alpha^2+3)A^2k^2\right)A\cos\theta + \frac{1}{2}kA^2\cos 2\theta + \frac{3}{64}\left[8\alpha^6+(\alpha^2-1)^2\right]A^3k^2\cos 3\theta. \tag{2.142}$$

The description of the second-order irregular waves in the Earth-fixed coordinate system with finite water depth can be found in, for instance Dalzell (1999). A third-order stochastic wave model was proposed by Stokka (1994) to simulate the third-order deep-water waves.

Let $\vec{X}_e = \left(X_e, Y_e, Z_e\right)$ be the position vector of a point in the Earth-fixed coordinate system, i.e. $O_eX_eY_eZ_e$ in Fig.2.1, and $\vec{X} = \left(X, Y, Z\right)$ as the corresponding position vector in the inertial coordinate system moving the steady forward speed, i.e. OXYZ system. The incident wave field observed from the OXYZ system is obtained by substituting the relationship between $\vec{X}_e$ and $\vec{X}$, i.e.

$$\vec{X}_e = \vec{X} + \vec{U}t \tag{2.143}$$

into the expressions in the Earth-fixed frame, e.g. Eq.(2.134) - Eq.(2.137) and Eq.(2.140) - Eq.(2.142).

CHAPTER 3

Basis of the Time-Domain HOBEM in 2D

This chapter describes the basis of the two-dimensional higher-order boundary element method (HOBEM) in the time domain. All the discussions in this chapter are based on the formulation of the Boundary Value Problem (BVP) in the inertial coordinate system, which has been described in Chapter 2. We start with the boundary integral equation. The higher-order boundary elements are then used to discretize the boundary integral equation. Numerical issues associated with the time stepping of the free-surface conditions, the numerical damping zone and active wave absorber, the accurate way of getting the time differentiation of the velocity potential, i.e. ϕ_t , and the numerical calculation of the higher-order derivatives on both the free surface and body surface, will be discussed.

3.1 Boundary integral equation

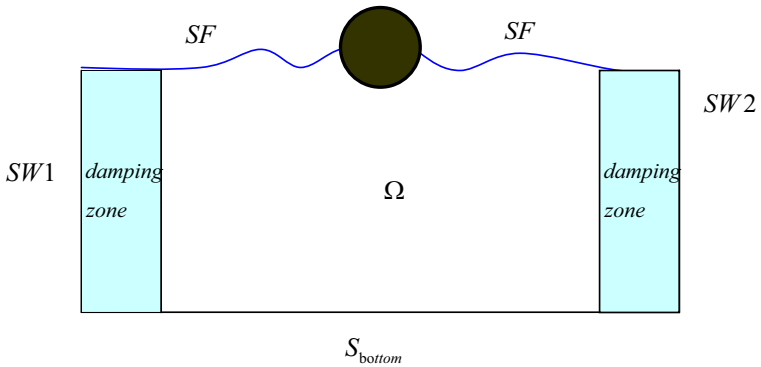

Fig.3.1. Sketch of the water domain and the enclosing boundaries.

As shown in Fig.3.1, a water domain Ω is enclosed by the instantaneous free surface SF, the wetted part of the instantaneous body surface SB, the sea bottom S_{bottom}, the vertical surfaces SW1 and SW2 away from the body. We denote SF_0 as the calm water surface and SB_0 as the wetted body surface when the body is at rest in calm water. The mean positions of SW1 and SW2 are denoted as $SW1_0$ and $SW2_0$. By mean position of a surface, it is meant the position around which the surface is oscillating.

The sea bottom is assumed to be stationary and horizontal. Applying the modified Green's third identity to the fluid domain enclosed by SF_0, SB_0, $SW1_0$ and $SW2_0$ and S_{bottom}, we obtain the following integral equation

$$C(P)\phi^{(k)}(P) = \oint_{\substack{SF_0+SB_0+SW1_0 \\ +SW2_0+S_{bottom}}} \left[\frac{\partial \phi^{(k)}}{\partial n}(Q) \cdot G(P,Q) - \phi^{(k)}(Q) \cdot \frac{\partial G}{\partial n}(P,Q) \right] ds \ . \tag{3.1}$$

Here $\phi^{(k)}$ (k=1, 2, 3) is the k-th order velocity potential. P denotes a field point and Q denotes the singularity position. C(P) is the solid angle coefficient to be discussed below. We call it a coefficient, because its value depends on the definition of the normal vector and the choice of Green function G(P,Q). In this study, $\vec{n}$ is the normal vector defined as positive pointing out of the fluid domain. The Green function G(P, Q) used in this study is

$$\mathrm{G(P,Q)=ln\left(r\right)=ln\left(\left|PQ\right|\right)}, \tag{3.2}$$

where r is the distance between P and Q. Therefore, C(P) is -2π when P is in the fluid and away from the boundaries, and $-\alpha(P)$ when P is on the boundary. Here $\alpha(P)$ is the exterior angle (solid angle) of the boundaries within the fluid domain.

When the field point P approaches the singularity located at Q, the integral of the normal derivative of the Green function only exists in a Cauchy principal value (CPV) sense. In a constant or linear boundary element method, this term becomes zero. However, it is not necessary to be zero if a HOBEM is used.

3.2 Quadratic boundary element method

The first step to solve the integral equation by using the higher-order BEM is to discretize the boundary surfaces with a number of higher-order elements. In the present study, we use 3-node isoparametric quadratic elements. The isoparametric elements were first studied by Zienkiewicz and his associates (See Zienkiewicz, 1971). The name 'isoparametric' is due to the fact that the 'same' parametric function which describes the geometry may be used for interpolating spatial variations of a variable within an element (see also Chung, 2002). The 3-node element is considered as quadratic, because the corresponding shape functions used for the description of the geometry and other variables are 2nd-order polynomials. Fig.3.2a shows an example of the 3-node quadratic element in the physical plane with its mapping in ξ-plane shown in Fig.3.2b. Within each element, the boundary surfaces, the velocity potential and its normal derivatives are approximated by the same shape function N_j:

$$[x,z] = \sum_{j=1}^{3} N_j(\xi)\left[x_j, z_j\right], \tag{3.3}$$

$$\phi^{(k)}(P) = \sum_{j=1}^{3} N_j(\xi)\left(\phi^{(k)}\right)_j \text{, k=1, 2, 3,} \tag{3.4}$$

$$\partial\phi^{(k)}/\partial n(P) = \sum_{j=1}^{3} N_j(\xi)\left(\partial\phi^{(k)}/\partial n\right)_j \text{ , k=1, 2, 3,} \tag{3.5}$$

where $\left(\phi^{(k)}\right)_j$ and $\left(\partial\phi^{(k)}/\partial n\right)_j$ are the velocity potential and its normal derivative at the j-th node of the reference element, respectively. The superscript k indicates the order of the magnitude. The

quadratic shape function N_j is given, for instance, by Brebbia & Dominguez (1992) as

$$N_1(\xi)=\frac{1}{2}\xi(\xi-1),\quad N_2(\xi)=(1-\xi)(\xi+1),\quad N_3(\xi)=\frac{1}{2}\xi(\xi+1), \tag{3.6}$$

with ξ as the local intrinsic coordinate of the reference element. The transformed coordinates $(\xi_j,0)$ corresponding to the coordinates (x_j, z_j) in the physical plane are defined in Fig.3.2b.

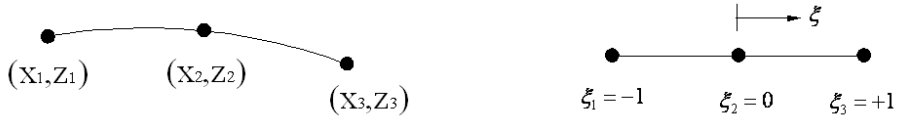

(a) (b)

Fig.3.2 (a) The quadratic element in the xz-plane. (b)The quadratic element in the ξ - plane.

After the discretization, the integrals on the boundary surfaces in Eq.(3.1) can thus be converted into a sum on the elements, each being calculated on the reference element. Eq.(3.1) can be rewritten as

$$\begin{aligned} &C(P)\phi^{(k)}(P)+\sum_{e=1}^{NE}\sum_{j=1}^{3}\left(\phi^{(k)}\right)_j\int_{-1}^{1}N_j(\xi)\frac{\partial G}{\partial n}(P,Q(\xi))\left|\mathbf{J}^e(\xi)\right|d\xi \\ &=\sum_{e=1}^{NE}\sum_{j=1}^{3}\left(\frac{\partial\phi^{(k)}}{\partial n}\right)_j\int_{-1}^{1}N_j(\xi)G(P,Q(\xi))\left|\mathbf{J}^e(\xi)\right|d\xi \end{aligned}. \tag{3.7}$$

NE is the total number of elements on the boundaries of the fluid domain. By assuming that the discretized equations are satisfied exactly at a set of collocation points, we obtain a system of equations.

$$\sum_{k=1}^{NOD}H_{ik}\phi_k=\sum_{k=1}^{NOD}A_{ik}\left(\frac{\partial\phi}{\partial n}\right)_k,\ \text{i=1, 2, … , NOD.} \tag{3.8}$$

where

$$H_{ik}=\sum_{e=1}^{NE}\sum_{j=1}^{3}\delta_{k,s}\hat{H}_{ij}^{e}+C_i\delta_{i,k}, \tag{3.9}$$

$$A_{ik}=\sum_{e=1}^{NE}\sum_{j=1}^{3}\delta_{k,s}\hat{A}_{ij}^{e}. \tag{3.10}$$

NOD is the total number of the nodes. $\delta_{i,k}$ is the Kronecker delta function. s=IEP(e, j) is a coefficient of the connectivity matrix, which represents the global index of the j-th node of e-th element. NE is the total number of elements. C_i is the solid angle coefficient at the i-th node P_i. $\hat{H}_{ij}^{e}$ and $\hat{A}_{ij}^{e}$ are defined respectively as

$$\hat{H}_{ij}^{e}=\int_{-1}^{1}N_j(\xi)\frac{\partial G}{\partial n}(P_i,Q(\xi))\left|\mathbf{J}^e(\xi)\right|d\xi, \tag{3.11}$$

$$\hat{A}_{ij}^{e}=\int_{-1}^{1}N_j(\xi)G(P_i,Q(\xi))\left|\mathbf{J}^e(\xi)\right|d\xi. \tag{3.12}$$

The Jacobian of the e-th element, i.e. $\left|\mathbf{J}^e(\xi)\right|$, is defined as

$$\left|\mathbf{J}^e(\xi)\right|=\sqrt{\left(\frac{\partial x}{\partial\xi}\right)^2+\left(\frac{\partial y}{\partial\xi}\right)^2}. \tag{3.13}$$

In this study, the collocation points are chosen as the nodes of the quadratic elements. The influence coefficients H_{ik} and A_{ik} are evaluated according to Brebbia & Dominguez (1992). The diagonal terms H_{ii} are obtained indirectly by a 'rigid-mode' method (Brebbia & Dominguez，1992), i.e.

$$H_{ii} = -\sum_{k=1,k\neq i}^{NOD} H_{ik} . \tag{3.14}$$

This method was referred as 'rigid-mode' method by analogy with structural analysis problems (see e.g. Brebbia, 1978). In the structural elasticity problems, a similar equation to Eq.(3.8) can be derived, except that ϕ_k on the left-hand side should be replaced by the displacement on the k-th node of the boundaries and $\left(\partial\phi/\partial n\right)_k$ on the right-hand side be replaced by the tractions (surface force intensities) on the same node. If the structure suffers from interior forces, one has to add additional terms to Eq.(3.8) associated with the volume integral of the interior forces. By assuming unit rigid-body displacements of the body without tractions and interior forces, Brebbia (1978) obtained the following relationship relating the diagonal terms H_{ii} and the off-diagonal terms H_{ik} (k=1,…,NOD; k≠i)

$$\sum_{k=1}^{NOD} H_{ik} = 0 \text{ , i=1, 2, … , NOD.} \tag{3.15}$$

By isolating the diagonal terms in the left-hand side of Eq.(3.15), we see that Eq.(3.14) holds.

Similarly in the potential flow problems, if we consider an uniform velocity potential field with $\phi = \text{constant} \neq 0$ and $\nabla\phi = 0$, and apply $\phi = \text{constant} \neq 0$ and $\partial\phi / \partial n = 0$ over the whole boundaries enclosing the water domain, we can obtain the same relationship as Eq.(3.15). Physically, for potential flows the rigid-mode method corresponds to numerically specifying that the discretized problem exactly satisfies a zero global mass flux condition when there is no flow motion.

When the collocation point is at a node other than any of those three in an element, the integrals for H_{ik} and A_{ik} are obtained by standard Gauss quadrature. If the collocation point is at the end nodes of the element with $\xi = \pm 1$ (see Fig.3.2b), the straight line $\xi \in [-1, 1]$ is stretched by using a transformation $\eta = \left(\xi \pm 1\right)/2$. The resulting integral then gives two parts, one with a singular term $\ln\left(1/\eta\right)$ and the other one with no singularity. The first part is integrated by means of a one-dimensional logarithmic Gaussian Quadrature with respect to the variable η. The second part is integrated by the standard Gauss quadrature formula in terms of the variable ξ. When the collocation point is at the middle node of the element, i.e. at $\xi = \xi_2 = 0$, we divide the straight line into two parts with $\xi \in [-1, 0]$ and $\xi \in [0, 1]$, respectively. Each part is then mapped into a straight line with $\eta \in [0, 1]$ in the η-plane. Again, the resulting integrals contain a regular part which can be obtained by standard Gauss quadrature and a logarithmic singular part which is evaluated by a logarithmic Gaussian Quadrature. Interested readers are referred to Brebbia & Dominguez (1992) for more details.

At the intersection points of different surfaces, the normal vectors may be ill-defined. The double-node technique is used to enforce the continuity of velocity potential at the intersection points of different surfaces (see Grilli & Svendsen, 1990). In the double-node method, two nodes with the same coordinates are used at the intersection of different surfaces. Applying Eq.(3.7) at the

intersection can only give one equation (the other one is identical). The continuity of the velocity potential acts as another equation at the intersection point. Consequently, there is only one unknown at the intersection point. For example, at the intersection points of the free surface and the body surface, the normal velocity of the intersection point is taken as known on the body surface but unknown on the free surface. The velocity potential at the intersection on the body is the same as that on the free surface, which is known. The normal velocity at the intersection on the free surface side is obtained by solving the boundary integral equation.

3.3 Time marching of the free-surface conditions

When a time-domain solution is pursued, the problem is considered as an initial value problem. The initial conditions used in this study are that the scattered wave elevation, the scattered velocity potential on the free surface and the body motion are zero. In the two-dimensional studies, we used an explicit fourth-order Runge-Kutta method to update the wave elevation and velocity potential on the free surface. Free-surface conditions, e.g. Eq.(2.48) and Eq.(2.49), are used as the evolution equations.

According to the explicit fourth-order Runge-Kutta method, the solution for a first-order ordinary equation $\dot{y} = f(y,t)$ takes the following form (Riley et al., 2006)

$$y_{i+1} = y_i + \frac{1}{6}(c_1 + 2c_2 + 2c_3 + c_4), \tag{3.16}$$

where

$$\begin{aligned} c_1 &= \Delta t \cdot f(y_i, t_i), \\ c_2 &= \Delta t \cdot f(y_i + 0.5c_1, t_i + 0.5\Delta t), \\ c_3 &= \Delta t \cdot f(y_i + 0.5c_2, t_i + 0.5\Delta t), \\ c_4 &= \Delta t \cdot f(y_i + c_3, t_i + \Delta t). \end{aligned} \tag{3.17}$$

3.4 Numerical damping zone and active wave absorber

The simple source, i.e. a source in infinite fluid, is chosen as the Green function in this work. Using the simple source as the Green function allows the solutions of linear as well as nonlinear formulation of wave-body interaction problems. Because the simple source does not satisfy the radiation condition, one has to truncate the computational domain at a finite distance and absorb the outgoing waves before the waves approach the end of the computational domain. A comprehensive review of the numerical techniques can be found in Romate (1992).

The most commonly used techniques in the time-domain wave-body analysis are the Orlanski's condition (Orlanski, 1976) and the numerical damping zone. The use of the Orlanski's condition is restricted to the cases of regular incident waves of known frequency, or to very long waves (see

Clement, 1996). The numerical damping zone (DZ) is very efficient for high frequency waves, provided that the damping zone length is longer than the typical wavelength. Clement (1996) proposed to use the combination of a piston-like absorbing boundary condition (PABC) which is effective for low frequencies and a numerical damping zone. In the 2D studies of this work, the coupling of DZ and PABC suggested by Clement (1996) is used.

The mechanism of the numerical beach used here is similar to that of Greco (2001). In the damping zone, artificial damping terms are introduced into the free-surface conditions. In general, the kinematic and dynamic free-surface conditions take the following form

$$\frac{\partial \eta^{(m)}}{\partial t} = \frac{\partial \phi^{(m)}}{\partial Z} + F_1^{(m)} - \mu(r)\eta_s^{(m)}, \quad \text{on Z = 0,} \tag{3.18}$$

$$\frac{\partial \phi^{(m)}}{\partial t} = -g\eta^{(m)} + F_2^{(m)} - \mu(r)\phi_s^{(m)}, \quad \text{on Z = 0.} \tag{3.19}$$

Here $\eta_s^{(m)}$ and $\phi_s^{(m)}$ (m=1, 2, 3) are the scattered part of the wave elevation and velocity potential, respectively. The damping coefficient $\mu(r)$ is defined as

$$\mu(r) = \mu_0 \sqrt{\frac{g}{\lambda}} \left[-2\left(\frac{r}{L}\right)^3 + 3\left(\frac{r}{L}\right)^2 \right]. \tag{3.20}$$

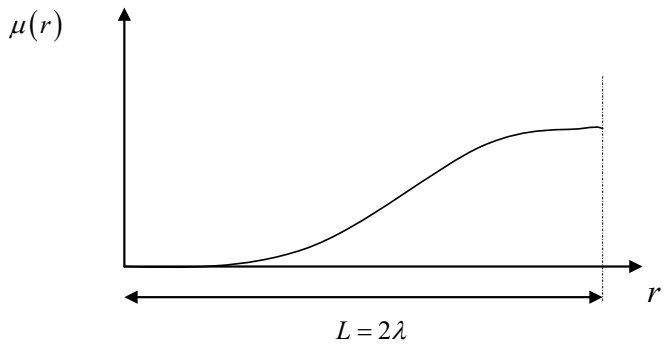

Fig.3.3. The sketch of the damping coefficient $\mu(r)$.

Here r is the horizontal distance of a point in the damping zone relative to the starting point of the damping zone. L is the length of the damping zone (see the definitions in Fig.3.3). In the present study we have chosen L=2λ, where λ is the linear wave length. The empirical damping coefficient μ_0 in Eq.(3.20) is defined as

$$\mu_0 = -\frac{g \ln(\gamma)}{2\omega L} \sqrt{\lambda / g}, \tag{3.21}$$

where ω is equal to the fundamental wave frequency in the first-order problem and twice of the fundamental wave frequency in the second-order problem. The non-dimensional empirical coefficient γ was set to be 0.5×10^{-5} in all the calculations. Within the range of the wave frequencies studied in this work, the numerical tests show that the results are not sensitive to this parameter when γ is

chosen between 10^{-6} and 10^{-5}. Note that in the second-order problem, the numerical damping zone mechanism, i.e. Eq.(3.18) and Eq.(3.19), is expected to damp out not only the free waves but also the locked waves following from the inhomogeneous part of the free-surface condition. This type of damping zone mechanism was used by Greco (2001) in two-dimensional fully-nonlinear analysis of wave-body interaction. Kim et al. (1997) has applied the same damping zone mechanism to second-order diffraction in 3D.

When the body is present and the incident wave field is prescribed, the piston-like active absorber is applied to the vertical control surfaces SW1 and SW2 (Fig.3.1). The damping zones are applied near SW1 and SW2. Fig 3.1 can also represent a numerical wave tank (NWT). In that case, the surface SW1 acts as a wave maker and SW2 is the piston-like wave absorber. Further, only the damping zone near SW2 is switched on. The non-dimensional horizontal velocity applied on the piston-like wave absorber in a fully-nonlinear NWT was given by Clement (1996) as

$$\frac{\partial \phi}{\partial X} = \int_{-1}^{\eta} \left(-\frac{\partial \phi}{\partial t} \right) dZ \,, \tag{3.22}$$

where the length is nondimensionalized with respect to water depth h and the time is nondimensionalized by $\sqrt{h/g}$. Based on Eq.(3.22), we use the following normal velocity on the piston-like wave absorbers SW1 and SW2 (Fig.3.1)

$$\frac{\partial \phi}{\partial n} = \sqrt{\frac{1}{gh}} \frac{1}{h} \int_{-h}^{0} \left(-\frac{\partial \phi}{\partial t} \right) dZ \,. \tag{3.23}$$

The position of the wave absorber is assumed to be fixed throughout the analysis and only a flux is given on the wave absorber. The $\partial \phi / \partial t$ term in Eq.(3.23) can be obtained in different ways (see Section 3.5). The mode-decomposition method (Vinje & Brevig (1981a, 1981b)) is used in the 2D studies of this work.

3.5 Solution of ϕ_t

The accurate calculation of the time derivative of the velocity potential, i.e. ϕ_t, is essential in obtaining correct pressure and forces/moments on the body surface at each time step. If the body is fixed or the body motion is prescribed, the calculation of ϕ_t can be achieved as a post-processing task by a finite difference scheme from the solution of the ϕ problem. Strictly speaking, for a freely floating body, solving the coupled fluid motion and body motion simultaneously is the most accurate way.

In the 2D studies of this work, a boundary value problem for ϕ_t is solved. The formulation for the ϕ_t problem is based on that of Wu (1998). The governing equation for ϕ_t is still the Laplace equation, i.e.

$$\nabla^2 \left(\phi_t \right) = 0 \,. \tag{3.24}$$

This can be seen from the Bernoulli's equation and that ϕ and its derivatives satisfy the Laplace equation.

ϕ_t can be expanded into series expansions by neglecting the higher-order terms

$$\phi_t = \phi_t^{(1)} + \phi_t^{(2)} + \phi_t^{(3)} + O\left(\varepsilon^4\right). \tag{3.25}$$

The free-surface conditions for $\phi_t^{(m)}$ can be found in Section 2.4 and Section 2.5 of Chapter 2. One should note that the formulations presented in Chapter 2 are for general three-dimensional cases. One has to neglect the y-dependent terms in order to use them in the 2D analysis.

Wu (1998) has given the body boundary condition for ϕ_t at the instantaneous position of the body surface. We will start from Wu's (1998) formula

$$\frac{\partial}{\partial n}\left(\phi_t\right) = \left[\dot{\vec{U}}_B + \dot{\vec{\Omega}}_B \times \vec{r}\right] \cdot \vec{n} - \vec{U}_B \cdot \frac{\partial \nabla \phi}{\partial n} + \dot{\vec{\Omega}}_B \cdot \frac{\partial}{\partial n}\left[\vec{r} \times \left(\vec{U}_B - \nabla \phi\right)\right], \tag{3.26}$$

where $\vec{U}_B$ and $\vec{\Omega}_B$ are the translatory and rotational velocity of the body. $\vec{r}$ is the position vector of a point on the body with respect to the body-fixed coordinate system. An overhead dot indicates time differentiation. By introducing the series expansions of the body motions and the velocity potential, and Taylor expanding the body boundary condition at the mean body surface, we obtain the following body boundary conditions for $\phi_t^{(m)}$ (m=1, 2) for the zero forward speed case

$$\nabla \phi_t^{(1)} \cdot \vec{n}^{(0)} = \vec{n}^{(0)} \cdot \left(\ddot{\vec{\xi}}^{(1)} + \ddot{\vec{\alpha}}^{(1)} \times \vec{r}\right), \tag{3.27}$$

$$\begin{aligned} \nabla \phi_t^{(2)} \cdot \vec{n}^{(0)} = \vec{n}^{(0)} \cdot \Bigg\{ & \left(\ddot{\vec{\xi}}^{(2)} + \ddot{\vec{\alpha}}^{(2)} \times \vec{r}\right) + \ddot{\mathbf{R}}_{b \to i}^{(1)} \vec{r} - \left[\left(\dot{\vec{\xi}}^{(1)} + \dot{\vec{\alpha}}^{(1)} \times \vec{r}\right) \cdot \nabla\right] \nabla \phi^{(1)} \\ & - \left[\left(\vec{\xi}^{(1)} + \vec{\alpha}^{(1)} \times \vec{r}\right) \cdot \nabla\right] \nabla \phi_t^{(1)} \Bigg\} + \left(\vec{\alpha}^{(1)} \times \vec{n}^{(0)}\right) \cdot \left(\ddot{\vec{\xi}}^{(1)} + \ddot{\vec{\alpha}}^{(1)} \times \vec{r} - \nabla \phi_t^{(1)}\right) \\ & + \left(\dot{\vec{\alpha}}^{(1)} \times \vec{n}^{(0)}\right) \cdot \left(\dot{\vec{\xi}}^{(1)} + \dot{\vec{\alpha}}^{(1)} \times \vec{r} - \nabla \phi^{(1)}\right) \end{aligned} \tag{3.28}$$

The definitions of the variables in Eq.(3.27) and Eq.(3.28) have been given in Section 2.3. The overhead double dots means that time differentiation has been taken twice.

As seen from Eq.(3.27) and Eq.(3.28), the accelerations of the body motion, i.e. $\ddot{\vec{\xi}}^{(m)}$ and $\ddot{\vec{\alpha}}^{(m)}$, are required as the input of the BVP for $\phi_t^{(m)}$. In order to evaluate the accelerations, one needs the forces and moments acting on the body, which can be obtained by integrating the pressure over the wetted body surface. However, according to the Bernoulli's equation, $\phi_t^{(m)}$ is needed when calculating the pressure. It means that the solutions of $\phi_t^{(m)}$ and the body motion have to be obtained by solving an implicit loop. Tanizawa (2000) has given a thorough review of existing methods which can be used to solve this implicit loop, i.e. the iterative method (Cao et al. (1994) and Sen (1994)), the modal decomposition method (Vinje & Brevig (1981a, 1981b) and Cointe et al. (1990)), the indirect method (Wu & Eatock Taylor (1996) and Kashiwagi (1998)) and the implicit boundary condition method (Tanizawa & Sawada (1990) and Tanizawa (1995)).

The modal decomposition method is used in the 2D cases studied in this thesis. We will briefly show how we can use this method to solve the motions of the piston wave absorber SW2 of a NWT without considering the presence of the body. In the NWT, the boundary SW1 acts as the wave generator. The idea for solving the problem of a general freely floating body is the same and no further details will be

given due to the limited space. Interested readers should be referred to for instance Vinje & Brevig (1981a, 1981b), Cointe et al. (1990) and Tanizawa (2000).

Firstly we decompose $\phi_t^{(m)}$ into two parts

$$\phi_t^{(m)}=a\psi_1^{(m)}+\psi_2^{(m)}. \tag{3.29}$$

Here *a* is the amplitude of the 'mode' of the piston motion of active wave absorber, which is unknown. $\psi_1^{(m)}$ and $\psi_2^{(m)}$ satisfy the following BVP respectively:

$$\psi_1:\begin{cases}\nabla^2\psi_1^{(m)}=0 & \\ \dfrac{\partial\psi_1^{(m)}}{\partial n}=1, & on\ SW2\\ \psi_1^{(m)}=0, & on\ SF_0\\ \dfrac{\partial\psi_1^{(m)}}{\partial n}=0, & on\ S_{bottom}\ and\ SW1\end{cases}\qquad \psi_2^{(m)}:\begin{cases}\nabla^2\psi_2^{(m)}=0 & \\ \dfrac{\partial\psi_2^{(m)}}{\partial n}=0, & on\ SW2\ and\ S_{bottom}\\ \psi_2^{(m)}=-g\eta^{(m)}+F_2^{(m)}, & on\ SF_0\\ \dfrac{\partial\psi_2^{(m)}}{\partial n}=V_{wm}^{(m)}, & on\ SW1\end{cases} \tag{3.30}$$

where the forcing term $F_2^{(m)}$ (m=1, 2, 3) is defined in Section 2.4 and Section 2.5. $V_{wm}^{(m)}$ (m=1, 2, 3) is the prescribed normal velocity at the wave maker SW1. $\eta^{(m)}$ is the wave elevation.

From Eq.(3.23) the normal velocity applied on SW2 can be expressed as

$$\frac{\partial\phi}{\partial n}=-\frac{1}{h}\sqrt{\frac{1}{gh}}\int_{-h}^{0}\left(a\psi_1^{(m)}+\psi_2^{(m)}\right)dZ. \tag{3.31}$$

Eq.(3.31) acts as a governing equation of the motion of the piston wave absorber, which plays a similar role as the Newton's 2nd law for the body motions of a freely floating body. The Runge-Kutta scheme also gives a prediction of the normal velocity $u_{n,ap}^{(m)}$ of SW2 for each sub time step, which has to be consistent with Eq.(3.31). So the unknown amplitude of the 'mode' of piston motion of SW2 can be expressed as

$$a=\frac{-h\sqrt{gh}\cdot u_{n,ap}^{(m)}-\int_{-h}^{0}\psi_2^{(m)}dZ}{\int_{-h}^{0}\psi_1^{(m)}dZ}. \tag{3.32}$$

When the amplitude of the 'mode' of the piston motion of active wave absorber, i.e. *a*, is obtained, $\phi_t^{(m)}$ can be obtained through Eq.(3.29).

3.6 Calculation of the higher-order derivatives

One of the difficulties in solving a weakly-nonlinear problem by the perturbation scheme is associated with the higher-order derivatives in both the free-surface conditions and the body boundary conditions. The derivatives can in theory be obtained through the differentiation of the shape functions. However, the accuracy is usually not sufficient when the order of the shape function is low and the results

become zero when the order of the derivative is higher than that of the shape function. In this study, the curve fitting technique is adopted in the 2D studies. The one-dimensional cubic B-spline is used to fit the variables on the free surface or the body surface with respect to the arc-length (Wang & Wu, 2006). These variables could be the spatial coordinates, the potential or the velocities on the free surface or the body surface. The first-order and the second-order derivatives are then obtained by taking the derivatives of the cubic B-spline functions.

3.7 Fourier analysis

What one obtains from the time-domain solution are the time histories of, for instance the forces and moments acting on the body. Fourier transform is often needed in order to get the amplitudes and the phases for the Fourier components from the time histories. A fast Fourier transform (FFT) is not used since the component frequencies are a function of the time interval and will not be easily applicable to arbitrary, unequal frequency intervals. A direct integration of the Fourier series suggested by Kim et al. (1997) is adopted in this study. It takes the following form

$$\int_{t_1}^{t_2} f(t) e^{i\omega_n t} dt = \sum_{m=1}^{N} (F_R + \mathrm{i}F_I) \int_{t_1}^{t_2} e^{i\omega_m t} e^{i\omega_n t} dt \text{, n=1,…, N.} \tag{3.33}$$

Here ω_m is a basis frequency of the time history f(t) with a complex amplitude $F_R + \mathrm{i}F_I$. ω_n is a test frequency. Eq.(3.33) is valid for arbitrary test frequencies and there is no restriction on the selection of the basis and test frequencies. The application of N test frequencies to this integral equation gives us a linear system of equations for $F_R + \mathrm{i}F_I$. The integral on the left-hand side of Eq.(3.33) is performed numerically. Specifically, we firstly interpolate every 4 neighboring points of the time history f(t) by cubic polynomials and numerical integrals are then performed within each cubic polynomials. This scheme gives an accuracy of O(Δt^3).

CHAPTER 4

Basis of the Time-Domain HOBEM in 3D

This chapter describes the basis of the three-dimensional Higher-Order Boundary Element Method (HOBEM) in the time domain. The 3D HOBEM adopted in this study is based on the cubic shape functions. The direct computation of the solid angles and the Cauchy principal value (CPV) integrals will be addressed. The method for the calculation of higher-order derivatives of the velocity potential and wave elevation is also presented. Other numerical issues, such as the time stepping of free surface conditions, numerical damping zone and the low-pass filter will also be discussed. The Fast Multipole Method (FMM) is also implemented combined with the cubic HOBEM. Suggestions for the selection of a proper matrix solver in 3D wave-body problem will also be given.

4.1 Boundary integral equation

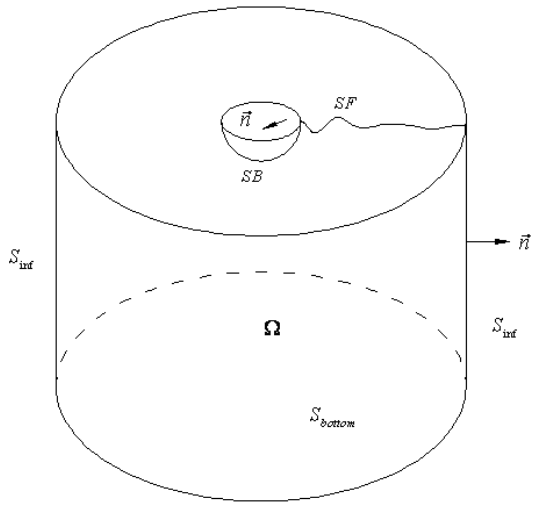

Fig.4.1. Sketch of the water domain and the enclosing boundaries.

We define a water domain Ω that is enclosed by the free surface SF, the wetted part of body surface SB, the sea bottom S_{bottom}, the vertical surfaces S_{inf} away from the body. We denote SF_0 as the calm water surface and SB_0 as the wetted body surface when the body is at rest in calm water.

The sea bottom is assumed to be stationary and horizontal. See Fig.4.1 for the definitions. A modified Green's third identity gives the following integral equation

$$C(\mathbf{x})\phi^{(k)}(\mathbf{x}) = \iint_{\substack{SF_0+SB_0 \\ S_{bottom}+S_{\inf}}} \left[\frac{\partial \phi^{(k)}}{\partial n}(\mathbf{y}) G(\mathbf{x},\mathbf{y}) - \phi^{(k)}(\mathbf{y}) \frac{\partial G}{\partial n}(\mathbf{x},\mathbf{y}) \right] dS(\mathbf{y}). \tag{4.1}$$

Here $\phi^{(k)}$ (k=1, 2, 3) is the k-th order velocity potential. $\mathbf{x}$ and $\mathbf{y}$ are the location vectors of the field point and the singularity point, respectively. $C(\mathbf{x})$ is the solid angle coefficient. $\vec{n}$ is the normal vector defined as positive pointing out of the fluid domain. The Rankine source is chosen as the Green function, i.e.

$$G(\mathbf{x},\mathbf{y}) = \frac{1}{r} = \frac{1}{|\mathbf{x}-\mathbf{y}|}. \tag{4.2}$$

4.2 HOBEM based on cubic shape functions

4.2.1 Shape functions

The 12-node cubic higher-order boundary elements are used to discretize the boundary surfaces enclosing the fluid domain. An example of the element is shown in Fig.4.2a with its mapping in $\xi-\eta$ plane in Fig.4.2b. The boundary geometry, the velocity potential and its normal derivative are approximated by

$$[x, y, z] = \sum_{j=1}^{12} N_j(\xi,\eta)[x_j, y_j, z_j], \tag{4.3}$$

$$\phi^{(m)}(\mathbf{x}) = \sum_{j=1}^{12} N_j(\xi,\eta)\left(\phi^{(m)}\right)_j, \text{ m=1, 2, 3,} \tag{4.4}$$

$$\frac{\partial \phi^{(m)}}{\partial n}(\mathbf{x}) = \sum_{j=1}^{12} N_j(\xi,\eta)\left(\frac{\partial \phi^{(m)}}{\partial n}\right)_j, \text{ m=1, 2, 3.} \tag{4.5}$$

Here $\left(\phi^{(m)}\right)_j$ and $\left(\partial\phi^{(m)}/\partial n\right)_j$ are the velocity potential and its normal derivative at the j-th node of the reference element, respectively. The superscript *m* indicates the order of the magnitude. The shape function N_j can be found in, for instance, Chung (2002):

$$N_j(\xi,\eta) = \begin{cases} \frac{1}{32}(1+\xi_j\xi)(1+\eta_j\eta)\left[9(\xi^2+\eta^2)-10\right], & j=1,4,7,10 \\ \frac{9}{32}(1+\xi_j\xi)(1-\eta^2)(1+9\eta_j\eta), & j=5,6,11,12 \\ \frac{9}{32}(1+\eta_j\eta)(1-\xi^2)(1+9\xi_j\xi), & j=2,3,8,9 \end{cases}. \tag{4.6}$$

ξ and η are the local intrinsic coordinates of the reference element. The transformed coordinates $(\xi_j, \eta_j, 0)$ corresponding to the coordinates (x_j, y_j, z_j).

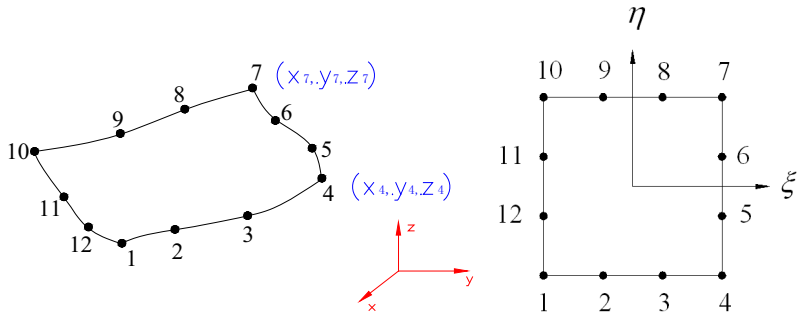

(a) (b)

Fig.4.2. (a) The 12-node cubic element in the physical plane. (b) The 12-node cubic element in the ξ-η plane. The numbers are indices for the transformed coordinates $(\xi_j, \eta_j, 0)$ corresponding to the coordinates (x_j, y_j, z_j) in the physical plane. The lengths of the four sides are identical and equal to 2.

Due to the discretization, the integral equation (4.1) can be rewritten as

$$C(\mathbf{x})\phi^{(m)}(\mathbf{x}) + \sum_{e=1}^{NE}\sum_{j=1}^{12}\left(\phi^{(m)}\right)_j \int_{-1}^{1}\int_{-1}^{1} N_j(\xi,\eta)\frac{\partial G}{\partial n}\left(\mathbf{y}(\xi,\eta),\mathbf{x}\right)\left|\mathbf{J}^e(\xi,\eta)\right| d\xi d\eta$$
$$= \sum_{e=1}^{NE}\sum_{j=1}^{12}\left(\frac{\partial \phi^{(m)}}{\partial n}\right)_j \int_{-1}^{1}\int_{-1}^{1} N_j(\xi,\eta) G\left(\mathbf{y}(\xi,\eta),\mathbf{x}\right)\left|\mathbf{J}^e(\xi,\eta)\right| d\xi d\eta, \quad m = 1,2,3. \tag{4.7}$$

NE is the total number of elements.

$\left|\mathbf{J}^e(\xi,\eta)\right|$ is the Jacobian on the *e*-th element, defined as

$$\left|\mathbf{J}^e(\xi,\eta)\right| = \left|\frac{\partial \vec{r}}{\partial \xi} \times \frac{\partial \vec{r}}{\partial \eta}\right| , \tag{4.8}$$

where $\vec{r} = (x, y, z)$. The Jacobian allows us to describe the differentials of surface in the Cartesian system in terms of the curvilinear coordinates. A differential of area $ds(x, y, z)$ will be given by

$$ds(x, y, z) = \left|\mathbf{J}(\xi,\eta)\right| d\xi d\eta . \tag{4.9}$$

We should note that $\left|\mathbf{J}(\xi,\eta)\right|$ is simply the magnitude of the normal vector $\vec{n}(x, y, z)$, i.e.

$$\vec{n}(x, y, z) = \left(\frac{\partial \vec{r}}{\partial \xi} \times \frac{\partial \vec{r}}{\partial \eta}\right) \Big/ \left|\frac{\partial \vec{r}}{\partial \xi} \times \frac{\partial \vec{r}}{\partial \eta}\right| . \tag{4.10}$$

Choosing the collocation points at the nodes of the elements leads us to the following equations system

$$\sum_{k=1}^{NOD} H_{ik}\phi_k^{(m)} = \sum_{k=1}^{NOD} A_{ik}\left(\frac{\partial \phi^{(m)}}{\partial n}\right)_k , \text{ i=1, 2,..., NOD.} \tag{4.11}$$

where

$$H_{ik} = \sum_{e=1}^{NE} \sum_{j=1}^{12} \delta_{k,s} \hat{H}_{ij}^{e} + C_i \delta_{i,k}, \tag{4.12}$$

$$A_{ik} = \sum_{e=1}^{NE} \sum_{j=1}^{12} \delta_{k,s} \hat{A}_{ij}^{e}, \tag{4.13}$$

with

$$\hat{H}_{ij}^{e} = \int_{-1}^{1} \int_{-1}^{1} N_j(\xi,\eta) \frac{\partial G}{\partial n}\left(\mathbf{x}(\xi,\eta), \mathbf{x}_i\right) \left|\mathbf{J}^{e}(\xi,\eta)\right| d\xi d\eta \tag{4.14}$$

$$\hat{A}_{ij}^{e} = \int_{-1}^{1} \int_{-1}^{1} N_j(\xi,\eta) G\left(\mathbf{x}(\xi,\eta), \mathbf{x}_i\right) \left|\mathbf{J}^{e}(\xi,\eta)\right| d\xi d\eta \tag{4.15}$$

NOD is the total number of the nodes. $\delta_{i,k}$ is the Kronecker delta function. s=IEP(e, j) is a coefficient of the connectivity matrix, which represents the global index of the *j*-th node of the e-th element. C_i is the solid angle coefficient at the *i*-th node. The superscript *e* indicates that the integrals are taken on the *e*-th element.

The double-node technique (see for instance Grilli & Svendsen, 1990) is used at the intersection lines of different surfaces where the normal vector is ill-defined. See also Section 3.2. This brings modifications to the corresponding lines of equations in Eq.(4.11) and gives us the final algebraic equation system.

4.2.2 Solid angle and CPV integrals

When the field point $\mathbf{x}_i$ is on the surface of the element, the field point and singularity point may coincide to generate singularities $1/r(\mathbf{x},\mathbf{x}_i) \to \infty$ and $1/r^2(\mathbf{x},\mathbf{x}_i) \to \infty$. Most of the singularities can be removed by using polar coordinate system on the local element and locating the coordinate origin at the singular point. However, this transformation yields still another singularity $1/\rho$ in the term $\hat{H}_{ij}^{e}$ when IEP(e, j) = i. Here ρ is the radial coordinate (see for instance Liu et al. (1991)). Either the indirect method or the direct method can be adopted for the evaluation of the diagonal terms H_{ii} (i=1,…,NOD).

Indirect method

In order to solve the $1/\rho$ singularity, an indirect procedure was suggested by Liu et al. (1991). The unknown velocity potential ϕ in Eq.(4.1) is replaced by a chosen (known) velocity potential φ_1. The consequence is that a relationship between the diagonal term and the off-diagonal terms can be established, which avoids the direct calculation of the solid angle term and the CPV integrals. When φ_1=constant$\neq 0$ and $\partial\varphi_1/\partial n = 0$, this method is the same as the rigid-mode method that we have described in Section 3.2, i.e.

$$H_{ii} = -\sum_{k=1,k\neq i}^{NOD} H_{ik}. \tag{4.16}$$

Direct calculation of the solid angles

When H_{ii} is evaluated directly, we need to calculate the solid angle term C_i and the CPV terms $\hat{H}_{ij}^{e}$

directly. The method for the calculation of the solid angles presented here is based on Montic (1993). This method has also been used by Teng et al. (2006) and Ning et al. (2010) in the analysis of the wave-body interactions by HOBEM. Interested readers are referred to Montic (1993), Teng et al. (2006) and Ning et al. (2010).

In the integral process, singularity can exist if the field source point $\mathbf{x}_i$ approaches the source/dipole point $\mathbf{x}$. Generally, there exists a sphere with a radius ε near to $\mathbf{x}_i$ by taking $\mathbf{x}_i$ as the origin of the sphere. The solid angle is defined as the angle occupied by the fluid domain, which can be related to the ratio of the spherical surface in the fluid domain to the whole spherical surface, i.e.

$$C_i = \frac{S_\varepsilon}{4\pi\varepsilon^2}\cdot 4\pi = \frac{S_\varepsilon}{\varepsilon^2}, \tag{4.17}$$

where S_ε is the spherical surface in the fluid domain.

Based on the relation of the spherical geometry, the spherical surface interpolated by N fluid boundary element boundary elements as shown in Fig.4.3 can be expressed by

$$S_\varepsilon = \varepsilon^2\left[\sum_{j=1}^{N}\alpha_j - (N-2)\pi\right], \tag{4.18}$$

where α_j is the included angle between the fluid boundary elements and the spherical surface. See Fig.4.3 for the definition. The angle α_j can according to Montic (1993) be expressed as

$$\alpha_j = \pi + \operatorname{sgn}\left[\left(\vec{n}_{j-1,j}\times\vec{n}_{j,j+1}\right)\cdot\vec{\tau}_i\right]\arccos\left(\vec{n}_{j-1,j}\cdot\vec{n}_{j,j+1}\right), \tag{4.19}$$

where

$$\operatorname{sgn}(x) = \begin{cases} -1, & x<0, \\ 0, & x=0, \\ 1, & x>0. \end{cases} \tag{4.20}$$

$\vec{\tau}_j$ is the unit vector superposed on the intersecting element edges and directs into the sphere center. $\vec{n}_{j,j+1}$ is the unit normal vector on the element.

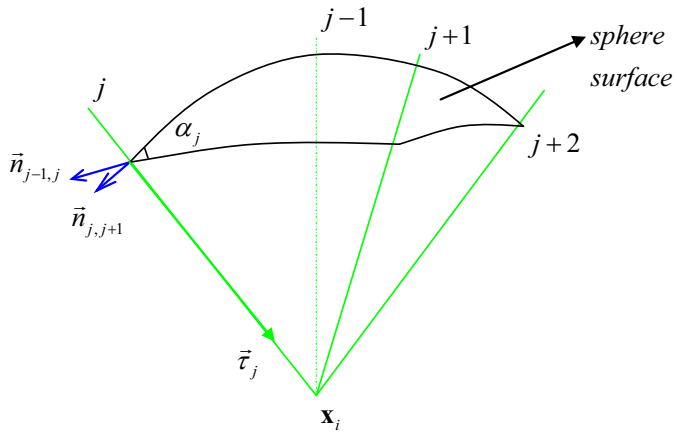

Fig.4.3. The definitions of $\vec{n}_{j,k}$, $\vec{\tau}_j$ and α_j. The radius of the spherical surface is ε.

Direct calculation of the CPV integrals

When the field point $\mathbf{x}_i$ coincides with the *j*-th node in the *e*-th element, the integral for $\hat{H}_{ij}^e$ is still singular which contributes to the diagonal term H_{ii}. The other singular integrals on the same element can be shown to be integrable by a transformation to polar coordinate system (Liu et al., 1991) or the triangular polar-coordinate transformation technique (see Li et al. (1985) and Eatock Taylor & Chau (1992)) adopted in this study. We will in the following text show how the $\hat{H}_{ij}^e$ term can be handled combined with the triangular polar-coordinate transformation.

If the field point $\mathbf{x}_i$ is located on a corner point (local point 1, 4, 7, 10), we split the element in the ξ-η plane into two triangles. Otherwise, if $\mathbf{x}_i$ drops on an edge point (local point 2, 3, 5, 6, 8, 9, 11, 12), the cubic element in the ξ-η plane is divided into three triangles. Fig.4.4a and Fig.4.4b show how the element is splitted when $\mathbf{x}_i$ coincides with the corner point 1 and the edge point 2, respectively.

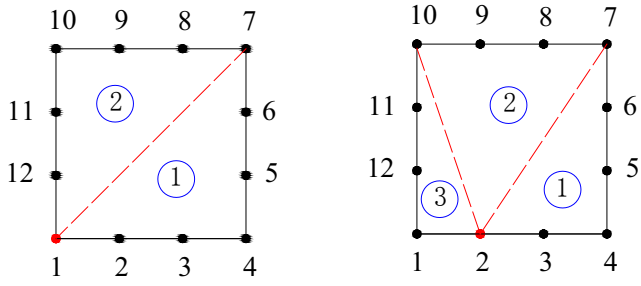

Fig.4.4. The cubic element in ξ-η plane splitted into triangles. (a) The field point is superposed on a corner point. (b) The field point is superposed on an edge point.

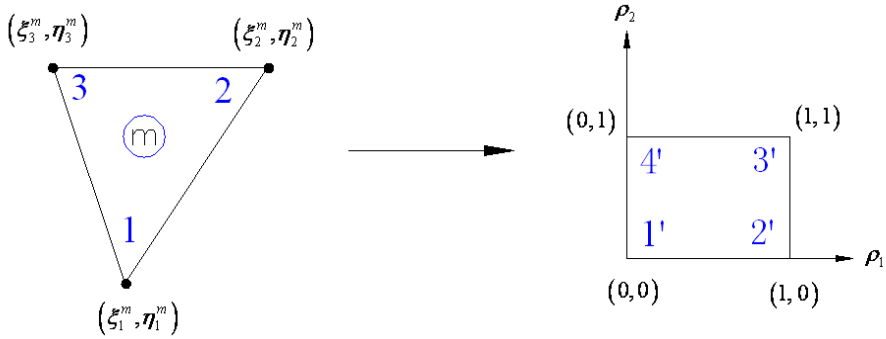

Fig.4.5. (a) The *m*-th triangle of an element in the ξ-η plane. The first node (ξ_1^m,η_1^m) of the triangle is the singularity point. (b) The square $\rho_1 \in [0\ 1]$ and $\rho_2 \in [0\ 1]$ in the ρ_1-ρ_2 plane, which is the mapping of the triangle in part (a).

We will firstly re-number the three nodes of each triangle by an anti-clockwise rule and take the singularity point as the first node. See Fig.4.5a. Then the following transformation can be used to map the triangles in ξ-η plane into a ρ_1-ρ_2 plane

$$\begin{Bmatrix}\xi\\ \eta\end{Bmatrix}=\begin{Bmatrix}\xi_1^m & \xi_2^m & \xi_3^m\\ \eta_1^m & \eta_2^m & \eta_3^m\end{Bmatrix}\begin{Bmatrix}1-\rho_1\\ \rho_1(1-\rho_2)\\ \rho_1\rho_2\end{Bmatrix}. \tag{4.21}$$

Here the superscript *m* means the *m*-th triangle of the square element after splitting (see Fig.4.4). ξ_j^m and η_j^m (j=1, 2, 3) are the ξ and the η coordinates of the *j*-th node of the *m*-th triangle. After the transformation (4.21), the triangle is stretched into a square in the ρ_1-ρ_2 plane, with the length of the four edges equal to 1. See Fig.4.5b. The first node $\left(\xi_1^m,\eta_1^m\right)$ where the singularity point is located has been stretched to a line $1'4'$ in the ρ_1-ρ_2 plane.

The integrals in Eq.(4.14) and Eq.(4.15) can be expressed as the sum of the integrals over the triangle areas. In the following text, we will take the case depicted in Fig.4.4a as an example, i.e. the singularity locates at a corner point, and show how we can rewrite the integrals in Eq.(4.14) and Eq.(4.15). The consideration for the case when the singularity is at an edge point is very similar and will not be repeated.

The transformation (4.21) for the first triangle in Fig.4.4a is

$$\xi=-1+2\rho_1,\quad \eta=-1+2\rho_1\rho_2. \tag{4.22}$$

Plugging Eq.(4.22) into Eq.(4.6), the shape function $N_j(\xi,\eta)$ can be written as a function of ρ_1 and ρ_2, i.e.

$$N_j(\xi,\eta)=N_j(\rho_1,\rho_2)=\begin{cases}1+\rho_1H_j(\rho_1,\rho_2), & j=1\\ \rho_1H_j(\rho_1,\rho_2), & j\neq 1\end{cases}. \tag{4.23}$$

The expressions for $H_j(\rho_1,\rho_2)$, j=1,…,12, are lengthy and thus not provided here. However, it is very straightforward to get $H_j(\rho_1,\rho_2)$ by putting Eq.(4.22) into Eq.(4.6) and comparing the resulting equations with Eq.(4.23).

Eq.(4.15) is then rewritten as

$$\hat{A}_{ij}^e=\sum_{m=1}^{2}\int_0^1\int_0^1\frac{2N_j(\rho_1,\rho_2)\left|\mathbf{J}^e(\rho_1,\rho_2)\right|\rho_1A_m}{\rho_1R(\rho_1,\rho_2)}d\rho_1d\rho_2=\sum_{m=1}^{2}\int_0^1\int_0^1\frac{2N_j(\rho_1,\rho_2)\left|\mathbf{J}^e(\rho_1,\rho_2)\right|A_m}{R(\rho_1,\rho_2)}d\rho_1d\rho_2. \tag{4.24}$$

Here A_m is the area of the *m*-th triangle in the ξ-η plane. And

$$R(\rho_1,\rho_2)=\sqrt{R_x^2(\rho_1,\rho_2)+R_y^2(\rho_1,\rho_2)+R_z^2(\rho_1,\rho_2)}, \tag{4.25}$$

with

$$\begin{cases}x_i-x=x_i-\sum_{j=1}^{12}N_jx_j=-\rho_1\sum_{j=1}^{12}H_jx_j=\rho_1R_x(\rho_1,\rho_2)\\ y_i-y=y_i-\sum_{j=1}^{12}N_jy_j=-\rho_1\sum_{j=1}^{12}H_jy_j=\rho_1R_y(\rho_1,\rho_2)\\ z_i-z=z_i-\sum_{j=1}^{12}N_jz_j=-\rho_1\sum_{j=1}^{12}H_jz_j=\rho_1R_z(\rho_1,\rho_2)\end{cases}. \tag{4.26}$$

Note that $1/R(\rho_1,\rho_2)$ with $0\le\rho_1\le 1$ and $0\le\rho_2\le 1$ is regular. Thus the singularity in the integral of Eq.(4.15) has been removed through the transformation Eq.(4.21).

Similarly, we can rewrite $\hat{H}_{ij}^e$ in Eq.(4.14) as

$$\begin{aligned}\hat{H}_{ij}^e &= \int_{-1}^{1}\int_{-1}^{1} N_j(\xi,\eta)\frac{\vec{n}(\xi,\eta)\cdot\vec{r}\left(\mathbf{x}(\xi,\eta),\mathbf{x}_i\right)}{r^3\left(\mathbf{x}(\xi,\eta),\mathbf{x}_i\right)}\left|\mathbf{J}^e(\xi,\eta)\right|d\xi d\eta \\ &= \sum_{m=1}^{2}\int_0^1\int_0^1 \frac{N_j(\rho_1,\rho_2)\left[j_1R_x+j_2R_y+j_3R_z\right]}{\rho_1 R^3(\rho_1,\rho_2)}2A_m d\rho_1 d\rho_2,\end{aligned} \tag{4.27}$$

where we have used

$$\vec{n}(\xi,\eta)=\frac{(j_1,j_2,j_3)}{\left|\mathbf{J}^e(\xi,\eta)\right|}=\frac{\left(y_\xi z_\eta - y_\eta z_\xi, z_\xi x_\eta - z_\eta x_\xi, x_\xi y_\eta - x_\eta y_\xi\right)}{\left|\mathbf{J}^e(\xi,\eta)\right|}. \tag{4.28}$$

If $j\neq 1$, i.e. the *j*-th node is not a singularity, Eq.(4.27) can be further simplified by using the second formula in Eq.(4.23) as

$$\hat{H}_{ij}^e = \sum_{m=1}^{2}\int_0^1\int_0^1 \frac{H_j(\rho_1,\rho_2)\left[j_1R_x+j_2R_y+j_3R_z\right]}{R^3(\rho_1,\rho_2)}2A_m d\rho_1 d\rho_2 . \tag{4.29}$$

It is seen from Eq.(4.29) that the singularity in $\hat{H}_{ij}^e$ has been eliminated if the *j*-th node of the element is not at the same position of the field point *i*. Standard numerical procedure, e.g. Gauss-Legendre quadrature can be used to evaluate the integration.

However, when *j*=1, $\hat{H}_{ij}^e$ contains a $1/\rho_1$-type singularity. Let us define

$$f(\rho_1,\rho_2)=\frac{2N_j(\rho_1,\rho_2)\left[j_1(\rho_1,\rho_2)R_x(\rho_1,\rho_2)+j_2(\rho_1,\rho_2)R_y(\rho_1,\rho_2)+j_3(\rho_1,\rho_2)R_z(\rho_1,\rho_2)\right]}{R^3(\rho_1,\rho_2)}A_m \tag{4.30}$$

and add and subtract the singular kernel in Eq.(4.27)

$$\hat{H}_{ij}^e = \underbrace{\sum_{m=1}^{2}\int_0^1\int_0^1 \frac{f(\rho_1,\rho_2)-f(0,\rho_2)}{\rho_1}d\rho_1 d\rho_2}_{I_1} + \underbrace{\lim_{\varepsilon\to 0}\sum_{m=1}^{2}\int_{\bar{\rho}_1(\varepsilon)}^1\int_0^1 \frac{f(0,\rho_2)}{\rho_1}d\rho_1 d\rho_2}_{I_2}. \tag{4.31}$$

The two terms in the first integral I_1 in Eq.(4.31) include the same singular kernel and they can be counteracted during integral. Then the standard numerical integration can be performed. ε is the radius of the sphere which is defined in the calculation of the solid angle. See the text associated with Eq.(4.17) and Eq.(4.18). $\bar{\rho}_1(\varepsilon)$ is the value of ρ_1 corresponding to the intersection line of the sphere and the boundary element. $\bar{\rho}_1(\varepsilon)$ is approximated as

$$\varepsilon=\bar{\rho}_1(\varepsilon)\left[\left(R_x\right)^2+\left(R_y\right)^2+\left(R_z\right)^2\right]^{1/2}_{\rho_1=0}+O(\rho_1^2)=\bar{\rho}_1(\varepsilon)R(\rho_1=0,\rho_2)+O(\rho_1^2). \tag{4.32}$$

Taylor expansion of Eq.(4.26) with respect to ρ_1=0 was used in the derivation of Eq.(4.32). R(ρ_1, ρ_2) is defined in Eq.(4.25). The second integral I_2 can be rewritten by putting Eq.(4.32) into Eq.(4.31) as

$$I_2 = \sum_{m=1}^{2} -\lim_{\varepsilon \to 0} (\ln \varepsilon) \int_0^1 f(0, \rho_2) d\rho_2 + \sum_{m=1}^{2} \int_0^1 f(0, \rho_2) \ln[R(\rho_1 = 0, \rho_2)] d\rho_2 . \tag{4.33}$$

The limit of the first term in I_2 does not exist. However, the sum of the integrals in all the elements surrounding the singularity point must equal to zero. That means the first term in Eq.(4.33) does not contribute in the diagonal terms of H_{ii}. This is due to the fact that H_{ii} contains all the contributions from the elements adjacent to the source point. The line integral in the second term of Eq.(4.33) can be calculated by standard numerical integration.

Eq.(4.24), Eq.(4.27) and Eq.(4.31) are obtained when the singularity is located at a corner point of the element (see Fig.4.4a). The derivation is similar when the singularity is at an edge point (see Fig.4.4b) and will not be repeated here.

Teng et al. (2006) have proposed a similar technique for the evaluation of CPV integrals. A transformation to polar coordinate system with the origin at the singularity was used. Terms similar to that of I_1 and I_2 in Eq.(4.32) were obtained.

4.3 Time marching of the free-surface conditions

In the time-domain simulations, the method for the time integrating is very important to keep its accuracy and stability. In many practical time-domain analyses, the higher-order time integral schemes are used such as the fourth-order Runge-Kutta method (RK4), the fifth-order Runge-Kutta-Gil method (RKG5) and the fourth-order Adams-Bashforth-Moulton method (ABM4). RK4 and ABM4 have $O(\Delta t^4)$ accuracy. RKG5 has $O(\Delta t^5)$ accuracy for short time simulations but $O(\Delta t^4)$ accuracy for long time simulations. See for instance Tanizawa (2000).

The ABM4 method used by Skourup et al. (2000) in their time-domain analysis of second-order wave diffraction forces on fixed bodies is adopted in all the three-dimensional studies in this thesis. In the 3D time-domain BEM, we have to solve the matrix equation with fully-populated matrices at each time step. Even though the computational boundaries are invariant in time and the influence matrix only needs to be evaluated (and inverted) once when the perturbation method is adopted, any possibility to reduce the CPU time while retaining the accuracy is welcomed in the 3D time-domain analysis. ABM4 has the same accuracy as RK4. However, the AMB4 only needs to call the BEM solver two times at each time step while the RK4 needs four calls of the BEM solver. That is why the ABM4 is adopted in the 3D studies instead of RK4 which was applied in the two-dimensional cases (see Chapter 3).

Firstly, an explicit fourth-order Adams-Bashforth predictor is used for the updating of the scattered part of the velocity potential $\phi_s^{(m)}$ and the wave elevation $\eta_s^{(m)}$ from time t to time $t + \Delta t$, i.e.

$$\phi_s^{(m)}(t + \Delta t) = \phi_s^{(m)}(t) + \Delta t \sum_{k=1}^{4} a_k \frac{\partial \phi_s^{(m)}}{\partial t}(t + \Delta t - k\Delta t), \tag{4.34}$$

$$\eta_s^{(m)}\left(t+\Delta t\right)=\eta_s^{(m)}\left(t\right)+\Delta t\sum_{k=1}^{4}a_k\,\frac{\partial\eta_s^{(m)}}{\partial t}\left(t+\Delta t-k\Delta t\right), \tag{4.35}$$

where $(a_1, a_2, a_3, a_4) = (55/24, -59/24, 37/24, -9/24)$.

Then the updated values of $\phi_s^{(m)}$ and $\eta_s^{(m)}$ and the dynamic free-surface condition are used to approximate the $\partial\phi_s^{(m)}/\partial t$ at time $t+\Delta t$. This value is used as predictor in a fourth-order Adams-Moulton corrector method for the semi-implicit updating of $\phi_s^{(m)}$ from time t to time $t+\Delta t$

$$\phi_s^{(m)}\left(t+\Delta t\right)=\phi_s^{(m)}\left(t\right)+\Delta t\sum_{k=1}^{4}b_k\,\frac{\partial\phi_s^{(m)}}{\partial t}\left(t+2\Delta t-k\Delta t\right), \tag{4.36}$$

where $(b_1, b_2, b_3, b_4) = (9/24, 19/24, -5/24, 1/24)$. Using the updated value of $\phi_s^{(m)}$ and the dynamic free-surface condition, this semi-implicit updating can be repeated until a sufficient convergence has been achieved. A similar iterative semi-implicit updating of the wave elevation is expensive since the normal derivative of the velocity potential on the free surface at time $t+\Delta t$ requires another call of the BEM solver.

The numerical damping zone presented in Section 3.4 without active wave absorber is applied in the three-dimensional analysis.

4.4 Treatment of ϕ_t-term and the time integration of body motion equations

In order to be robust and efficient, the time-domain simulation of body motions require a stable numerical integration scheme for the solution of Newton's rigid-body equations of motion (see e.g. Eq.(2.126) and Eq.(2.127)) excited by wave forces which depend on not only the displacement and velocity but also the acceleration of the body. It is known that most ordinary differential equation (ODE) solvers are designed for cases where the highest order of differentiation occurs on the left-hand side of the equation only, e.g.

$$\frac{d\mathbf{y}}{dt}=\mathbf{f}\left(\mathbf{y},t\right). \tag{4.37}$$

However, the Eq.(2.126) and Eq.(2.127) take the following form

$$\frac{d\mathbf{y}}{dt}=\mathbf{f}\left(\frac{d\mathbf{y}}{dt},\mathbf{y},t\right), \tag{4.38}$$

which means that iterations are needed in order to get accurate and stable results. However, this indicates the increase of CPU time in the time-domain analysis, because each iteration needs a call of the BEM solver.

A natural modification to Eq.(4.38) is to move the *dy/dt* terms on the right-hand side to the left. Inspired by the canonical form of the equation of the equations of motion as proposed by Cummins (1962) and Ogilvie (1964) which by virtue of the physics of the free-surface flow are stable, Kring

(1994) decomposed the hydrodynamic loads into an instantaneous or 'time localized' part and a 'memory' component. The result of such decomposition is that the body acceleration appears explicitly and linearly in the left-hand side of motion equations, while the forcing in the right-hand side which accounts for memory effects is shown to depend upon the ship displacement and velocity. The stability of the rigid-body motion equations is well prescribed in Kring & Sclavounos (1995). The decomposition method proposed by Kring (1994) is valid not only for the linear but also the nonlinear seakeeping analysis. This was later demonstrated by Huang (1996) using a weak scatter model.

Based on the understanding that the instability of body motion equations is due to the impulsive term in the hydrodynamic force proportional to the acceleration, Kim et al. (2008) obtained a stable form of the motion equations by merely adding an infinite-frequency added mass (m_∞) on both sides of the equation. Taking the first equation of Eq.(2.126) as an example, we have

$$\left[m+m_\infty\right]\ddot{\xi}_g^{(1)} = \vec{F}_g^{(1)} + \left[m_\infty\right]\ddot{\xi}_g^{(1)}. \tag{4.39}$$

Let us look at the first component of Eq.(4.39), explain why it is a stable form, and show how we handle the integral of ϕ_t. The merit of the way we handle the ϕ_t term is that part of the influence of ϕ_t has been moved to the left-hand side of the motion equation and the rest parts of its contribution may be approximated by a backward finite difference scheme.

The first component of Eq.(4.39) becomes

$$m\ddot{\xi}_{1,g}^{(1)} + \sum_{k=1}^{6} m_{1k}^{\infty}\ddot{\xi}_{k,g}^{(1)} = F_{1,g}^{(1)} + \sum_{k=1}^{6} m_{1k}^{\infty}\ddot{\xi}_{k,g}^{(1)}. \tag{4.40}$$

We will now decompose the scattered velocity potential into two parts

$$\phi_s^{(1)} = \phi_1^{(1)} + \phi_2^{(1)}. \tag{4.41}$$

The first part $\phi_1^{(1)}$ satisfies the Laplace equation and the following boundary conditions

$$\begin{cases} \phi_1^{(1)} = 0 \quad on\ Z = 0 \\ \dfrac{\partial \phi_1^{(1)}}{\partial n} = \left(\dot{\vec{\xi}}^{(1)} + \dot{\vec{\alpha}}^{(1)} \times \vec{r}\right)\cdot \vec{n} \quad on\ SB_0 \end{cases}, \tag{4.42}$$

while the second part $\phi_2^{(1)}$ takes care of the rest of the boundary conditions. According to the definition of the infinite-frequency added mass, we know that

$$-\iint_{SB_0} \rho \frac{\partial \phi_1^{(1)}}{\partial t} n_1^{(0)} ds = -\sum_{k=1}^{6} m_{1k}^{\infty}\ddot{\xi}_{k,g}^{(1)}. \tag{4.43}$$

Considering Eq.(4.41), Eq.(4.43) and the expressions for the forces and moments in Section 2.4.3, we notice that the terms associated with the body accelerations on the right-hand size of Eq.(4.40) cancel out with each other. So Eq.(4.40) takes a similar form to Eq.(4.37) instead of Eq.(4.38). We can do the similar to the other components of the body motion equations. Thus a standard procedure, for instance the Adams-Bsshforth-Moulton predictor-corrector method or the Runge-Kutta method, can be used for the time integral to get the velocity and displacement of the body motion. In this work, the

fourth-order Adams-Bashforth-Moulton method is used for the time integration. Note that the contribution of ϕ_t term to the right-hand side of the motion equations Eq.(4.39), which depends merely on the body displacement and velocity, is approximated by a fourth-order backward finite difference scheme. In order to reduce the errors in doing that, it is suggested that one firstly integrates ϕ on the mean wetted body surface and takes the time differentiation afterwards. This is simply due to the fact that

$$-\iint_{SB_0} \rho \vec{n}^{(0)} \phi_t^{(m)} dS = -\frac{d}{dt} \iint_{SB_0} \rho \vec{n}^{(0)} \phi^{(m)} dS \text{ , m=1, 2.} \tag{4.44}$$

For exactly evaluating of the influence of ϕ_t term, one may use one of the acceleration velocity potential methods. See Tanizawa (2000) and Koo & Kim (2004) for the details of the methods. One of the acceleration velocity potential methods, i.e. the modal decomposition method has been applied to the active wave absorber in the studies in 2D. See also Section 3.4 and Section 3.5. In the 3D studies, however, these kinds of exact methods will not be employed in order to save computational time.

4.5 Low-pass filter on the free surface

The short-wave instabilities have been reported since the first papers were published where BEM was used for modeling the free-surface waves in the time domain. See e.g. Longuet-Higgins & Cokelet (1976). However the reason for the instabilities has not been fully understood even though it may be associated with the fact that we partly solve a Fredholm integral equation of the first kind which is known to have numerical problems (e.g. Delves & Walsh (1974) and Arfken & Weber (2001)).

It was suggested by Vada & Nakos (1993) and by Kim et al. (1997) that the instabilities observed in their models are caused by the energy from external forcing, which should be accumulated on a wave number with zero group velocity, a so-called resonant mode. This argument fails to explain the instabilities observed by Büchmann (2000b) in a case with zero external forcing. Based on the observation, Büchmann (2000b) conjectured that the instabilities are in fact due to the non-uniformity in the spatially discretized models.

Another different argument was made by Prins (1995): The Laplace equation has harmonic functions as its solution. The boundary conditions serve to determine what harmonic function is the overall solution of the complete system. Solving the Laplace equation and the boundary conditions separately can be viewed as satisfying the boundary condition with a harmonic forcing function. The solution will then be a superposition of a harmonic function and the eigen-functions of the differential operator in the free-surface conditions. In the absence of forward speed, these eigen-functions are harmonic as well, and determine the dispersion relation. However, in the presence of forward speed not all eigen-functions of the free-surface condition are harmonic; some are exponentially increasing and some exponentially decreasing. This means that at every time step an error is introduced which disturbs the accuracy of the solution. This also explain why filtering may be successful. Prins (1995) proposed a new algorithm for forward speeds by combining the Laplace equation and the boundary conditions, thus imposing harmonic solutions to the boundary conditions. Prins (1995) also showed by numerical experiments that the new algorithm was stable in all the studies considered in his thesis. However, no analytical analysis supports that his scheme is unconditionally stable.

In the wave-body analysis with the presence of forward speed or current effect, a practical option is to use the smoothing or low-pass filter to suppress the short-wave instabilities. The upwind difference scheme for the tangential derivatives in the convective terms has also been shown to be efficient to stabilize the calculation. Bunnik (1999) suggested that the second-order upwind difference scheme is the best among some others. However, the upwind difference scheme can introduce artificial damping to the system through the free surface condition. Thus it is essentially the same technique as the low-pass filter or the smoothing technique.

In all the cases without forward speed studied in this study, no instability was observed. However, we saw strong instability when taking into account the forward speed effect in the free-surface conditions. It was noted from the simulations that the instabilities are located close to the waterline of the body. We have attempted other time integration schemes of the free-surface conditions, such as the fourth-order Runge- Kutta scheme, the same instabilities were still there.

Consequently, in the cases with forward speeds, a low-pass filter is implemented and applied on the collocation points at the waterline and on points adjacent to these. In this study, a three-point low-pass filter used by Büchmann (2000a) in the linear BEM based numerical wave tank (NWT) is adopted

$$\overline{\mathrm{w}}_{\mathrm{j}} = c\mathrm{w}_{\mathrm{j\text{-}1}} + (1-2c)\,\mathrm{w}_{\mathrm{j}} + c\mathrm{w}_{\mathrm{j+1}}\,. \tag{4.45}$$

Here j is a local numbering of the collocation points in azimuthal or radial direction and $c \in [0 \;\; 0.5]$ is the strength of the filter. w_{j} and $\overline{\mathrm{w}}_{\mathrm{j}}$ are the qualities before and after smoothing. w_{j} could be the velocity potential or the wave elevation. Büchmann (2000a) has successfully applied this low-pass filter in the second-order wave diffraction of a bottom-mounted vertical cylinder with the presence of a weak current.

The filter is only applied to the wave elevation $\eta^{(k)}$ (k=1, 2). Its smoothing effect will come into the velocity potential indirectly through the dynamic free-surface condition. It is suggested that the smoothing should not be applied directly on the velocity potential, because this may introduce a 'shock' to the pressure field and consequently the body changes its motion behavior suddenly. At each time step the filter is first applied in the azimuthal direction for all points on the water line of the body of interest and subsequently the filter is applied in the radial direction to the points adjacent to the waterline points. To avoid that the amount of the smoothing (filtering) depends on the time step size, the filter strength is given as a function of the time step size as

$$c = \frac{4\Delta t}{T}\,, \tag{4.46}$$

where Δt is the time increment, T is the wave period. The filter should be able to remove the instabilities without affecting the physical solution. On the other hand, the solution should not depend on the chosen value of c as long as it is small enough. We will in Chapter 8 show that the obtained solutions are in fact invariant in a large range of the filtering strength.

4.6 Direct calculation of the higher-order derivatives

It is seen from the free-surface conditions and the body boundary conditions formulated in the inertial

coordinate system in Section 2.4 and Section 2.5 that higher-order derivatives occur. The highest derivatives in the second-order free surface conditions (Eq.(2.48) and Eq.(2.49)) with the presence of a small forward speed is of second order, while the third-order derivative appear in the third-order kinematic free-surface conditions (Eq.(2.73) and Eq.(2.74)). However, the third-order derivative term can be rewritten by applying the Laplace equation as

$$\frac{\partial^3 \phi^{(1)}}{\partial Z^3} = -\frac{\partial}{\partial Z}\left(\frac{\partial^2 \phi^{(1)}}{\partial X^2} + \frac{\partial^2 \phi^{(1)}}{\partial Y^2}\right) = -\frac{\partial^2}{\partial X^2}\left(\frac{\partial \phi^{(1)}}{\partial Z}\right) - \frac{\partial^2}{\partial Y^2}\left(\frac{\partial \phi^{(1)}}{\partial Z}\right). \tag{4.47}$$

Therefore, the third-order term $\partial^3 \phi^{(1)} / \partial Z^3$ can be considered as the sum of two second-order derivatives of $\partial \phi^{(1)} / \partial Z$ in the horizontal OXY-plane. At each time step, $\partial \phi^{(1)} / \partial Z$ on OXY-plane is obtained as a solution of the boundary integral equation.

The derivatives in the body boundary conditions are more difficult to deal with from numerical point of view. In the linear body boundary condition with the forward speed effect, the double-gradient term in Eq.(2.57) is associated with the m_j-terms in the seakeeping analysis of ship with forward speed. We also note from Eq.(2.56) and Eq.(2.58) that the second-order body boundary condition is very complicated due to the fact that it involves a triple gradient of the steady velocity potential $\phi^{(0)}$ and three double-gradient terms. In reality, it may represent great numerical difficulties for typical marine structures with high curvatures, e.g. ships.

The indirect way of treating the m_j-terms is to use Stokes-like theorem. By assuming that the body surface is without sharp corner, the ship hull is wall-sided at the waterline, and the steady wave field can be approximated by the double-body flow, Ogilvie & Tuck (1969) used the Stokes theorem to reduce the second-order derivative of velocity potential in the integral equation by one in their studies of forced heave and pitch of a ship of relevance for regular head sea waves. The cost of doing so is the evaluation of integrals involving the first-order derivatives and the normal derivative of the first-order derivatives of the Green function. However, it is not straightforward to generalize the indirect method using Stokes theorem for the integral of third-order derivatives on the body surface.

Because the cubic HOBEM is adopted in this study, the first-order and second-order derivatives can be calculated directly by using the higher-order shape functions, as it was suggested by Liu et al. (1995) and Kim & Kim (1997). The tangential derivative of the velocity potential along ξ and η in the ξ-η plane, i.e. $\partial \phi / \partial \xi$ and $\partial \phi / \partial \eta$, and the normal derivative $\partial \phi / \partial n$ are expressed in the matrix form:

$$\begin{pmatrix} \phi_\xi \\ \phi_\eta \\ \phi_n \end{pmatrix} = \begin{pmatrix} x_\xi & y_\xi & z_\xi \\ x_\eta & y_\eta & z_\eta \\ n_1 & n_2 & n_3 \end{pmatrix} \begin{pmatrix} \phi_x \\ \phi_y \\ \phi_z \end{pmatrix}. \tag{4.48}$$

Here $\vec{n} = (n_1, n_2, n_3)$ is the normal vector of the boundary surface. The subscripts indicate partial differentiation. The gradient of the velocity potential $\nabla \phi$ can thus be obtained by simply using Eq.(4.48). At each time step, ϕ and ϕ_n are known either from the boundary condition or the solution of Laplace equation. The tangential derivatives with respect to ξ and η are obtained by taking the derivatives of the shape functions.

Once the velocity vector is obtained, one uses the shape functions to represent its distribution on each element as

$$\nabla\phi = \sum_{j=1}^{12} \left(\nabla\phi\right)_j \cdot N_j\left(\xi,\eta\right). \tag{4.49}$$

Then the tangential derivatives of the velocity vector $\nabla\phi$ along ξ and η coordinates can be obtained by differentiating the shape function in the form

$$\frac{\partial\nabla\phi}{\partial\xi} = \nabla\left(\nabla\phi\right)\cdot\frac{\partial\vec{r}}{\partial\xi}, \quad \frac{\partial\nabla\phi}{\partial\eta} = \nabla\left(\nabla\phi\right)\cdot\frac{\partial\vec{r}}{\partial\eta}, \tag{4.50}$$

where $\vec{r} = \left(x, y, z\right)$ is the position vector.

Considering the Laplace equation for the velocity potential, one obtain the following matrix equation for the second-order derivatives of the velocity potential

$$\begin{pmatrix} \phi_{x\xi} \\ \phi_{x\eta} \\ \phi_{y\xi} \\ \phi_{y\eta} \\ \phi_{z\xi} \\ \phi_{z\eta} \end{pmatrix} = \begin{pmatrix} x_\xi & y_\xi & z_\xi & 0 & 0 \\ x_\eta & y_\eta & z_\eta & 0 & 0 \\ 0 & x_\xi & 0 & y_\xi & z_\xi \\ 0 & x_\eta & 0 & y_\eta & z_\eta \\ -z_\xi & 0 & x_\xi & -z_\xi & y_\xi \\ -z_\eta & 0 & x_\eta & -z_\eta & y_\eta \end{pmatrix} \begin{pmatrix} \phi_{xx} \\ \phi_{xy} \\ \phi_{xz} \\ \phi_{yy} \\ \phi_{yz} \\ \phi_{zz} \end{pmatrix} = \left[S\right] \begin{pmatrix} \phi_{xx} \\ \phi_{xy} \\ \phi_{xz} \\ \phi_{yy} \\ \phi_{yz} \\ \phi_{zz} \end{pmatrix}. \tag{4.51}$$

Then the second-order derivatives of the velocity potential are expressed as

$$\begin{pmatrix} \phi_{xx} \\ \phi_{xy} \\ \phi_{xz} \\ \phi_{yy} \\ \phi_{yz} \\ \phi_{zz} \end{pmatrix} = \left\{\left[S\right]^T\left[S\right]\right\}^{-1}\left[S\right]^T \begin{pmatrix} \phi_{x\xi} \\ \phi_{x\eta} \\ \phi_{y\xi} \\ \phi_{y\eta} \\ \phi_{z\xi} \\ \phi_{z\eta} \end{pmatrix}, \tag{4.52}$$

where the tangential derivatives of ϕ_x, ϕ_y and ϕ_z along ξ and η on the right-hand side of Eq.(4.52) can be obtained by the differentiation of Eq.(4.49) in terms of ξ and η.

The direct calculation of the third-order derivatives with desired accuracy seems to be very difficult for typical marine structures, e.g. ships. In Chapter 5, we will present a new approach which does not require any derivatives on the right-hand side of the body boundary conditions. The feature of this new approach is that the formulation in the body-fixed coordinate system is used in the near field and we keep a formulation in the inertial reference frame in the outer domain. Unfortunately, we are not able to find any analytical results to validate the new method. Therefore, we will use the traditional formulation in the inertial coordinate system for the validation purpose. The comparison between the results of the traditional method and that of the new method will be presented in Chapter 8. Only a smooth body with simple geometry is considered in the comparisons. With this smooth and simple geometry, we are able to apply the desingularized BEM (see Cao et al., 1991) to solve the basis flow and the higher-order derivatives of the basis flow. In the calculations based on the traditional formulation, we use the desingularized BEM only for the basis flow $\phi^{(0)}$ and the HOBEM is used

for solution of the unsteady flow. One should note that the desingularized BEMs are not applicable for wave-body interactions with sharp corners.

In the desingularized BEM, the singularities are offset outside of the water domain, so that the difficulty associated with the singular behavior of the Green function is avoided. Once the strength of the sources is obtained, the derivatives of the velocity potential can be evaluated by differentiating the Green functions. However, one has to be careful when choosing the offset distance. If the offset distance is too large from the collocation points, the resulting solution will not be able to represent arbitrary local flow patterns. If the distance is too small, an irregular highly oscillatory behavior of the flow is seen. This numerical error is due to the discontinuity between the individual elements (see the summary made by Bertram (2000)). The desingularized BEM need special efforts for instance for very slender ship bows. However, for a body with smooth and simple geometry, the desingularized BEM is expected to give acceptable results. A variant of the desingularized BEM is the raised panel method (Raven, 1996). The desingularized raised panel method uses connected elements instead of the isolated singularities. Examples of the desingularized isolated sources and the desingularized raised panels are shown in Fig.4.6a and Fig.4.6b, respectively.

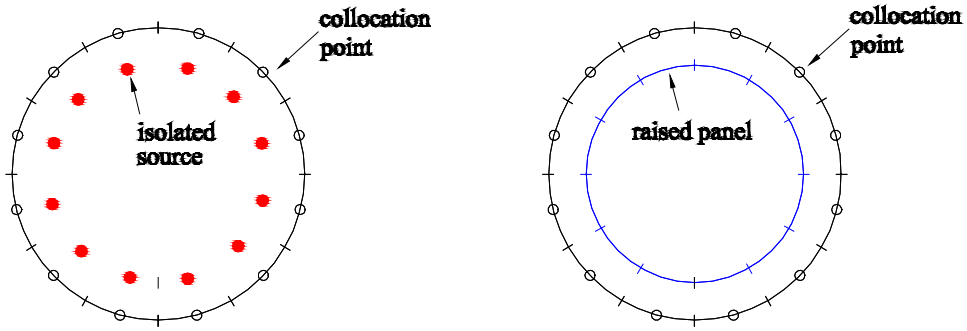

(a) (b)

Fig. 4.6. (a) Desingularized isolated sources. (b) Desingularized raised panels.

The following empirical formula is used to calculate the offset distance

$$L_{offset} = l_d \left(D_m\right)^{\beta}, \quad \left(l_d > 0, \beta \le 1\right) \tag{4.53}$$

where l_d is a constant coefficient. D_m is the size of the mesh which can be approximated by the square root of the area of the local element. β=0.5 is used in this study.

We have firstly applied the desingularized BEM to a sphere moving in infinite fluid. The analytical solution of the moving sphere is known as a dipole in infinite fluid with direction in the ambient flow direction. Studying a moving body in infinite fluid is relevant to the double-body basis flow. Because the double-body flow satisfies the rigid-wall free-surface condition, we can then take an image of the mean wetted body surface about the mean water plane. The consequence is that the double-body flow problem is equivalent to a moving body in infinite fluid. By testing with different offset distances and comparing with the analytical results of the velocity potential and its first-order, second-order and third-order derivatives, we obtain an optimal offset distance. Numerical results showed that $1.6 \le l_d \le 2.5$ gives quite accurate results for both the velocity potential and its higher-order

derivatives. The experience will then be applied in the case of an axisymmetric body without sharp corner studied in Chapter 8 when we solve a second-order problem with forward speed effect by using the formulation in the inertial reference frame.

Fig.4.7 - Fig.4.10 show respectively the velocity potential, first-order, second-order and third-order derivatives of the velocity potential on the surface of a moving sphere (radius R=1.0) in infinite fluid with unit velocity in positive X-direction. The results are for $\psi = \pi / 2$ and only the nonzero terms are presented. Here (r, ψ, θ) is the spherical coordinates. $l_d = 1.8$ was used in the calculations.

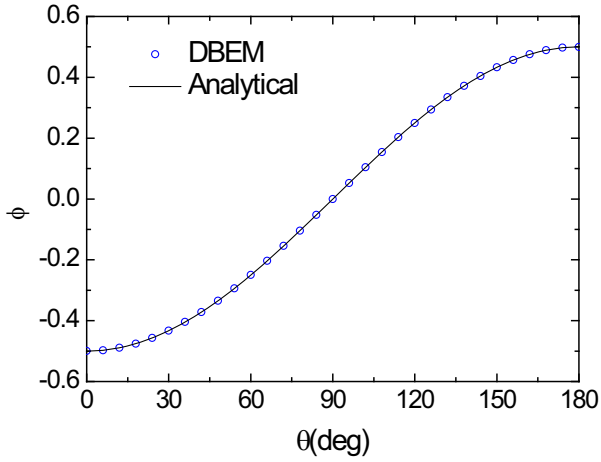

Fig. 4.7. Velocity potential of a moving sphere in infinite fluid. The results are for $\psi = \pi / 2$. The radius R=1.0. Forward speed U=1.0.

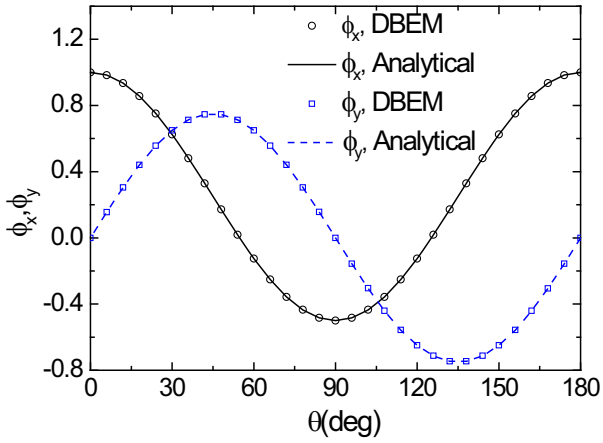

Fig. 4.8. First-order derivatives of the velocity potential of a moving sphere in infinite fluid. The results are for $\psi = \pi / 2$. The radius R=1.0. Forward speed U=1.0.

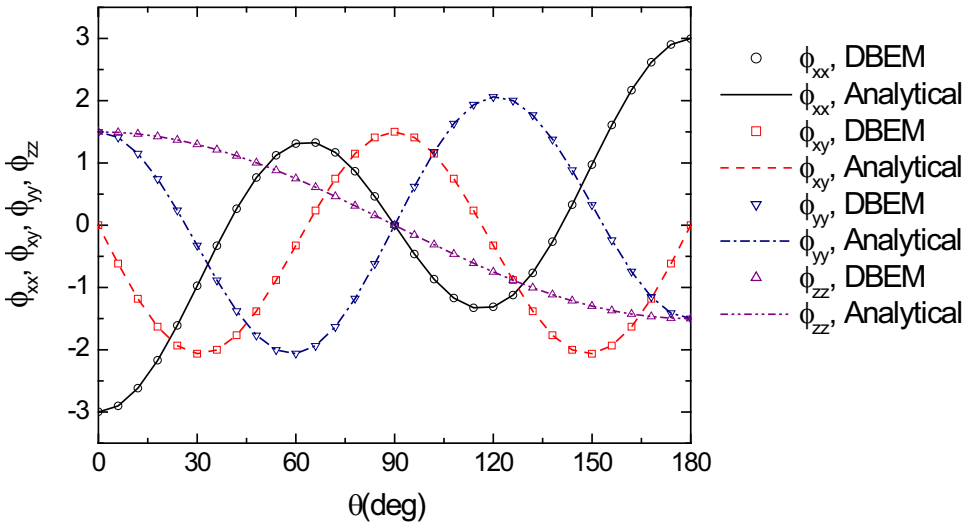

Fig. 4.9. Second-order derivatives of the velocity potential of a moving sphere in infinite fluid. The results are for $\psi = \pi / 2$. The radius R=1.0. Forward speed U=1.0.

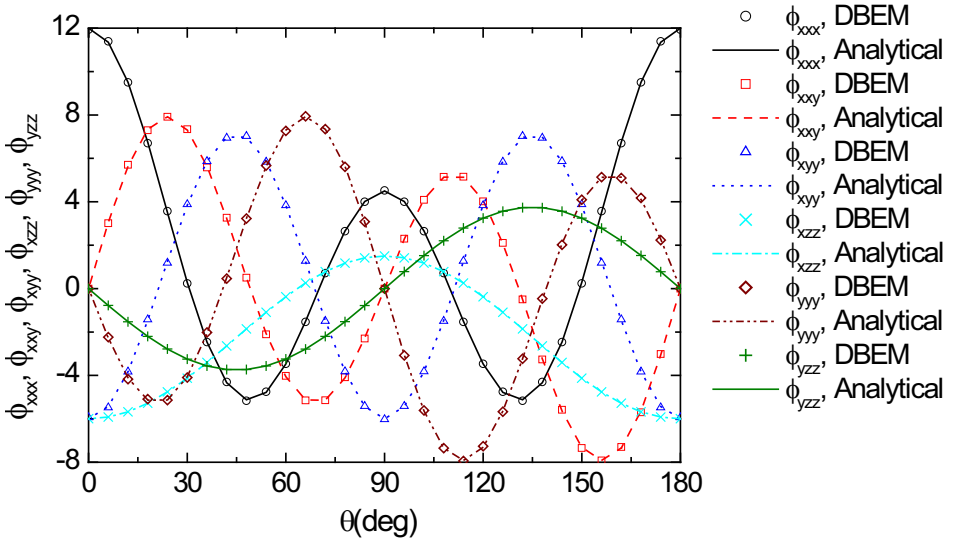

Fig. 4.10. Third-order derivatives of the velocity potential of a moving sphere in infinite fluid. The results are for $\psi = \pi / 2$. The radius R=1.0. Forward speed U=1.0.

4.7 Types of grid on the free surface

Two types of meshes on the free surface are popular in the application of panel methods for the ship motion analysis, i.e. the rectangular grid and the oval grid. A special case of the oval grid is the circular grid. In this study, the oval grid is adopted. Fig.4.11 shows an example of the oval grid on the free surface. Only half of the mesh is shown due to symmetry.

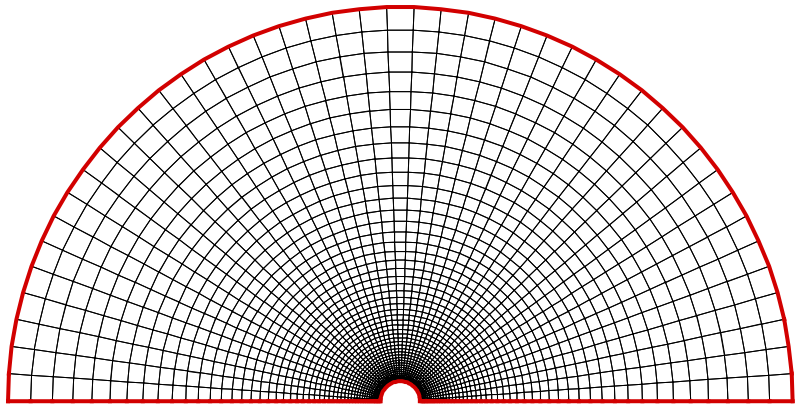

Fig.4.11. An example of the oval grid on the free surface.

It was shown in Huang (1996) by using a weak scatter model that the two types of the grids virtually give the same predictions in terms of forces on the ship exerted by the flow, which justified the use of the oval-type grid. It was observed by Kim & Kim (2008) in the time-domain seakeeping analysis of a ship with forward speed that the oval grid generally provides smoother and more reasonable solutions for diffraction and radiation problems. Since the disturbed waves due to the existence and the motion of a body propagate in the radial direction eventually, the oval grid type seems to have generally better prediction of radiating wave. They also pointed that the rectangular meshes would be a right choice if a wave-resistance problem becomes more important. This may be associated with the fact that the configuration of the rectangular grid is more close to the stream lines of the steady flow.

The main reason why the oval grid is chosen in this study is that, in order to obtain the same accuracy in the solution, fewer panels are needed in the oval grid than that in the rectangular grid. Therefore, the selection of the oval grid can greatly reduce the CPU time. On the other hand, the oval grid requires less memory. This has also been discussed in Huang (1996).

4.8 Matrix Solver

One of the biggest problems related to the BEM is that in general the CPU time and the memory requirements needed to solve a problem increase rapidly with the number of the unknowns in the

problem. The memory required is proportional to N^2 with N as the number of unknowns. Before proceeding to the numerical calculations, we have to choose a robust and time-efficient method based on the computer sources at hand.

4.8.1 Why HOBEM?

The BEM solver is adopted as the tool of solving the Laplace equation through the boundary integral equations. Unlike the field solver, e.g. Finite Element Method (FEM) and Finite Difference Method (FDM), BEM needs unknowns only on the boundaries enclosing the fluid domain, and thus reduces the dimensions of the problem by one. On the other hand, it is easier to generate mesh required in the BEM analysis compared that in the field solvers. The bottleneck of the BEM appears when the number of the unknowns increases. It was argued by Wu & Eatock Taylor (1995) and Ma et al. (2001a, 2001b) that although the BEM has far fewer unknowns, for the nonlinear wave-body interaction problem it usually requires much more memory because at each time step the unknowns are coupled by a fully populated matrix. By contrast, the FEM needs less memory and is computationally far more efficient. However, the bottleneck of the BEMs will no longer exist if the accelerated methods, e.g. the predictor-FFT method (p-FFT) and the fast multipole method (FMM), are combined with the BEM solvers. Asymptotically, the p-FFT method needs O(*NlogN*) memory and O(*NlogN*) CPU time, and the FMM needs O(*NlogN*) memory and O(*N*) CPU time. According to the author's knowledge that in the field of marine hydrodynamic, no comparative study has been made between the field solvers and the accelerated BEM solvers regarding to memory and CPU time requirements. However, we found from other fields that, for large-scale problems, the accelerated BEM has advantage over the field solvers from the computational point of view, and that the memory requirement is acceptable on a PC. Liu (2009) conducted a thermal analysis and compared the results obtained with FEM and the constant BEM accelerated by FMM. With the FEM using the commercial software ANSYS, more than 363,000 volume elements are applied. With the BEM, only about 42,000 triangular constant surface elements are applied with the same number of DOFs. On a desktop PC, the FEM solution took about 50 minutes to finish, whereas the BEM solution took about only 16 minutes. Considering the possibility that the numerical codes developed during this doctoral study could be modified to study the large-scale problems, for instance Very Large Floating Structure (VLFS) and Mobile Offshore Base (MOB), and fully-nonlinear wave-body problems, the author decided to use BEM as the numerical tool.

The cubic HOBEM is adopted instead of lower-order ones. The advantage of the HOBEM over the lower-order BEM was reported by Liu & Kim (1991).

4.8.2 Complexity of BEM solvers

In the conventional BEMs, setting up the influence matrices takes O(N^2) operations and thus O(N^2) time usage. Different methods can be used for solving a matrix equation. A direct method such as the Gaussian elimination or LU-factorization needs O(N^3) operations. In the time-domain simulations, if the matrices remain the same with the evolution of time, the direct method may be a good choice. This is the case in the weakly-nonlinear hydrodynamic problems when the perturbation method is adopted. One only needs to invert the matrix once and use it later in all the time steps. The solution at each time step is obtained by multiplying the inverse of the matrix and a known vector, which takes only O(N^2) operations.

Alternatively, one can use the iterative solvers. Typical iterative solvers, e.g. the Gauss-Seidel method

and the Krylov subspace Generalized Minimal Residual (GMRES) method, yield O(N^2) CPU time. Major CPU time is spent in the matrix-vector product during the iterations. The number of the iterations needed to get a convergent result strongly depends on the condition number of the matrix. Among the BEMs, the constant BEM has in general better conditioning than that of the higher-order BEMs. It was noted by Maniar (1995) that the conditioning may worsen dramatically as the order of the basis function increases. The conditioning of the desingularized method is very sensitive to the offset distance. If the offset of the singularity is too large from the collocation point, the resulting equation system may be of very poor condition. The preconditioners can be used to speed up the convergence.

4.8.3 Algorithm of FMM

In order to minimize the CPU time used in the matrix-vector products during the iterations and thus speed up the iterations, the p-FFT (see e.g. Phillips & White (1997) and Kring et al. (2000)) and FMM (see e.g. Rokhlin (1985), Greengard (1988), Cheng et al. (1999), Yoshida (2001), Nishimura (2002) and Liu (2009)) have been attempted in solving the matrix equation.

A comprehensive review of the history of the development of FMM can be found in, for instance Nishimura (2002). FMM was introduced by Rokhlin (1985) as an O(N) numerical method for solving an integral equation for 2D Laplace equation. This method was further developed and made famous by Greengard (1988) as he applied FMM to multi-body problems. FMM and related methods found applications in various fields in science and engineering, such as astrophysics (e.g. Warren and Salmon (1992)), molecular dynamics (Board et al., 1992), fluid mechanics (the vortex methods, e.g. Salmon et al. (1994)), etc. The influence of FMM to science and engineering was so profound that this method is ranked among the top ten algorithms of the 20th century along with the Krylov subspace iteration, QR algorithm, FFT, etc. See Board & Schulten (2000).

The applications of FMM in marine hydrodynamic and costal engineering have been made by for instance Utsunomiya et al. (2001, 2002), Utsunomiya & Watanabe (2003), Utsunomiya & Okafuji (2007), Ning et al. (2005) and Fochesato & Dias (2006). These applications are either in frequency domain or the fully-nonlinear numerical wave tank (NWT). In order to investigate to what extent the accelerated method can speed up the calculation and to see if the accelerated method is applicable to the weakly-nonlinear wave-body analysis based on perturbation scheme, a numerical module based on the FMM has been developed to accelerate the cubic HOBEM described in Section 4.2.

We will now briefly summarize the algorithm of the FMM. For further details, the readers are referred to the references listed above. The basic idea behind these accelerating methods is that a point ‘far away’ from the source/dipole points does not strongly feel the individual singularities, therefore the influence of the far-away sources/dipoles can be approximated by a clustering technique. The influence of the sources/dipoles in the neighborhood of the field point is calculated directly without approximation. Consequently the operation count is O(N). In order to judge if the sources/dipoles can be considered as far-away singularities, all boundary elements (or panels) are organized into an oct-tree structure by introducing cells to which a number of elements belongs. At the top level of the tree is a cell containing the whole set of the boundary elements. The cell is cut into eight children cells to create the first level. The tree is built recursively until a number of levels are reached. The cells without children cells are called the leaf cells of the tree. Then one can work mainly in terms of the cells of the oc-tree rather than the elements or the individual singularities. In fact, one considers the

contributions of groups of sources/dipoles belonging to a same cell. The regular portioning automatically gives distance criteria to determine the cells for which it is possible to use the multipole expansions. Therefore interaction lists are created for each cell. Interactions between well-separated pairs can then be computed by multipole expansions. Fig.4.12 shows an example of the 2D representation of the tree structure. The rectangulars with the filled circles as the nodes are the boundary elements. The other rectangulars with unfilled circles as the nodes are the cells.

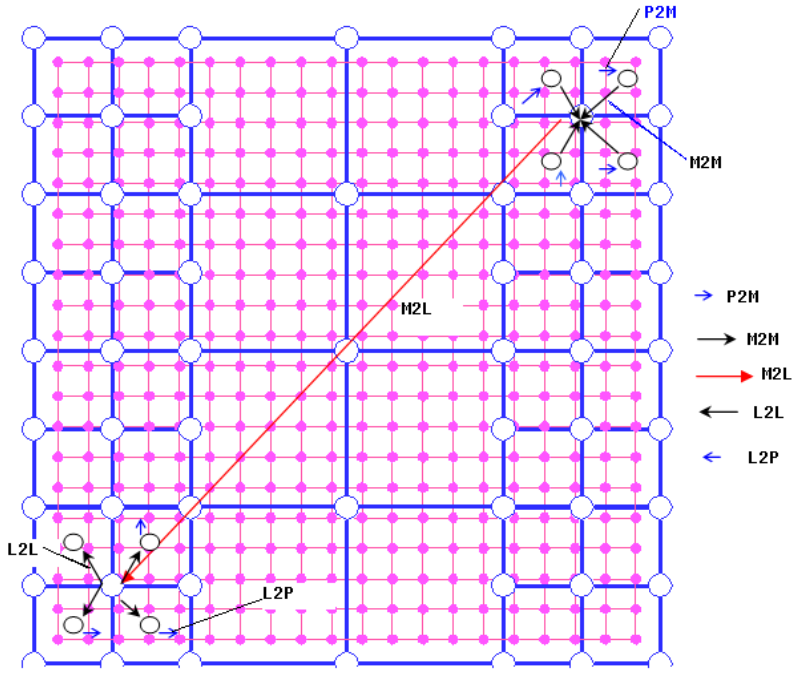

Fig 4.12. Schematic representation of fast multipole algorithm.

After the oc-tree structure is built up, the algorithm of the FMM consists of the following steps:

- Preparing the multipole expansions referred to as ***P2M***;
- Moving the multipole expansion point of the leaf cell to the center of the parent cell and by gathering all of the multipole expansion coefficients of the child cells, we obtain the multipole expansion coefficients for the parent cell. This is referred to as ***M2M***.
- If two well-separated cells A and B are in the same level and that the parent cell of A and that of B are neighbors, we convert the multipole coefficients of the cell A(or B) to the local expansion coefficients of cell B(or A). Gathering the local expansion coefficients, we obtain the local expansion coefficients from the far cells belonging to the parent cell. This procedure is referred to as ***M2L***.
- If the parent cell has local expansion coefficients, by moving the local expansion points to the center of the child cells, we obtain the local expansion coefficients of the specified cell. We refer this step as ***L2L***.
- Evaluating the contribution from far field via the coefficients of the local expansion. This is called ***L2P***. The total contribution is obtained by adding the far-field contribution and the contribution from boundary elements in adjacent cells via direct integration.

See also the illustration of P2M, M2M, M2L, L2L and L2P in Fig. 4.12.

P2M

The kernels $G(\mathbf{x},\mathbf{y})$ and $\partial G/\partial n(\mathbf{x},\mathbf{y})$ in Eq.(4.1) can be expanded respectively as (see for instance Nishimura (2002), Shen & Liu (2007) and Yoshida (2001))

$$G(\mathbf{x},\mathbf{y})=\frac{1}{r}=\sum_{n=0}^{\infty}\sum_{m=-n}^{n}\overline{S}_{n,m}(\mathbf{x}-\mathbf{y}_c)R_{n,m}(\mathbf{y}-\mathbf{y}_c),\quad |\mathbf{y}-\mathbf{y}_c|<|\mathbf{x}-\mathbf{y}_c|\ , \tag{4.54}$$

and

$$\frac{\partial G}{\partial n}(\mathbf{x},\mathbf{y})=\sum_{n=0}^{\infty}\sum_{m=-n}^{n}\overline{S}_{n,m}(\mathbf{x}-\mathbf{y}_c)\frac{\partial R_{n,m}(\mathbf{y}-\mathbf{y}_c)}{\partial n(\mathbf{y})},\quad |\mathbf{y}-\mathbf{y}_c|<|\mathbf{x}-\mathbf{y}_c|\ . \tag{4.55}$$

Here $\mathbf{y}_c$ is the expansion center close to singularity point $\mathbf{y}$ and the overbar indicates the complex conjugate. The functions $R_{n,m}$ and $S_{n,m}$ are called solid harmonic functions, given as

$$R_{n,m}(\mathbf{x})=\frac{1}{(n+m)!}P_n^m(\cos\theta)e^{im\psi}\rho^n, \tag{4.56}$$

$$S_{n,m}(\mathbf{x})=(n-m)!P_n^m(\cos\theta)e^{im\psi}\frac{1}{\rho^{n+1}}, \tag{4.57}$$

where (ρ,θ,ψ) are the spherical coordinates of vector $\mathbf{x}$. P_n^m is the associated Legendre function.

The merit of expanding the kernels $G(\mathbf{x},\mathbf{y})$ and $\partial G/\partial n(\mathbf{x},\mathbf{y})$ by the solid harmonic functions is that the dependence of the kernel on $\mathbf{x}$ and $\mathbf{y}$ are separated. If the expansions of the kernels are plugged into the boundary integral equation, the integrals explicitly associated $\mathbf{y}$ are only needed to be calculated once and can be used for any far-away field point $\mathbf{x}$. Consequently the amount of work is O(Np) where p is the number of terms kept in the summation of the expansions. This estimate is based on the far field expansion and is therefore related to only one part of the distribution of sources/dipoles. For singularities that are close to each other, direct computations of the interactions are necessary.

The integrals on the right-hand side of Eq.(4.1) over a subset of the integral surface denoted by S_y for $\mathbf{x}$ which is away from S_y can now be evaluated as

$$\iint_{S_y}G(\mathbf{x},\mathbf{y})\frac{\partial\phi^{(k)}}{\partial n}(\mathbf{y})dS(\mathbf{y})=\sum_{n=0}^{\infty}\sum_{m=-n}^{n}\overline{S}_{n,m}(\mathbf{x}-\mathbf{y}_c)M_{n,m}(\mathbf{y}_c),\quad |\mathbf{y}-\mathbf{y}_c|<|\mathbf{x}-\mathbf{y}_c|, \tag{4.58}$$

$$\iint_{S_y}\frac{\partial G(\mathbf{x},\mathbf{y})}{\partial n}\phi^{(k)}(\mathbf{y})dS(\mathbf{y})=\sum_{n=0}^{\infty}\sum_{m=-n}^{n}\overline{S}_{n,m}(\mathbf{x}-\mathbf{y}_c)\tilde{M}_{n,m}(\mathbf{y}_c),\quad |\mathbf{y}-\mathbf{y}_c|<|\mathbf{x}-\mathbf{y}_c|, \tag{4.59}$$

where $M_{n,m}$ and $\tilde{M}_{n,m}$ are the multiple moments centered at $\mathbf{y}_c$ and defined respectively as

$$M_{n,m}=\iint_{S_y}R_{n,m}(\mathbf{y}\text{-}\mathbf{y}_c)\frac{\partial\phi^{(k)}}{\partial n}(\mathbf{y})dS(\mathbf{y}), \tag{4.60}$$

$$\tilde{M}_{n,m}(\mathbf{y}_c)=\iint_{S_y}\frac{\partial R_{n,m}(\mathbf{y}\text{-}\mathbf{y}_c)}{\partial n(\mathbf{y})}\phi^{(k)}(\mathbf{y})dS(\mathbf{y}). \tag{4.61}$$

The moments for a certain cell are obtained by adding the contributions of all the boundary elements

in that cell. An element is considered to be within the cell if the center point of the element drops in the cell. Only the moments in the leaf cells are calculated. The moments in a non-leaf cell is obtained by adding the contributions of children cells together. However, the moments in each child cell are expressed with respect to its own center $\mathbf{y}_c$. We therefore need to transfer the moment at $\mathbf{y}_c$ to the center of the parent cell $\mathbf{y}_{c'}$.

M2M

When the multipole expansion center is moved from $\mathbf{y}_c$ to $\mathbf{y}_{c'}$, we apply the following M2M translation

$$M_{n,m}\left(\mathbf{y}_{c'}\right)=\iint_{S_y} R_{n,m}(\mathbf{y}\text{-}\mathbf{y}_{c'})\frac{\partial\phi^{(k)}}{\partial n}(\mathbf{y})dS(\mathbf{y})=\sum_{n'=0}^{n}\sum_{m'=-n'}^{n'} R_{n',m'}(\mathbf{y}_c\text{-}\mathbf{y}_{c'})M_{n-n',m-m'}\left(\mathbf{y}_c\right), \quad (4.62)$$

which is also valid for $\tilde{M}_{n,m}$. The M2M translations are used recursively from the lowest-level cells, i.e. the leaf cells, to the top levels.

M2L

The local expansion at the field point **x** for the kernel $G(\mathbf{x},\mathbf{y})$ on S_y is given as

$$\iint_{S_y} G(\mathbf{x},\mathbf{y})\frac{\partial\phi^{(k)}}{\partial n}(\mathbf{y})dS(\mathbf{y})=\sum_{n=0}^{\infty}\sum_{m=-n}^{n} R_{n,m}\left(\mathbf{x}-\mathbf{x}_L\right)L_{n,m}\left(\mathbf{x}_L\right), \quad \left|\mathbf{y}-\mathbf{y}_c\right|<\left|\mathbf{x}-\mathbf{y}_c\right|. \quad (4.63)$$

The coefficients $L_{n,m}\left(\mathbf{x}_L\right)$ are given by the following M2L translation

$$L_{n,m}\left(\mathbf{x}_L\right)=(-1)^n\sum_{n'=0}^{\infty}\sum_{m'=-n'}^{n'}\overline{S}_{n'+n,m'+m}(\mathbf{x}_L\text{-}\mathbf{y}_c)M_{n',m'}\left(\mathbf{y}_c\right), \quad \left|\mathbf{x}-\mathbf{x}_L\right|<\left|\mathbf{y}_c-\mathbf{x}_L\right|. \quad (4.64)$$

Here $\mathbf{x}_L$ is the center of the local expansion. A similar expansion for the moment involving the integral of $\partial G/\partial n(\mathbf{x},\mathbf{y})$ is also valid.

For a considered cell *A*, the M2L translations are only applied to the well-separated cells at the same level which belong to the neighborhood of the parent cell of *A*. The contributions from even further cells are inherited from its parent cell by using the L2L translations.

L2L

By using the following L2L translations, a parent cell passes down its moments to its children cells

$$L_{n,m}\left(\mathbf{x}_{L'}\right)=(-1)^n\sum_{n'=n}^{\infty}\sum_{m'=-n'}^{n'} R_{n'-n,m'-m}(\mathbf{x}_{L'}-\mathbf{x}_L)L_{n',m'}\left(\mathbf{x}_L\right), \quad (4.65)$$

where $\mathbf{x}_L$ is the center of a mother cell and $\mathbf{x}_{L'}$ is the center of one of its children cell.

The L2L translations are applied recursively from the top cells to the lower-level cells. The moments of a certain cell are obtained by summing up the contributions of the M2L translations and that of L2L.

L2P

After the M2L and L2L operations, the moments in the leaf cells are all known. For a field point **x**, the contribution of the well-separated boundary elements in the boundary integral equation can be

obtained by local expansions. For example, we have for $\partial G/\partial n$ kernel integral that

$$\iint_{S_y} G(\mathbf{x},\mathbf{y})\frac{\partial \phi^{(k)}}{\partial n}(\mathbf{y})dS(\mathbf{y}) = \sum_{n=0}^{\infty}\sum_{m=-n}^{n}\frac{\partial R_{n,m}(\mathbf{x}-\mathbf{x}_L)}{\partial n}L_{n,m}(\mathbf{x}_L), \quad |\mathbf{x}-\mathbf{x}_L| < |\mathbf{x}-\mathbf{y}|, \qquad (4.66)$$

where $\mathbf{x}_L$ is the center of the leaf cell. $\mathbf{x}$ is the location of a field point in the cell. A similar expansion for the *G* kernel integral exists. The contributions from the nearby elements are obtained by the direct calculation. See Section 4.2.

4.8.4 Selection of a proper solver

Consideration on memory

For an ordinary type of BEM, setting up the fully populated matrices needs $O(N^2)$ memory. The memory needed for the storage of a $N \times N$ matrix with double precision is $8 \cdot N \cdot N / 1024 \cdot 1024 \cdot 1024$ Giga Bytes (GBs). In the wave-body analysis by the ordinary type of BEMs, we need at least two $N \times N$ matrices. This is obvious from Eq.(4.11). That means we are limited to problems with ≈ 20000 unknowns for a PC with 4 GBs memory and to problems with ≈ 30000 unknowns for a workstation with 8 GBs memory, considering that some additional memory is needed for the storage of other variables for instance the velocity potential and velocities on the body surface and the free surface. When the number of the unknowns is beyond the memory capacity of the computer source at hand, it is suggested that one choose the field solvers, e.g. the FEM, or the combination of FMM and BEMs.

Consideration on CPU time

As illustration, a linear NWT without the presence of structure was studied by different matrix solvers. Fig.4.13 shows the comparison of CPU time spent in the first time step of the calculation. The iterative HOBEM in the comparison uses the diagonal pre-conditioner (Saad & Schultz, 1986) which was widely used in the fully-nonlinear NWT analysis (see e.g. Kim et al.(1999) and Tanizawa (2000)) The block diagonal pre-conditioner (see e.g. Nishida & Hayami (1997) and Wang et al. (2005)) was used in the iterative FMM+HOBEM. Fig.4.14 shows an example of the boundary elements of the NWT and the oc-tree structures. The results in Fig.4.13 confirm that the FMM accelerated BEM is an asymptotically O(N) method while the ordinary iterative BEM is an $O(N^2)$ method.

The CPU time by HOBEM shown in Fig.4.13 consists of setting up the fully-populated matrices and solving the matrix equation iteratively by GMRES. The CPU time by FMM+BEM includes setting up the diagonal and near-diagonal terms of the matrices, the multipole expansion coefficients and solving the matrix equation iteratively by GMRES. In the FMM+BEM used in Fig.4.13, we have used 100 terms in the multipole expansions and the maximum number of sources/dipoles in a leaf cell was 200. A convergence criterion of $O(10^{-4})$ was used in the iterative solvers of HOBEM and FMM+HOBEM.

Even though the comparison shown in Fig.4.13 is made for only one time step, it gives indication of the CPU time for the frequency-domain and fully-nonlinear wave-body analysis. In the fully-nonlinear wave-body analysis, because the computational boundary is moving with the evolution of the solution, one needs to calculate the influence coefficients and solve the resulting equation system at each time step.

It was also seen from the comparison that the FMM+HOBEM is faster than the HOBEM as long

as $N \geq 1000$, which is in most cases true in 3D studies. That means the FMM+HOBEM is always preferred compared with iterative HOBEM solvers in both the frequency-domain analysis and the fully-nonlinear analysis.

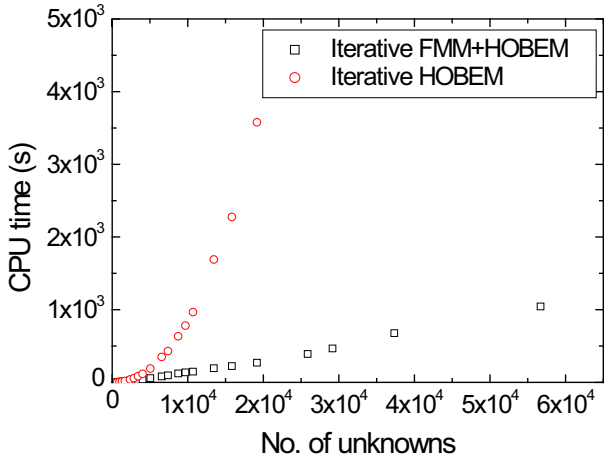

Fig.4.13. Comparison of CPU time of the ordinary iterative HOBEM solver and that of the FMM accelerated HOBEM in the first step of a linear NWT analysis. The results are shown for different numbers of unknowns.

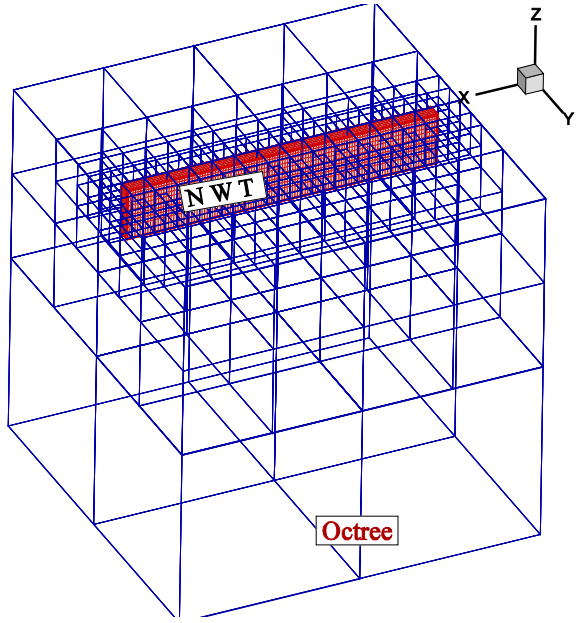

Fig.4.14. An example of the meshes on the surfaces of numerical wave tank and the octree structure used in the FMM algorithm.

When a weakly nonlinear wave-body problem based on perturbation scheme is considered in the time domain (which is the focus of this thesis), the computational domain remains unchanged. Therefore

the influence matrix is not needed to be set up and invert once and can be used later on in all the time steps. Our numerical experiments on a workstation with 8GB memory showed that this strategy is even more time-efficient than the FMM+HOBEM solver for $N \le 20000$. However, this strategy needs more memory since the LU factors (or the inverse of the influence matrix) need some additional memory. It is suggested to use the FMM accelerated HOBEM for problems with unknowns more than 20000. Suggestion on selection of the matrix solvers is listed in Table 4.1 based on our numerical experience. This may not always be true depending on the computer sources at hand. However, one should always consider a similar procedure here and choose an efficient and practical way of solving the large matrix system for 3D studies.

Table 4.1 Empirical suggestion on selection of the matrix solvers for fully-nonlinear, frequency-domain and perturbation-based time-domain wave-body analysis. N is the number of unknowns. The LU-factorization used in the perturbation-based time-domain analysis requires that one calculates the influence matrices (and the inverse if necessary) and uses these matrices later in all the time steps.
[1]: This number depends on the computer source at hand, especially the memory of the computer.

	LU-factorization	Iterative BEM	Iterative FMM+BEM
Fully nonlinear		$N \le 1000$	$N \ge 1000$
Frequency domain		$N \le 1000$	$N \ge 1000$
Perturbation-based time domain	$N \le 20000$[1]		$N \ge 20000$[1]

CHAPTER 5

Use of the Body-Fixed Coordinate System in Weakly-Nonlinear Wave-Body Problems

When a weakly-nonlinear wave-body problem is considered in an inertial coordinate system, high-order derivatives appear in the higher-order body boundary conditions and make it difficult to get convergent and accurate results, especially for bodies with sharp corners or high surface curvatures. In this chapter, a new method taking the advantage of the accelerated body-fixed coordinate system is proposed to avoid derivatives of the velocity potential on the right-hand side of the body boundary conditions. A domain decomposition method is applied with the use of the body-fixed coordinate system in the inner domain and the inertial coordinate system in the outer domain. The resulting boundary integral equation of the new method is valid for cases with and without sharp corners.

5.1 Comparison of the weakly-nonlinear formulations in inertial and body-fixed coordinate systems

5.1.1 Free-surface conditions

The formulations of a weakly-nonlinear wave-body problem considering a small forward speed have been presented in Chapter 2 in both the inertial coordinate system and body-fixed coordinate system. In this section, we will discuss the difficulties associated with the inertial coordinate system and with body-fixed coordinate system, respectively.

The free-surface conditions formulated in the inertial coordinate system (see Eq.(2.48) and Eq.(2.49)) are simpler than that in the body-fixed coordinate system (see Eq.(2.88) and Eq.(2.89)). The free-surface conditions in the inertial frame do not depend on the instantaneous rigid-body motions, while the body motions come into the free-surface conditions in the body-fixed coordinate system. This indicates that when the seakeeping of a ship with forward speed is considered by a frequency-domain approach, the solution procedure in the body-fixed coordinate system is more complicated than that in inertial coordinate system.

As it was mentioned in Section 2.6.1, the free-surface conditions based on Taylor expansion about z=0 of the body-fixed coordinate system are only valid near the body when the distance between the origin of the coordinate system oxyz and the point (x, y, 0) is not too large.

5.1.2 Body boundary conditions

The body boundary conditions formulated in the inertial coordinate system is very complicated (see Eq.(2.56)- Eq.(2.58)). The second-order derivatives of the steady velocity potential in the first-order body boundary condition are associated with the so-called m_j-terms. The m_j-terms are important in the linear seakeeping analysis of ships with forward speed. For ships with point ends, the effects of m_j-terms are more important at the ship ends. This may be explained by the fact that the ship ends are stagnation points in potential flow theory without flow separation, and that the m_j-terms are associated with the first-order derivatives of the velocity of the basis flow at the mean body surface. This fact increases the complexity of the direct calculation of the m_j-terms for ships without sharp corners, because the ships bows and sterns are normally with high surface curvatures. For ships with the transom stern, the stern cannot be considered as a point end. The fact that the flow leaves tangentially from the transom stern causes hull-lift damping (Faltinsen, 2005), which can be understood from the fact that the ship is a low-aspect ratio lifting surface beyond a Froude number based on the transom draft.

The indirect way of treating the m_j-terms is to use Stokes-like theorem. By assuming that the body surface is without sharp corner, the ship hull is wall-sided at the waterline, and the steady wave field can be approximated by the double-body flow, Ogilvie & Tuck (1969) used the Stokes theorem to reduce the second-order derivative of velocity potential in the integral equation by one in their studies of the forced heave and pitch of a ship of relevance for regular head sea waves. The cost of doing so is the evaluation of integrals involving the first-order derivatives and the normal derivative of the first-order derivatives of the Green function.

The direct calculation of m_j-terms was early attempted by Zhao & Faltinsen (1989a). Based on the fact that the singularity of the Rankine sources is weakened away from the body surface, they firstly calculated the second-order derivatives on some points offset from the body. The m_j-terms are then obtained through extrapolation. This technique has been shown to be accurate for smooth bodies without sharp corners. Wu (1991) proposed to solve a series of Dirichlet-type problems using the first-order derivatives of velocity potential as the right-hand-side term of the condition on the mean body surface. A similar method was suggested by Chen & Malenica (1998) based on the idea of Wu (1991). There are also successful examples by using a higher-order boundary element method (HOBEM) for the calculations of the m_j-terms, see for instance Bingham & Maniar (1996) and Chen et al. (2000).

When the body is with sharp corners, the Taylor expansion about the mean body surface is invalid and the integral equation used for the smooth bodies is not applicable any more. This is associated with the fact that m_j-terms are not integrable on the body surface. The leading order of the local solution near the sharp corner can be explained by a 2D corner flow (see Newman, 1977). The corner flow solution in the vicinity of the sharp corner can be written as

$$W(\mathbf{z}) = C_1 \mathbf{z}^{1/\lambda} + C\,, \tag{5.1}$$

where C_1 and C are constants. λ is defined as $\lambda = 2 - \theta/\pi$ with $\theta \in [0, 2\pi)$ as the interior angle

of the body at the corner. The leading-order first-order and second-order derivatives of the velocity potential are $O(|\mathbf{z}|^{1/\lambda-1})$ and $O(|\mathbf{z}|^{1/\lambda-2})$. This indicates that the velocity at the sharp corner is always integrable. However, the derivatives of the velocity are integrable only when $\theta \geq \pi$, which explains why the m_j-terms at the sharp corners are not integrable. The reason why the integrals are not integrable when the body boundary condition is satisfied on the mean position of the body boundary is that the formulation of the body boundary condition is wrong with the presence of the sharp corner. The double-gradient term in the body boundary condition (see Eq.(2.56) - Eq.(2.58)) has been derived by a Taylor expansion about the mean body surface. This is not valid at a sharp corner.

In order to avoid this difficulty, Zhao & Faltinsen (1989b) decomposed the velocity potential into two parts, with the first part satisfying the body boundary condition associated with the m_j-terms, and the second part satisfying the body boundary condition with the m_j-terms excluded. By doing that, they finally obtained an integral equation which is valid for cases with sharp corners.

When the second-order solution is pursued, it involves the second-order derivatives of the first-order unsteady velocity potential and the second-order and third-order derivatives of the steady velocity potential on the body (see Section 2.4.2). It is not straightforward to generalize the indirect method using Stokes theorem for the integral of third-order derivatives on the body surface without sharp corners. Furthermore, if the body is with sharp corner, the method proposed by Zhao & Faltinsen (1989b) may in principle be extended to get a proper integral equation. However, we then have to divide the velocity potential into several parts since the second-order body boundary condition contains some terms similar to the m_j-terms and terms involving the third-order derivatives. It may also be difficult to find the corresponding artificial velocity potential for all the m_j-like terms.

However, body boundary conditions described in the body-fixed coordinate system is very simple and without any derivatives on the right-hand sides. Therefore, the resulting boundary integral equation is valid for bodies with and without sharp corners.

5.2 Domain-decomposition approach using body-fixed coordinate system in the near field

The formulation in the body-fixed coordinate system presented in Section 2.6 can be directly applied to an interior problem, e.g. sloshing in tank, as long as the tank motion and the liquid motion in the tank are small. For a 2D tank under forced surge motion, Wu (2007) formulated the second-order sloshing problem in the body-fixed coordinate system and obtained a time-domain solution based on modal expansion. The purpose of his study was to identify the second-order sloshing resonance in a tank, i.e. a possible resonance occurring when the forcing frequency is half of a natural frequency. When it comes to an exterior problem, e.g. seakeeping of ships, the free-surface conditions Eq.(2.88) and Eq.(2.89) are only applicable to a small portion of the free surface near the body.

In order to avoid derivatives on the right-hand side of the body boundary conditions of weakly-nonlinear wave-body problems, a new method based on domain decomposition and body-fixed coordinate system in the inner domain (near-field) was proposed by Shao & Faltinsen

(2010a, 2010b) to avoid derivatives on the right-hand side of the body boundary conditions of weakly-nonlinear wave-body problems with/without forward speed. An inertial coordinate system is used in the outer domain. This section reviews the basis of the new method. Part of the materials presented in this section can also be found in Shao & Faltinsen (2010a, 2010b).

As shown in Fig.5.1, a control surface (SC) is introduced to divide the computational domain into two parts, i.e. the inner domain and the outer domain. The inner domain is enclosed by a projection of the free surface on the oxy-plane near the body (SF1), the body surface (SB) and the control surface (SC). See also Fig.5.2. The outer domain contains the mean free surface away from the body ($SF2_0$), the mean position of the control surface SC_0, the sea bottom S_{bottom} and the vertical surface connecting the free surface and the sea bottom. See also Fig.5.3. In the inner domain close to the body, the problem was solved in a body-fixed coordinate system, while the solution in the outer domain was obtained in an inertial coordinate system. The solutions of the inner and outer domains are then matched at the control surface. The body boundary condition based on this formulation is 'body exact' so that no derivatives are required on the right hand side of the body boundary conditions. The free-surface condition remains as a second-order approximation. It is called 'body exact' because the body boundary condition is formulated at the instantaneous position but only the mean wetted body surface area is considered. That means that the effect of the small variations of the wetted body surface due to the wave elevation and body motion will be handled by the Taylor expansion about the oxy-plane. The velocity potential and its normal derivative on SC are also related to those on SC_0 by Taylor expansions, which will be used as matching condition between the inner domain solution and the outer domain solution.

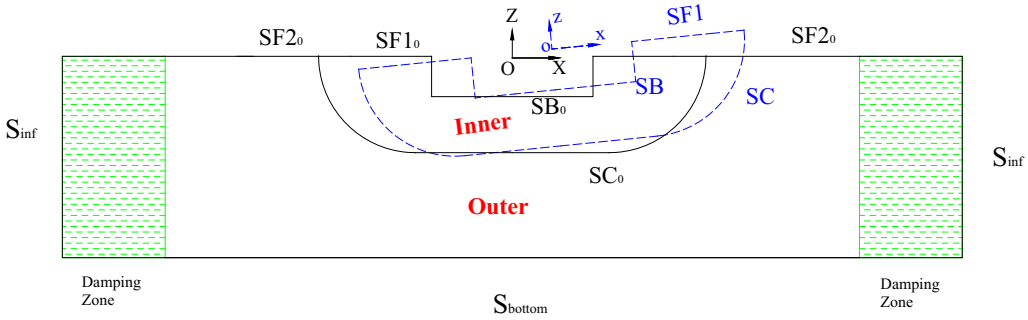

Fig.5.1. Definition of the coordinate systems and the illustration of fluid domain, body boundary, free surfaces, control surface, bottom surface and damping zone.

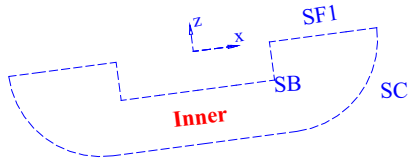

Fig. 5.2. Sketch of the inner domain.

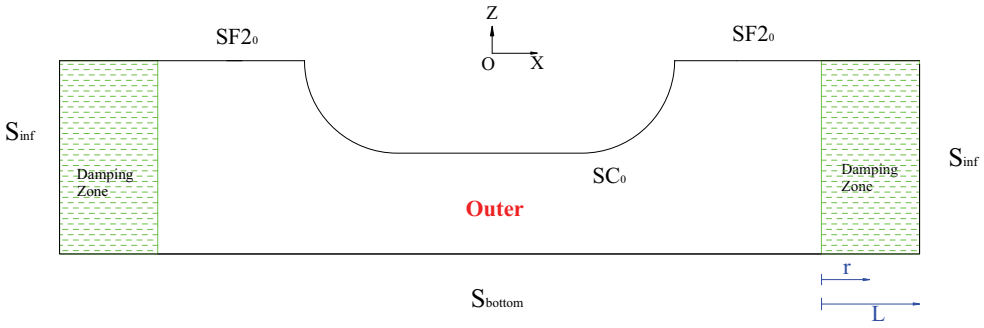

Fig. 5.3. Sketch of the outer domain.

We will show how the domain decomposition strategy works by taking the higher-order BEM as an example. A time-domain approach is followed which means that the scattered part of the velocity potential and wave elevation are zero at the initial time t=0. Applying the modified Green's 3rd identity in the inner domain and the outer domain respectively, we obtain the following boundary integral equations relating the velocity potential, the Green function G(P, Q) and their derivatives

$$C(P)\phi_{\mathrm{II}}^{(k)}(P)=\iint\limits_{\substack{SF2_0+SC_0\\+S_{\inf}+S_{bottom}}}\left[\frac{\partial\phi_{\mathrm{II}}^{(k)}}{\partial n}(Q)\cdot G(P,Q)-\phi_{\mathrm{II}}^{(k)}(Q)\cdot\frac{\partial G}{\partial n}(P,Q)\right]dS \quad \text{, k=1, 2,} \tag{5.2}$$

$$C(P)\phi_{\mathrm{I}}^{(k)}(P)=\iint\limits_{SB+SC+SF1}\left[\frac{\partial\phi_{\mathrm{I}}^{(k)}}{\partial n}(Q)\cdot G(P,Q)-\phi_{\mathrm{I}}^{(k)}(Q)\cdot\frac{\partial G}{\partial n}(P,Q)\right]dS \quad \text{, k=1, 2.} \tag{5.3}$$

Here $\phi_{\mathrm{I}}^{(k)}(P)$ and $\phi_{\mathrm{II}}^{(k)}(P)$ are the velocity potential in the inner and outer domain, respectively. The superscript indicates the order of the solution. k=1 and k=2 mean the first-order and second-order solution, respectively. P denotes a field point and Q denotes the singularity position. The subscript I indicates the inner domain and II the outer domain. C(P) is the solid angle coefficient. $\vec{n}$ is the normal vector defined as positive pointing out of the fluid domain.

The first step to solve the integral equation by using the higher-order BEM is to discretize the boundary surfaces with a number of higher-order elements and use Eq.(4.3) - Eq.(4.5) to approximate the geometry, velocity potential, and the velocities on the boundaries by shape functions. The cubic shape functions in Eq.(4.6) will be used.

After the discretization, the integrals on the boundary surfaces in Eq.(5.2) and Eq.(5.3) can thus be converted into a sum on the elements, each being calculated on the reference element. Eq.(5.2) can be rewritten as

$$\begin{aligned}&C(P)\phi_{\mathrm{II}}^{(k)}(P)+\sum_{i=1}^{NE_{\mathrm{II}}}\int_{-1}^{1}\int_{-1}^{1}\sum_{j=1}^{12}\left(\phi_{\mathrm{II}}^{(k)}\right)_j N_{\mathrm{j}}(\xi,\eta)\frac{\partial G}{\partial n}\left(P,Q(\xi,\eta)\right)\left|\mathbf{J}^i(\xi,\eta)\right|d\xi d\eta\\&=\sum_{i=1}^{NE_{\mathrm{II}}}\int_{-1}^{1}\int_{-1}^{1}\sum_{j=1}^{12}\left(\frac{\partial\phi_{\mathrm{II}}^{(k)}}{\partial n}\right)_j N_{\mathrm{j}}(\xi,\eta)G\left(P,Q(\xi,\eta)\right)\left|\mathbf{J}^i(\xi,\eta)\right|d\xi d\eta,\quad k=1,2.\end{aligned} \tag{5.4}$$

NE_{II} is the total number of elements on the boundaries of the outer domain. By assuming that the discretized equations are satisfied exactly at a set of collocation points, we obtain a system of

equations

$$
\begin{aligned}
&-\sum_{j\in SF2_0} A_{ij}\left(\frac{\partial \phi_{\mathrm{II}}^{(k)}}{\partial n}\right)_j + \sum_{j\in SC_0} H_{ij}\left(\phi_{\mathrm{II}}^{(k)}\right)_j - \sum_{j\in SC_0} A_{ij}\left(\frac{\partial \phi_{\mathrm{II}}^{(k)}}{\partial n}\right)_j \\
&= -\sum_{j\in SF2_0} H_{ij}\left(\phi_{\mathrm{II}}^{(k)}\right)_j, i=1,\cdots,NE_{\mathrm{II}}, k=1,2.
\end{aligned}
\tag{5.5}
$$

Here A_{ij} and H_{ij} are the influence coefficients. In Eq.(5.5), we have dropped the integrals on S_{inf} because the wave motion there is assumed to be very small. This is true if an efficient damping zone is used at the outer layer of the free surface so that most of the energy of the wave is damped out when it reaches S_{inf}. It is also a good approximation if S_{inf} is chosen sufficiently far away from the body, so that the wave motion has not reached S_{inf}, see Faltinsen (1977). The integrals on S_{bottom} do not explicitly show up in Eq.(5.5). Their influences are considered by choosing a Green function satisfying the sea bed condition. It implicitly means that a horizontally sea bed is assumed, because in general it is difficult to find a Green function satisfying the boundary condition for an uneven sea bed.

Similarly we can get a set of equations for the inner domain

$$
\begin{aligned}
&-\sum_{j\in SF1} A_{ij}\left(\frac{\partial \phi_{\mathrm{I}}^{(k)}}{\partial n}\right)_j + \sum_{j\in SB} H_{ij}\left(\phi_{\mathrm{I}}^{(k)}\right)_j + \sum_{j\in SC} H_{ij}\left(\phi_{\mathrm{I}}^{(k)}\right)_j - \sum_{j\in SC} A_{ij}\left(\frac{\partial \phi_{\mathrm{I}}^{(k)}}{\partial n}\right)_j \\
&= -\sum_{j\in SF1} H_{ij}\left(\phi_{\mathrm{I}}^{(k)}\right)_j + \sum_{j\in SB} A_{ij}\left(\frac{\partial \phi_{\mathrm{I}}^{(k)}}{\partial n}\right)_j, \quad i=1,\cdots,NE_{\mathrm{I}}, k=1,2,
\end{aligned}
\tag{5.6}
$$

with NE_{I} being the total number of elements on the boundaries of the inner domain.

In Eq.(5.5) and Eq.(5.6), both the velocity potential and its normal derivative on the control surfaces (SC_0 in the outer domain and SC in the inner domain) are considered as unknowns. However, the quantities on SC_0 in the outer domain can be related to those on SC in the inner domain. These relationships are the matching conditions of the inner-domain solution and the outer-domain solution. Because the body motions are assumed to be small and that the control surface is chosen to be not too far from the body (see Fig.5.1), we can take Taylor expansion from SC to SC_0, which gives

$$
\phi_{\mathrm{I}}^{(k)} = \phi_{\mathrm{II}}^{(k)} + \Delta\phi^{(k)}, \text{ k=1, 2,} \tag{5.7}
$$

$$
\frac{\partial \phi_{\mathrm{I}}^{(k)}}{\partial n} = \frac{\partial \phi_{\mathrm{II}}^{(k)}}{\partial n} + \Delta\phi_n^{(k)}, \text{ k=1, 2,} \tag{5.8}
$$

where

$$
\Delta\phi^{(1)} = \left[\vec{x}^{(1)}\cdot\nabla\phi_{\mathrm{II}}^{(0)}\right]_{SC_0}, \tag{5.9}
$$

$$
\Delta\phi_n^{(1)} = \left[\vec{n}^{(1)}\cdot\nabla\phi_{\mathrm{II}}^{(0)} + \vec{n}^{(0)}\cdot\nabla\phi_{\mathrm{II}}^{(1)}\right]_{SC_0}, \tag{5.10}
$$

$$
\Delta\phi^{(2)} = \left[\vec{x}^{(2)}\cdot\nabla\phi_{\mathrm{II}}^{(0)} + \vec{x}^{(1)}\cdot\nabla\phi_{\mathrm{II}}^{(1)} + \frac{1}{2}\left(\vec{x}^{(1)}\cdot\nabla\right)^2\nabla\phi_{\mathrm{II}}^{(0)}\right]_{SC_0}, \tag{5.11}
$$

$$\Delta\phi_n^{(2)} = \left[\nabla\phi_{\mathrm{II}}^{(0)}\cdot\vec{n}^{(2)}\right]_{SC_0} + \left\{\left[\nabla\phi_{\mathrm{II}}^{(1)} + \left(\vec{x}^{(1)}\cdot\nabla\right)\nabla\phi_{\mathrm{II}}^{(0)}\right]\cdot\vec{n}^{(1)}\right\}_{SC_0}$$
$$+\left\{\left[\left(\vec{x}^{(2)}\cdot\nabla\right)\nabla\phi_{\mathrm{II}}^{(0)} + \left(\vec{x}^{(1)}\cdot\nabla\right)\nabla\phi_{\mathrm{II}}^{(1)} + \frac{1}{2}\left(\vec{x}^{(1)}\cdot\nabla\right)^2\nabla\phi_{\mathrm{II}}^{(0)}\right]\cdot\vec{n}^{(0)}\right\}_{SC_0}. \tag{5.12}$$

Here $\phi_{\mathrm{II}}^{(0)}$ is the zeroth-order velocity potential in the outer domain. Its corresponding part in the inner domain is $\phi_{\mathrm{I}}^{(0)}$. Physically, $\phi_{\mathrm{I}}^{(0)}$ and $\phi_{\mathrm{II}}^{(0)}$ can not be interpreted as exactly the same as the classical double-body basis flow $\phi^{(0)}$ defined in the inertial coordinate system. However, it is shown in Appendix A that, the solution of $\phi_{\mathrm{I}}^{(0)}$ and $\phi_{\mathrm{II}}^{(0)}$ to zeroth-order are the same as the inner and outer part of $\phi^{(0)}$ respectively. Therefore, we can use $\phi^{(0)}$ as the solutions of $\phi_{\mathrm{I}}^{(0)}$ and $\phi_{\mathrm{II}}^{(0)}$.

By putting Eq.(5.7) and Eq.(5.8) into Eq.(5.6), we get

$$-\sum_{j\in SF1} A_{ij}\left(\frac{\partial\phi_{\mathrm{I}}^{(k)}}{\partial n}\right)_j + \sum_{j\in SB} H_{ij}\left(\phi_{\mathrm{I}}^{(k)}\right)_j + \sum_{j\in SC} H_{ij}\left(\phi_{\mathrm{I}}^{(k)}\right)_j + \sum_{j\in SC} A_{ij}\left(\frac{\partial\phi_{\mathrm{II}}^{(k)}}{\partial n}\right)_j$$
$$= -\sum_{j\in SF1} H_{ij}\left(\phi_{\mathrm{I}}^{(k)}\right)_j + \sum_{j\in SB} A_{ij}\left(\frac{\partial\phi_{\mathrm{I}}^{(k)}}{\partial n}\right)_j - \sum_{j\in SC} H_{ij}\left(\Delta\phi^{(k)}\right)_j - \sum_{j\in SC} A_{ij}\left(\Delta\phi_n^{(k)}\right)_j, \quad i=1,\cdots,NE_1, k=1,2. \tag{5.13}$$

The double-node technique (e.g. Grilli & Svendsen, 1990) is used at the intersection lines of different surfaces where the normal vector is ill-defined. This brings modifications to the corresponding lines of equations in Eq.(5.5) and Eq.(5.13) and gives us the final algebraic equation system. A consequence of the described procedure is that the surface elements are time-independent.

It is noticed that the dimension of the matrix equation is increased because of the introduction of the control surface and the boundary elements on it. However, the number of the elements on the control surface is small compared with that on the free surface. Furthermore, because a simple smooth geometry is used as the control surface, one can distribute fewer elements than that on the body without losing any accuracy.

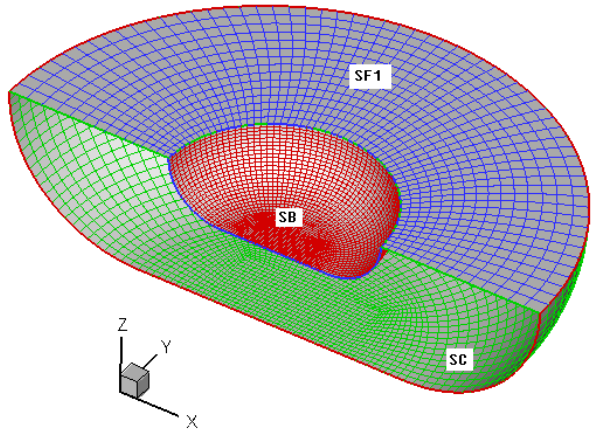

Fig.5.4. An example of the meshes on SB, SF1 and SC of the inner domain.

In principle, the control surface used in the method based on domain decomposition can be chosen arbitrarily. However simple and smooth geometries without sharp corner are always preferred. An example of the control surface is shown in Fig.5.4. Typical meshes on the free surfaces are shown in Fig.5.5.

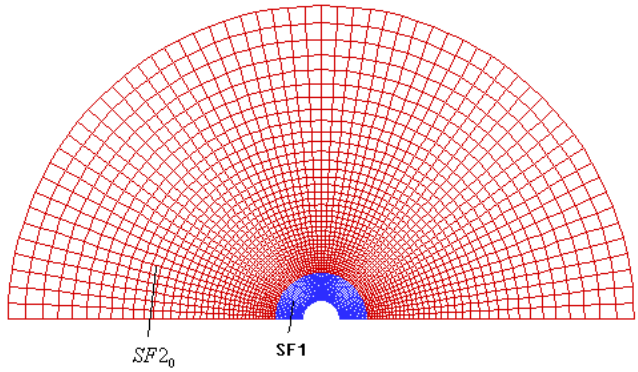

Fig.5.5. An example of meshes on the free surfaces SF1 and $SF2_0$.

It is noticed from Eq.(5.9) - Eq.(5.12) that we still have to calculate higher-order derivatives of $\phi^{(0)}$ on the control surface SC_0. However, when the basis flow $\phi^{(0)}$ is being solved, the domain decomposition solver is switched off and no source/dipole distribution is distributed on the control surface. Since the control surface is enclosed by the computational boundaries of the water domain, the velocity potential $\phi^{(0)}$ and its high-order derivatives there can be calculated very accurately by using the boundary integral equation (BIE) and the spatial derivatives of the BIE. The first-order and second-order derivatives of $\phi_{\mathrm{II}}^{(1)}$ on the control surface are much easier to calculate compared with that on the body, because we are free to construct relatively simpler geometry as the control surface. On the other hand, the solution at the control surface will always be regular even though it may be singular at the body surface. The integrals of the higher-order derivatives of steady velocity potential on the control surface are less important than that on the body surface. The values of these integrals decay depending on the distance between the control surface and the body surface. A qualitative estimation of the decay can be made by taking a hemisphere as an example and assuming the double-body flow as the basis flow. The double-body flow of a moving hemisphere can be obtained analytically (see also Section 4.6). The control surface is chosen as a hemisphere with radius R_1. See Fig. 5.6 for illustration. The integrals of the first-order, second-order and third-order derivatives of $\phi^{(0)}$ on the control surface decay with R_0/R_1, $\left(R_0/R_1\right)^2$ and $\left(R_0/R_1\right)^3$, respectively. Assume R_0/R_1 is small, then the results are what should be expected by the far-field expansions (see e.g. Newman, 1977) for a body in infinite fluid. In a case with general free-surface conditions, the decay of the velocity potential and its derivatives is slower than that of the double-body flow due to the wave effect.

The domain decomposition based method with body-fixed coordinate system described in this section does not need any derivatives on the right-hand side of the body boundary conditions, and thus the resulting BIEs are integrable for bodies without submerged sharp corners. In principle, this method

can be generalized to multi-body interaction problems. However, increased complexity obviously occurs by using the body-fixed coordinate system for multi-body problems. The practicality of the procedure for multi-body interactions will need a dedicated investigation and it is not the focus of this study.

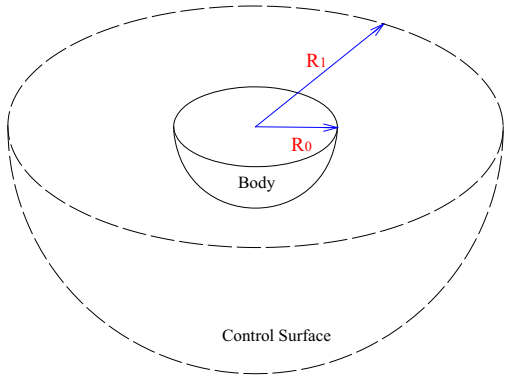

Fig. 5.6. Sketch of a hemispherical body and hemispherical type of control surface.

5.3 Generation of incident wave field in body-fixed coordinate system

The expressions for Stokes second-order wave can be found in many text books, for instance Dean & Dalrymple (1991). See also the introduction in Section 2.8 of Chapter 2. The description of the incident wave field in the body-fixed coordinate system is not straightforward. However, it is not necessary to separate the velocity potential and the wave elevation into the known incident part and the unknown scattered part, as it was done by for instance Büchmann (2000) and Wang & Wu (2007). In the new method based on domain decomposition, the incident wave is only specified in the outer domain which has a formulation in the inertial coordinate system. In the inner domain, the total velocity potential and the total wave elevation are solved through the free-surface conditions Eq.(2.88) and Eq.(2.89) in Section 2.6. Physically the free-surface conditions in the outer domain act as a wave generator. The generated incident wave enters the inner domain and is then influenced by the body. A damping zone will be used in the outer layer of the free surface in the outer domain. The damping zone applies only for the scattered part of the waves and its nonlinear interactions with the incident waves.

The boundary integral equations Eq.(5.5) and Eq.(5.13) are formulated by using the total velocity potentials in the outer and inner domain, respectively. When the incident wave is prescribed in the outer domain, the contributions of the incident part of the velocity potential $\phi_{\mathrm{II}}^{(k)}$ should be moved to the right-hand sides of Eq.(5.5) and Eq.(5.13) and treated explicitly.

5.4 The consistency between body-fixed coordinate system and inertial coordinate system

The coordinate systems are nothing but mathematical tools used to facilitate the analysis of a physical problem. That means the method using the body-fixed coordinate system should be able to give consistent results with the methods in inertial coordinate systems. In a weakly-nonlinear problem, the difference between the results of the body-fixed coordinate system and the inertial coordinate system are expected be of higher order. In order to demonstrate the consistency between body-fixed coordinate system and inertial coordinate system, we will firstly consider two simple cases with analytical solutions. Both of them are 2D cases. For the purpose of verifying the domain-decomposition based method presented in Section 5.2, more time-domain results on the first-order and second-order forces/moments on floating bodies in waves will be shown in Chapter 7 and Chapter 8.

Case 1: Forced oscillation of an infinitely long circular cylinder

The first case considered here is an infinitely long horizontal circular cylinder under forced sinusoidal surging motion. Infinite fluid domain is assumed. This case rules out the influence of the free surface. All the nonlinearities in the solution are due to the body boundary conditions. The definition of the problem is shown in Fig.5.7.

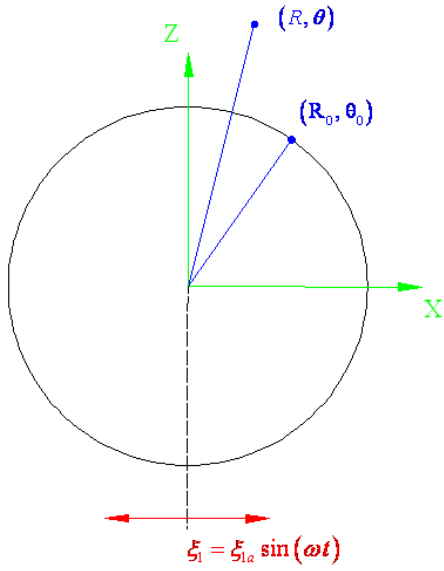

Fig.5.7. Definition of a circle under forced sinusoidal surge motion.

The first-order and second-order body boundary conditions (Eq.(B.4) and Eq.(B.5)) formulated in the inertial coordinate system is based on Taylor expanding the exact body boundary condition about the mean body position. Thus we have implicitly assumed that the amplitude of the sinusoidal surge

motion is small. However, the body boundary condition formulated in the body-fixed coordinate system is body exact and valid for large body motions.

The boundary value problems are solved analytically both in the inertial coordinate system and the body-fixed coordinate system. The details of the derivation are given in Appendix B. The strategy of solving the boundary integral equation analytically has been applied in the solution of a moving circle in infinite fluid with constant speed (see e.g. Faltinsen & Timokha (2009) and Shao (2009)). It has also been used by Shao & Faltinsen (2008) to study the surging and heaving of a semicircle with infinite-frequency free-surface condition (see also Section 6.5).

It is seen from Eq.(B.11) and Eq.(B.14) that the second-order approximation of the hydrodynamic pressure is the same as the exact solution. This indicates the consistency of the body-fixed coordinate system and the inertial coordinate system.

Case 2: Forced oscillation of a 2D rectangular tank

The second case considered is a 2D rectangular sloshing tank under forced sinusoidal surge motion. See Fig.5.8 for the definition. The problem is solved up to second order in both the inertial coordinate system and body-fixed coordinate system by assuming a steady-state solution, which means the transient effects are not considered. The response is assumed to be $O(\varepsilon)$ where the small parameter ε characterizes the order of magnitude of the forced surge amplitude relative to the breadth of the tank. The general formulation of the problem in inertial coordinate system can be found in Section 2.4, while the formulation in body-fixed reference frame was given in Section 2.6.

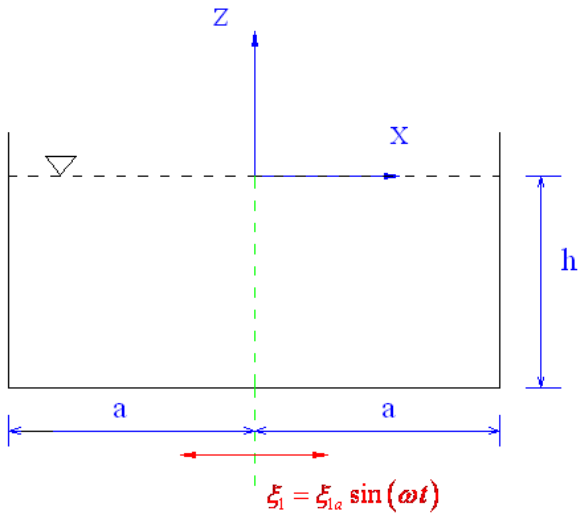

Fig.5.8. Definition of a 2D rectangular tank under sinusoidal surge motion.

In reality, the transient effects are very important in the sloshing tank. This is due to the fact the damping in a sloshing tank is very small. The potential damping which is associated with the radiated wave in an exterior problem is zero in a tank. The damping sources in a sloshing tank are discussed in Faltinsen & Timokha (2009). A distinct feature of the sloshing motion was modulated (or beating)

waves as a consequence of interaction between transient and forced oscillations of the free surface flow. A frequency analysis by Rognebakke & Faltinsen (1999) showed the presence of both the lowest natural frequency and the forced oscillation frequency. Therefore, a steady-state solution would not capture this behavior. Faltinsen (1978) presents a linear initial value solution for 2D sloshing in a harmonically oscillating rectangular tank. See also Faltinsen & Timokha (2009) and Shao (2009). A second-order initial value problem was solved by Rognebakke & Faltinsen (1999) using a formulation in the inertial coordinate system. However, in their derivation of the second-order solution, only the first mode in the first-order solution was considered in the forcing term of second-order free-surface condition. Later, the same problem was solved by Wu (2007) to second order in the time domain by using a formulation in the body-fixed coordinate system. The complete first-order solution was considered in the second-order forcing terms.

On the other hand, strong nonlinear effects matter in many cases, indicating that it is not valid to assume the response to be of $O(\varepsilon)$. This occurs in cases, for instance, at resonance frequency, with large forcing amplitude or relatively shallow liquid depth. Then one needs a proper nonlinear multimodal theory (e.g. Faltinsen & Timokha, 2009) which is out of the scope of this thesis.

The purpose of solving the steady-state sloshing problem by assuming the fluid response to be $O(\varepsilon)$ is just to show the consistency between the body-fixed coordinate system and the inertial coordinate system. The details of the derivations are given in Appendix C. The solutions obtained are semi-analytical based on modal expansions.

When the solution to the velocity potential is obtained, the Bernoulli's equation can be used to determine the hydrodynamic pressure. In the inertial coordinate system, the first-order and second-order hydrodynamic pressure are expressed by Eq. (C.43) and Eq.(C.44), respectively. The first-order and second-order hydrodynamic pressure in the body-fixed coordinate system are given in Eq.(C.61) and Eq.(C.62), respectively. One should note that the first-order solutions in the inertial coordinate system and the body-fixed coordinate system are the same. See Eq.(C.12) and Eq.(C.47). Therefore we will not show the comparison of the first-order results. According to the derivation in Appendix C, with a forced surge motion $\xi_1 = \xi_{1a}\sin(\omega t)$, the steady-state solution for the second-order pressure can be expressed in the following form

$$p^{(2)} = p_0^{(2)} + p_a^{(2)}\cos(2\omega t), \tag{5.14}$$

where $p_0^{(2)}$ is the second-order mean pressure. The second term on the right-hand side of Eq.(5.14) represents the sum-frequency pressure.

The comparison for the second-order mean pressure $p_0^{(2)}$ and $p_a^{(2)}$ associated with the sum-frequency pressure are made in Fig.5.9 - Fig.5.12. Fig.5.9 and Fig.5.10 show the distribution of $p_0^{(2)}$ and $p_a^{(2)}$ along the tank bottom, respectively. Fig.5.11 and Fig.5.12 show the distribution of $p_0^{(2)}$ and $p_a^{(2)}$ along the tank wall, respectively.

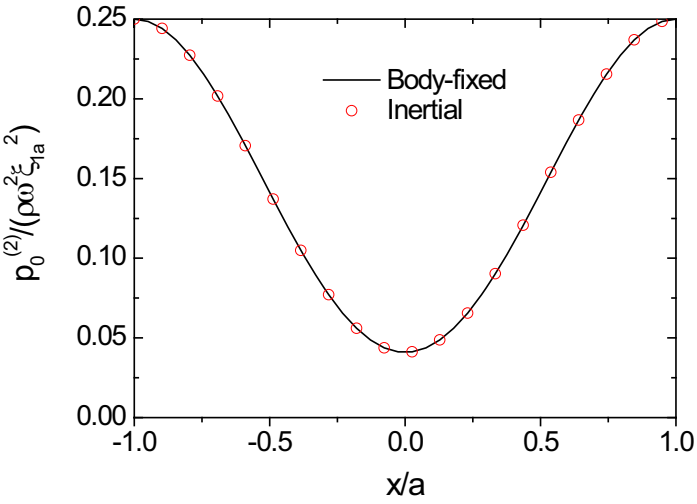

Fig 5.9. Distribution of $p_0^{(2)}$ along the bottom of the tank. The number of terms used in the modal expansion N=200. 'Body-fixed' and 'Inertial' correspond to results based on the formulations in the body-fixed reference frame and the inertial coordinate system, respectively. ξ_{1a} is the amplitude of the sinusoidal surge motion. ω is the frequency of forced oscillation.

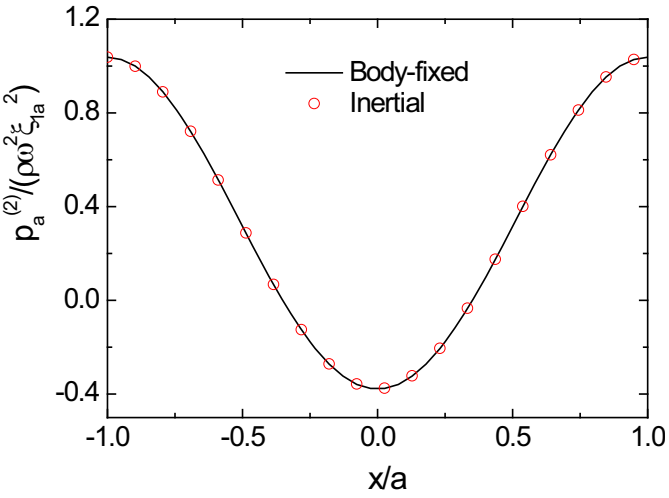

Fig 5.10. Distribution of $p_a^{(2)}$ along the bottom of the tank. The number of terms used in the modal expansion N=200. 'Body-fixed' and 'Inertial' correspond to results based on the formulations in the body-fixed reference frame and the inertial coordinate system, respectively. ξ_{1a} is the amplitude of the sinusoidal surge motion. ω is the frequency of forced oscillation.

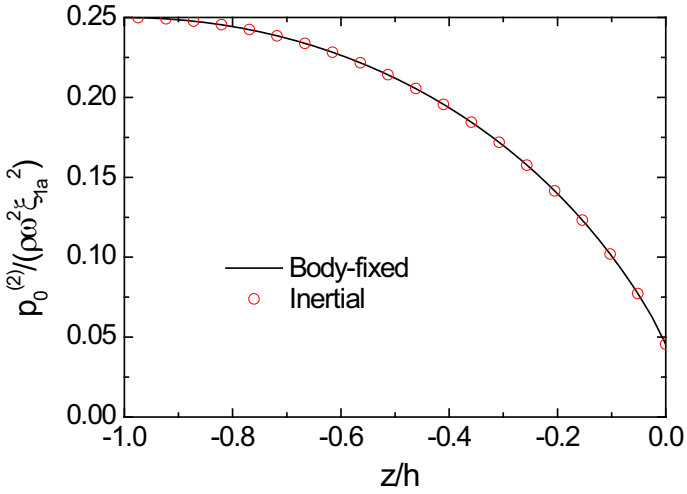

Fig 5.11. Distribution of $p_0^{(2)}$ along the tank wall. The number of terms used in the modal expansion N=200. 'Body-fixed' and 'Inertial' correspond to results based on the formulations in the body-fixed reference frame and the inertial coordinate system, respectively. ξ_{1a} is the amplitude of the sinusoidal surge motion. ω is the frequency of forced oscillation.

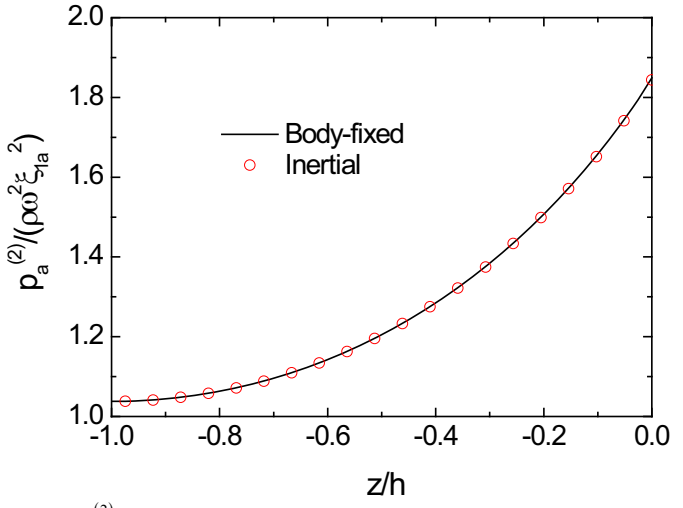

Fig 5.12. Distribution of $p_a^{(2)}$ along the tank wall. The number of terms used in the modal expansion N=200. 'Body-fixed' and 'Inertial' correspond to results based on the formulations in the body-fixed reference frame and the inertial coordinate system, respectively. ξ_{1a} is the amplitude of the sinusoidal surge motion. ω is the frequency of forced oscillation.

CHAPTER 6

Studies on Two-Dimensional Weakly-Nonlinear Problems

The accuracy of the numerical method is an important issue. With the purpose of verification, studies were carried out in some two-dimensional cases, including

- ✓ The steady-state third-order solution of a sloshing tank
- ✓ Free oscillations and forced oscillations in a rectangular tank
- ✓ Stokes-drift effect and numerical simulation of the Stokes second-order waves
- ✓ Secularity conditions and numerical simulation of the Stokes third-order waves
- ✓ Second-order diffraction of a horizontal cylinder
- ✓ Second-order radiation of a horizontal cylinder

The numerical results based on the 2D quadratic boundary element method (QBEM) are compared with some existing theoretical results and experimental results. Good agreements have been obtained. All the studies carried out in the time domain are based on the formulation in the inertial coordinate system (see Chapter 4). Parts of the results shown in this chapter have been presented in the 23rd International Workshop on Water Wave and Floating Bodies (IWWWFB). See Shao & Faltinsen (2008).

The study in this chapter is relevant for cases when the two-dimensional effects are dominant and the nonlinearity matters. One example is a long barge or flexible tube in the beam sea. When combined with a proper strip theory, the analysis in this chapter may also be extended to study the second-order wave loads on a slender ship.

6.1 The steady-state third-order solution of sloshing in a rectangular tank

One of the difficulties in solving a weakly-nonlinear hydrodynamic problem is associated with the higher-order derivatives in the boundary conditions. In this section, the sloshing in a two-dimensional rectangular tank is studied to third order by using a combined numerical and analytical approach,

which was proposed by Solaas (1995) and Solaas & Faltinsen (1997) for two-dimensional tanks with arbitrary tank shapes. In this method, the natural frequencies and corresponding natural modes are obtained by a boundary element formulation. The higher-order derivatives appear in the nonlinear free-surface conditions will be calculated by the curve-fitting technique described in Section 3.6. The steady-state third-order analytical results for the two-dimensional rectangular tank can be found in Faltinsen (1974b) and Solaas (1995). We will compare the numerical results with the analytical results in order to demonstrate the accuracy of our 2D QBEM solver and that the higher-order derivatives in the free-surface conditions can be obtained accurately by standard numerical methods.

The tank was assumed to be oscillating harmonically with small amplitudes $\xi_1 = \xi_{1a}\sin(\omega t)$ in the transverse/surge direction. See the definition in Fig.5.8. The general formulation of the third-order steady-state sloshing problem by Faltinsen (1974b), Solaas (1995) and Solaas & Faltinsen (1997) is used. A Moiseev (1958) type of ordering is followed for forced oscillations near resonance, which means the fluid response is of the same as or lower orders than the forcing. This formulation is essentially different with the ordering adopted in the weakly-nonlinear formulation presented in Chapter 2, where the responses are assumed to be as the same as or higher orders than the forcing. The reason why we have to use a different ordering for sloshing near the resonance, e.g. Moiseev type of ordering, is that the damping in the tank is very small and the response near resonance can be very large, which results in energy transfer from the lower-order modes to the higher-order modes. More discussion on the orderings of the resonant fluid response in the sloshing tanks can be found in for instance Faltinsen & Timokha (2009).

Only some important features of the Moiseev-type formulation will be summarized here. The interested readers are referred to Faltinsen (1974b), Solaas (1995) and Solaas & Faltinsen (1997) for further details. In this formulation, the frequency of the oscillation ω is near the lowest resonance frequency σ_1 of the sloshing tank

$$\omega^2 = \sigma_1^2 + \varepsilon^{2/3}\alpha\,, \tag{6.1}$$

with $\varepsilon = \xi_{1a}/2a$. a is half of the breadth of the tank (see Fig.5.8). The total velocity potential is written correctly to third order as

$$\Phi = \varepsilon^{1/3}\Phi_1 + \varepsilon^{2/3}\Phi_2 + \varepsilon^{1}\Phi_3 + \Phi_c \tag{6.2}$$

where, in accordance with the analytical solutions, the velocity potentials are assumed to have the form

$$\begin{aligned}
\Phi_1 &= \phi_1 N\cos(\omega t)\\
\Phi_2 &= \alpha_0 + \phi_2\frac{N^2}{2}\sin(2\omega t)\\
\Phi_3 &= \phi_3^{(3)}N^3\cos(3\omega t) + \phi_3^{(1)}N^3\cos(\omega t) + \phi_3^{(0)}\cos(\omega t)
\end{aligned} \tag{6.3}$$

and the velocity potential for the tank motion is

$$\Phi_c = 2a\omega x\cos(\omega t). \tag{6.4}$$

The constant *N* will be determined in the third-order problem.

A rectangular tank with breadth 2a=1.0m and water depth h=0.5m is considered. The frequency of the

forced oscillation is equal to the first natural frequency, i.e. $\omega = \sigma_1$. In Table 6.1, the first 10 of the analytically obtained eigenperiods are compared with the eigenperiods obtained from the numerical method with 40, 80, 160 quadratic elements on the free surface. The element length is taken to be constant over both the free surface and the tank surface. With 160 elements on the free surface, the total number of element is 480 and the length of the elements is 1/160 *m*. It is seen from Table 6.1 that the values of the natural frequencies are getting closer to the analytical results when the number of the elements increases. The most accurate result is obtained for *n*=1, i.e. the first natural period, while the difference between the numerical results and the analytical results increase with increasing *n*. This can be understood that higher modes correspond to shorter wave length and the number of the boundary elements distributed within each wave length is smaller in higher modes.

Table 6.1. Comparison between analytically and numerically obtained eigenperiods for a rectangular tank with breadth 2*a*=1.0m and water depth *h*=0.5m. Numerical results are given for the cases with 40, 80 and 160 quadratic elements on the free surface.

n	T_n analytical	T_n numerical N_{free}=40	T_n numerical N_{free}=80	T_n numerical N_{free}=160
1	1.182017	1.181971	1.182010	1.182016
2	0.801937	0.801815	0.801918	0.801933
3	0.653610	0.653381	0.653574	0.653601
4	0.566000	0.565644	0.565942	0.565985
5	0.506244	0.505744	0.506163	0.506224
6	0.462135	0.461479	0.462029	0.462108
7	0.427854	0.427027	0.427720	0.427820
8	0.400221	0.399212	0.400057	0.400180
9	0.377332	0.376130	0.377136	0.377282
10	0.357968	0.356565	0.357739	0.357911

The first-order, second-order and third-order solutions are also compared with the analytical results. Fig.6.1 and Fig.6.2 show the results for ϕ_1 and ϕ_2 in the first-order and second-order velocity potential, respectively. The results for $\phi_3^{(0)}$, $\phi_3^{(1)}$ and $\phi_3^{(3)}$ in the third-order solution are presented in Fig.6.3, Fig.6.4 and Fig.6.5, respectively. $\phi_3^{(0)}$ and $\phi_3^{(1)}$ are associated with the $\cos(\omega t)$ terms of the third-order results. $\phi_3^{(3)}$ is associated with the $\cos(3\omega t)$ terms. The numerical results in Fig.6.1 - Fig.6.5 are given for N_{free}=80 and 160. It is seen from Fig.6.1 that N_{free}=80 is sufficient for the first-order results. However, some small differences between the numerical results with N_{free}=80 and the analytical results are observed in the second-order and third-order results. The results were improved by using a finer mesh resolution with N_{free}=160.

The author of this thesis has also tried to study the same problem by using both the constant boundary element method (CBEM) and the linear boundary element method (LBEM). It turned out that the first-order results based on CBEM show small wiggles near the intersections between the free surface and the tank walls. The consequence was that large errors occur in the second-order and third-order results near the intersections, because the higher-order derivatives in the forcing terms in the second-order and third-order free surface conditions are calculated numerically based on the lower-order solutions. The reason for the wiggles near the intersections is probably that the CBEM

satisfies the boundary conditions at the mid-point of the element, therefore the continuity of the velocity potential at the intersection points are not guaranteed. The wiggles disappeared when the LBEM or the QBEM was used. In the LBEM and QBEM, the double-node technique has been used to enforce the continuity of the velocity potential at the intersection points between the free surface and the body surface. See Section 3.2 for the details of the double-node technique. The higher-order methods, e.g. QBEM, are preferred, because the convergences of higher-order methods are much faster than that of the lower-order ones.

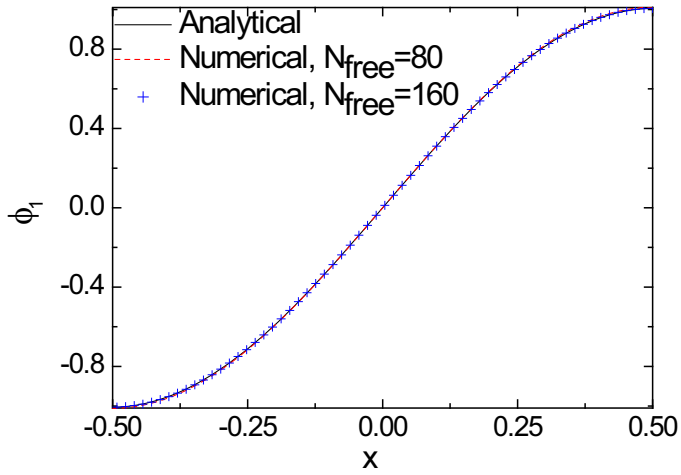

Fig.6.1. Comparison between the analytical and the numerical results for ϕ_1 in the first-order solution (see Eq.(6.3)) for a rectangular tank with breadth $2a$=1.0m and water depth h=0.5m. The oscillation frequency is $\omega = \sigma_1$. Numerical results are given for the cases with 80 and 160 quadratic elements on the free surface.

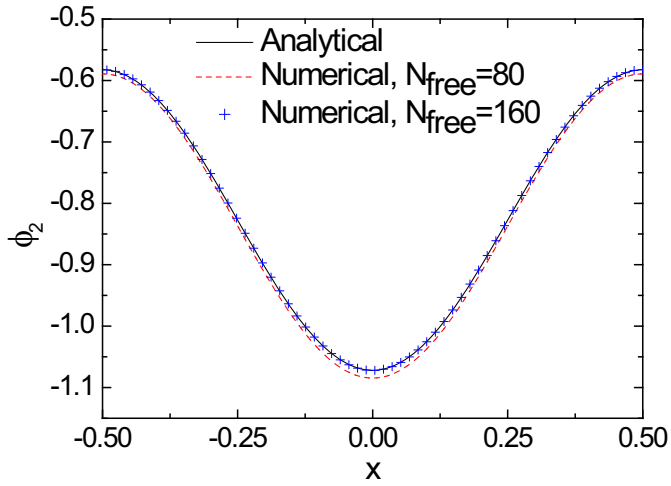

Fig.6.2. Comparison between the analytical and the numerical results for ϕ_2 in the second-order solution (see Eq.(6.3)) for a rectangular tank with breadth $2a$=1.0m and water depth h=0.5m. The oscillation frequency is $\omega = \sigma_1$. Numerical results are given for the cases with 80 and 160 quadratic elements on the free surface.

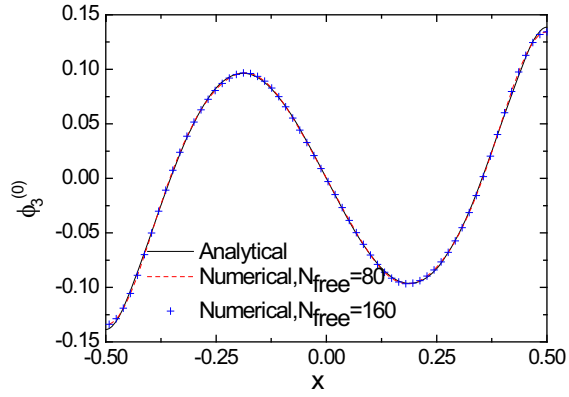

Fig.6.3. Comparison between the analytical and the numerical results for $\phi_3^{(0)}$ in the third-order solution (see Eq.(6.3)) for a rectangular tank with breadth 2*a*=1.0m and water depth *h*=0.5m. The oscillation frequency is $\omega = \sigma_1$. Numerical results are given for the cases with 80 and 160 quadratic elements on the free surface.

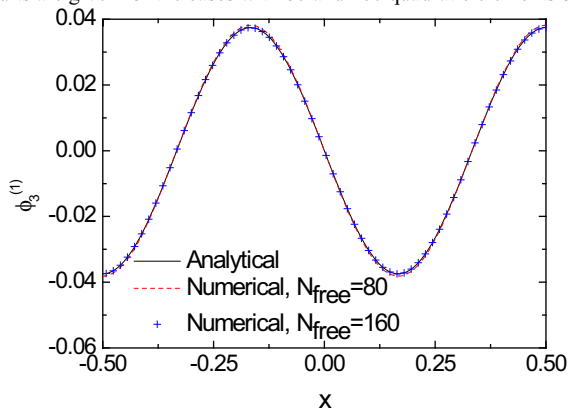

Fig.6.4. Comparison between the analytical and the numerical results for $\phi_3^{(1)}$ in the third-order solution (see Eq.(6.3)) for a rectangular tank with breadth 2a=1.0m and water depth h=0.5m. $\omega = \sigma_1$.

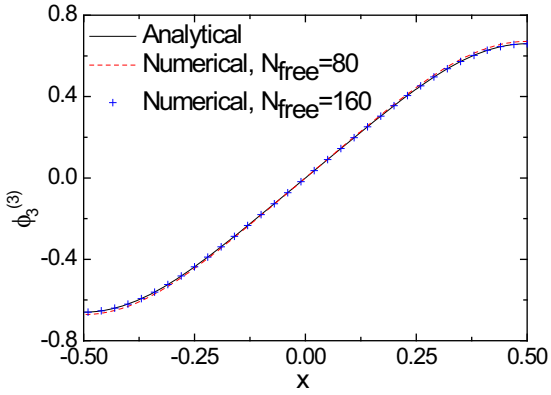

Fig.6.5. Comparison between the analytical and the numerical results for $\phi_3^{(3)}$ in the third-order solution (see Eq.(6.3)) for a rectangular tank with breadth 2*a*=1.0m and water depth *h*=0.5m. $\omega = \sigma_1$.

6.2 Free oscillations and forced oscillations in a rectangular tank

The problem the author wish to analyze in this section is the time-evolution of transient waves in a two-dimensional rectangular tank. Keeping in mind that the final goal of this study is to simulate the nonlinear wave-body interactions, the simple test cases studied here permit us to concentrate on the difficulties associated with the presence of free-surface piercing bodies. The free oscillation and forced oscillations studied by Cointe et al. (1988) are re-investigated in this section.

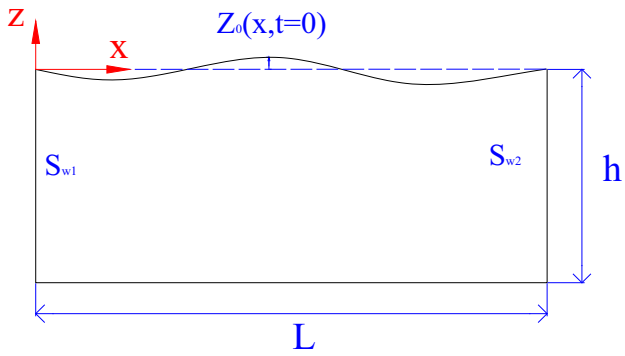

Fig.6.6. Sketch of the rectangular tank.

In the free oscillation problem, there is no energy supplied into the fluid domain. For simplicity, we assumed the velocity potential and its time derivative are zero at t=0. The motion of the liquid is, therefore, only due to its initial elevation. The analytical solution up to second order of this initial boundary value problem can be found in, for instance Cointe et al. (1988).

The free oscillation in the 2D rectangular tank is studied in time domain by using the time-domain QBEM presented in Chapter 3. In the numerical simulation, L=1.0m, h=0.2m and Z_0=0.02cos(πx) m are used, where L is the length of the tank. h is the water depth and Z_0 is the initial displacement of free surface. See the definitions in Fig.6.6.

The nonlinear free-surface conditions formulated in the inertial coordinate system, i.e. Eq.(2.48) and Eq.(2.49) are used. Note that Eq.(2.48) and Eq.(2.49) are expressed in three dimensions with a small forward speed effect included. Therefore, when applied to a two-dimensional case without forward speed, the y-dependent terms and the terms associated with the forward speed have to be dropped. For free oscillations, the first-order and second-order body boundary conditions are zero-Neumann conditions. The fourth-order Runge-Kutta method described in Section 3.3 is used for the time stepping of the free-surface conditions. The time increment $\Delta t = T/100$ is used in the numerical calculations. Here T is the first natural period of the tank.

Fig.6.7 and Fig.6.8 show the first-order and second-order components of the wave elevation at x=L/8, respectively. Very good agreement between the numerical results and analytical results has been obtained.

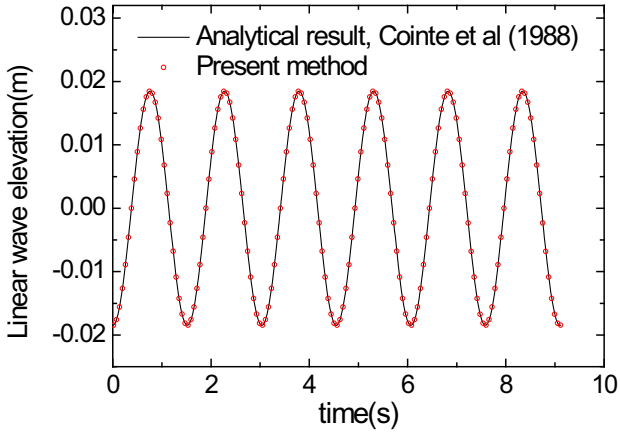

Fig.6.7. The first-order component of the wave elevation at x=L/8. L=1.0m, h=0.2m and Z_0=0.02cos(πx) m are used in the numerical simulations.

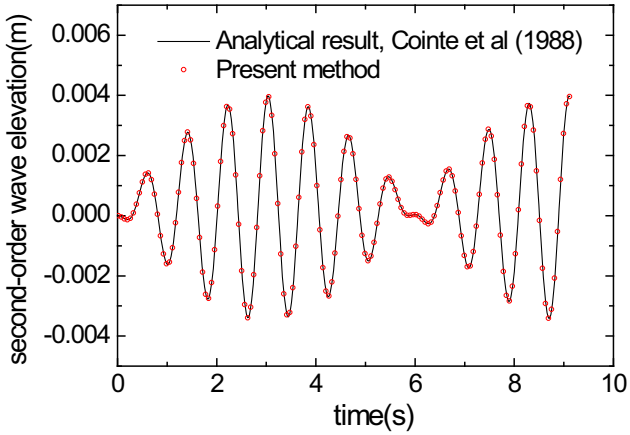

Fig.6.8. The second-order component of the wave elevation at x=L/8. L=1.0m, h=0.2m and Z_0=0.02cos(πx) m are used in the numerical simulations.

In the forced oscillation problem (wave maker problem), the fluid is assumed to be at equilibrium and that the energy is supplied for $t \geq 0$ through the motion of the left vertical wall, i.e. S_{W1} in Fig.6.6.

As a useful test to check the accuracy of the second-order numerical results, Cointe et al. (1988) suggest the following second order equation to control the mass conservation:

$$\int_0^L \eta^{(2)}(x,t)dx = l_1(t)\eta^{(1)}(0,t)\,. \tag{6.5}$$

Here L is the length of the tank. $\eta^{(1)}$(0, t) is the first-order wave elevation at S_{W1}. $\eta^{(2)}$(x,t) is the second-order component of the wave elevation. $l_1(t)$ is the displacement of S_{W1}. In this study we have used $l_1(t)$=$F(t)\cdot A_{w1}\sin(\omega t)$. $F(t)$ is a sinusoidal ramp function applied over the first two wave periods. A_{w1} is the amplitude of the displacement of S_{W1}.

Eq.(6.5) expresses that the volume of fluid scanned by the wave maker (S_{W1}) above the x-axis is distributed over the whole second-order free-surface elevation. The conservation of mass correctly to first order can be checked by

$$\int_0^L \eta^{(1)}(x,t)dx = l_1(t)h\,, \tag{6.6}$$

where h is the mean water depth.

The first-order and second-order free-surface conditions in the forced oscillations are the same as that of the free oscillations. The general formulation of the first-order and second-order body boundary conditions was given in Eq.(2.56) - Eq.(2.58). The body boundary conditions on S_{W2} and the tank bottom are homogeneous Neumann conditions. The first-order and second-order body boundary condition on S_{W1} are respectively

$$\frac{\partial \phi^{(1)}}{\partial x} = \frac{dl_1(t)}{dt}\,, \tag{6.7}$$

$$\frac{\partial \phi^{(2)}}{\partial x} = -l_1(t)\frac{\partial^2 \phi^{(1)}}{\partial x^2}\,. \tag{6.8}$$

The fourth-order Runge-Kutta method described in Section 3.3 is used for the time evolution of the free-surface flow. The time increment $\Delta t = T/100$ is used in the numerical calculations. $T = 2\pi/\omega$ is the period of the forced oscillation.

The relative errors of the first-order and second-order mass conservation at t≈2.15T are plotted in Fig.6.9, showing the convergence with the increasing number of elements on the free surface. The relative errors at first-order and second-order, i.e. $err^{(1)}$ and $err^{(2)}$ in Fig.6.9, are defined respectively as

$$err^{(1)} = \left| \frac{l_1(t)h - \int_0^L \eta^{(1)}(x,t)\,dx}{l_1(t)h} \right|, \tag{6.9}$$

$$err^{(2)} = \left| \frac{l_1(t)\eta^{(1)}(0,t) - \int_0^L \eta^{(2)}(x,t)\,dx}{l_1(t)\eta^{(1)}(0,t)} \right|. \tag{6.10}$$

It is seen that the first-order and second-order relative errors decrease as the number of unknowns on the free surface increase. The rate of the convergence of the first-order results is much faster than that of the second-order results. This is partly due to the fact that the second-order free-surface conditions require the higher-order derivatives of the first-order quantities, which are calculated numerically. On the other hand, the sum-frequency components, i.e. $\omega_i + \omega_j$ and $\omega + \omega_i$ components, of the second-order waves have much shorter wave lengths, which means that higher-resolution meshes are needed in order to achieve the results of the same accuracy as the first-order results. Here ω_i (i=1, 2, 3…) is the i-th natural frequency of the rectangular tank.

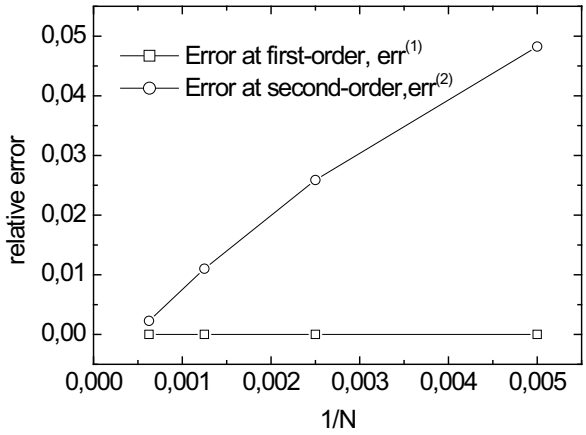

Fig.6.9. The first-order and second-order relative errors of the mass conservation versus the 1/N. N is the number of nodes on the free surface.

6.3 Stokes-drift effect and numerical simulation of the Stokes second-order waves

The numerical wave tank (NWT) has received a lot of interest and exhaustive review of the progress in the development of numerical wave tank can be found in, for instance, Kim et al. (1999) and Tanizawa (2000). Most of the numerical wave tanks are developed following a fully nonlinear formulation. There also exist some studies on the numerical wave tanks by using a finite-order Stokes theory, e.g. Büchmann (1995), Zhang & William (1996, 1999) and Stassen et al.(1998).

In this section, a two-dimensional numerical wave tank is implemented by using the time-domain QBEM presented in Chapter 3. The purpose is to reproduce the Stokes second-order waves. The formulation of the boundary conditions based on finite-order Stokes theory in the inertial coordinate system is used.

The first-order and second-order free surface conditions follow Eq.(2.48) and Eq.(2.49). In order to make use of Eq.(2.48) and Eq.(2.49), we have to ignore the terms associated with y-coordinates and the forward speed (and steady velocity potential). Furthermore, $\phi_{in}^{(m)}$ and $\eta_{in}^{(m)}$ (m=1, 2) are zero in this wave-maker problem.

In order to generate Stokes waves, the velocity profile from Stokes wave theory is introduced on the mean position of the S_{W1}. See Fig.6.6 for the definition of S_{W1}. There are other kinds of the wave makers, such as the piton-type and flap-type wave makers which are used in the physical tanks. The submerged sources have also been to generate waves, e.g. Brorsen & Larsen (1987). The explanation of the linear wave-maker theory for the piston-type and flap-type wave makers can be found in Dean

& Dalrymple (1991). The complete second-order wave-maker theory can be found in, for instance, Schäffer (1996). One problem associated with the piston or flap wave makers is the generation of the spurious free waves. A second-order signal has to be given to the wave maker to suppress the spurious free-wave generation. See for instance Madsen (1971) and Schäffer (1996). If the Stokes wave velocity profile is input to the control surface at S_{W1}, no second-order free waves will be generated. However, it does not mean that the way of generating Stokes waves by feeding velocity profile at the control surface (S_{W1}) is without problems. The second-order mass transport known as the Stokes drift leads to the increase of the mass in the numerical wave tank, and therefore increase the mean water level. This is not a problem if one is only interested in the first-order waves. However, the influence of this mass transport to the second-order component of the wave elevation is not ignorable since they are of the same order of magnitude. The second-order rate of the mass transport can according to, for instance Dean & Dalrymple (1991), be predicted as

$$D = \frac{\rho g A^2 k}{2\omega}. \tag{6.11}$$

where g is the gravity acceleration. k is the wave number. ω is the wave frequency. A is the linear wave amplitude.

In order to exam the effect of mass transport through S_{W1}, we have firstly switched off the numerical damping zone and the active wave absorber. That means the body boundary condition at the tank wall S_{W2} and the tank bottom are all zero-Neumann conditions. The following parameters have been used:

$$\lambda = 0.5\pi\ m;\quad A = 0.1m;\quad L = 15\lambda = 23.562\ m;\quad h = 5m, \tag{6.12}$$

where λ and A are the linear wave length and the linear wave amplitude, respectively. L and h are the tank length and water depth, respectively.

A sinusoidal ramp function over the first four wave periods is applied to the velocity profile feed on S_{W1}. The estimated time T_e for the wave front to arrive at S_{W2} can be estimated by the group velocity $c_g = d\omega / dk$, regardless of the effect of the ramp function. It gives T_e=30T. The simulation is stopped at t=20T, so that the waves generated by the wave maker have not arrived at S_{W2} and that the wave reflect from S_{W2} is sufficiently small. 20 quadratic elements per linear wave length are used in the QBEM solver and $\Delta t = T/100$ is adopted in the time marching of the free surface conditions. The numerical techniques associated with the two-dimensional time-domain QBEM have been discussed in Chapter 3 and will not be repeated here. The resolution of the meshes and the time increment was seen to be sufficient for a second-order problem by performing the spatial and temporal convergence study, which will not be shown here.

Fig.6.10 and Fig.6.11 show the first-order and second-order component of the wave profile at t=20T. The numerical results are compared with the analytical results by Stokes second-order wave theory. The first-order numerical results agree well with that of the given by Stokes theory, while large difference was found between the second-order numerical and theoretical results. A close look at the time history of the second-order wave elevation indicates that the mean water level (or mass) in the tank is approximately linearly increasing with time, and the total second-order results were destroyed due to this increasing of mass. The mean water level is defined as the integral of the wave elevation along the tank divided by the tank length, i.e.

$$\eta_0 = \frac{1}{L}\int_0^L \eta^{(2)} dx \,. \tag{6.13}$$

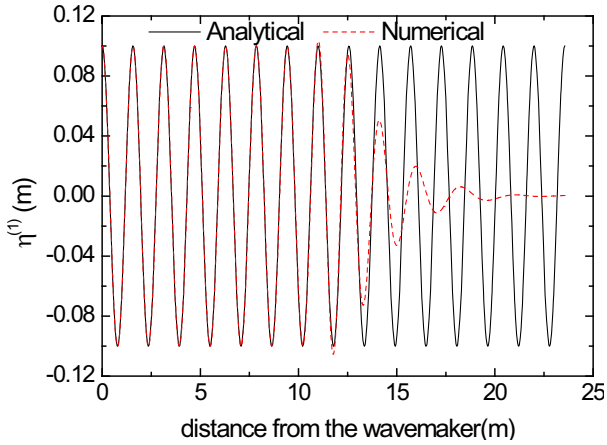

Fig.6.10. Comparison of the first-order component of the wave profile at t=20T. T is the linear wave period. The size of the tank and the wave parameters in Eq.(6.12) are used in the numerical simulation.

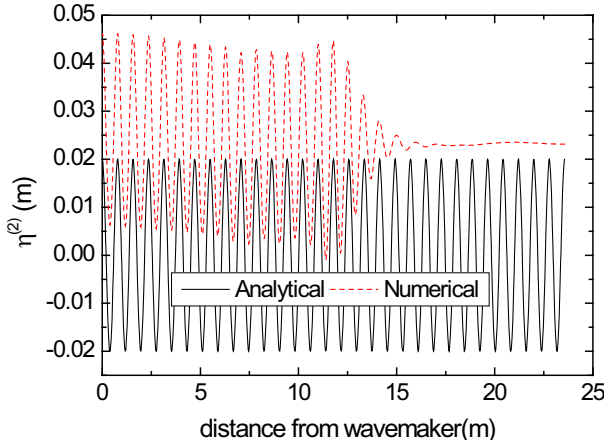

Fig.6.11. Comparison of the second-order component of the wave profile at t=20T. T is the linear wave period. The size of the tank and the wave parameters in Eq.(6.12) are used in the numerical simulation.

However, examination of the net flux showed that net flux through all the computational boundaries enclosing the computational water domain are negligible and the mass increasing observed in the second-order results is not due to the errors of the QBEM solver. See Fig.6.12 and Fig.13 for the time history of the first-order and the second-order net flux through the boundaries. The net flux through all the computational surfaces is defined as

$$Q^{(m)} = \oint_S \frac{\partial \phi^{(m)}}{\partial n} ds \,, \text{ m=1, 2.} \tag{6.14}$$

It is also believed that the mass increase observed in the second-order results is not due to the set down effect. According to Stokes second-order wave theory, the set down of the mean water level is zero for deepwater regular waves. The wave studied here can be considered as a deepwater case, since the ratio between the water depth and the wave length is $h/\lambda > 3.0$. See e.g. Faltinsen (1990).

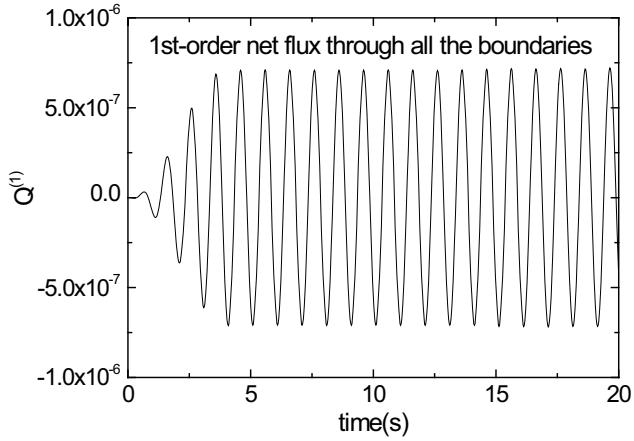

Fig.6.12. Time history of the first-order mass flux through the computational boundaries enclosing the computational water domain. The size of the tank and the wave parameters in Eq.(6.12) are used in the numerical simulations.

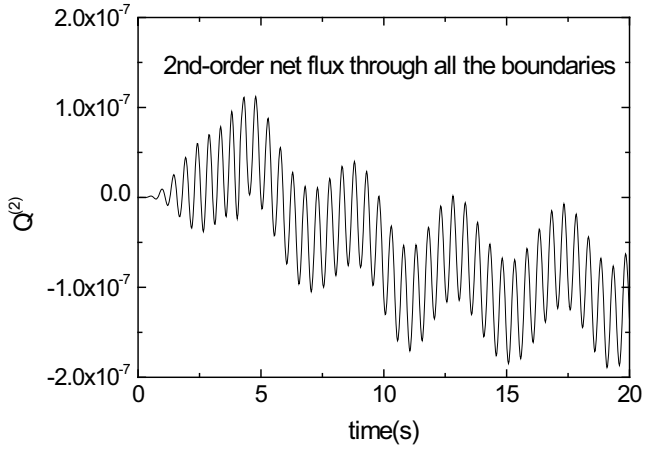

Fig.6.13. Time history of the second-order mass flux through the computational boundaries enclosing the computational water domain. The size of the tank and the wave parameters in Eq.(6.12) are used in the numerical simulations.

In Fig.6.14, the mass change observed in the second-order results is compared with the mass transport through S_{W1} due to Stokes drift (see Eq.(6.11)). The dash line representing the numerical results is parallel to the solid line showing the analytical prediction. The mass change shown in Fig.6.14 has been divided by $\rho g A^2 k / 2\omega$, therefore the solid line is a straight line through (0, 0) with slope equal to 1. It is seen from Fig.6.14 that, the mass change observed in the second-order simulation can be

explained by the Stokes drift in Eq.(6.11). Note that the offset of the two curves is due to the ramp function which is used to give a smooth start of the flow.

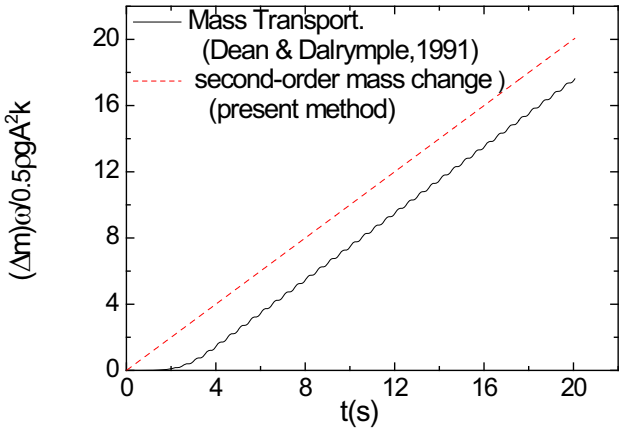

Fig.6.14. The mass change Δm due to the second-order mass transport through S_{W1}. The size of the tank and the wave parameters in Eq.(6.12) are used in the numerical simulations.

In order to simulate the Stokes second-order waves in a numerical wave tank by feeding the velocity profile at the control surface S_{W1}, we have to minimize the effect of the mass transport. The strategy adopted in this study is to use a damping zone mechanism that can take mass out of the system. A damping zone is applied at the end of the tank (near to S_{W2} in Fig.6.6). The damping zone mechanism is described in Section 3.4. From Eq.(3.18), we see that an important feature of this damping zone mechanism is that it can 'drain' water out of the tank. Numerical experiments showed that both the first-order and the second-order results are not sensitive to the damping coefficients as long as the coefficient γ (see Eq.(3.21)) is chosen between 10^{-6} and 10^{-5}. An active wave absorber is applied on S_{W2}, which is coupled with the damping zone. See details in Section 3.4 for the combined numerical damping zone and the active wave absorber.

After the activation of the damping zone and the wave absorber, the numerical results agree well with the analytical results given by the Stokes second-order wave theory. See the comparisons in Fig.6.15 - Fig.6.18. In order to reduce the computational cost, the tank size is chosen to be $L = 6\lambda$ and h=1m. The length of the damping zone is 2λ. The following parameters are used in the calculations

$$\lambda = 0.5\pi\ m;\quad A = 0.1m;\quad L = 6\lambda \approx 9.425\ m;\quad h = 1\ m. \tag{6.15}$$

The duration of the numerical simulation is 200T, with T the linear wave period. Fig.6.15 and Fig.6.16 show respectively the time histories of the first-order and the second-order wave elevations at a position $x = 3\lambda$, i.e. the mid of the tank. Only the results in the last 10 periods are shown. It is seen that even though the simulation was made over a very long period, there is no visible wave reflection from the numerical damping zone and the vertical surface S_{W2}. In Fig.6.17 and Fig.6.18, the linear and second-order wave profiles at the end of the simulation, i.e. t=200T, are shown. Comparisons are made with the analytical results. The good agreement between the numerical and analytical results indicates the capability of the time-domain QBEM solver presented in Chapter 3 in solving the second-order wave-body problems.

The experience obtained here also applies to the fully-nonlinear numerical wave tank which generates waves by feeding the Stokes wave velocity profile at control surface. One would expect second-order and higher-order mass transports through the control surface. The mass transport would not cause numerical problems associated with mass increase in the tank if a real wave maker, e.g. the piston or flap wave maker, is used. In that case, the returning current will occur due to the second-order mass transport.

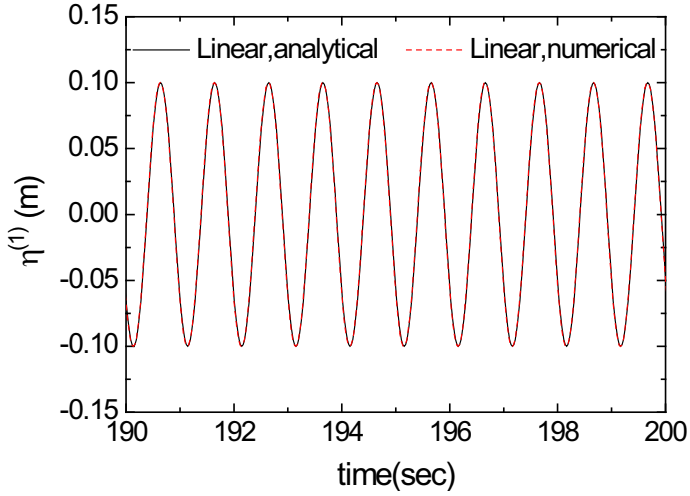

Fig.6.15. Time history of the first-order component of wave elevation of a point with a distance to the wave maker $x = 3\lambda$. Only the result for the last 10 linear wave period is shown. The size of the tank and the wave parameters in Eq.(6.15) are used in the numerical simulations.

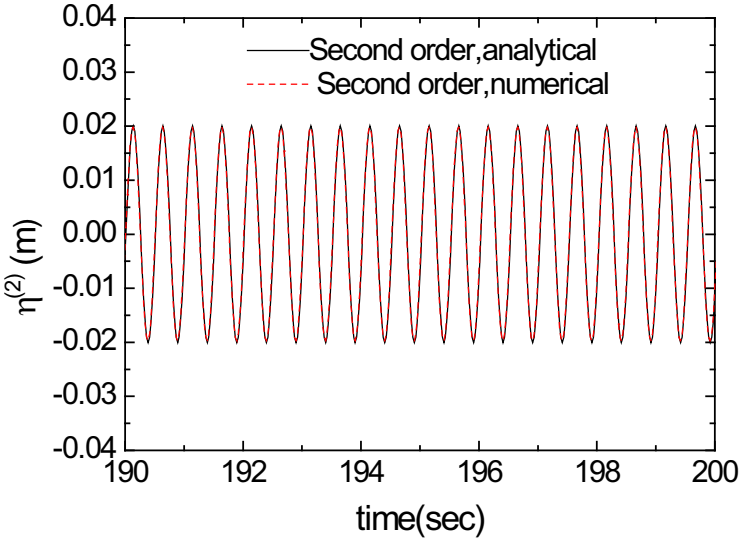

Fig.6.16. Time history of the second-order component of wave elevation of a point with a distance to the wave maker $x = 3\lambda$. Only the result for the last 10 linear wave period is shown. The size of the tank and the wave parameters in Eq.(6.15) are used in the numerical simulations.

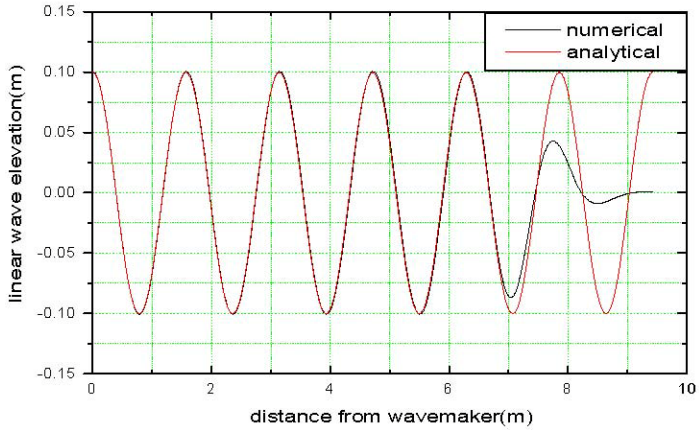

Fig.6.17. The linear component of the wave profile at t=200T. The size of the tank and the wave parameters in Eq.(6.15) are used in the numerical simulations.

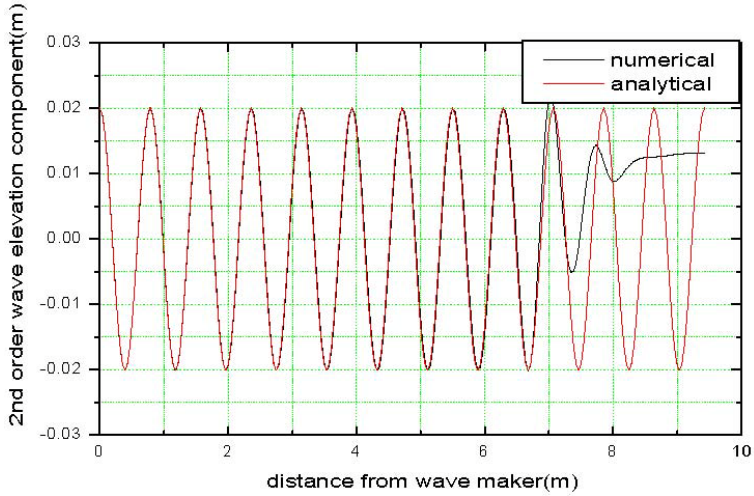

Fig.6.18. The second-order component of the wave profile at t=200T. The size of the tank and the wave parameters in Eq.(6.15) are used in the numerical simulations.

6.4 Secularity condition and numerical simulation of the Stokes third-order waves

It was shown in the previous section that the present time-domain HOBEM is able to reproduce the Stokes second-order waves with satisfactory accuracy. This makes it possible for us to pursue an even higher-order solution, i.e. the third-order solution. The third-order problem represents one of the most challenge problems in the weakly-nonlinear analysis. Another difficult problem in the

weakly-nonlinear analysis is the second-order problem with the presence of the forward speed or current effect, which we will look into in Chapter 8.

It is known (Whitham (1999), Section 13.13) that, in order to get physical result, one has to impose a secularity condition at third-order in the regular perturbation expansion of the velocity potential for a propagating wave. The secularity condition acts as a solvability condition. A correction must be done to the wave length or wave frequency to avoid unphysical results. Otherwise the wave amplitude would slowly vary with time t or with the horizontal distance x. In the two-dimensional numerical wave tank, if no secularity condition is enforced, the consequence would be that the third-order component of the wave amplitude increases steadily as the wave travels down the wave tank. Therefore the third-order wave amplitude may become of the same order of magnitude as the second-order or even the first-order wave amplitude. This violates the assumption of the Stokes expansion that the third-order component of wave elevation and velocity potential are of higher order than that of the second order and first order. A typical result of the third-order component of wave elevation without secularity condition is shown in Fig.6.19. It is seen that the third-order wave amplitude increases linearly with the horizontal coordinate x. This phenomenon was also observed in the third-order numerical wave tank by Stassen et al. (1998). Büchmann (1995) in his master thesis developed a third-order numerical wave tank in order to simulate weakly-nonlinear waves. However, nothing was reported whether he has used a solvability condition in the third-order solution.

By taking the deepwater third-order wave as an example, Stassen et al. (1998) explained the reason why the third-order wave amplitude is linearly increasing with the horizontal coordinate. We will explain the increasing of the third-order wave amplitude with the horizontal coordinate in Fig.6.19 by starting with a general case with finite water depth. The analytical solution of the third-order problems formulated in an unbounded domain for the case of the regular waves in finite depth is (see Section 2.8):

$$\eta^{(1)}(x,t) = A\cos(kx-\omega t) \quad , \tag{6.16}$$

$$\eta^{(2)}(x,t) = \frac{1}{4}\alpha(3\alpha^2-1)kA^2\cos 2(kx-\omega t), \tag{6.17}$$

$$\begin{aligned}&\eta^{(1)}(x,t)+\eta^{(2)}(x,t)+\eta^{(3)}(x,t)\\ &=\left(1-\frac{3}{8}(\alpha^4-3\alpha^2+3)A^2k'^2\right)A\cos\theta+\frac{1}{2}k'A^2\cos 2\theta+\frac{3}{64}\left[8\alpha^6+(\alpha^2-1)^2\right]A^3k'^2\cos 3\theta\end{aligned} \quad , \tag{6.18}$$

where

$$\alpha = \coth kh\,, \tag{6.19}$$

and

$$\theta = k'x-\omega t\,. \tag{6.20}$$

k' satisfies the nonlinear dispersion relationship

$$\omega^2 = gk'\tanh(k'h)\left\{1+k'^2A^2\left[\frac{9}{8}\left(\alpha^2-1\right)^2+\alpha^2\right]\right\}. \tag{6.21}$$

The wave number k in Eq.(6.16) and Eq.(6.17) satisfies

$$\omega^2 = gk\tanh(kh)\,. \tag{6.22}$$

Comparison between Eq.(6.21) and Eq.(6.22) suggests that

$$k' = k\left(1 - k^2 A^2 C\right) + O(\varepsilon^3), \tag{6.23}$$

with C as a constant. ε is the small parameter associated with the wave slope.

Plugging Eq.(6.23) into Eq.(6.21) and neglecting the terms higher than $O(\varepsilon^2)$, we can explicitly express C as

$$C = \frac{\frac{9}{8}\left(\alpha^2 - 1\right)^2 + \alpha^2}{1 + (\alpha - 1/\alpha)kh}, \tag{6.24}$$

where β is defined in Eq.(6.19).

In deepwater cases, we have $\alpha = 1$ and C=1. Therefore, Eq.(6.21) and Eq.(6.23) becomes respectively

$$\omega^2 = k' g\left(1 + k'^2 A^2\right), \tag{6.25}$$

and

$$k' = \left(1 - k^2 A^2\right)k + O(\varepsilon^3). \tag{6.26}$$

The expression of $\eta^{(3)}(x,t)$ can be obtained by subtracting Eq.(6.16) and Eq.(6.17) from Eq.(6.18). Note that we have not replaced k by k' in Eq.(6.16) and Eq.(6.17). Making use of Eq.(6.23) and Taylor expanding the resulting $\eta^{(3)}(x,t)$ around x=0, we obtain for the wave in finite water depth that

$$\begin{aligned}\eta^{(3)}(x,t) = A^3 k^2 \Big\{ & Ckx\sin(kx - \omega t) - \frac{3}{8}(\alpha^4 - 3\alpha^2 + 3)\cos(kx - \omega t) \\ & + \frac{3}{64}\left[8\alpha^6 + (\beta^2 - 1)^2\right]\cos 3(kx - \omega t)\Big\} + O\left(A\left(k^3 A^2 x\right)^2\right)\end{aligned} \tag{6.27}$$

where C is given by Eq.(6.24).

Although Eq.(6.27) is valid only for small values of x, it shows under this restriction that the third-order solution grows linearly with the horizontal coordinate x and the slope is Ck^3A^3.

Fig.6.19 shows the third-order component of wave profile at a time step when the steady-state solution has been obtained. The solid line represents the numerical wave profile. The dash line is the theoretical envelope of the third-order component of the wave amplitude, which can according to Eq.(6.27) be written as

$$\left|f(x)\right| = Ck^3 A^3 x, \qquad x \geq 0. \tag{6.28}$$

The following parameters are used in the calculations:

$$\lambda = 2\,m;\quad A = 0.04m;\quad L = 8\lambda = 16\,m;\quad h = 3\lambda = 6\,m. \tag{6.29}$$

The water depth was chosen as three times the wave length in order to simulate the deep-water wave cases. The two-dimensional version of the third-order free surface conditions Eq.(2.73) and Eq.(2.74) are used. The prescribed incident wave velocity potential $\phi_{in}^{(m)}$ and wave elevation $\eta_{in}^{(m)}$ are set to be zero. The wave profile shown in Fig.6.19 is for t=80T, where T is the linear wave period. Twenty quadratic elements are used per wave length. The increment of time step is $\Delta t = T/100$. A numerical damping zone was applied at the end of the tank and $x \in [12,16]$, i.e. twice the linear wave length. A sinusoidal ramp function was used in the first 8 wave periods. The other numerical details can be found in Chapter 3.

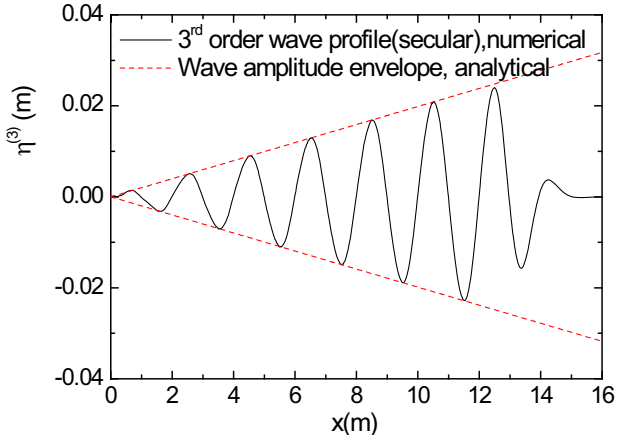

Fig.6.19. Numerical wave profile along the tank at t=80T and the envelope of the third-order wave amplitude. No secularity condition is applied. The size of the tank and the wave parameters in Eq.(6.29) are used in the numerical simulation.

As seen in Fig.6.19, the numerical results for the maximum third-order wave amplitude become the same order of magnitude of the first-order wave amplitude (A=0.04m). Further, it is much larger than the second-order wave amplitude, which can be seen by comparing the second-order wave amplitude in Fig.6.21 with the third-order wave amplitudes in Fig.6.19 without secularity condition. This violates the assumption behind the Stokes expansions. If the tank has an infinitely long length, it is expected from Fig.6.19 that the third-order wave amplitude is infinite near the end of the tank. Obviously, the numerical result in Fig.6.19 is not physical. Therefore, a solvability (secularity) condition is needed.

In the frequency-domain analysis of propagating waves, a wave amplitude-dependent nonlinear dispersion relationship is imposed as a solvability condition. Molin & Stassen (1998) suggested a technique by stretching the coordinate system. A mapping between the computational domain and the physical domain is considered. The third-order solution is thus modified while the first-order and second-order solutions are the same in both physical and computational domains. This technique was used in the third-order numerical wave tank in Stassen et al. (1998). The comparison with the experimental results made by Stassen et al. (1998) showed that the phase shift between the measurement and second-order model can be significantly reduced by adopting the third-order model.

The nonlinear dispersion relationship Eq.(6.21) indicates the modification of the wave length for a

given wave frequency. If we keep the wave length as unchanged, it means that the time scale has to be modified correspondingly. In this study, an approach based on two time scales is adopted. Therefore, the third-order free surface conditions (Eq.(2.73) and Eq.(2.74)) will be modified by replacing $\partial/\partial t$ by $\left(1+0.5Ck^2A^2\right)\partial/\partial t$. Taking a deep-water regular wave as an example, we show in Appendix D that this modification is able to cancel out the secular term contained in the third-order free-surface conditions. Note that we have implicitly assumed that only the steady-state solutions are of interest.

Fig.6.20 compared the time history of the third-order wave elevations at $x=3\lambda$ with and without secularity conditions. The result with secularity condition is based on the two-time scale model. It is seen that steady state has been obtained for both the results with and without secularity conditions. The third-order wave amplitude at $x=3\lambda$ without secularity condition is about 0.012m which is expected from Eq.(6.28). We have also compared the numerical second-order and third-order wave elevations with the analytical results of Stokes third-order wave theory. The comparison for the time history is shown in Fig.6.21. Good agreement has been achieved when the secularity condition is applied.

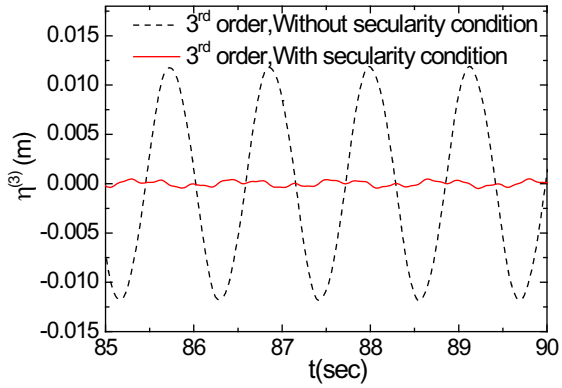

Fig.6.20 The time history of the third-order wave elevation at $x=3\lambda$ with and without secularity condition. The size of the tank and the wave parameters in Eq.(6.29) are used in the numerical simulation.

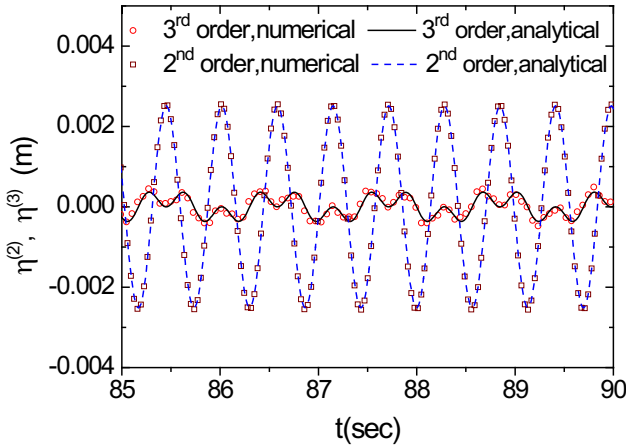

Fig.6.21. The time history of the second-order and the third-order wave elevation at $x=3\lambda$. The size of the tank and the wave parameters in Eq.(6.29) are used in the numerical simulation.

6.5 Second-order diffraction of a horizontal semi-submerged circular cylinder

The time-domain second-order method described in Chapter 3 was developed for a surface piecing body with arbitrary shapes. In order to verify and validate the numerical method, the second-order diffraction of a stationary horizontal cylinder is studied numerically in the time domain. This case has been studied by for instance Kyozuka (1980), Miao & Liu (1989) and Wu & Eatock Taylor (1989) in the frequency domain and Isaacson & Cheung (1991) in the time domain. Comparisons will be made between the present numerical results and some of the existing theoretical and experimental results.

The definition of the problem can be found in Fig.3.1. The second-order formulation in the inertial coordinate system is used (see Section 2.4 for details). The wave field is separated into the prescribed incident wave field and the unknown scattered wave field. The incident wave field is given as the Stokes second-order wave and only the scattered part of the wave field is solved. The cylinder is located at the center of the tank shown in Fig.3.1. Half of the cylinder is submerged. Two numerical damping zones are applied at the ends of the tank. The length of the damping zone is chosen as twice of the incident wave length. The mechanism of the damping zone is described in Section 3.4. A sinusoidal ramp function is applied in the first three wave periods to allow for a gentle start of the fluid motion. 20 quadratic elements are used per wave length. The time increment $\Delta t = T/100$ is used in all the simulations.

The amplitudes of the first-order horizontal and vertical forces are presented in Fig.6.22 and Fig.6.23, respectively. The present numerical results are compared with the theoretical and experimental results by Kyozuka (1980). The amplitudes of forces are obtained by the Fourier integral method presented in Section 3.7. The present method agrees well with Kyozuka's theoretical and experimental results.

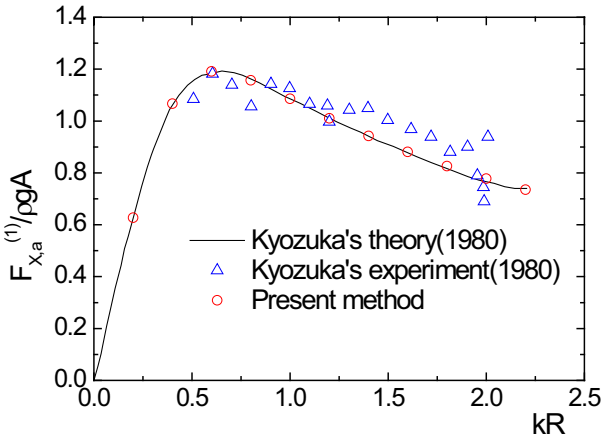

Fig.6.22. Comparisons of non-dimensional amplitude of the first-order horizontal wave force on a horizontal semi-submerged circular cylinder with Kyozuka's (1980) theoretical and experimental results. The cylinder is fixed in the incident wave. Deep water condition is assumed. k is the wave number. R is the radius of the cylinder. A is the linear wave amplitude of the incident wave.

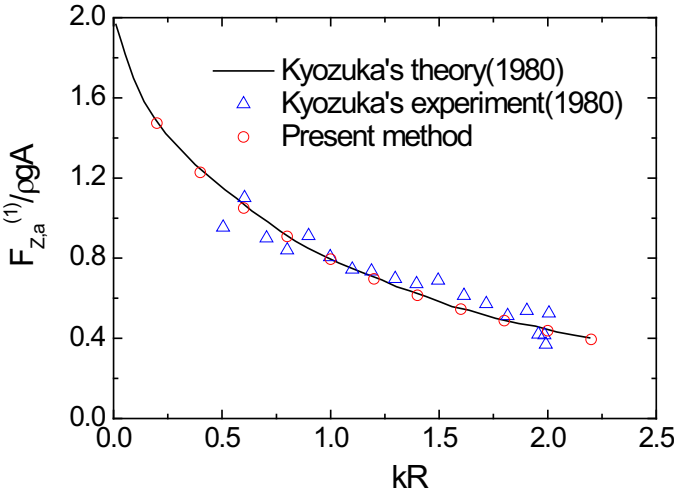

Fig.6.23. Comparisons of non-dimensional amplitude of the first-order vertical wave force on a horizontal semi-submerged circular cylinder with Kyozuka's (1980) theoretical and experimental results. The cylinder is fixed in the incident wave. Deep water condition is assumed. k is the wave number. R is the radius of the cylinder. A is the linear wave amplitude of the incident wave.

The second-order mean forces in the horizontal and vertical directions are presented in Fig.6.24. Comparison is made with the numerical results of Isaacson & Cheung (1991). Good agreement has been obtained. In the range of the wave numbers considered in this study, it was seen that the horizontal mean drift force is always positive, while the vertical mean drift force is always negative. It can be shown by using the momentum conservation and energy conservation that the horizontal wave-drift force according to second-order potential flow theory with no current or constant forward speed is always acting in the wave propagating direction, provided that the body is not an active wave power device. See for instance Faltinsen (1990). The horizontal mean drift force is a special case of the low-frequency force in irregular waves, which is relevant to the analysis of the mooring systems. A stationary surface-piercing body with finite draft in waves experiences a frequency-dependent mean vertical 'suction' force. This may not be true in other cases. For a freely-floating surface-piercing body, the mean vertical force can be either positive or negative depending on the wave frequency and the natural frequency of the body motions. See the relevant results in Fig.8.29 for the mean wave forces on a floating truncated vertical circular cylinder. It is also understood that the submarines are generally sucked up to the free surface.

The near-field method for the force calculation is adopted in this study. Near-field method means direct integration of the pressure on the instantaneous body position. An alternative is to use the far-field approach based on momentum and energy conservation. In Fig.6.25, the horizontal mean drift force calculated by the near-field approach is compared with that of the far-field method. Maruo's (1960) formula is used in the far-field method

$$F_{X0}^{(2)} = 0.5\rho g A_R^2 . \tag{6.30}$$

Here A_R is the wave amplitude of the reflected wave at far upstream of the body. Good agreement between the near-field and far-field approach was obtained. Eq.(6.30) shows that the wave-drift forces

are connected with the body's ability to cause waves. For long wavelengths relative to the cross-sectional dimensions the body will not disturb the incident wave field. This means the reflected wave amplitude A_R and the wave drift force become negligible. When the wavelengths are very short, the incident waves are totally reflected from a surface-piercing body with vertical hull surface in the wave zone. This means that A_R is equal to the linear amplitude of the incident wave and $F_{X0}^{(2)}/\rho g A^2$ =0.5. See also the discussions in e.g. Faltinsen (1990), Chapter 5. For intermediate wavelengths, parts of the wave are transmitted to the downstream and the other parts reflected to the upstream. Therefore, A_R is smaller than the linear incident wave amplitude and $F_{X0}^{(2)}/\rho g A^2$ <0.5. This has been confirmed in the numerical results in Fig.6.25.

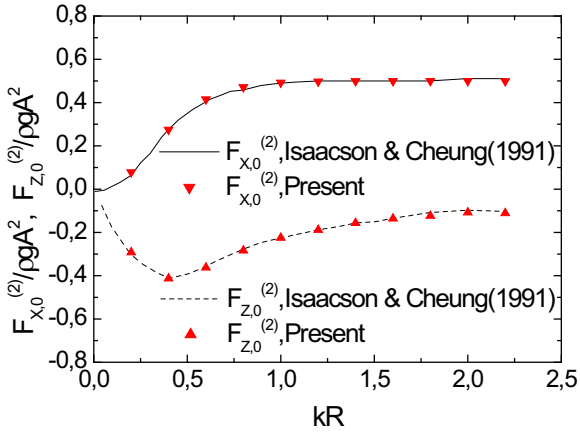

Fig.6.24. Comparisons of the non-dimensional amplitude of the mean wave forces on a horizontal semi-submerged circular cylinder with Isaacson & Cheung's (1991) results. Both the horizontal and vertical mean wave forces are presented. The cylinder is fixed in the incident wave. Deep water condition is assumed. k is the wave number. R is the radius of the cylinder. A is the linear wave amplitude of the incident wave.

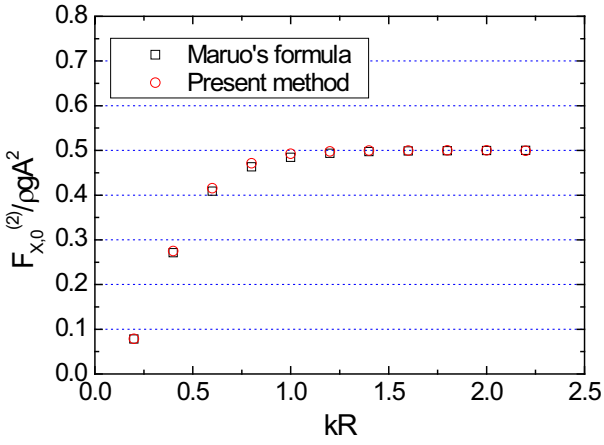

Fig.6.25. Comparison of the calculated horizontal mean drift force for a horizontal semi-submerged circular cylinder with that predicted by Maruo's formula (1960). The cylinder is fixed in the incident wave. Deep water condition is assumed. k is the wave number. R is the radius of the cylinder. A is the linear wave amplitude of the incident wave.

The comparisons of the second-order oscillatory force components have been made with the frequency-domain numerical results of Wu & Eatock Taylor (1989) and those obtained by the numerical and experimental study of Kyozuka (1980). See Fig.6.26 and Fig.6.27 for the horizontal and vertical sum-frequency forces, respectively. The present results agree well with that of Wu & Eatock Taylor (1989), while Kyozuka's (1980) numerical results show relatively large difference. Kyozuka's experimental results exhibit some scatter but have the same trend as the present results and the numerical results of Kyozuka (1980) and Wu & Eatock Taylor (1989). It is shown from both the experimental results and different numerical results that, the amplitudes of the horizontal and vertical sum-frequency forces in the high-frequency region increase monotonically with the increasing non-dimensional wave numbers. This can be explained by the asymptotic behavior of the sum-frequency forces on a two-dimensional stationary body in the incident waves. McIver (1994) obtained the high-frequency approximations of the horizontal and vertical forces on a two-dimensional body, which are accurate to O(*ka*). Here *k* is the incident wave number. *a* is the characteristic cross-sectional dimension of the body. According to McIver's (1994) high-frequency approximations, the amplitude of the sum-frequency vertical force is proportional to *ka*, while the amplitude of the sum-frequency horizontal force contains a component that increases linearly with the increasing *ka*.

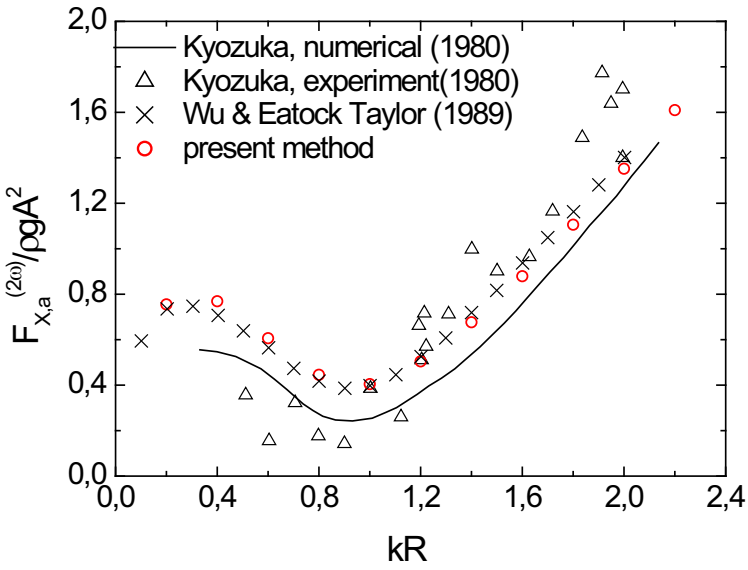

Fig.6.26. Comparisons of non-dimensional amplitude of the second-order horizontal wave force on a horizontal semi-submerged circular cylinder with the numerical results of Wu & Eatock Taylor's (1989) and Kyozuka's (1980) numerical and experimental results. The cylinder is fixed in the incident wave. Deep water condition is assumed. *k* is the wave number. *R* is the radius of the cylinder. *A* is the linear wave amplitude of the incident wave.

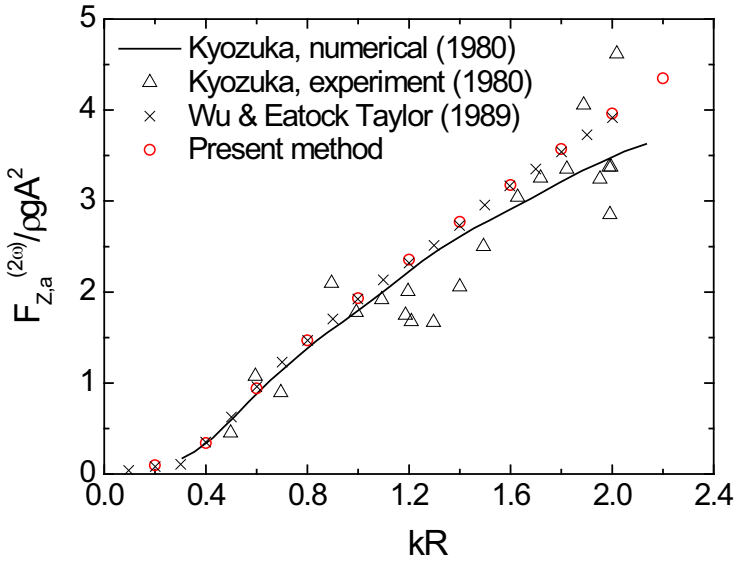

Fig.6.27. Comparisons of non-dimensional amplitude of the second-order vertical wave force on a horizontal semi-submerged circular cylinder with the numerical results of Wu & Eatock Taylor's (1989) and Kyozuka's (1980) numerical and experimental results. The cylinder is fixed in the incident wave. Deep water condition is assumed. k is the wave number. R is the radius of the cylinder. A is the linear wave amplitude of the incident wave.

In order to further validate the second-order sum-frequency results, we have used an alternative approach to calculate the second-order oscillatory forces due to the scattered velocity potential $\phi_s^{(2)}$. This approach is based on the Green's 2nd identity, which does not need the solution of second-order velocity potential. Instead, one introduces an artificial problem boundary value problem. In the frequency-domain analysis, an auxiliary radiation problem can be used to avoid the direct solution of second-order velocity potential. See for instance Faltinsen (1976). In the present time-domain study, an artificial velocity potential ψ_i is introduced which satisfies the Laplace equation in the fluid domain, $\psi_i = 0$ on the mean free surface, $\partial\psi_i/\partial n = n_i$ on the mean body surface, $\partial\psi_i/\partial n = 0$ on the sea bottom and $\psi_i \to 0$ on a control surface at infinity. The details of the formulation of the artificial velocity potential are given in Appendix E. This approach has been used by for instance by Wu and Eatock Taylor (2003) in the fully nonlinear time-domain wave-body analysis. With the solution of ψ_i and the second-order boundary conditions, one can obtain the second-order forces due to the second-order scattered velocity potential $\phi_s^{(2)}$ without solving a second-order problem as

$$F_{i,scatter}^{(2)} = -\rho\left[\int_{SB_0} \psi_i \frac{\partial}{\partial n}\left(\frac{\partial \phi_s^{(2)}}{\partial t}\right) dS - \int_{SF_0} \frac{\partial \phi_s^{(2)}}{\partial t}\frac{\partial \psi_i}{\partial n} dS\right] \tag{6.31}$$

The derivations of Eq.(6.31) can be found in Appendix E.

In general, the solution for ψ_i can be solved numerically by for instance a BEM solver. However, for the special case we are studying, i.e. a semi-circle, it is possible to find an analytical solution for ψ_i. The analytical solution enables us to explain the logarithmic singularity of, for instance $\partial\psi_1/\partial z$, at the intersection between the body surface and free surface. It also explains that $\partial\psi_1/\partial z$ is

integrable, even though it may be singular at the intersection points.

The first step to solve ψ_i analytically is to take an image of the semicircle about z=0 and therefore the influence of the free surface is taken into account by the image of the body. See the illustration in Fig.6.28. ψ_i=0 (i=1 or 3) on the mean free surface means the flow is antisymmetric about z=0 for both the artificial surge and heave problems. Then a boundary integral equation can be set up with unknowns on only the body surface. The strategy of solving the boundary integral equation analytically is similar to that given in Appendix B when solving an oscillating circle in infinite fluid domain and will not be elaborated here. Only the final results will be given. The expression for $\partial\psi_i / \partial z$ on the free surface is found to be

$$\frac{\partial \psi_i}{\partial z} = \begin{cases} -\frac{2}{\pi}\left[\frac{1}{\tau} + \frac{1}{2}\ln\left|\frac{\tau-1}{\tau+1}\right|(1+\frac{1}{\tau^2})\right]; & i=1 \\ -\frac{1}{\tau^2}; & i=3 \end{cases} . \tag{6.32}$$

Here $\tau = x/R$. R is the radius of the cylinder. x is the horizontal coordinate of a point. See Fig.6.28 for the definitions.

The solution for ψ_1 is logarithmically singular at the intersection point of the body surface and z=0 plane. The consequence of the high-frequency free surface condition $\psi_1 = 0$ is that the horizontal velocities of the fluid particle on the free surface are zero and they can only move vertically. However, the body boundary condition for ψ_1 says that all the points on the body surface have to move horizontally. This causes an inconsistency at the intersection points of the body surface and the free surface. One should note that the ψ_1 problem exists only in a mathematical sense. In reality, spray will occur at the intersections of the body surface and the water surface as a consequence, with subsequent dissipation of kinetic and potential energy.

Fig.6.29 shows the comparison of the second-order oscillatory forces due to second-order scattered velocity potential $\phi_s^{(2)}$ by direct pressure integration and the indirect method based on Green's 2nd identity. Both the amplitude of the horizontal and vertical sum-frequency forces are presented. The agreement is very good.

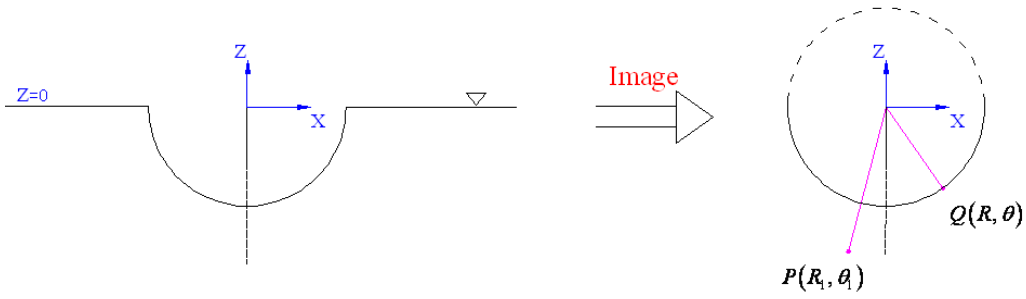

(a) (b)

Fig.6.28. Definition of the coordinates for the problem of ψ_i. (a) Definition of the original problem. (b) Problem after taking image of the semicircle about z=0.

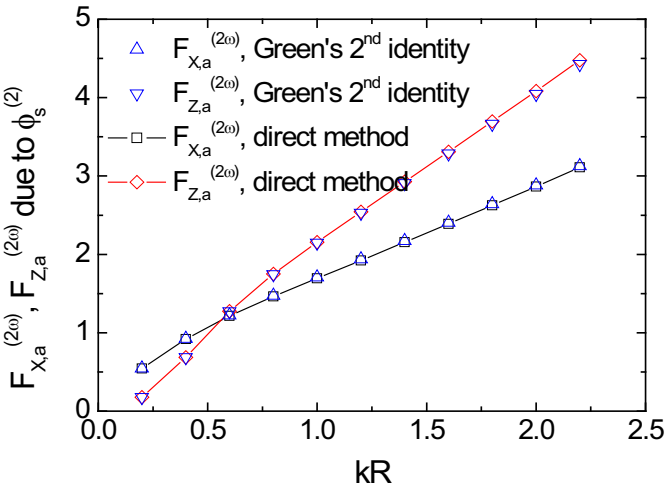

Fig.6.29. The non-dimensional amplitude of the second-order oscillatory forces due to the scattered velocity potential $\phi_s^{(2)}$ for a stationary horizontal semi-submerged circular cylinder in waves. Comparisons are made between the results of the direct method and that of the indirect method based on Green's 2nd identity. k is the wave number. R is the radius of the cylinder

6.6 Second-order radiation of a horizontal semi-submerged circular cylinder

The forced surging and heaving of the horizontal semi-submerged circular cylinder are studied up to second order. Infinite water depth is assumed. No incident wave effect is included.

The forced surge and heave motions are defined respectively as

$$\xi_1^{(1)} = Rm(t)\cdot\xi_{1a}\sin(\omega t), \xi_1^{(2)} = 0, \tag{6.33}$$

and

$$\xi_3^{(1)} = Rm(t)\cdot\xi_{3a}\sin(\omega t), \xi_3^{(2)} = 0. \tag{6.34}$$

Here Rm(t) is a ramp function used to allows for the gentle start of the flow. ω is the circular frequency of the oscillation. ξ_{1a} and ξ_{3a} are the amplitudes of the surge and heaving motion respectively.

Fig.6.30 shows the magnitude of the vertical mean force on a semi-submerged circular cylinder in surge motion compared with the theoretical and experimental results by Kyozuka (1982). Good agreement has been obtained between the present results and the numerical results of Kyozuka (1982). On the other hand, Kyozuka's (1982) experimental results are found to exhibit some scatter. Actually, Kyozuka (1982) has four groups of experimental results with different ratios between the amplitude of

the forced surging motion and the radius of the cylinder, i.e. ξ_{1a} /R=0.1, 0.2, 0.3 and 0.4. Only the results for ξ_{1a}/R=0.1 and 0.2 are used in the comparisons in Fig.6.30. The experimental data of Kyozuka (1982) for ξ_{1a} /R=0.3 and 0.4 was only given for very limited non-dimensional wave numbers, and therefore was not included in the comparisons. The reason for the scatter of the experimental results is unknown.

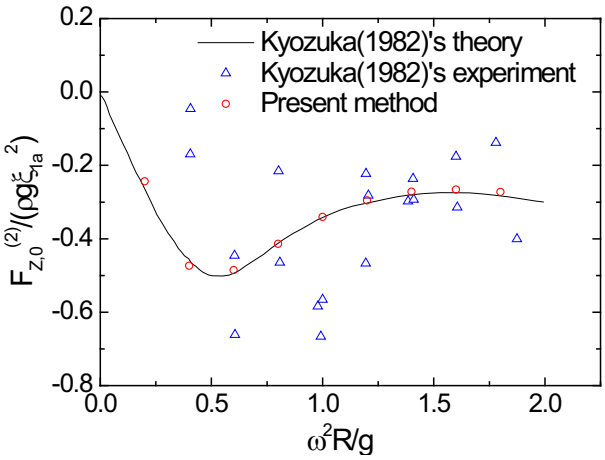

Fig.6.30. The non-dimensional vertical mean force on a horizontal semi-submerged cylinder under forced sinusoidal surging motion. No incident wave is present. R is the radius of the horizontal circular cylinder.

The magnitude of the vertical mean force on the horizontal cylinder in forced heaving motion is shown in Fig.6.31. The present numerical result is compared with the theoretical results by Potash (1971) with good agreement. The horizontal drift forces are zero in theory for the horizontal cylinder under forced surging and heaving, and will not be shown here.

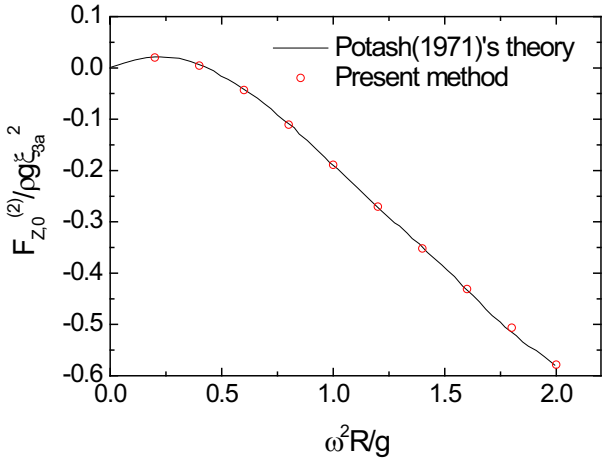

Fig.6.31. The non-dimensional vertical mean force on a horizontal semi-submerged cylinder under forced sinusoidal heaving motion. No incident wave is present. R is the radius of the horizontal circular cylinder.

Fig.6.32 shows the magnitude of the second-order oscillatory force in the z-direction on a forced surging cylinder. It is seen that the second-order oscillatory force in the z-direction appears to increase steadily at high frequencies and Kyozuka's (1982) theoretical solution tends to give higher predictions than the present results. Kyozuka's (1982) experimental results show the same order of magnitude of the second-order oscillatory force in z-direction but with some scatter. Only the experimental results for ξ_{1a} /R=0.1 and 0.2 are used in the comparisons in Fig.6.32.

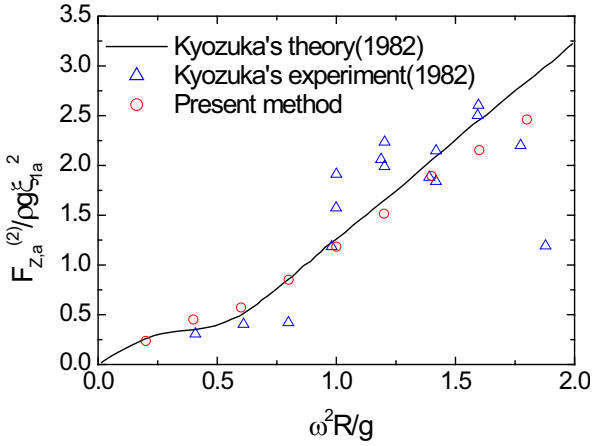

Fig.6.32. The non-dimensional amplitude of sum-frequency force in z-direction on a horizontal semi-submerged cylinder under forced sinusoidal surging motion. No incident wave is present. R is the radius of the horizontal circular cylinder.

The magnitude of the vertical sum-frequency force on the horizontal cylinder under forced heaving cylinder is presented in Fig.6.33. The present results agree well with theoretical and experimental results of Yamashita (1977). Yamashita's (1977) theoretical results at higher frequencies tend to be lower than the present results and Yamashita's (1977) experimental results.

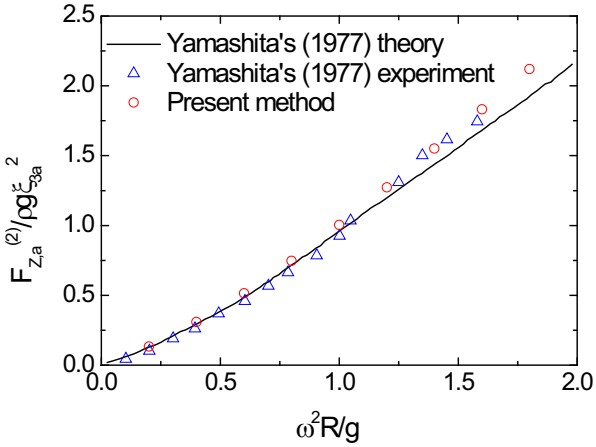

Fig.6.33. The non-dimensional amplitude of sum-frequency force in the z-direction on a horizontal semi-submerged circular cylinder under forced sinusoidal heaving motion. No incident wave is present. *R* is the radius of the cylinder.

The indirect method based on Green's 2nd identity is also used here to verify the second-order oscillatory force in z-direction due to the second-order velocity potential. The details of the indirect method have been presented in Section 6.5. Fig.6.34 shows the comparison of the results by the direct method and the indirect method based on Green's 2nd identity. Excellent agreement has been obtained.

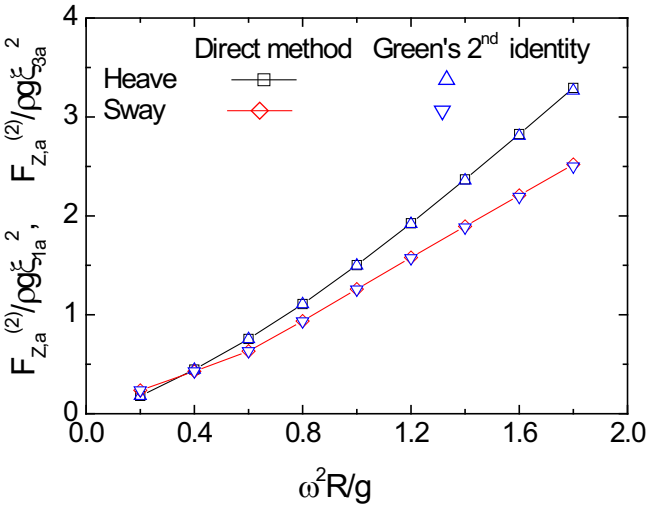

Fig.6.34. The non-dimensional amplitude of the sum-frequency force in the z-direction of a horizontal semi-submerged circular cylinder under forced sinusoidal surging and heaving motions. No incident wave is present. Comparisons are made between the results of the direct method and that of the indirect method based on Green's 2nd identity. k is the wave number. R is the radius of the cylinder.

CHAPTER 7

Three-Dimensional Weakly-Nonlinear Problems with Zero Forward Speed

This chapter is considered as the first step to verify the 3D time-domain HOBEMs in the inertial coordinate system (see Chapter 4) and the new method using body-fixed coordinate system in the near field (see Chapter 5). We will hereafter call the method using the formulation in the inertial coordinate system the 'traditional method', and the domain decomposition based method using body-fixed reference frame near the body the 'new method'. When the body with sharp corners has unsteady motions, the traditional method using the Taylor expansions for both the free-surface conditions and the body boundary conditions is only applicable for a linear wave-body problem without forward speed. However, the new method proposed in Chapter 5 is valid for any order nonlinear wave-body problem with the presence of forward speed effects, no matter the body is with or without sharp corners. The nonlinear diffraction and radiation problems are studied and verified. The forward speed effect which is not considered in this chapter will be discussed in Chapter 8.

7.1 Second-order and third-order wave diffraction on a fixed body

7.1.1 Second-order diffraction in monochromatic waves

This section studies the second-order diffraction of a fixed body in monochromatic waves. A bottom-mounted vertical circular cylinder, a hemisphere and a truncated vertical circular cylinder are studied by using the domain decomposition based method presented in Chapter 5. As described in Section 5.3, the incident wave is prescribed and only the scattered wave is solved in the outer domain. In the inner domain, the total velocity potential and wave elevation are solved. Comparisons of the present numerical results with some existing analytical/semi-analytical and numerical results will be made.

For the fixed bodies, since the body-fixed coordinate system oxyz is the same as the inertial coordinate system OXYZ, it is expected that the traditional method using the inertial coordinate system works as well as the new method based on domain decomposition. In fact, the numerical

results show that the new method gives the same steady-state results as the traditional method using inertial coordinate system. Only small difference was observed in the initial stage of the time history of the results, e.g. forces. This is believed to be caused by the fact that we have in the traditional method separated the incident waves from the total wave field in the whole fluid domain, whereas the new method solves the whole velocity potential in the inner domain and the incident wave field is only prescribed in the outer domain.

Due to the symmetry of the body surface and the incident wave, only unknowns on half of the fluid domain are needed in the computations. The sensitivity on the position of the control surface is also studied for the nonlinear diffraction of a bottom-mounted vertical circular cylinder.

Bottom-mounted vertical circular cylinder

The second-order diffraction in monochromatic waves without forward speed is studied for a bottom-mounted vertical circular cylinder. In this section, only the numerical results obtained by the new method based on domain decomposition are presented and compared with the existing analytical or semi-analytical results. The present numerical results are compared with the linear analytical result of MacCamy & Fuchs (1954) and the second-order semi-analytical results of Eatock Taylor & Hung (1987). The bottom-mounted vertical circular cylinder considered in this section has a draft h=R with R as the radius of the cylinder. An example of the meshes on the body surface (SB), mean free surface (SF1) and the cylindrical control surface (SC) of the inner domain is shown in Fig.7.1. Fig7.2 shows an example of the bird-view of the grids on the inner and outer free surfaces.

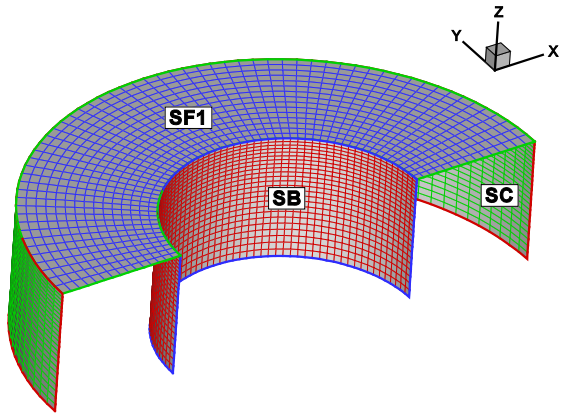

Fig.7.1. An example of the meshes on the body surface (SB), mean free surface (SF1) and the cylindrical control surface (SC) of the inner domain.

The amplitudes of the linear wave run-up around a cylinder with kR=1.0 is presented in Fig.7.3 together with the analytical results based on MacCamy & Fuchs's (1954) theory. The amplitudes of the run-up were obtained by Fourier analysis of the time history of the wave elevations. The comparison of the amplitude of the linear in-line force is also presented in Fig.7.4. Approximately, 8 cubic elements per linear wave length were used in order to get the linear results presented in Fig.7.3 and Fig.7.4. The time increment $\Delta t = T/100$ is adopted in the time-domain simulations. T is the linear wave period of the incident wave. The radius of the cylindrical control surface R_C=2.0R is used

in the numerical calculations. It is seen from Fig.7.3 and Fig.7.4 that the present linear numerical results agree very well with the analytical results of MacCamy & Fuchs (1954).

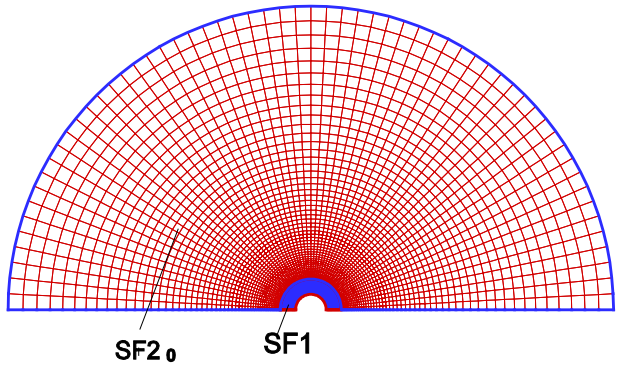

Fig.7.2. A bird-view of the meshes on the free surfaces SF1 and $SF2_0$.

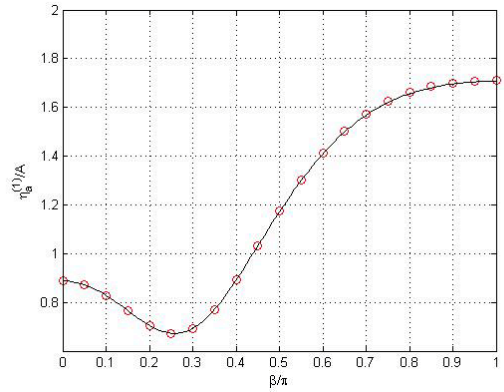

Fig.7.3. Comparison of the non-dimensional amplitudes of first-order run-up around the bottom-mounted circular cylinder. The solid line is based on the analytical result by MacCamy & Fuchs (1954). The circles are the present numerical results. A is the incident wave amplitude. kR=1.0, h=R.

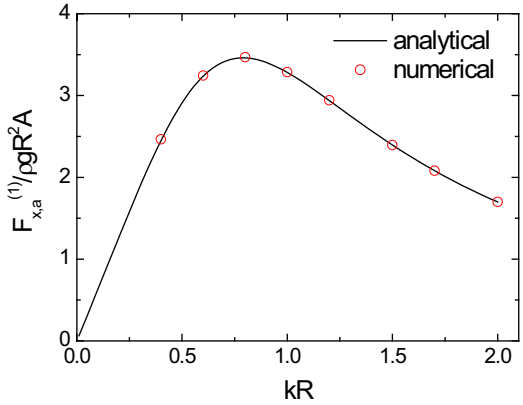

Fig.7.4. Comparison of the non-dimensional amplitude of first-order in-line diffraction force with the analytical results based on MacCamy & Fuchs's (1954) theory. A is the incident wave amplitude. h=R.

Eatock Taylor & Hung (1987) have developed a semi-analytical solution for the second-order diffraction of a bottom-mounted vertical circular cylinder. The comparison of the present second-order results and that of Eatock Taylor & Hung (1987) are presented in Fig.7.5 - Fig.7.7. 30 cubic elements per linear wave length are used and a time increment $\Delta t = T/200$ is adopted in the time-domain simulations. The radius of the cylindrical control surface R_C=2.0R is used in the numerical calculations. Fig.7.5 shows the non-dimensional horizontal mean-drift forces with different wave numbers. The comparisons of the amplitude of the second-order oscillatory force $F_{x,a}^{(2\omega)}$ and the corresponding phase angle ψ are given in Fig.7.6 and Fig.7.7, respectively. Good agreement has been obtained in the studied wave number region.

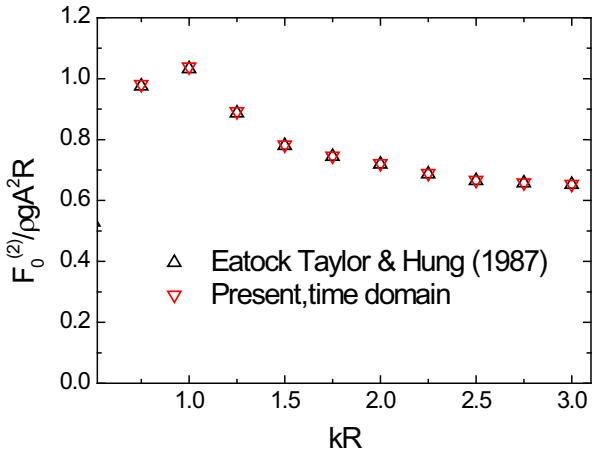

Fig.7.5. Comparison of the non-dimensional mean-drift force on a bottom-mounted circular cylinder. *A* is the incident wave amplitude. *h*=*R*.

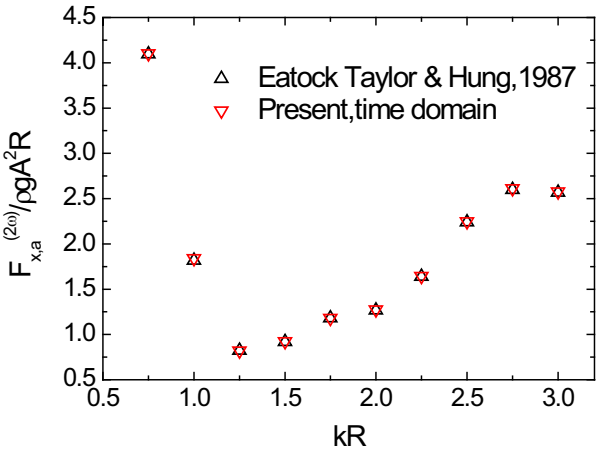

Fig.7.6. Comparison of the non-dimensional amplitude of the horizontal sum-frequency force on a bottom-mounted circular cylinder. A is the incident wave amplitude. *h*=*R*.

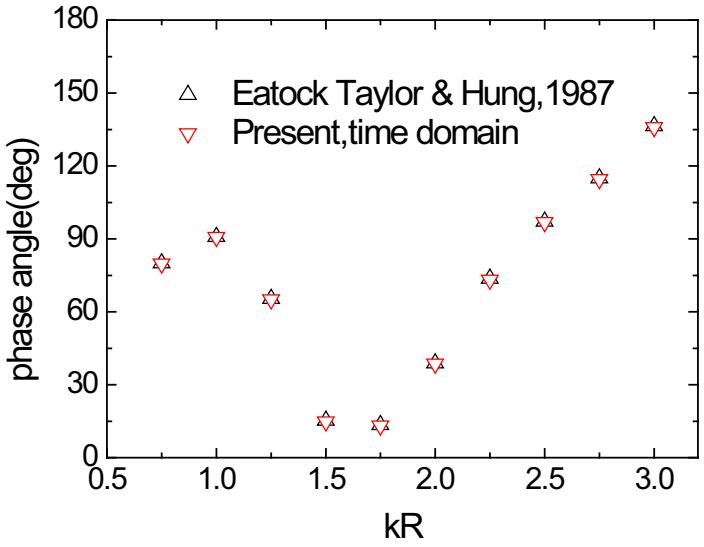

Fig.7.7. Comparison of the phase of the sum-frequency force in x-direction on a bottom-mounted circular cylinder. A is the incident wave amplitude. h=R.

The phase angle is defined relative to the incident wave at the origin of the OXYZ coordinate system, i.e. the oscillatory part of the second-order force is expressed as $F_{x,a}^{(2\omega)}\cos\left(2\omega t+\psi\right)$. The expressions for the first-order and second-order velocity potential of the incident waves are obtained by replacing (X_e,Y_e,Z_e) with (X,Y,Z) and setting β=0 in Eq.(2.134) and Eq.(2.135), respectively.

In order to investigate the influence of the size of the inner domain on the numerical results, the author has studied the second-order diffraction of a bottom-mounted vertical circular cylinder with kR=1.0 and h=R by varying the radius of the inner domain (R_C) from 1.25R to 2.0R. R is the radius of the bottom-mounted cylinder. An artificial bottom-mounted cylinder is used as the control surface. Fig.7.8 and Fig.7.9 show respectively the time histories of the linear and second-order horizontal forces with different radius of the control surface. 35 cubic elements per linear wave length are used near the water line. The meshes away from the water line are stretched in a smooth way. In the case of R_C=1.25R, the body surface and the control surface are very close to each other. Only 2 cubic elements are distributed on the part of the free surface between SB and SC along the radial direction and no numerical problem was encountered.

It is seen from Fig.7.8 and Fig.7.9 that only small differences occur in the time histories of the linear and second-order forces at very initial stage with different 'radius' of the inner domain. This is thought to be caused by the different treatment of the free-surface conditions in the inner domain and the outer domain. The velocity potential and wave elevation are decomposed into the prescribed incident part and the unknown scattered part in the outer domain, whereas in the inner domain the total velocity potential and wave elevations are solved. The steady-state first-order and second-order numerical results did not show any clear dependence on the choice of the 'radius' of the inner domain.

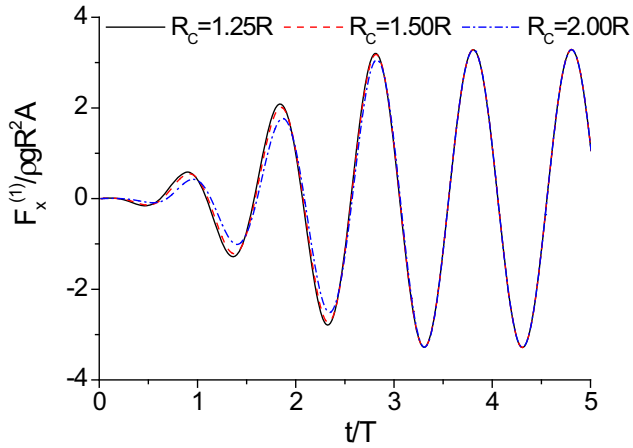

Fig.7.8. The time histories of the linear horizontal force of a bottom-mounted vertical circular cylinder in regular wave. T is the linear wave period. A is the incident wave amplitude. R_C is the radius of the cylindrical control surface SC in Fig.7.1. kR=1.0, h=R.

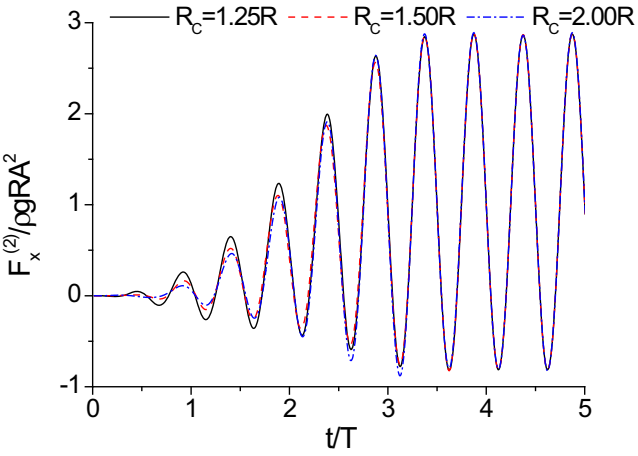

Fig.7.9. The time histories of the total second-order horizontal force of a bottom-mounted vertical circular cylinder in regular wave. T is the linear wave period. A is the incident wave amplitude. R_C is the radius of the cylindrical control surface SC in Fig.7.1. kR=1.0, h=R.

Hemisphere

A hemisphere in regular waves is also studied by the domain decomposition based method in Chapter 5. The water depth is chosen to be h=3R, with R being the radius of the hemisphere. The cylindrical control surface like the one shown in Fig.7.1 is used as the control surface. The radius of the control surface is taken as R_C=1.5R. Approximately 30 cubic elements are used on both the free surface and the body surface near the water line. The same diffraction problem was studied by Kim & Yue (1989) and Choi et al. (2001). Kim & Yue (1989) solved the problem in the frequency domain by using a ring source distribution. Choi et al. (2001) obtained the frequency-domain results based on a 3D quadratic HOBEM.

The steady-state linear excitation forces of the hemisphere agree favorably with the frequency-domain analytical results by Kudou (1977) and will not be shown here. The results for the amplitude of the sum-frequency forces in X-direction and Z-direction are shown in Fig.7.10 and Fig.7.11, respectively. The forces are divided into different parts according to Kim & Yue (1989). In Fig.7.10 and Fig.7.11, $F_a^{(2)}$ indicates the amplitude of the total second-order sum-frequency force, while F_q and F_p are the sum-frequency forces caused by the quadratic terms of first order quantities and the second-order velocity potential, respectively.

The comparison shows that the present results are very close to the results by Kim & Yue (1989) for all the components and the total forces. The results by Choi et al. (2001) show some differences especially for the forces component due to the second-order potential. As mentioned by Choi et al. (2001), this might be caused by the oscillations of the auxiliary surge potential used near the body surface in their numerical study.

It is seen from Fig.7.10 that the quadratic force part F_q and the second-order velocity part F_p have strong cancellation effect on the total horizontal sum-frequency force with the non-dimensional wave frequency regime studied. Ignoring F_p part and approximating the total horizontal sum-frequency force by the F_q part give overestimated results.

For the vertical sum-frequency force, we see from Fig.7.11 that the F_p part dominates over the F_q over the whole frequency range studied. For relatively short waves, e.g. $\omega^2 R/g \geq 1.6$, most of the contribution to the total vertical sum-frequency force is from the second-order velocity potential. That means one must take into account of the second-order velocity potential effect and can not simply approximate the total vertical sum-frequency force by the quadratic component, especially for short waves. Here ω is the frequency of the incident waves.

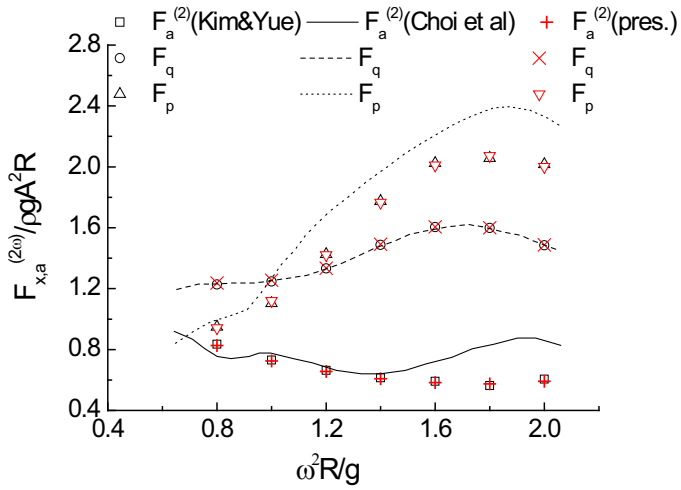

Fig.7.10. The amplitude of the non-dimensional sum-frequency force in the X-direction of a stationary hemisphere. h=3R. h is the water depth, R is the radius of the hemisphere. $F_a^{(2)}$ indicates the amplitude of the total second-order sum-frequency force, while F_q and F_p are the sum-frequency forces caused by the quadratic terms of first order quantities and the second-order velocity potential, respectively.

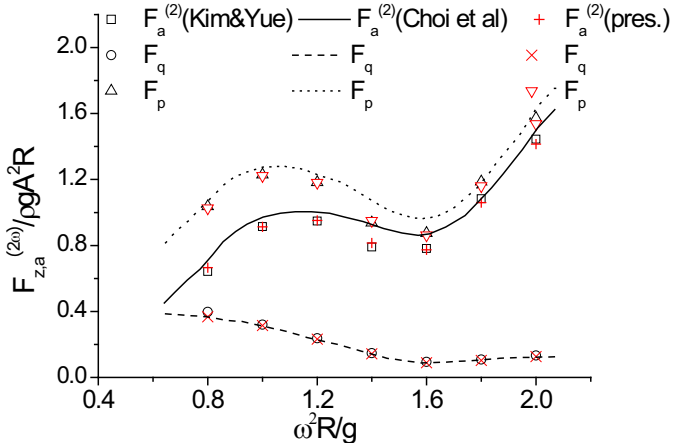

Fig.7.11. The amplitude of the non-dimensional the sum-frequency force in the Z-direction of a stationary hemisphere. h=3R. h is the water depth, R is the radius of the hemisphere. $F_a^{(2)}$ indicates the amplitude of the total second-order sum-frequency force, while F_q and F_p are the sum-frequency forces caused by the quadratic terms of first order quantities and the second-order velocity potential, respectively.

Truncated vertical circular cylinder

The diffraction of a truncated vertical circular cylinder with radius R and draft d=R is studied in order to study the linear and second-order wave excitation forces. The considered water depth is h=2R. The same cylinder has been studied numerically by Kinoshita et al. (1997) in the frequency domain with a quadratic HOBEM.

In this study, the so-called near-field method is used for the forces calculation, i.e. the hydrodynamic forces are obtained by integrating the hydrodynamic pressure on the instantaneous wetted body surface. If only the mean drift forces are of interest, the far-field approach which applies the momentum conservation to the entire fluid domain can be used. The far-field method is known as more robust and efficient than the near-field method in calculating the mean wave forces. Our interest in the present work is not only on the mean forces but also the higher-order oscillatory forces, and therefore the near-field approach is adopted.

One of the problems associated with the near-field method is that it requires a high degree of numerical precision of the solution on the body surface. This difficulty is especially significant for bodies with sharp corner, where the flow is singular with infinite velocity. See also the discussion associated with Eq.(5.1). The integration of the quadratic term of the velocity at the sharp corner is still integrable. However, the convergence could be very slow. In the low-order panel method, non-uniform spacing of the panels near the corner improves the accuracy of the near-field analysis, as shown by Newman & Lee (1992). The higher-order panel method was reported by for instance Lee et al. (2002) to be more sensitive to this singularity in the near-field approach. To minimize this problem, a non-uniform geometric mapping near the corner used by Newman & Lee (2002) is adopted. This is based on the local two-dimensional flow around the corner. If r is the distance from the corner and θ is the interior angle of the body at the corner, the leading-order corner flow velocity potential in the vicinity of the sharp corner can be expressed by Eq.(5.1). The velocity near the corner is proportional to $r^{1/\lambda-1}$, where $\lambda = 2-\theta/\pi$. Since the velocity potential ϕ is assumed to be regular in the parametric variable in the same direction, say u, the inverse mapping of $u(r)$ should have the same singularity as the solution at the corner so that $d\phi/dr = (d\phi/du)(du/dr) \sim r^{1/\lambda-1}$. This suggests

using a mapping with the local non-uniformity with $r \sim u^{\lambda}$. For a truncated vertical circular cylinder with a right-angle corner, we have $\lambda = 1.5$. Fig.7.12. shows an example of the meshes on half of the truncated vertical circular cylinder with draft d=2R. Non-uniform meshes with the non-uniformity coefficient λ=1.5 are used at the corner and the waterline.

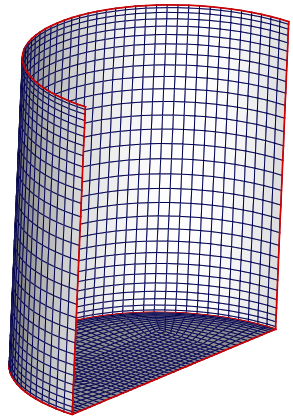

Fig.7.12. Meshes on half of the truncated vertical circular cylinder with draft d=2R. Non-uniform meshes with the non-uniformity coefficient λ=1.5 are used at the corner and the waterline.

Presented in Fig.7.13 and Fig.7.14 are the amplitudes of the linear wave excitation forces in surge and heave directions, respectively. The present time-domain results are compared with numerical results of Kinoshita et al. (1997) with favorable agreement. The horizontal wave drift forces in X-direction are plotted in Fig.7.15. Comparison is made between the present results and the frequency-domain numerical results of Kinoshita et al. (1997) and the semi-analytical results of Kinoshita & Bao (1996). Good agreement is observed. The present mean drift forces are slightly higher than Kinoshita et al.'s (1997) numerical result. However, it can be seen that the present results are more closer to Kinoshita & Bao's (1996) semi-analytical results, even though they are not presented at the same wave number kR. All the results of Kinoshita et al. (1997) and Kinoshita & Bao (1996) shown in Fig.7.13 - Fig.7.15 are digitalized data from Kinoshita et al. (1997).

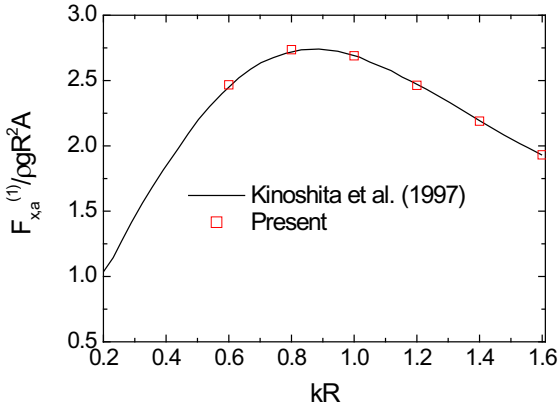

Fig.7.13. The amplitude of the linear excitation force on a truncated circular cylinder in surge direction. h=2R, d=R. k is the wave number of the incident waves.

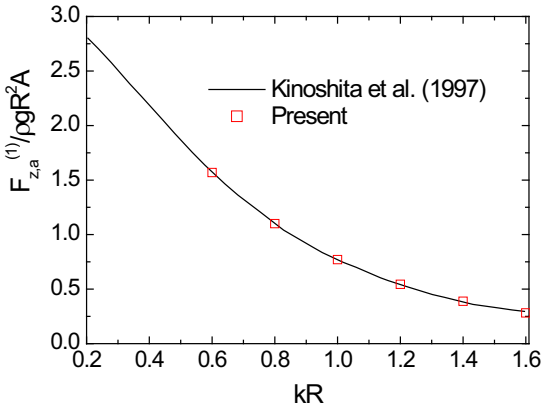

Fig.7.14. The amplitude of the linear excitation force on a truncated circular cylinder in heave direction. h=2R, d=R. k is the wave number of the incident waves.

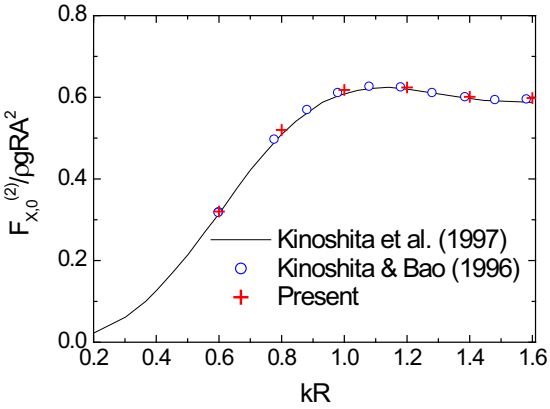

Fig.7.15. The horizontal wave drift force on a fixed truncated circular cylinder. h=2R, d=R. k is the wave number of the incident waves.

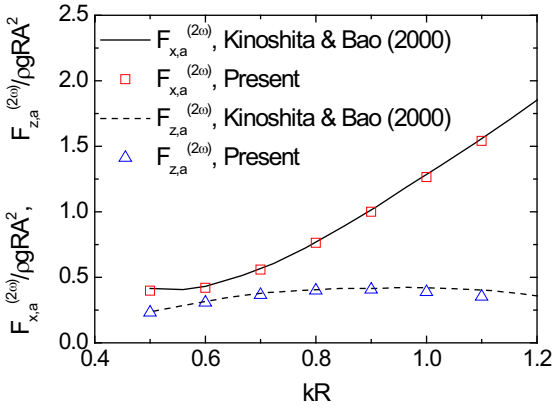

Fig.7.16. The amplitude of the sum-frequency forces on a fixed truncated circular cylinder in both the horizontal and vertical directions. h=10R. d=4R. k is the wave number of the incident waves.

Fig.7.16 presents the horizontal and vertical sum-frequency forces for a truncated vertical circular cylinder with draft d=4R. The water depth is h=10R. The numerical results are compared with the semi-analytical results of Kinoshita & Bao (2000). Good agreement has been obtained.

7.1.2 Second-order diffraction in bichromatic waves

We have also studied the second-order diffraction of the stationary bottom-mounted vertical circular cylinder in bichromatic waves. The domain decomposition based method in Chapter 5 is used. The radius of the control surface is taken as R_C=1.5R with R as the radius of the cylinder.

The sum-frequency and difference-frequency Quadratic Transfer Functions (QTFs) of the horizontal forces are recovered from the numerical time history of the forces by Fourier analysis. The details of the Fourier analysis used in this study were given in Section 3.7. The sum-frequency QTF (F_{ij}^{+}) and difference-frequency QTF (F_{ij}^{-}) are defined respectively as

$$F_{ij}^{+} = \frac{F^{+}}{\rho g R A_i A_j}, \quad F_{ij}^{-} = \frac{F^{-}}{\rho g R A_i A_j} \tag{7.1}$$

where F^{+} and F^{-} are total sum-frequency and difference frequency horizontal forces, respectively.

Comparisons are made with the semi-analytical results by Eatock Taylor & Huang (1997) and Moubayed & Williams (1995) and the numerical results of Kim & Yue (1990). Table 7.1 shows the comparison of the sum-frequency surge force QTF for a bottom-mounted circular cylinder with h=R. h is the water depth and R is the radius of the cylinder. The sum-frequency and difference-frequency QTF are presented in Table 7.2 for a bottom-mounted circular cylinder with h=4R. Good agreement has been achieved for both the sum-frequency and difference-frequency forces.

Table 7.1. Comparison of the sum-frequency surge force QTF for a bottom-mounted circular cylinder with h=R. h is the water depth and R is the radius of the cylinder. υ_i is defined as $\omega_i^2 R/g$. ω_i and ω_j are the frequencies of the two components of the bichromatic wave. At each frequency pair, three numbers are given, corresponding successively from the top line to the present results, those of Eatock Taylor & Huang (1997), and those of Kim & Yue (1990).

	υ_j=1.0	υ_j=1.4	υ_j=1.8
υ_i=1.0	0.941	0.782	0.902
	0.946	0.769	0.909
	0.939	0.778	0.903
υ_i=1.4		0.973	1.100
		0.972	1.115
		0.971	1.105
υ_i=1.8			1.225
			1.222
			1.226

Table 7.2. Comparison of the sum-frequency and difference-frequency surge force QTF for a bottom-mounted circular cylinder with h=4R. h is the water depth and R is the radius of the cylinder. υ_i is defined as $\omega_i^2 R/g$. ω_i and ω_j are the frequencies of the two components of the bichromatic wave. At each frequency pair, four numbers are given, corresponding successively from the top line to the present results, those of Kim & Yue (1990), Eatock Taylor & Huang (1997) and Moubayed & Williams (1995).

υ_i=1.0; υ_j=1.6		υ_i=1.2; υ_j=1.8		υ_i=1.4; υ_j=2.0	
sum-freq.	diff-freq.	sum-freq.	diff-freq.	sum-freq.	diff-freq.
1.868	0.861	2.190	0.788	2.088	0.759
1.853	0.856	2.182	0.788	2.094	0.765
1.883	0.849	2.294	0.769	2.114	0.777
1.783	0.840	2.091	0.761	1.998	0.734

Some important numerical issues of the time-domain simulation of bichromatic waves are associated with the selection of the meshes sizes and how to efficiently enforce the radiation conditions for both the long waves and short waves. Taking the second-order diffraction problem as an example, the total wave system contains different components of waves. The shorted waves are the sum-frequency waves with frequency $\omega_i + \omega_j$ (i=1,2; j=1,2). Here ω_i (i=1, 2) is the frequency of one component of the bichromatic wave. The longest wave is the difference-frequency waves with frequency $\left|\omega_i - \omega_j\right|$ (i=1, 2; j=1, 2; $i \neq j$) if ω_i and ω_j are very close to each other. It can partly be understood from the dispersion relationship of the second-order free waves, i.e.

$$\left(\omega_i \pm \omega_j\right)^2 = k_{\pm} g \cdot tanh\left(k_{\pm} h\right). \tag{7.2}$$

Here k_+ and k_- are the wave numbers of the high-frequency and difference-frequency free waves, respectively.

The maximum panel size depends on shortest wave length. It is suggested by Faltinsen (1990) based on the experience on constant boundary element method that the characteristic length of an element ought to be at most 1/8 of the wave length. Around a vertical column with a circular cross-section there ought to be 15-20 circumferential elements at any height. If there is a conflict between these two recommendations, the more conservative is required. A similar criterion holds for the HOBEM depending on the required accuracy on the results.

In the time-domain studies, the fluid domain is truncated at a certain distance away from the body. The 'length' of the computational domain depends on both the characteristic dimension of the body and the maximum length of the incident and scattered wave. The artificial damping zone is often used to enforce the radiations of the outgoing waves generated by the body. The length of the numerical damping zone is typically chosen as 1-3 times the wave length of the waves that are of interest. The numerical damping zone is known to be less efficient for waves with low frequencies than for high-frequency waves. The combination of the numerical damping zone with, for instance, the Sommerfeld-Orlanski condition (Orlanski, 1976) would allow us to use a relatively shorter damping zone.

In this section, the numerical damping zone is used without Sommerfeld-Orlanski condition. The length of the damping zone is chosen as twice the wavelength of the difference-frequency free waves. The mesh size is selected based on the shorter linear wave. Approximately 25 cubic elements are used

per wavelength of the shorter wave near the waterline. Smoothly stretched meshes are used on both free surface and body surface away from the waterline.

The non-dimensional wave numbers studied here do not include cases where υ_i and υ_j $(i \neq j)$ are very close. These cases require very large computational domain relative to the characteristic body length and result in huge-dimension matrix equation system. This is a common issue in the numerical computations when multi-scale problems are considered. However, one can on one hand use the combination of the numerical damping zone with, for instance, the Sommerfeld-Orlanski condition to reduce the size of the computational domain. On the other hand, one has to always keep in mind what physical effects are of interest. For instance, if the difference-frequency effect is a major concern, larger mesh sizes can be used compared to that in a problem where sum-frequency effects are dominant. If the sum-frequency effects are of more interest, a much smaller computational domain can be designed compared to that in a difference frequency dominant problem.

7.1.3 Third-order diffraction in regular waves

It has been shown in the previous sections that the present time-domain HOBEM is able to predict accurately the linear and second-order wave diffraction effect on the stationary bodies. In this section, we will try to study the third-order diffraction effect on a fixed body in regular waves by the time-domain HOBEM described in Chapter 4. The free-surface conditions and the body boundary conditions for the third-order diffraction problem have been given in Section 2.5.

The triple-harmonic part of the third-order diffraction problem was studied by, for instance Malenica & Molin (1995) and Teng & Kato (1997) in the frequency domain. Faltinsen et al. (1995) obtained an asymptotic solution to the third-order diffraction problem with a long wave length approximation. In the present study, we study the complete third-order diffraction, which means that the solution contains not only the triple-harmonic effect but also the third-order contribution with fundamental frequency. The third-order wave loads are, in most cases of small magnitudes compared with the linear part of the wave loads. However, the triple-harmonic third-order wave loads may be an important excitation source of the ringing response of the TLPs and deep-water gravity-based platforms. The first-harmonic third-order wave force is not as important as its triple-harmonic counterpart for conventional offshore structures.

According to Malenica & Molin (1995), we decompose the total third-order forces into three parts (see also Section 2.5.3)

$$\vec{F}^{(3)} = \vec{F}_1^{(3)} + \vec{F}_2^{(3)} + \vec{F}_3^{(3)}, \tag{7.3}$$

where

$$\vec{F}_1^{(3)} = -\rho \int_{CW_0} [\frac{1}{2}(\eta^{(1)})^2 \phi_{tZ}^{(1)} + \frac{1}{2}(\nabla\phi^{(1)} \cdot \nabla\phi^{(1)})\eta^{(1)}] \vec{n} dl, \tag{7.4}$$

$$\vec{F}_2^{(3)} = -\rho \iint_{SB_0} \nabla\phi^{(1)} \cdot \nabla\phi^{(2)} \vec{n}\, dS - \rho \int_{CW_0} \eta^{(1)} \phi_t^{(2)}\, \vec{n} dl, \tag{7.5}$$

$$\vec{F}_3^{(3)} = -\rho \iint_{SB_0} \phi_t^{(3)} \vec{n}\, ds. \tag{7.6}$$

The first part $\vec{F}_1^{(3)}$ is contributed by the products of the first-order quantities. $\vec{F}_2^{(3)}$ consists the products of the first-order and second-order quantities, whereas $\vec{F}_3^{(3)}$ is the consequence of the

third-order velocity potential. CW_0 and SB_0 are the mean waterline and the mean wetted body surface, respectively. We will hereafter in this section denote the third-order horizontal force in the direction of wave heading as $F^{(3)}$ with its three components as $F_1^{(3)}$, $F_2^{(3)}$ and $F_3^{(3)}$ corresponding to the decomposition in Eq.(7.3).

The third-order diffraction of a bottom-mounted vertical circular cylinder with draft d=10R studied by both Malenica & Molin (1995) and Teng & Kato (1997) is re-investigated in this section. Here R is the radius of the cylinder. The triple-harmonic forces obtained from the present time-domain method will be compared with that of Malenica & Molin (1995) and Teng & Kato (1997). The comparisons are shown in Fig.7.17 - Fig.7.20. $F_1^{(3\omega)}$, $F_2^{(3\omega)}$ and $F_3^{(3\omega)}$ in Fig.7.17 - Fig.7.20 are the triple-harmonic parts of the third-order forces, i.e. $F_1^{(3)}$, $F_2^{(3)}$ and $F_3^{(3)}$ respectively. Fig.7.17 presents the amplitudes of the real and the imaginary parts of $F_1^{(3\omega)}$, whereas these of $F_2^{(3\omega)}$ are depicted in Fig.7.18. Comparisons are made with the results of Malenica & Molin (1995) showing very good agreement. This is not surprising since $F_1^{(3\omega)}$ and $F_2^{(3\omega)}$ are contributed only by the first-order and second-order solutions, which have been shown to be accurate in the previous sections of this chapter. Differences were observed for $F_3^{(3\omega)}$ between the present results and results of Malenica & Molin (1995) and Teng & Kato (1997). See the comparison of the amplitude of the real and imaginary parts of $F_3^{(3\omega)}$ in Fig.7.19 and Fig.7.20, respectively.

Some numerical details for the results in Fig.7.17 - Fig.7.20 are summarized as follows: The density of mesh near the waterline was selected as NE0=40, where NE0 represents the number of cubic elements per linear wavelength. The meshes near the waterline are finer and become coarser in a smooth way away from the waterline. The time increment $\Delta t = T/300$ was used in the time stepping of the fluid motion. Here T is the linear wave period. The lengths of damping zones in the first-, second- and third-order solution are twice the linear wavelength. The numerical damping zone described in Section 3.4 without active wave absorber was used to enforce the radiations conditions. The empirical coefficient γ in Eq.(3.21) was set to be 0.5×10^{-5} in all the calculations. In order to absorb the third-order wave with the fundamental frequency, the damping zone used in the third-order problem is the same as that in the first-order problem. The first-order and second-order derivatives on both the free surface and body boundary are calculated with the assistance of the cubic shape functions of the higher-order boundary elements. The third-order derivative term $\partial^3\phi^{(1)}/\partial Z^3$ in the third-order kinematic free-surface conditions (see Eq.(2.73)) was rewritten as the second-order derivatives of the vertical velocity on the free surface. See Section 4.6 for the discussion of the direct calculation of higher-order derivatives. Other numerical details can be found in the related sections in Chapter 4.

Sensitivity studies on the mesh density and the size of time increment have been made in order to show that the present numerical results in Fig.7.19 and Fig.7.20 are convergent results. Fig.7.21 shows the time records of the third-order wave force component $F_3^{(3)}$ with different mesh densities for the bottom-mounted circular cylinder (d=10R) in regular wave with non-dimensional wave number kR=1.0. NE0 is the number of cubic elements per linear wavelength near the waterline. The three curves with NE0=30, 40 and 45 respectively are almost identical, indicating that the meshes used in the previous analysis (see Fig.7.19 and Fig.7.20) are sufficient. Time records of the total third-order wave force $F^{(3)}$ with different time increments for the same bottom-mounted circular cylinder in regular waves (kR=1.0) are presented in Fig.7.22. Four results with $T/\Delta t$ =200, 400, 600 and 800 respectively are shown. Because it is sufficient with $T/\Delta t$ =200 to get convergent results, the four curves actually coincide with each other.

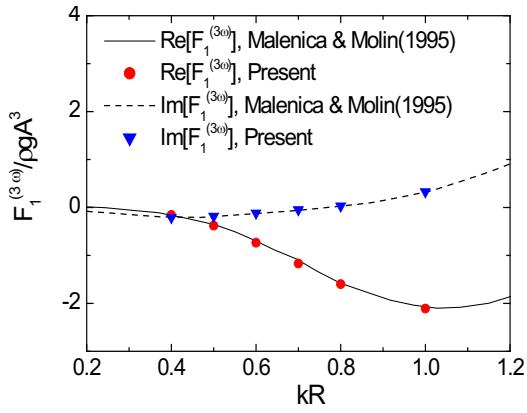

Fig.7.17. The amplitude of the real and the imaginary part of $F_1^{(3\omega)}$ on a bottom-mounted circular cylinder with draft d=10R. A is the linear incident wave amplitude. k is the wave number.

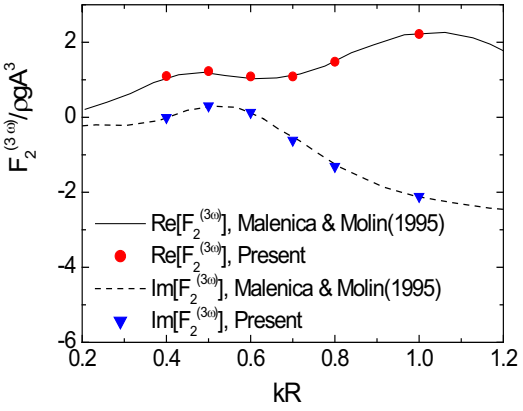

Fig.7.18. The amplitude of the real and the imaginary part of $F_2^{(3\omega)}$ on a bottom-mounted circular cylinder with draft d=10R. A is the linear incident wave amplitude. k is the wave number.

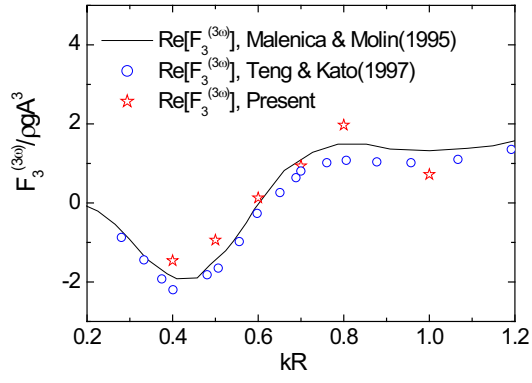

Fig.7.19. The amplitude of the real part of $F_3^{(3\omega)}$ on a bottom-mounted circular cylinder with draft d=10R. A is the linear incident wave amplitude. k is the wave number.

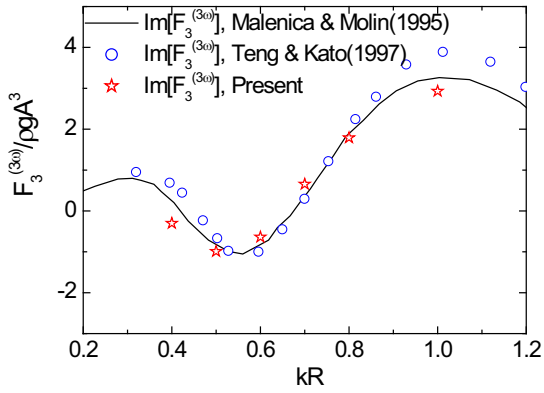

Fig.7.20. The amplitude of the imaginary part of $F_3^{(3\omega)}$ on a bottom-mounted circular cylinder with draft d=10R. A is the linear incident wave amplitude. k is the wave number.

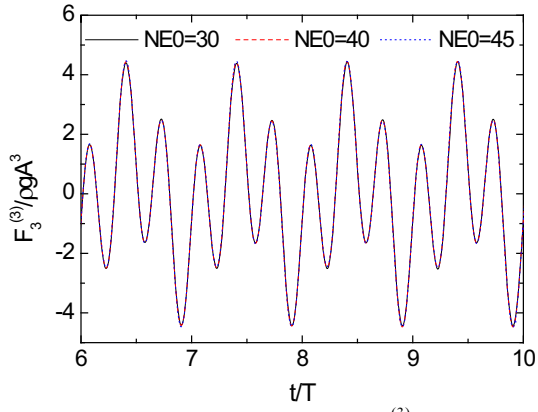

Fig.7.21. Time records of the third-order wave force component $F_3^{(3)}$ with different meshes densities for a bottom-mounted circular cylinder in regular wave. d=10R. kR=1.0.

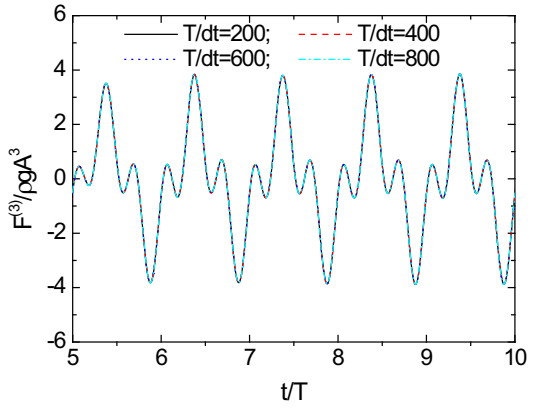

Fig.7.22. Time records of the total third-order wave force $F^{(3)}$ with different time increments for a bottom-mounted circular cylinder in regular wave. d=10R. kR=1.0.

In order to exam the effect of the numerical damping zone on the third-order results, we have studied the sensitivity of the results on the lengths of the damping zones and the empirical coefficients in the dissipative terms in the numerical damping zone.

The length of the free surface, defined as the distance from the waterline to the end of the free surface along the radial direction, is kept as three times the linear wave length, i.e. $L=3\lambda$. Here λ is the linear wavelength. The length of the damping zone is defined as L_2, whereas the length of the free surface part with the damping zone excluded is defined as L_1. See Fig.7.23 for the illustration of L_1, L_2 and L. Three different damping zone lengths have been considered, i.e. $L_2=1.5\lambda$, 2λ and 2.5λ with corresponding $L_1=1.5\lambda$, λ and 0.5λ, respectively. Because we have kept the total free surface length as a constant, the change of the damping zone length results in the change of relative position of the damping zone to the body (L_1). The empirical coefficient $\gamma=0.5\times10^{-5}$ is used in the formula of the damping coefficient, see Eq.(3.21). The different damping zone lengths have to be substitute into Eq.(3.21) in order to get the damping coefficient.

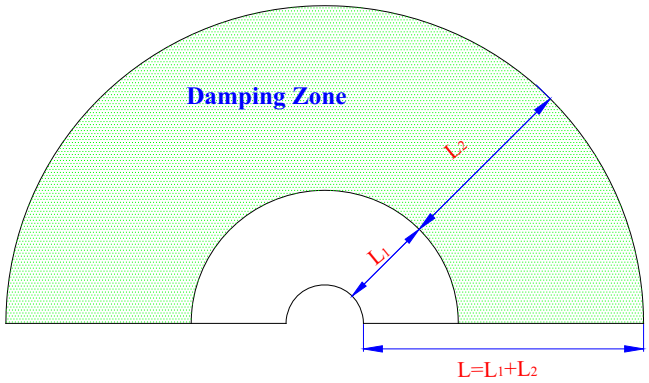

Fig.7.23. Definition the length of the damping zone (L_2), the total length of the free surface (L) and the length of the free surface part with the damping zone excluded (L_1).

Fig.7.24 shows the time history of the total horizontal second-order wave force on the bottom-mounted cylinder with d=10R in regular wave. The non-dimensional wave number is kR=1.0. The time history of the third-order wave force due to the third-order velocity potential, i.e. $F_3^{(3)}$, is plotted in Fig.7.25. Both Fig.7.24 and Fig.7.25 consist of three curves with different damping-zone lengths. It is difficult to find any differences between the curves since they are very close. It is seen from Fig.7.24 and Fig.7.25 that the present numerical results are not sensitive to the location and the length of the damping zone as long as it is well designed so that it can sufficiently damp out most of the energy of the scattered waves.

Our numerical tests also showed a clear lack of sensitivity on the damping coefficient γ in Eq.(3.21) when it is selected in between 10^{-5} and 10^{-6} and the length of the damping zone is chosen to be larger than about 1.5λ. The results will not be shown here.

The $F_3^{(3)}$-component in Eq.(7.6) can be further divided into the sum of two parts, with the first part $F_{3,in}^{(3)}$ due to the third-order incident wave velocity potential $\phi_{in}^{(3)}$ and the other part $F_{3,s}^{(3)}$ due to the third-order scattered wave velocity potential $\phi_s^{(3)}$. As an alternative way of obtaining the third-order force contributed by the third-order scattered velocity potential, i.e. $F_{3,s}^{(3)}$, the indirect method based on

Green's 2nd identity is also used here to validate the numerical results for $F_{3,s}^{(3)}$. We introduce an artificial velocity potential ψ_1 satisfying the Laplace equation in the fluid domain, $\psi_1=0$ on the mean free surface, $\partial\psi_1/\partial n=n_1$ on the mean body surface, $\partial\psi_1/\partial n=0$ on the sea bottom and $\psi_1\to 0$ on a control surface at infinity. n_1 is the X-component of the unit normal vector on the body surface. The consequence of using the indirect method is that the third-order force contributed by the third-order velocity potential can be obtained without solving the third-order problem. The details of the indirect method can be found in Appendix E. It has also been used in the Chapter 6 as an alternative approach to get second-order diffraction and radiation forces in two-dimensional problems.

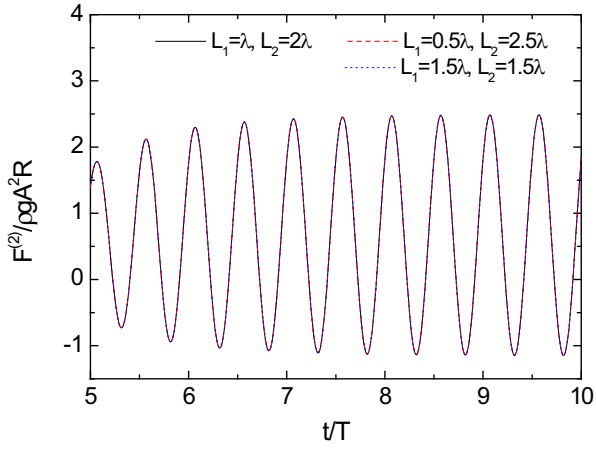

Fig.7.24. The time history of the total horizontal second-order wave force on a bottom-mounted circular cylinder in regular wave. Different lengths of damping zone (L_2) are considered. The total length of the free surface is kept as 3λ with λ as the linear wavelength. The draft of the cylinder is d=10R. The non-dimensional wave number is kR=1.0.

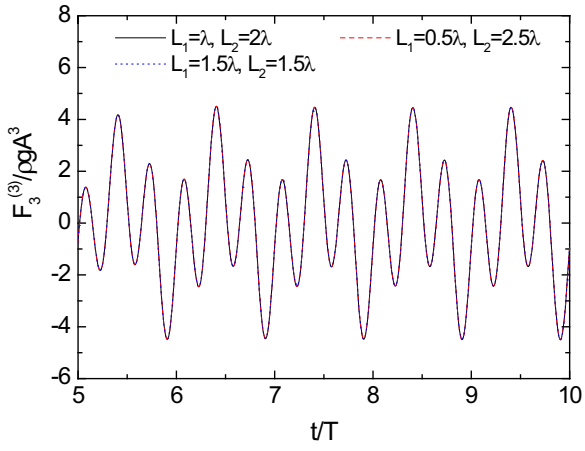

Fig.7.25. The time history of the third-order wave force due to the third-order velocity potential on a bottom-mounted circular cylinder in regular wave. Different lengths of damping zone (L_2) are considered. The total length of the free surface is kept as 3λ with λ as the linear wavelength. The draft of the cylinder is d=10R. The non-dimensional wave number is kR=1.0.

Presented in Fig.7.26 are the time histories of $F_{3,s}^{(3)}$ on the bottom-mounted vertical circular cylinder with h=10R in a regular wave (kR=1.0) calculated by the direct pressure integration method and the indirect method based on Green's 2nd identity. With kR=1.0 and h=10R, we are actually studying a deep-water case, since h>1.5λ (see e.g. Faltinsen, 1990). Therefore, the third-order velocity potential is negligible, i.e. $\phi_{in}^{(3)} \approx 0$. The results of the direct method and the indirect method are consistent. Here the free surface length $L=5\lambda$ is used with the damping zone length $L_2=2\lambda$ and $L_1=3\lambda$. One should note that the vertical velocity of ψ_1 at the waterline is singular but still integrable. A similar singularity for the artificial ψ_1 problem was found analytically for a two-dimensional semi-circle. See Section 6.5 and Section 6.6.

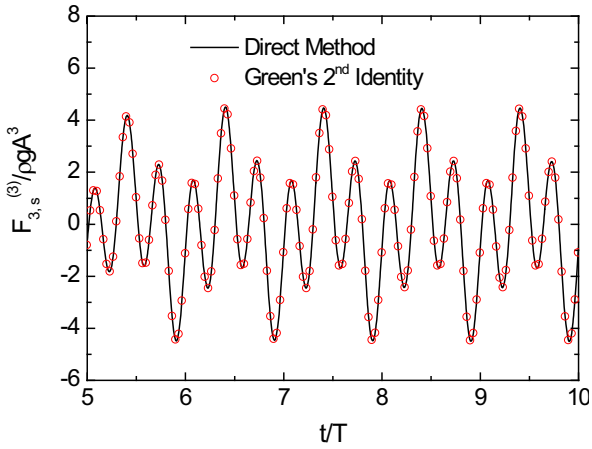

Fig.7.26. The time history of the third-order wave force due to the third-order scattered velocity potential on a bottom-mounted circular cylinder in regular wave. Comparison is made between the results by the direct method and that of the indirect method based on Green's 2nd identity. kR=1.0. h=10R.

The sensitivity studies on the discretization, the time increment of time stepping of the free-surface conditions, the empirical damping coefficients in the numerical damping zone, the location and length of the damping zone suggest that the numerical results presented in Fig.7.19 - Fig.7.20 are convergent.

Theoretically speaking, the third-order free-surface conditions Eq.(2.73) and Eq.(2.74) used in the present study contain secular terms. That means the secularity (solvability) conditions are needed. See more discussions on the secularity (solvability) condition in Section 6.4. Unfortunately, there is no rational way to impose a secularity condition in the time-domain simulations for a general three-dimensional problem. Our experiences with the third-order time-domain studies in two dimensions suggest that the third-order solution without a secularity condition shows an increase of the third-order wave amplitude with the increase of the distance to the body. However, the results close to the body should still be reliable, which indicates that integrating the pressure on the body would give the correct results for e.g. the forces and moments. No obviously strong secular effects have been observed in the three-dimensional numerical results of the third-order wave field. This was not true in the two-dimensional studies. See the discussion in Section 6.4.

The third-order results of Malenica & Molin (1995) in Fig.7.19 and Fig.7.20 are considered as the most accurate since they have been confirmed by some other frequency-domain studies for instance

Kinoshita & Bao (2000). At the present work, we were not able to explain the differences between the present numerical results and that of Malenica & Molin (1995). We cannot, of course, exclude the possibility of a bug in the numerical code developed during this study even though careful convergence studies and alternative way of calculating the force have been made with very satisfactory results.

7.2 Second-order studies of a body under forced oscillations

This section studies the linear and second-order wave loads on floating bodies under forced oscillations. For a vertical circular cylinder and a hemisphere, the linear hydrodynamic coefficients, i.e. the added mass and damping coefficients, obtained from the Fourier transformation of the time history of the first-order numerical results are compared with the analytical results. For a vertical axisymmetric body without sharp corners, the forced surge, heave and pitch are studied by both the traditional method with the formulation in the inertial coordinate system and the new method based on domain decomposition. Consistent results of the two methods are obtained. The forced surging and heaving of a truncated vertical circular cylinder with sharp corner in otherwise calm water are studied up to second order by the new method. The present results agree well with some of the existing numerical results. Attempt has been made to study the same truncated cylinder by the traditional method and calculating the second-order derivatives in the second-order boundary conditions directly. It turns out that no convergent second-order results are obtained with very fine mesh resolution.

7.2.1. Linear hydrodynamic coefficients

A vertical circular cylinder under forced surge is first studied. The draft of the cylinder is equal to the water depth. Malenica et al. (1995) provided the linear hydrodynamic coefficients with zero or small Froude number within the context of potential flow theory. The way that they solved the problem is analytically based. The surge added mass A_{11} and damping coefficients B_{11} for Fr=0.0 are presented in Fig.7.27 and Fig.7.28, respectively. The present time-domain results agree well with the semi-analytical result by Malenica et al. (1995).

The definitions of variables in Fig.7.27 and Fig.7.28 are given as follows. R is the radius of the cylinder. The frequency of encounter ω_e, which should be interpreted as the frequency of oscillations in our case, was defined by Malenica et al. (1995) as

$$\omega_e = \omega_0 - kU\cos\beta, \tag{7.7}$$

with ω_0 as the fundamental frequency of incoming wave. U is the forward speed defined positively in X-direction. β is the angle between the wave direction and the x-axis. The results shown in Fig.7.27 and Fig.7.28 correspond to β=0. k as the wave number of the incident waves, which is the real root of the dispersion relationship for the incident waves

$$\omega_0^2 = \left(\omega_e - kU\right)^2 = kg\tanh\left(kh\right), \tag{7.8}$$

where g is the gravity acceleration and h is the water depth.

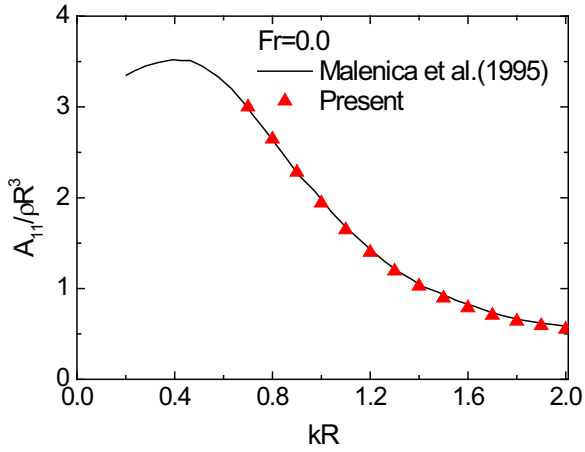

Fig.7.27. The non-dimensional surge added mass for a vertical circular cylinder compared with the semi-analytical results by Malenica et al. (1995). The draft is equal to the water depth h and the radius R. Fr=0.0.

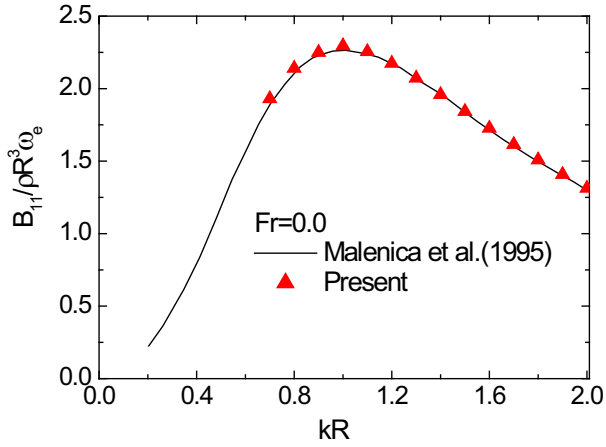

Fig.7.28. The non-dimensional surge damping coefficient for a vertical circular cylinder compared with the semi-analytical results by Malenica et al. (1995). The draft is equal to the water depth h and the radius R. Fr=0.0.

The added mass and damping coefficients of a hemisphere have also been studied by Fourier-analyzing the time-domain results. The water depth is infinite. Comparisons are made with Hulme's (1982) analytical results. Fig.7.29 shows the surge added mass and damping coefficients. The heaving added mass and damping coefficients are shown in Fig.7.30. It is immediately apparent that there is a satisfactory correspondence between the present numerical results and the analytical results by Hulme (1982).

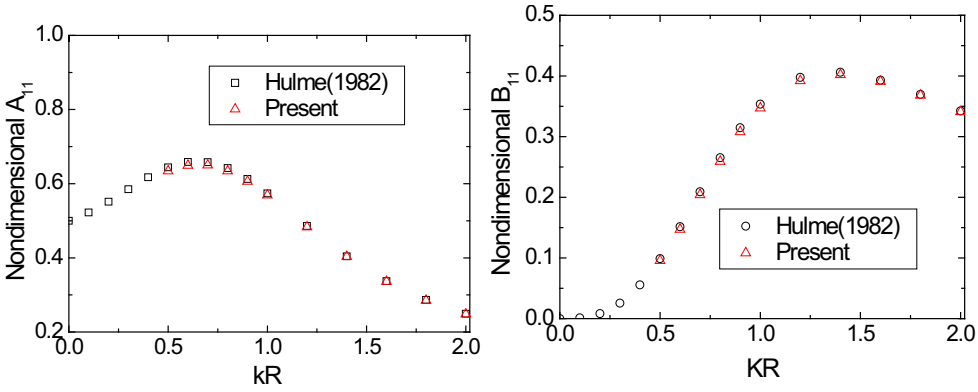

(a) (b)

Fig.7.29. (a) Surge added mass coefficients of a hemisphere. (b) Surge damping coefficients of a hemisphere.

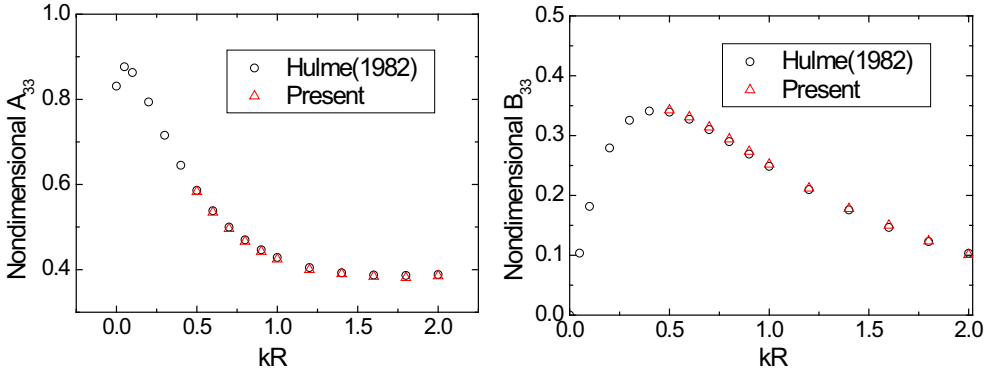

(a) (b)

Fig.7.30. (a) Heave added mass coefficients of a hemisphere. (b) Heave damping coefficients of a hemisphere.

7.2.2. Second-order loads on forced oscillating bodies

Vertical axisymmetric body without sharp corner

We firstly study the forced oscillation of a vertical axisymmetric body without sharp corners. Both the traditional method formulated in the inertial coordinate system and the new method with a body-fixed frame near the body have been used. In the traditional method, the second-order boundary condition contains second-order derivatives of the linear velocity potential. The derivatives of the velocity potential on the body surface and the derivatives of the velocity potential and wave elevation are numerically calculated with the differentiation with respect to the cubic shape functions of the higher-order boundary elements. The details have been given in Section 4.6.

The dimensions of a cross-section of the body in the oxz-plane are shown in Fig.7.31. The center of gravity (COG) is located at (0, 0, -0.25R) with R=1.0. The water depth h is chosen as 1.5R.

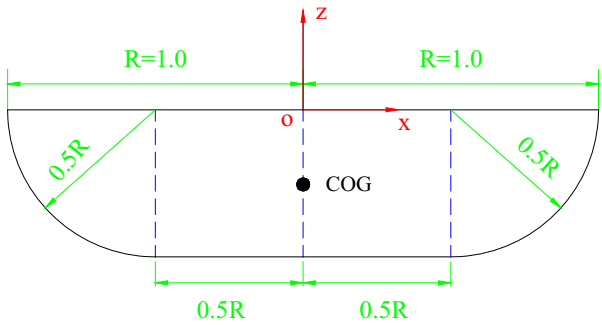

Fig.7.31. Sketch of the cross-section of the vertical axisymmetric body in the oxz-plane.

The forced sinusoidal surge, heave and pitch of the axisymmetric body in otherwise still water are considered, i.e. the influence of the incident wave is excluded here. The surge, heave and pitch about the COG of the body are defined as

$$\xi_{1,g}^{(1)} = Rm(t)\cdot\xi_{1a}\sin(\omega t),\ \ \xi_{1,g}^{(2)} = 0, \tag{7.9}$$

$$\xi_{3,g}^{(1)} = Rm(t)\cdot\xi_{3a}\sin(\omega t),\ \ \xi_{3,g}^{(2)} = 0, \tag{7.10}$$

$$\alpha_{5,g}^{(1)} = Rm(t)\cdot\alpha_{5a}\sin(\omega t),\ \ \alpha_{5,g}^{(2)} = 0, \tag{7.11}$$

where $Rm(t)$ is a ramp function used to allow for the gentle start of the flow. ω is the circular frequency of the oscillations. ξ_{1a}, ξ_{3a} and α_{5a} are the amplitudes of surge, heave and pitch motions, respectively. In the present study, we have used $\xi_{1a} = 0.05R$, $\xi_{3a} = 0.05R$ and $\alpha_{5a} = 0.05$ radians. $\xi_{1,g}^{(i)}$, $\xi_{3,g}^{(i)}$ and $\alpha_{5,g}^{(i)}$ (i=1, 2) may not be the same as $\xi_1^{(i)}$, $\xi_3^{(i)}$ and $\alpha_5^{(i)}$ respectively, which are defined with respect to the origin of the coordinate system OXYZ (see Section 2.3 for the definitions). With our choice of the position of COG, the pure pitching about the COG represents the coupled surge and pitch if the motions are defined with respect to the origin of the reference frame, which is the case when we are formulating the free-surface conditions and body boundary conditions in Chapter 2.

In order to make the comparison between the results of the traditional method and that of the new method possible, one has to define the forces and moments consistently. The formulas for the forces and moments in Eq.(2.67) - Eq.(2.72) and Eq.(2.108) - Eq.(2.113) were defined with respect to the inertial coordinate system OXYZ. In this section, the forces and moments will be presented with respect to the body-fixed coordinate system oxyz. That means we have replace $\vec{r}$ and $\vec{r}_c$ in Eq.(2.67) - Eq.(2.72) and Eq.(2.108) - Eq.(2.113) by $\vec{r}'$ and $\vec{r}_c'$ respectively, and setting the terms associated with $\vec{n}^{(1)}$ or $\vec{n}^{(2)}$ to be zero. $\vec{r}' = (x, y, z)$ and $\vec{r}_c' = (x_c, y_c, z_c)$ are the position vectors of points corresponding to $\vec{r}$ and $\vec{r}_c$ respectively.

Fig.7.32 shows the time history of the non-dimensional first-order force in x-direction for the axisymmetric body undergoing sinusoidal pitching motion about COG. The non-dimensional wave number is kR=1.0. The corresponding non-dimensional second-order component of the force in z-direction is shown in Fig.7.33. Both the results of the traditional method and the new method are presented.

It is seen that the hydrodynamic forces start to reach the steady state when the ramp function is over at

t=3T, with T as the period of the body motion. There appears a difference of the second-order results between the new method and the traditional method in the first three periods, during which the ramp function is applied. This can partly be explained from the free-surface conditions. The second-order free-surface condition used by the new method in the inner domain involves the rigid-body motions (see Eq.(2.88) - Eq.(2.93)), while the second-order free-surface condition formulated in the inertial coordinate system do not contain any body motions (see Eq.(2.48) - Eq.(2.53)). The first-order results of the two methods do not show similar difference because the corresponding free-surface conditions are homogeneous and do not have any forcing from the rigid-body motions.

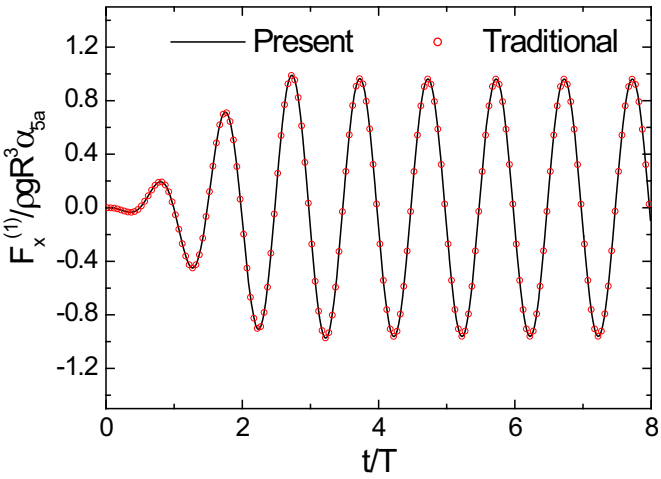

Fig.7.32. Time history of the non-dimensional first-order force in x-direction for a vertical axisymmetric body defined in Fig.7.31 under forced pitch motion about COG with steady-state amplitude $\alpha_{5a} = 0.05$ radians. Comparison is made between the results of the new method and that of the traditional method. kR=1.0.

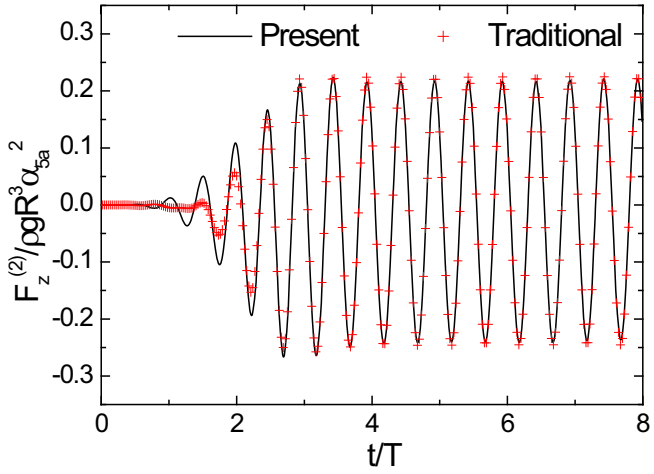

Fig.7.33. Time history of the non-dimensional second-order force in z-direction for a vertical axisymmetric body defined in Fig.7.31 under forced pitch motion about COG with steady-state amplitude $\alpha_{5a} = 0.05$ radians. Comparison is made between the results of the new method and that of the traditional method. kR=1.0.

In Fig.7.34 - Fig.7.36, the amplitudes of the non-dimensional steady-state sum-frequency vertical force versus non-dimensional wave number are shown for the forced pitch, heave and surge motion, respectively. The second-order horizontal force and pitch moment are zero due to symmetry properties. Comparison is made between the results of the present and traditional method showing that consistent results have been obtained by the two methods.

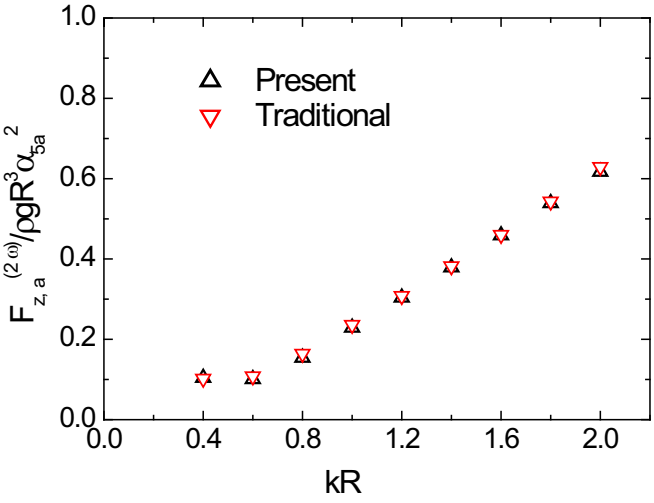

Fig.7.34. The non-dimensional amplitude of the second-order force in z-direction versus kR for a vertical axisymmetric body defined in Fig.7.31 under forced pitch motion about COG with steady-state amplitude $\alpha_{5a} = 0.05$ radians. Comparison is made between the results of the new method and that of the traditional method.

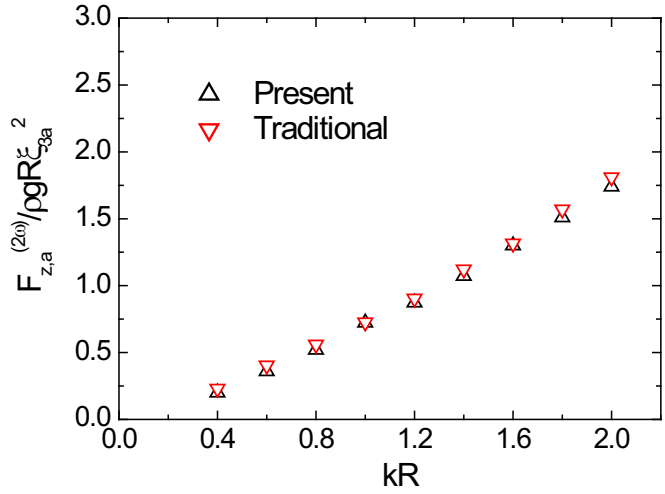

Fig.7.35. The non-dimensional amplitude of the second-order force in z-direction versus kR for a vertical axisymmetric body defined in Fig.7.31 under forced heave motion with steady-state amplitude $\xi_{3a} = 0.05R$. Comparison is made between the results of the new method and that of the traditional method.

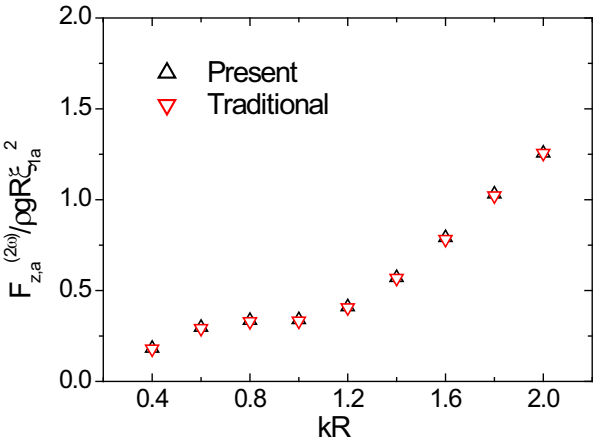

Fig.7.36. The non-dimensional amplitude of the second-order force in z-direction versus kR for a vertical axisymmetric body defined in Fig.7.31 under forced surge motion with steady-state amplitude $\xi_{1a} = 0.05R$. Comparison is made between the results of the new method and that of the traditional method.

Truncated vertical circular cylinder with sharp corners

A truncated vertical circular cylinder under forced sinusoidal surge and heave motion is studied. The radius of the cylinder is chosen as R=1.0 with draft d=0.5R. The water depth considered here is h=1.5R. This problem has been solved to second order by Isaacson & Ng (1993b) by a time-domain lower-order panel method.

Because the second-order results of Isaacson & Ng (1993b) will be shown to have large difference compared with that of the present new method and some other existing numerical results, some important features of Isaacson & Ng's (1993b) numerical method is summarized as follows: They have used the traditional method based on the formulation in the inertial coordinate system was used. See Section 2.4. The second-order derivatives in the second-order body boundary condition are calculated directly by using a standard numerical method. The Sommerfeld-Orlanski radiation condition (see also Orlanski, 1976) is used at a control surface to enforce the first-order and second-order radiation conditions. A first-order Adams-Bashforth-Moulton predictor-corrector method was used for the time evolution of the free-surface conditions. The hydrodynamic forces were calculated by a direct integration of the pressure over the wetted body surface.

Teng (1995) studied the same problem in the frequency domain by a higher-order BEM, while Bai (2001) and Teng et al. (2002) applied a time-domain B-spline based BEM. The formulation in the Earth-fixed coordinate system was used. However, they avoid calculating the second-order derivatives in the second-order body boundary condition by using a Stokes-like theorem. The cost of doing so is an additional integral on the mean waterline and the evaluation of integrals involving the first-order derivatives and the normal derivative of the first-order derivatives of the Green function. The results by Bai (2001) show large difference when compared with those of Isaacson & Ng (1993b), but are much closer to Teng's (1995) results.

In this section, we firstly re-investigate the same problem by using the domain decomposition based method presented in Chapter 5. The higher-order BEM in the time domain is used. Fig.7.37 shows the

amplitude of the non-dimensional vertical sum-frequency forces for the surging truncated cylinder. Comparison is made between results of the new method and the other numerical results mentioned above. The comparison for heaving motion is shown in Fig.7.38. It is seen that our results are consistent with those of Bai (2001) and large differences with Isaacson & Ng (1993b) is observed. Bai (2001) attributed the difference to the fact that Isaacson & Ng (1993b) were using a constant panel method, which causes difficulties in getting accurate results of the second-order derivatives in the second-order boundary condition. Teng et al. (2002) also pointed out that, the computation of the second-order potential needs higher accuracy approaches, and care has to be paid in the computation of the first-order and second-order derivatives of the velocity potentials.

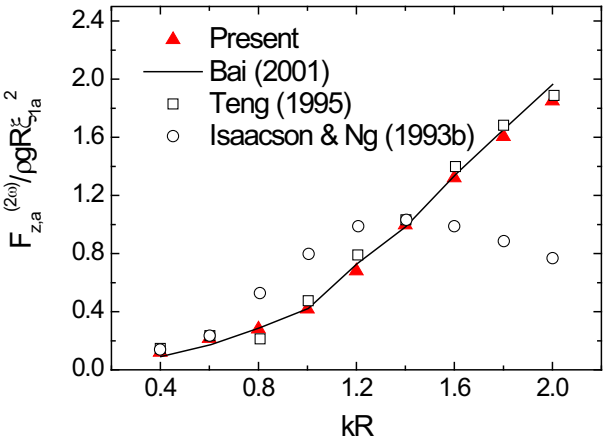

Fig.7.37. The non-dimensional amplitude of the vertical sum-frequency force versus non-dimensional wave number for a surging truncated vertical circular cylinder with amplitude $\xi_{1a} = 0.05R$. d=0.5R. h=1.5R.

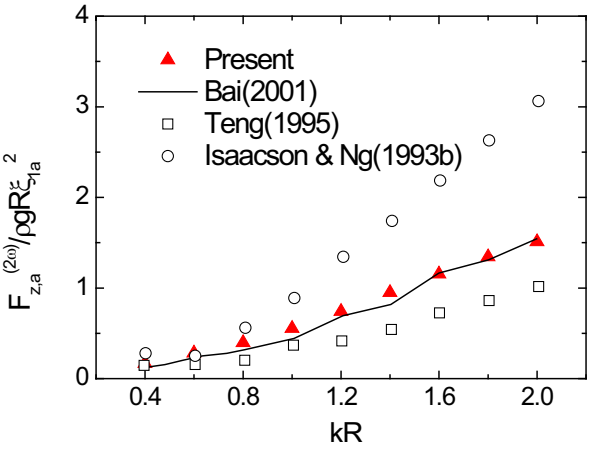

Fig.7.38. The non-dimensional amplitude of second-order vertical force versus non-dimensional wave number for a heaving truncated vertical circular cylinder with amplitude $\xi_{3a} = 0.05R$. d=0.5R. h=1.5R.

Convergence study of the amplitude of the vertical sum-frequency force with different element numbers for the surging truncated cylinder with kR=1.0 is listed in Table 7.1. The vertical

sum-frequency force defined with respect to oxyz system is divided into different components

$$F_z^{(2)} = F_{z,p2}^{(2)} + F_{z,q1}^{(2)} + F_{z,q2}^{(2)}, \tag{7.12}$$

with

$$F_{z,p2}^{(2)} = \iint_{SB} -\rho\phi_t^{(2)} n_3' ds\,, \tag{7.13}$$

$$F_{z,q1}^{(2)} = \iint_{SB} -\frac{1}{2}\rho\nabla\phi^{(1)}\cdot\nabla\phi^{(1)} n_3' ds\,, \tag{7.14}$$

$$F_{z,q2}^{(2)} = \iint_{SB} \rho\left[\left(\vec{u}^{(1)}\cdot\nabla\phi^{(1)}\right) - g x_3^{(2)}\right] n_3' ds\,. \tag{7.15}$$

Due to the fact that the truncated cylinder is wall-sided at the mean waterline, a waterline integral which takes care of the fluctuation of the wave elevation is not included here. From Table 7.1, it is seen that the convergence is achieved for all the three components when NE0 is about 40. In reality, NE0=35 does not give much visible different results with NE=50. It is noted that the component due to the second-order velocity potential $F_{z,p2}^{(2)}$ has even faster convergence rate than that of the other two components, which are the contributions of the first-order velocity potential.

Table 1. Convergence study on the element number for the amplitude of the vertical sum-frequency force calculated by the new method. The forced surging with amplitude $\xi_{1a} = 0.05R$ of a truncated vertical circular cylinder with kR=1.0, h=1.5R and d=0.5R is studied. The absolute value sign means the amplitude. NE0 is the element number distributed in one wavelength.

	$\left\|F_{z,p2}^{(2\omega)}\right\| / \rho g R \xi_{1a}^2$	$\left\|F_{z,q1}^{(2\omega)}\right\| / \rho g R \xi_{1a}^2$	$\left\|F_{z,q2}^{(2\omega)}\right\| / \rho g R \xi_{1a}^2$
NE0=20	0.424	0.140	0.479
NE0=30	0.423	0.146	0.482
NE0=35	0.424	0.148	0.483
NE0=40	0.424	0.150	0.482
NE0=45	0.424	0.151	0.483
NE0=50	0.423	0.151	0.483

We have also attempted to study the same problem by the traditional method with the second-order derivatives in the second-order body boundary condition calculated directly. This is similar to what was done by Issacson & Ng (1993b). Representing the velocity potential on each element by the shape functions, we can obtain the first-order derivative through the first-order derivative of the shape functions. Again, one uses shape functions to interpolate the distribution of the velocity, i.e. the first-order derivative of the velocity potential, and gets the second-order derivatives by differentiating the shape functions. See the details in Section 4.6. This approach has been shown by Liu et al. (1995) to be accurate for the calculation of the second-order derivatives. For the surging of the truncated cylinder, the result of the convergence study for different components of the vertical sum-frequency force is presented in Table 7.2. We decompose the vertical sum-frequency force into three parts:

$$F_z^{(2)} = F_{z,p2}^{(2)} + F_{z,q1}^{(2)} + F_{z,q2}^{(2)} \tag{7.16}$$

where

$$F_{z,p2}^{(2)} = \iint_{SB_0} -\rho\phi_t^{(2)} n_3^{(0)} ds\,, \tag{7.17}$$

$$F_{z,q1}^{(2)} = \iint_{SB_0} -\frac{1}{2}\rho\nabla\phi^{(1)} \cdot \nabla\phi^{(1)} n_3^{(0)} ds\,, \tag{7.18}$$

$$F_{z,q2}^{(2)} = \iint_{SB_0} -\rho\left[\left(\vec{x}^{(1)} \cdot \nabla\phi_t^{(1)}\right) + gx_3^{(2)}\right] n_3^{(0)} ds\,. \tag{7.19}$$

Convergence has been achieved for $F_{z,q1}^{(2)}$ and $F_{z,q2}^{(2)}$ when NE0 is about 40. However, $F_{z,p2}^{(2)}$ shows very slow convergence. No convergence was achieved even at NE0=50, which means a very fine mesh resolution. The time history of $F_{z,p2}^{(2)}$ calculated by the traditional method is plotted in Fig.7.39 showing the differences when different element numbers are used.

In Fig.7.40, the time history of the total second-order force calculated by the new method and the traditional method are plotted. Solutions for NE0=40 and NE0=50 are presented. It is observed that the traditional method is neither able to capture the amplitude nor the phase of the second-order force. Increasing the element number does not show any trend that the result is going to be closer to that of the new method.

For an axisymmetric body without sharp corner (defined in Fig.7.31) studied in the beginning of Section 7.2.2, we have obtained consistent results with the new method by using the traditional method. This indicates that the higher-order method we used for calculating the second-order derivatives are accurate. The difference of the results between the new method and the traditional method, and probably the difference of the results between Bai (2001) (or the new method in this article) and Isaacson & Ng (1993b) do not have too much to do with whether the higher-order methods are used or not. However, a higher-order method is always preferred compared with the lower-order methods, because the resulting equation system will be much smaller if a higher-order method is used.

The differences are more likely to be due to the singular behavior of the flow velocity at the sharp corner. It is known that the solution at the sharp corner may be singular depending on the orientation of the incident flow. We will take the heaving of the truncated cylinder as an example and make analogy of our problem to the wave-current-body problem with sharp corner (see e.g. Zhao & Faltinsen, 1989b). The leading order of the local solution near the sharp corner can be partly explained by a 2D corner flow (see e.g. Newman, 1977). The corner flow solution can be represented by Eq.(5.1). Therefore the leading order of the first-order and second-order derivatives of the velocity potential are $O(r^{-1/3})$ and $O(r^{-4/3})$ respectively. Here r is the distance to the sharp corner. The consequence is that the integral of the double-gradient terms, e.g. $\vec{n}^{(0)} \cdot \left[-\left(\vec{x}^{(1)} \cdot \nabla\right)\nabla\phi^{(1)}\right]$ (see Eq.(2.57) and Eq.(2.58)) on the mean body surface SB_0 is not integrable. The reason why the integrals are not integrable when the body-boundary condition is satisfied on the mean position of the body boundary is that, the formulation of the body boundary condition for a body with unsteady motions is wrong with the presence of the sharp corner. The double-gradient terms in Eq.(2.57) and Eq.(2.58) have been derived by a Taylor expansion about the mean body surface. This is not valid at a sharp corner. However, the body boundary conditions of the new method are formulated on the exact body position, and no Taylor expansion is needed. Therefore, the integral equations of the new method are valid for cases with and without sharp corners.

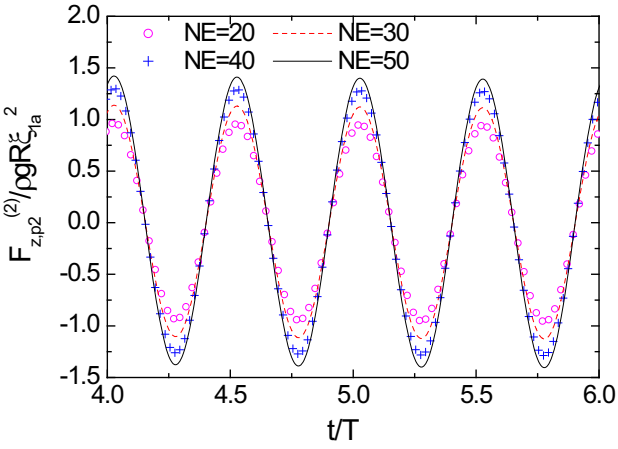

Fig.7.39. The time history of the second-order vertical force $F_{z,p2}^{(2)}$ due to the second-order velocity potential $\phi^{(2)}$. The calculation is for forced surging with steady-state amplitude $\xi_{1a} = 0.05R$ of a truncated vertical circular cylinder with kR=1.0, d=0.5R, h=1.5R. The traditional method calculating the second-order derivative in the second-order body boundary condition is used. NE0 is the number of the elements per wavelength.

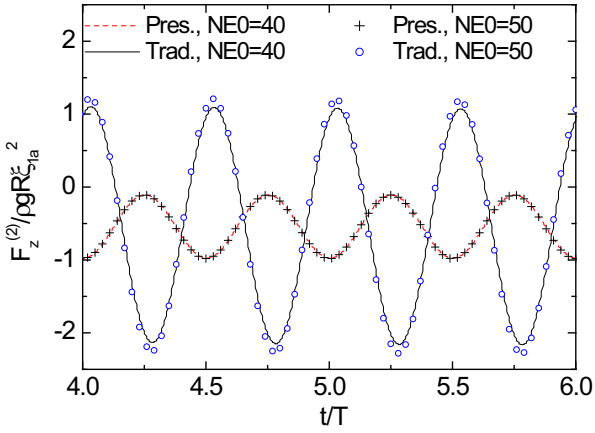

Fig.7.40. Comparison of the time history of total second-order vertical force. The calculation is for forced surging with steady-state amplitude $\xi_{1a} = 0.05R$ of a truncated vertical circular cylinder with kR=1.0, D=0.5R, h=1.5R. 'Pres.' means the new method presented in Chapter 5 is used. The 'Trad.' analysis calculates the second-order derivatives in the second-order boundary condition Eq.(2.58) directly.

Another way of handling the sharp corner cases may be that one introduces a finite bilge radius R at the corner. Then one can use a Stokes-like theorem to reduce the second-order derivatives to first-order derivatives. Afterwards one let R→0. This may explain that the results by Bai (2001) and Teng et al. (2002) are consistent with our results by the new method.

Special care has to be shown when the direct pressure integration is used for the calculation of the forces and moments. It was shown that the leading order of the first-order derivative of the velocity

potential is $O(r^{-1/3})$. Thus the $-1/2\rho\nabla\phi^{(1)}\cdot\nabla\phi^{(1)}n_3'$ term in Eq.(7.14) is $O(r^{-2/3})$ and the $\rho\left(\vec{u}^{(1)}\cdot\nabla\phi^{(1)}\right)n_3'$ term in Eq.(7.15) is $O(r^{-1/3})$. This indicates that the integrals in Eq.(7.14) and Eq.(7.15) are still integrable even though the convergence rate may be slow. The ordering of the singularity behavior may also explain the fact that $\left|F_{z,q2}^{(2\omega)}\right|$ in Table 7.1 has faster convergence rate than $\left|F_{z,q1}^{(2\omega)}\right|$. Eq.(7.13) does not have any singularity in the integrand, thus one should not be surprised that $\left|F_{z,p2}^{(2\omega)}\right|$ shows even faster convergence than $\left|F_{z,q1}^{(2\omega)}\right|$ and $\left|F_{z,q2}^{(2\omega)}\right|$, see Table 7.1.

Table 2. Convergence study on the element number for the vertical sum-frequency force calculated by the traditional method. The forced surging with amplitude $\xi_{1a}=0.05R$ of a truncated vertical circular cylinder with kR=1.0, h=1.5R and d=0.5R is studied. The absolute value sign means the amplitude. NE0 is the element number distributed in one wavelength.

	$\left\|F_{z,p2}^{(2\omega)}\right\|/\rho gR\xi_{1a}^2$	$\left\|F_{z,q1}^{(2\omega)}\right\|/\rho gR\xi_{1a}^2$	$\left\|F_{z,q2}^{(2\omega)}\right\|/\rho gR\xi_{1a}^2$
NE0=20	0.952	0.140	0.481
NE0=30	1.121	0.146	0.481
NE0=40	1.282	0.150	0.482
NE0=50	1.399	0.151	0.482

CHAPTER 8

Three-Dimensional Weakly-Nonlinear Problems with Small Forward Speeds

In Chapter 7, the nonlinear wave-body problems have been studied by using both the traditional method with a formulation in the inertial coordinate system and the new method using body-fixed coordinate system in the near field. No forward speed effect was included.

In this chapter, a small forward speed will be considered in the nonlinear wave-body analysis. Only the leading order of the forward speed effect is included in the present study, with its higher-order effects neglected. This makes possible for us to use the 'double-body' flow as the basis flow. The interactions between the steady flow and the first- and second-order unsteady flows are included in the present model. The details of the formulations of the boundary conditions in inertial and body-fixed coordinate system considering small forward speeds have been given in Chapter 2. In all the studies, the $\tau=\omega_e U / g$ parameter which is the product of the Froude number and non-dimensional encounter wave frequency is less than 0.25.

The wave diffraction on fixed bodies, bodies under forced oscillations and freely-floating bodies in waves will be studied with the consideration of a small forward speed. The bodies studied are free-surface piercing. Both the traditional method (if applicable) and the domain decomposition based method will be used. The domain decomposition based method using body-fixed coordinate system in the near field is valid for all the weakly-nonlinear problems of bodies with or without sharp corners with forward speed effects included. However, the traditional method is only applicable for a linear wave-body problem without forward speed, if the higher-order derivatives of the steady velocity potential are calculated directly. It is not straightforward to apply the Stokes-like theorems (see for instance Bai (2001) and Teng et al. (2002)) to the second-order wave-body problems when the forward-speed effect is included. The reason is associated with the third-order derivatives of the basis flow in the second-order body boundary condition.

The work in this chapter is relevant for the analysis of second-order wave effect on the offshore structures, e.g. TLP, in a weak current. The state-of-the-art nonlinear wave loads analysis for offshore structures does not include the influence of the current on the second-order wave loads. However, it does not mean the current effect is not important. This will be illustrated by our numerical results

presented in this chapter. The study may also be important for the evaluation of nonlinear hull-girder loads on ships with small forward speeds. The sum-frequency excitation hull-girder loads on a ship may be very small compared with the linear wave excitation loads. However, when the sum frequencies are in the resonant frequency regions of the ship hull girder, nonlinear springing occurs. The fatigue damage induced by the nonlinear wave excitation may be as important as that of the linear wave loads due to rigid-body motions. Linear springing may also occur when the encounter frequencies of the waves are equal to the lowest structural natural frequency. Because springing is a resonant phenomenon, the damping is important for both linear and nonlinear springing.

8.1 Second-order wave diffraction

Second-order wave diffraction of a body moving with a small forward speed is studied in this section. The domain-decomposition based time-domain HOBEM presented in Chapter 5 is adopted. The method described in Section 5.3 for the generation of incident wave in the inner domain is used to study the diffraction problem with a small forward speed.

In all the studies presented in Chapter 7, no forward speed or current effects are considered, and no short-wave instabilities were encountered. Therefore, we did not use any smoothing or low-pass filter for those studies. However, when the forward speed is included, we have observed obvious short-wave instabilities. The instabilities occur firstly close to the waterline and their influences propagate into the whole free surface if no smoothing is used to suppress the instabilities. The consequence is that the whole solution will be destroyed by the propagation of the instabilities. It was seen from our numerical tests that the instabilities increase with increasing forward speed or with finer mesh resolution. The reason for the instabilities when the forward speed effect is included has not been fully understood. See the discussions in Section 4.5. In the present work, a low-pass filter is applied to the wave elevation near the waterline in order to suppress the growth of the instabilities. The low-pass filter takes the form of Eq.(4.45), which has been used by Büchmann (2000a) in his linear BEM based numerical wave tank. The filter strength given in Eq.(4.46) is used throughout the cases studies in this section. The filter is applied every time step. More details of this low-pass filter can be found in Section 4.5. The results of the sensitivity study of the first- and second-order results on the filter strength and the time interval of smoothing will be shown for a bottom-mounted vertical circular cylinder.

Bottom-mounted vertical circular cylinder

A bottom-mounted vertical circular cylinder which has been studied by many others is chosen as a reference body. Taking into account a small current, Teng et al. (2008) and Cheung et al. (1996) have studied a linear diffraction problem by time-domain BEMs. Skourup et al. (2000) has studied the same wave-current-body problem up to second order in wave steepness and first order in current speed. One should note that the wave-current-body problem is essentially the same as the wave-body problem with forward speed with a negative sign of the current speed.

The cylinder studied has a radius R=1.0 and draft d=h. The water depth h=R is used in the calculations. The Froude number is defined as $Fr = U/\sqrt{gR}$ with U as the forward speed. The radius of the control surface introduced in the domain decomposition based method was chosen as R_C=1.5R.

We have shown in Section 7.1.1 for the diffraction of a fixed bottom-mounted vertical circular cylinder that, the steady-state first- and second-order results are not sensitive to the distance of the control surface to the body as long as the distance is not very large. This was shown to be true as well in our numerical tests (not shown here) for the wave-body analysis with a forward speed. 30 cubic elements are used per linear wave length in the calculations. The time increment for the updating the velocity potential on the free surface and wave elevation is $\Delta t = T_e / 200$. Here $T_e = 2\pi / \omega_e$ with ω_e as the encounter frequency.

The analytical solution of the double-body basis flow velocity potential $\phi^{(0)}$ is used for the bottom-mounted surface-piercing vertical circular cylinder moving with forward speed U in X direction, i.e.

$$\phi^{(0)}(X,Y,Z) = -\frac{U(X-X_0)R^2}{(X-X_0)^2+(Y-Y_0)^2} \tag{8.1}$$

where (X_0, Y_0) is the position of the cylinder axis in the horizontal plane.

Comparisons are made between the present numerical results and some existing numerical results in the literature, showing good agreement. Fig 8.1 and Fig.8.2 show the amplitude of the first-order wave run-up around the cylinder for *Fr*=0.1 and *Fr*=-0.1, respectively. The present results agree well with the other numerical studies based on time-domain BEMs by Kim & Kim (1997), Büchmann et al. (1998) and Teng et al. (2008). In the figures, θ denotes the angle of the location on the cylinder with respect to the X-axis. A is linear amplitude of the incident wave. $\eta^{(1)}$ is the total first-order wave elevation including the incident wave and scattered wave.

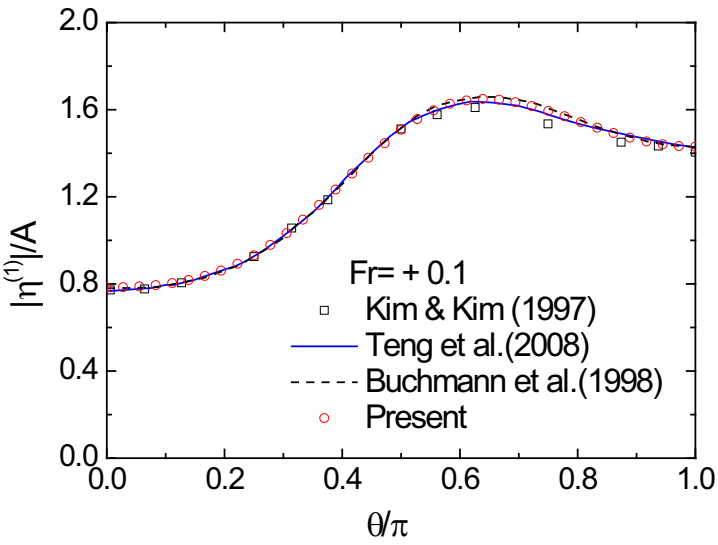

Fig.8.1. The first-order wave run-up around the bottom-mounted vertical circular cylinder. *kR*=1.0, *h*=*R*, *Fr*=0.1.

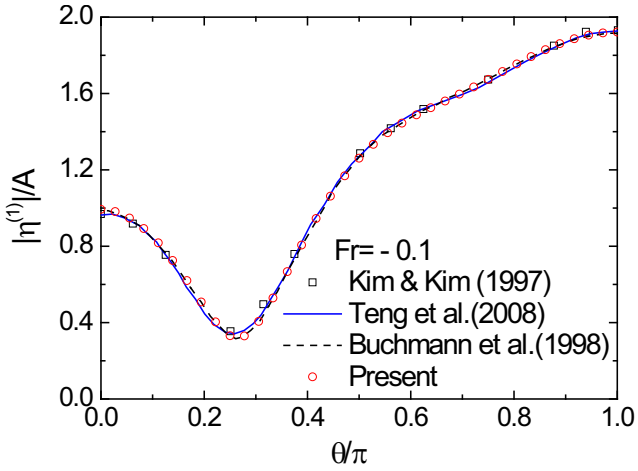

Fig.8.2. The first-order wave run-up around the bottom-mounted vertical circular cylinder. kR=1.0, h=R, Fr=-0.1.

In Fig.8.3 and Fig.8.4, the amplitude of the non-dimensional first-order horizontal force is plotted against non-dimensional wave number kR for Fr=0.1 and Fr=-0.1, respectively. In the figures, k is the wave number of the incident wave. The present results agree well with that of Teng et al. (2008) and Skourup et al. (2000). Our numerical results of the mean drift force for the cylinder with Fr=-0.1 is shown in Fig.8.5, together with the results by Cheung et al. (1996) and Skourup et al. (2000). In Fig.8.6, comparison for the amplitude of the in-line sum-frequency force is shown for Fr=0.05 and Fr= -0.05. The present results agree well with that of Skourup et al. (2000). The result for Fr=0.0 is in between that of Fr =0.05 and Fr =-0.05 and it is not shown here. It is noted that, even though the studied forward speed is not high, the sum-frequency force for $kR \geq 1.2$ changes significantly from a positive current to a negative current with the same strength.

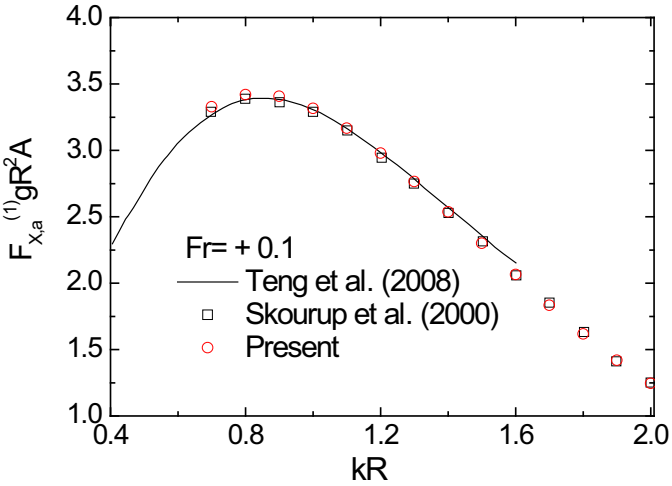

Fig.8.3. The amplitude of the non-dimensional first-order in-line force on a vertical circular cylinder versus kR. A is the wave amplitude. d=h=R, Fr=0.1. k is the incident wave number.

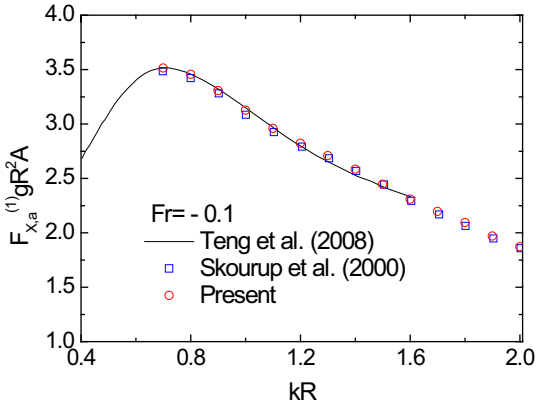

Fig.8.4. The amplitude of the non-dimensional first-order in-line force on a vertical circular cylinder versus *kR*. *A* is the wave amplitude. *d*=*h*=*R*, *Fr*=-0.1. *k* is the incident wavenumber.

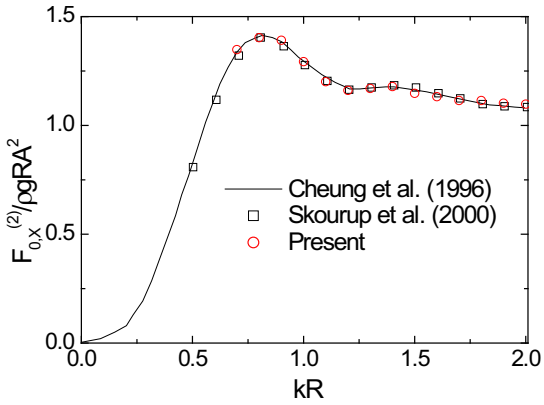

Fig.8.5. Non-dimensional horizontal mean drift force on a vertical circular cylinder versus *kR*. *A* is the wave amplitude. *d*=*h*=*R*, *Fr* =-0.1. *k* is the incident wavenumber.

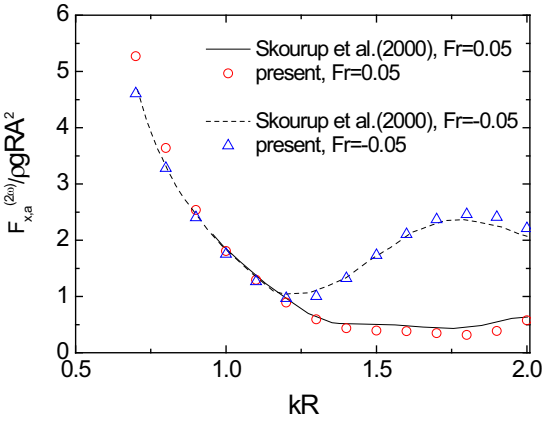

Fig.8.6. The non-dimensional amplitude of sum-frequency in-line force on a vertical circular cylinder versus *kR*. *d*=*h*=*R*. *k* is the incident wave number.

The low-pass filter should on one hand be able to remove energy of the spurious short-wavelength disturbance which is the source of the instability. On the other hand, the energy taken out by the filtering process should be kept at a minimum. In other words, the smart filter should retain the physical waves, which are accurately presented by the numerical solution, and weed out numerical noise, which is detrimental to the numerical solutions. The influence of low-pass filter used in the present work (Eq.(4.45)) has been studied by choosing different strengths of the low-pass filter and different frequencies of the application of the smoothing.

The Fig.8.7 and Fig.8.8 show the time histories of the linear and second-order horizontal wave forces on a moving circular cylinder with three different filter strengths ($c = 4\Delta t / T$, $6\Delta t / T$, $8\Delta t / T$ respectively in Eq.(4.46)). The cylinder has a draft d=R, which is equal to the water depth, i.e. d=h=R. The non-dimensional wavenumber of the incident wave is kR=1.2. The incident wave propagates in the X-direction. The Froude number considered is Fr=-0.08, which means that we are in head-sea conditions. The mesh density near the waterline NE0=35 and time increment $\Delta t = T_e / 200$ have been used in the numerical calculations. Here $T_e = 2\pi / \omega_e$ with ω_e as the encounter frequency. It is seen that both the first-order and second-order results are not sensitive to the strength of the filter.

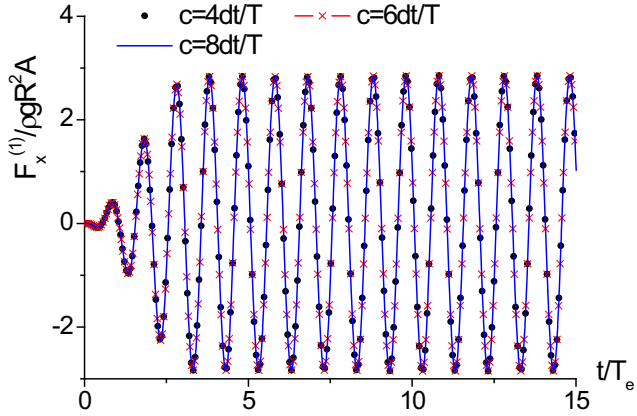

Fig.8.7. The first-order horizontal diffraction force on a vertical circular cylinder in regular wave. h=d=R. kR=1.2. Fr= -0.08. Different filter strengths are studied. The filter is applied every time step.

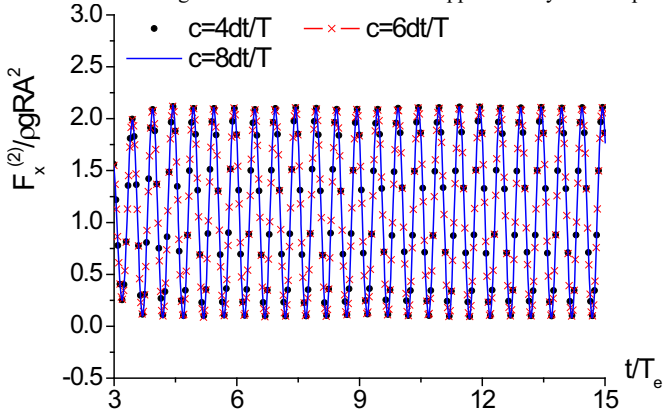

Fig.8.8. The second-order horizontal diffraction force on a vertical circular cylinder in regular wave. h=d=R. kR=1.2. Fr=-0.08. Different filter strengths are studied. The filter is applied every time step.

Presented in Fig.8.9 and Fig.8.10 are the time histories of the linear and second-order horizontal forces on the cylinder for different frequencies of application of the filter. The strength of the low-pass filter $c = 4\Delta t / T$ is used. It is seen from the results without using the low-pass filter that the instability occurs earlier in the second-order simulation than in the first order. Applying the low-pass filter with $c = 4\Delta t / T$ every 5 time steps is sufficient to suppress the instabilities in the first-order simulations within the first 15 wave periods. However, small 'noises' are observed in the second-order results during the first 15 wave periods, followed by strong eruption of the instabilities. Applying the low-pass filter with $c = 4\Delta t / T$ every time step is able to minimize the influence of the short-wave instabilities in both the first-order and second-order solutions and retain the physical wave solutions.

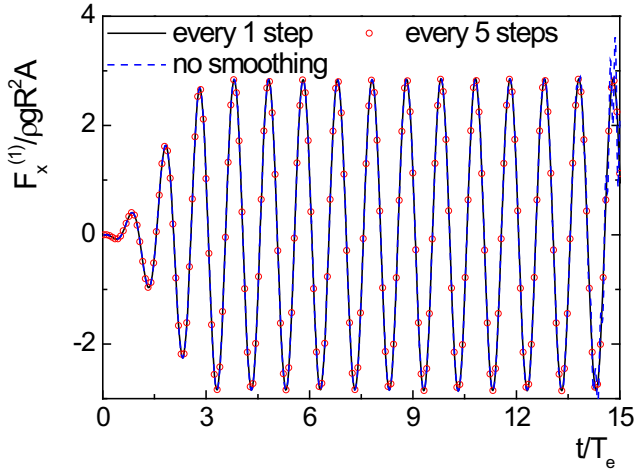

Fig.8.9. The first-order horizontal diffraction force on a vertical circular cylinder in regular wave. h=d=R. kR=1.2. Fr=-0.08. Different frequencies of applying the filter are investigated. The filter strength $c = 4\Delta t / T$ is used.

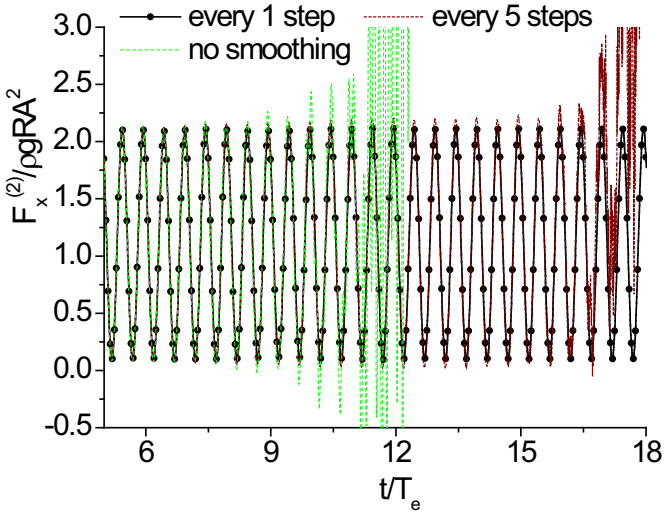

Fig.8.10. The second-order horizontal diffraction force on a vertical circular cylinder in regular wave. h=d=R. kR=1.2. Fr=-0.08. Different frequencies of applying the filter are investigated. The filter strength $c = 4\Delta t / T$ is used.

8.2 Second-order wave radiation

In this section, the forced oscillations of bodies moving with small forward speeds will be studied up to second order of the wave slope (and the unsteady body motions) and first order of the forward speed. A vertical circular cylinder, a vertical axisymmetric body and a truncated vertical circular cylinder are considered.

A vertical circular cylinder with draft equal to water depth

A moving vertical circular cylinder with a small forward speed under forced surge motion is studied. The draft of the cylinder is equal to the water depth. The same cylinder without forward speed has been studied in Section 7.1.1.

Fig.8.11 and Fig.8.12 show respectively the comparison for the surge added mass and damping coefficients with that of Malenica et al. (1995) when a small Froude number $Fr=U/\sqrt{gR}$ =-0.05 is considered. U is the forward speed. R is the radius of the cylinder. The frequency of encounter ω_e was defined by Malenica et al. (1995) as $\omega_e=\omega_0-kU\cos\beta$, with ω_0 as the fundamental frequency of incoming wave, k as the wave number of the incident waves and β as the angle between the wave direction and the x-axis. The results shown in Fig.8.11 and Fig.8.12 correspond to β=0. Our numerical results agree well with that of Malenica et al. (1995). However, exactly the same results should not be expected. This is due to the fact that different formulations have been used. In the perturbation procedure of Malenica et al. (1995), both the wave slope parameter ε and the current parameter δ proportional to U are used. How δ is precisely defined does not matter since it is just a measurement of the smallness of the forward speed. The $O(\varepsilon)$ problem without current effects is firstly solved and then the $O(\varepsilon\delta)$ problem considering the wave-current interaction is solved based on the result of $O(\varepsilon)$ problem. This formulation is strictly accurate to $O(\varepsilon)$ and $O(\delta)$ with terms of $O(\varepsilon\delta)$ included. The formulation adopted in this article is also accurate to $O(\varepsilon)$ and $O(\delta)$. However, some higher order effects in δ have been included (see also e.g. Zhao & Faltinsen (1989a) and Büchmann (2000a)).

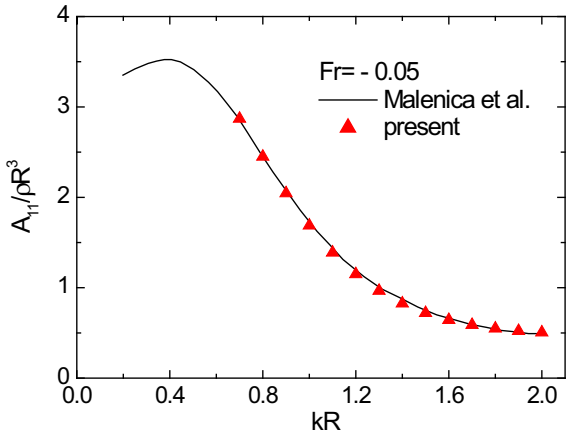

Fig.8.11. The non-dimensional surge added mass for a vertical circular cylinder compared with the analytical results by Malenica et al. (1995). The draft is equal to the water depth and the radius R. Fr=-0.05.

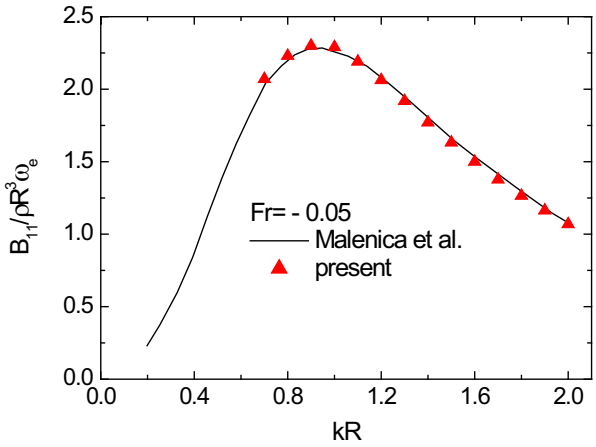

Fig.8.12. The non-dimensional surge damping coefficient for a vertical circular cylinder compared with the analytical results by Malenica et al. (1995). The draft is equal to the water depth h and the radius *R*. *Fr*=-0.05.

To the author's knowledge, no study on the second-order radiation problem considering the forward speed effect has been reported in the literature. This may be due to fact that the second-order body boundary condition in the traditional method using an inertial system (see Section 2.4) requires higher-order derivatives of both the steady velocity potential and the first-order solutions. However, the new method presented in Chapter 5 based on a body-fixed coordinate system in the near-field is free of derivatives on the right-hand side of the body boundary conditions.

In order to verify this new method, we studied the forced surge of the vertical circular cylinder up to second order. A small constant forward speed is considered. The forced surge motion is defined as

$$\xi_1^{(1)} = Rm(t)\cdot\xi_{1a}\sin(\omega t),\ \xi_1^{(2)} = 0\,. \tag{8.2}$$

Here Rm(t) is a ramp function used to allow for the gentle start of the flow. ω is the circular frequency of the oscillation. ξ_{1a} is the amplitude of the surge motion. $\xi_{1a} = 0.05R$ is used in the calculations.

Both the traditional method and the new method are used for cross verification. The traditional method we used here for a forced oscillating body may be considered as a generalization of the work by Skourup et al. (2000), who only studied the second-order diffraction problem with a weak current effect.

For a vertical circular cylinder with the draft equal to the water depth, the solution for the double-body steady flow is analytically known (e.g. Skourup et al., 2000). In this study, the analytical expressions for the steady velocity potential (see Eq.(8.1)) and its derivatives are used in the numerical calculations. The amplitude of the mean drift force and the amplitude of the sum-frequency force are given in Fig.8.13 for different non-dimensional wave numbers. The wave number k in Fig.8.13 is defined as the real root of $\omega^2 = kg\tanh(kh)$, with g as the gravity acceleration and h the water depth. Consistent results have been obtained by the traditional method and the new method.

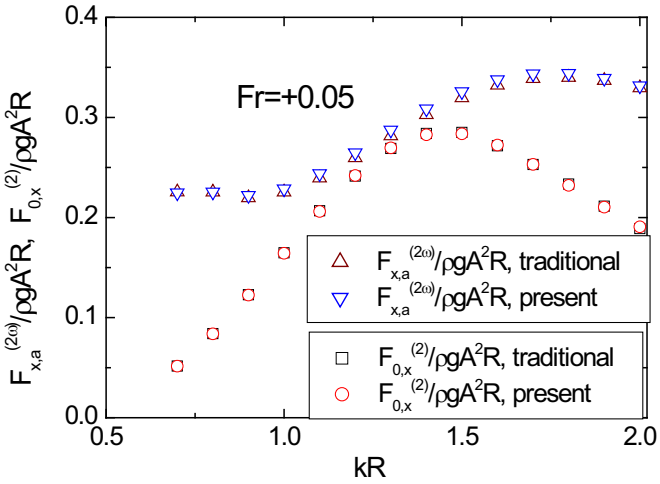

Fig.8.13. The mean drift force and the amplitude of the sum-frequency force on a vertical circular cylinder versus *kR*. The draft is equal to the water depth h and the radius *R*. *Fr*=0.05. The surge amplitude is 0.05*R*.

One should note that for the forced surging of the vertical circular cylinder without the presence of incident waves, if the Froude number is zero, i.e. no forward speed or current speed, the total second-order wave field is symmetric. So the second-order velocity potential gives no contribution to the second-order horizontal forces on the cylinder. Furthermore, the quadratic terms of the first-order solutions in the calculation of the second-order forces are also symmetric about the oyz-plane (see Eq.(2.110) and Eq.(2.117)), which result in zero quadratic forces on the cylinder. Therefore, both the sum-frequency and the mean-drift horizontal forces on the forced surging vertical circular cylinder with zero Froude number are zero. The presence of the forward speed makes the flow asymmetric and the resulting second-order horizontal forces are not zero. The importance of the forward speed effect on the second-order horizontal forces is evident from Fig.8.13.

A vertical axisymmetric body without sharp corners

The forced pitching oscillation of an axisymmetric body without sharp corners moving with small constant forward speed is studied. For this case, both the traditional method based on a formulation in the inertial coordinate system and the new method (Chapter 5) with body-fixed coordinate system near the body are applicable.

The draft of the axisymmetric body considered is 0.5R with R as the maximum radius of the axisymmetric body. The water depth is infinite. The dimensions of a cross-section of the body in oxz-plane are shown in Fig.7.31. The center of gravity (COG) is located at (0, 0, -0.25R) with R=1.0. The pitch motion with respect to the COG of the body is defined as

$$\alpha_{5,COG}^{(1)} = Rm(t)\cdot\alpha_{5a}\sin(\omega t),\quad \alpha_{5,COG}^{(2)} = 0 \tag{8.3}$$

where $Rm(t)$ is the ramp function used to allow for the gentle start of the flow. ω is the circular frequency of the oscillations. α_{5a} is the amplitude pitch motion. In the present study, we have used $\alpha_{5a} = 0.05$ radians. One should note that with our choice of the position of COG, the pure pitching about COG represents the coupled surge and pitch motion if the motions are defined with respect to

the origin of the reference frame, which is the case when we are formulating the free surface conditions and the body boundary conditions in Section 2.4 and Section 2.6 in Chapter 2.

We use both the traditional method based on a formulation in the inertial coordinate system and the new method (Chapter 5) with body-fixed coordinate system to study this problem up to second order of the wave slope and to first order of the forward speed. We are not able to find an analytical solution for the steady double-body flow for this case. Therefore, a numerical solution will be used.

In the traditional formulation in the inertial frame, the second-order body boundary condition contains second-order and third-order derivatives of the steady velocity potential. It is not straightforward to apply a Stokes-like theorem to the third-order derivatives as it was done for the second-order derivatives. In this study, the steady velocity potential and its derivatives in the traditional formulation are calculated by using a desingularized BEM, which can only be used for cases without sharp corners. The desingularized BEM offsets the singularities out of the fluid domain and thus avoids the singular behavior of the Green functions on the body surface when the collocation points coincide with the singularities. An optimal distance was obtained by applying the desingularized BEM to a sphere moving in infinite fluid. See Section 4.6. The experience is then applied in the case of the axisymmetric body. The first-order and second-order derivatives of the unsteady velocity potentials are calculated with the assistance of the cubic shape functions of the higher-order boundary elements. The details have been given in Section 4.6.

In the calculations based on the domain decomposition method, both the steady velocity potential $\phi^{(0)}$ and the unsteady velocity potentials $\phi^{(k)}$ (k=1, 2) are solved by using the HOBEM. Because we use a double-body flow as the basis flow, it is sufficient to only distribute singularities on the body surface and its image about oxy-plane when solving the $\phi^{(0)}$-problem. The domain decomposition is switched off for $\phi^{(0)}$-problem. $\phi^{(0)}$ and its derivatives of $\phi^{(0)}$ on both the free surface and control surface are obtained directly by the boundary integral equation. The first-order derivatives of $\phi^{(0)}$ on the body and the derivatives of $\phi^{(k)}$ (k=1, 2) on all the boundary surfaces are calculated with the help of the cubic shape functions. Note that the double-body flow used in the domain decomposition based method has different interpretation with the classical double-body flow with a formulation in the inertial coordinate system. See the discussion in Appendix A.

The comparison of the wave forces calculated by the domain decomposition based method and the traditional method is made in Fig.8.14 - Fig.8.18. In order to make the comparison possible, we have defined the forces and moments with respect to the axes of the body-fixed coordinate system oxyz. The moments are with respect to COG. Observed on an inertial coordinate system, these axes change orientations if the body has angular motions. Fig.8.14 and Fig.8.15 show the time history of the first-order force in x- and z-directions, respectively. kR=1.2 is used in the calculations for the time histories. Due to the symmetry of the body, the first-order vertical force will be zero if the Froude number is zero. However, with the presence of the forward speed, the resulting wave field will not be anti-symmetric about the oyz-plane and thus the linear vertical force is not zero, as shown in Fig.8.15. The time history of the first-order pitch moment about an axis through COG is shown in Fig.8.16. The time history of the total second-order force in z-direction is presented in Fig.8.17 for the same non-dimensional wave number kR=1.2. Fig.8.18 shows the amplitude of the non-dimensional sum-frequency force for different non-dimensional wave numbers. Consistent results have been obtained by the traditional method and the new method based on domain decomposition.

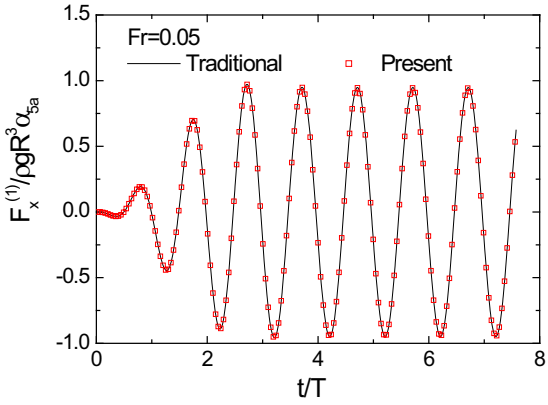

Fig.8.14. Time history of the first-order wave force in the x-direction on the axisymmetric body defined in Fig.7.31 under forced pitching about COG. Fr=$U/\sqrt{gR}$ =0.05, kR=1.2. The water depth is infinite.

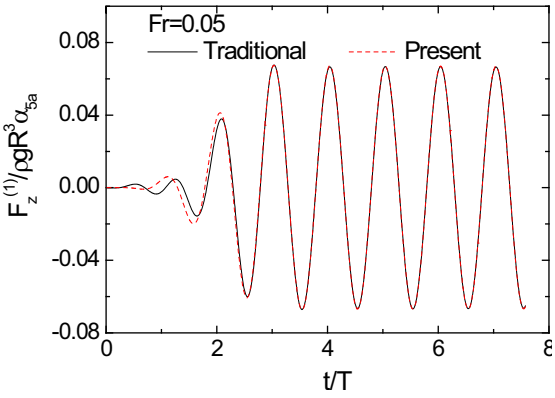

Fig.8.15. Time history of the first-order wave force in the z-direction on the axisymmetric body defined in Fig.7.31 under forced pitching about COG. Fr=$U/\sqrt{gR}$ =0.05, kR=1.2. The water depth is infinite.

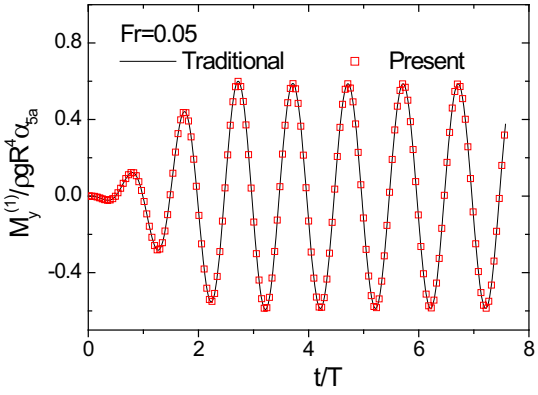

Fig.8.16. Time history of the first-order pitch moment about an axis through COG for the axisymmetric body defined in Fig.7.31 under forced pitching about COG. Fr=$U/\sqrt{gR}$ =0.05, kR=1.2. The water depth is infinite.

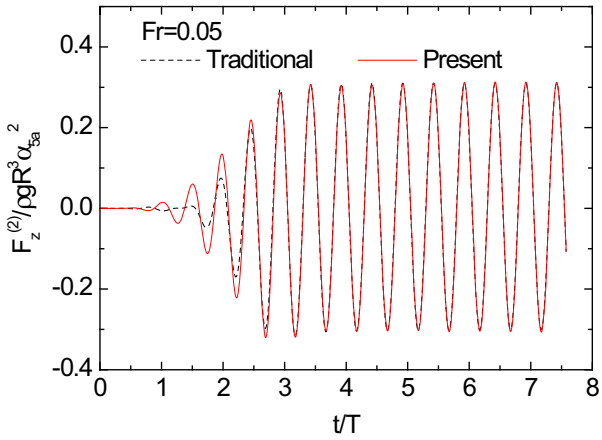

Fig.8.17. Time history of the second-order wave force in z-direction on the axisymmetric body defined in Fig.7.31 under forced pitching about COG. Fr=$U/\sqrt{gR}$ =0.05, kR=1.2. The water depth is infinite.

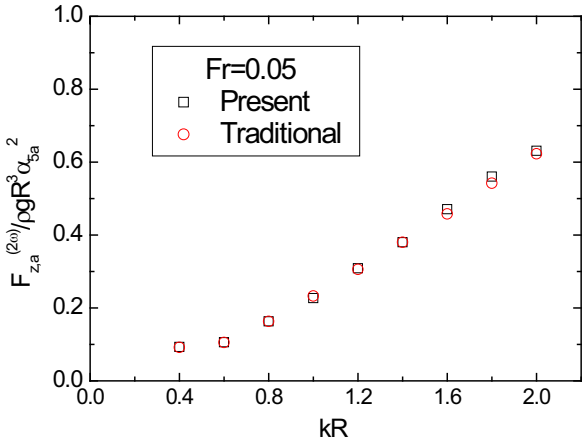

Fig.8.18. Amplitude of the sum-frequency force in z-direction versus kR for an axisymmetric body defined in Fig.7.31 under forced pitch motion about COG. F_r=$U/\sqrt{gR}$ =0.05. The water depth is infinite.

A truncated vertical circular cylinder with sharp corner

A truncated vertical circular cylinder with sharp corner under forced surging and heaving has also been studied. The surge and heave motions are defined respectively as

$$\xi_1^{(1)} = Rm(t)\cdot\xi_{1a}\sin(\omega t),\quad \xi_1^{(2)} = 0, \tag{8.4}$$

$$\xi_3^{(1)} = Rm(t)\cdot\xi_{3a}\sin(\omega t),\quad \xi_3^{(2)} = 0, \tag{8.5}$$

where $Rm(t)$ is a ramp function. ω is the circular frequency of the oscillations. ξ_{1a} and ξ_{3a} are the amplitude of surge and heave, respectively.

No incident wave is considered. The draft of the cylinder d=0.5R with R as the radius of the cylinder.

The water depth is infinite. A small constant forward speed with Froude number Fr=$U/\sqrt{gR}$ =0.05 is considered. U is the forward speed. R is the radius of the cylinder. g is the acceleration of gravity.

The domain decomposition based method using body-fixed coordinate system in the inner domain (see Chapter 5) is used. For this case, it is not suggested to use the formulation in the inertial coordinate system, because the resulting boundary integral equations (BIEs) are not integrable. Even though the domain decomposition based method gives BIEs which are integrable for the sharp corner cases, it is still difficult for the near-field approach to get convergent results for the second-order forces and moments. This is associated with the slow convergence rate of the integral of the velocity square terms. By near-field approach, it is meant the direct integration of the pressure on the body surface.

In order to improve the convergence rate, we will propose alternative formulas for the forces and moments contributed by the velocity square terms. Details are provided in Appendix F. These formulas are based on an equality (Eq.(F.3)) given by Newman (1977) and another similar equality (Eq.(F.7)). As a consequence, the integral of velocity square term on the body surface is transferred to the sum of two groups of integrals. See Eq.(F.5), Eq.(F.6), Eq.(F.8) and Eq.(F.9). The first group contains integrals on body surface with integrands whose singularities are weaker than that of the velocity square. The second group consists of regular integrals on the inner free surface and the control surface. Numerical tests show that the alternative formulas Eq.(F.5), Eq.(F.6), Eq.(F.8) and Eq.(F.9) give much faster convergence rate than the original ones, i.e. (F.1) and (F.2).

Fig.8.19 shows the amplitudes of the first-order forces in x- and z-directions on the truncated vertical circular cylinder under forced heaving. The results with Fr=0.05 are presented together with that of zero Froude number. The first-order horizontal force is zero when the forward speed is zero, which is expected due to the symmetry properties about oyz-plane. The first-order vertical force becomes nonzero because the presence of the forward speed makes the flow not anti-symmetric.

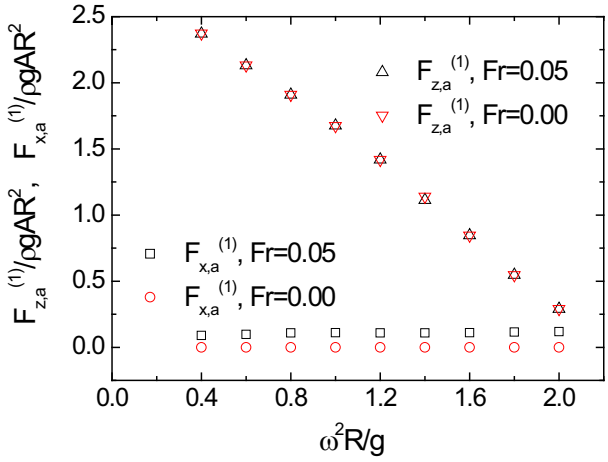

Fig.8.19. First-order forces in x- and z-directions of a forced heaving truncated vertical circular cylinder with draft d=R. R is the radius. Infinite water depth is assumed. Fr=$U/\sqrt{gR}$ =0.0 and Fr=0.05 are considered.

It is also noticed in Fig.8.19 that the small forward speed considered has negligible influence on the

amplitude of the linear vertical forces of the heaving truncated cylinder. Numerical results also show that the small forward speed has very small effect on the phase of the linear vertical force on the heaving truncated vertical circular cylinder. Fig.8.20 shows the time histories of the linear vertical force on a forced heaving cylinder with $\omega^2 R/g$ =1.0 for Fr=0.0 and Fr=0.05. ω is the frequency of forced oscillations. g is the gravitational acceleration.

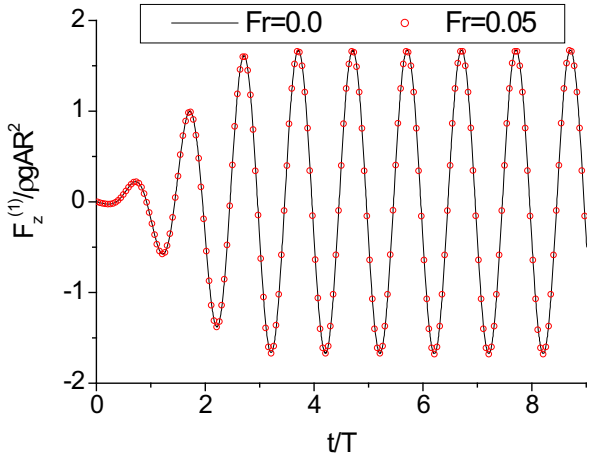

Fig.8.20. Time histories of linear vertical force of a forced heaving truncated vertical circular cylinder with draft d=R and $\omega^2 R/g$ =1.0. R is the radius. Infinite water depth is assumed. Fr=$U/\sqrt{gR}$ =0.0 and Fr=0.05 are considered. $T=2\pi/\omega$. ω is the frequency of forced heaving.

The negligible forward speed effect on the linear vertical force can be explained from the boundary conditions by decomposing the flow as the superposition of a symmetric part and an anti-symmetric part. For the forced heaving of a body symmetric about oyz-plane in otherwise calm water, the forcing terms in the first-order free surface conditions (2.88) and (2.89) can be simplified respectively as:

$$f_1^{(1)} = \eta^{(1)}\phi_{zz}^{(0)} - (\phi_x^{(0)}\eta_x^{(1)} + \phi_y^{(0)}\eta_y^{(1)}) + U\eta_x^{(1)}, \tag{8.6}$$

$$f_2^{(1)} = -\nabla\phi^{(0)}\cdot\nabla\phi^{(1)} + U\phi_x^{(1)}. \tag{8.7}$$

Let us further express the first-order solutions by series expansion in terms of a small parameter δ related to the Froude number, i.e.

$$\eta^{(1)} = \eta_0^{(1)} + \delta\eta_1^{(1)} + \delta^2\eta_2^{(1)} + \cdots \tag{8.8}$$

$$\phi^{(1)} = \phi_0^{(1)} + \delta\phi_1^{(1)} + \delta^2\phi_2^{(1)} + \cdots \tag{8.9}$$

Putting Eq.(8.8) and Eq.(8.9) into Eq.(8.6) and Eq.(8.7) and collecting consistent terms at the same order with respect to δ, we have that

$$f_1^{(1)} = \underbrace{\eta^{(1)}\frac{\partial^2\phi^{(0)}}{\partial z^2} - \left(\frac{\partial\phi^{(0)}}{\partial x}\frac{\partial\eta_0^{(1)}}{\partial x} + \frac{\partial\phi^{(0)}}{\partial y}\frac{\partial\eta_0^{(1)}}{\partial y}\right) + U\frac{\partial\eta_0^{(1)}}{\partial x}}_{O(\delta^1)} + O(\delta^2) \tag{8.10}$$

$$f_2^{(1)} = \underbrace{-\nabla\phi^{(0)}\cdot\nabla\phi_0^{(1)} + U\frac{\partial\phi_0^{(1)}}{\partial x}}_{O(\delta^1)} + O(\delta^2) \tag{8.11}$$

The $O(\delta^0)$ approximation solution of $\eta^{(1)}$ and $\phi^{(1)}$, i.e. $\eta_0^{(1)}$ and $\phi_0^{(1)}$, satisfy the homogenous free surface conditions. The body boundary condition for $\phi_0^{(1)}$ is symmetric about oyz-plane, i.e.

$$\frac{\partial\phi_0^{(1)}}{\partial n} = n_3'\dot{\xi}_3^{(1)} \qquad \text{on SB.} \tag{8.12}$$

Here n_3' is the z-component of the normal vector on body surface. Therefore, the flow represented by $\eta_0^{(1)}$ and $\phi_0^{(1)}$ is symmetric about oyz-plane. The $O(\delta^1)$ approximation solution of $\eta^{(1)}$ and $\phi^{(1)}$, i.e. $\eta_1^{(1)}$ and $\phi_1^{(1)}$, satisfy the inhomogeneous free surface conditions with forcing terms given in Eq.(8.10) and Eq.(8.11). $\phi_1^{(1)}$ satisfies zero-Neumann body boundary condition. Because the basis flow $\phi^{(0)}$ is anti-symmetric and the flow represented by $\eta_0^{(1)}$ and $\phi_0^{(1)}$ is symmetric about oyz-plane, it is obvious that the solutions for $\eta_1^{(1)}$ and $\phi_1^{(1)}$ are anti-symmetric. That means the $O(\delta^1)$ solution does not contribute to the first-order vertical force on the heaving truncated circular cylinder. Therefore, the difference between the results of the linear vertical forces with and without forward speed is of $O(\delta^2)$ and is negligible if the forward considered is small. Similar analysis can be made for the second-order problem. And the same conclusion holds. That is, if the geometry and the forced unsteady motions of a body with steady forward speed parallel to x-axis are symmetric about oyz-plane, the effect of a small forward speed on the second-order vertical force is of $O(\delta^2)$. δ is a measurement of the smallness of the forward speed. This is also confirmed by our second-order numerical results. Fig.8.21 shows the amplitudes of the second-order vertical forces. The results for Fr=0.0 and Fr=0.05 are almost the same. Presented in Fig.8.22 are the time histories of the second-order vertical forces of the forced heaving truncated cylinder with Fr=0.0 and Fr=0.05. It is immediately obvious to us that the small forward speed has negligible effect on the second-order vertical force on the forced heaving truncated circular cylinder.

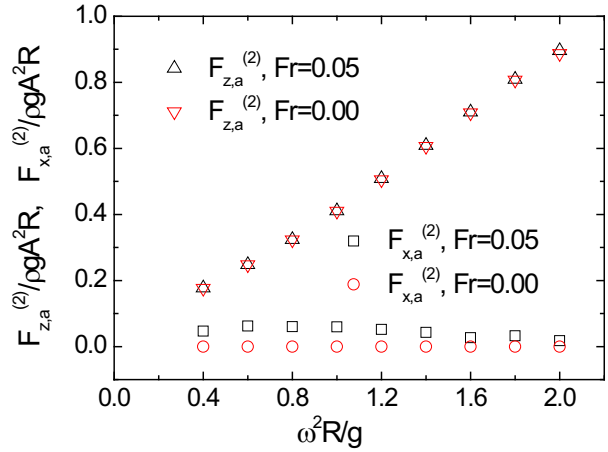

Fig.8.21. Second-order force in z-directions of a forced heaving truncated vertical circular cylinder with draft d=R. R is the radius. Infinite water depth is assumed. Fr=$U/\sqrt{gR}$ =0.0 and Fr=0.05 are considered.

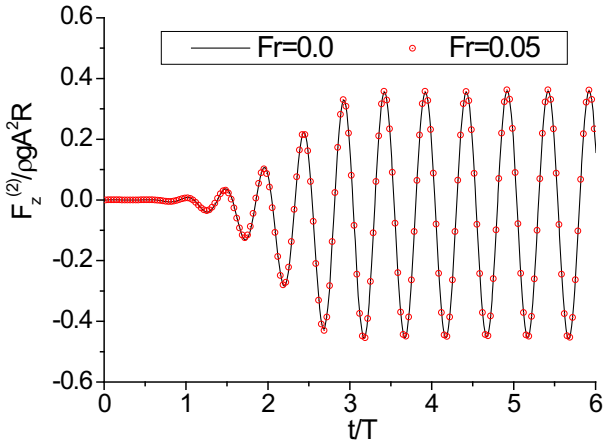

Fig.8.22. Time histories of second-order vertical force of a forced heaving truncated vertical circular cylinder with draft d=R and $\omega^2 R/g$ =1.0. R is the radius. Infinite water depth is assumed. Fr=$U/\sqrt{gR}$ =0.0 and Fr=0.05 are considered. $T=2\pi/\omega$. ω is the frequency of forced heaving.

By performing a similar analysis to Eq.(8.6) – Eq.(8.12), one can also show that for a forced surging body with oyz-plane as the symmetric plane, the forward speed effect on the first-order horizontal force and the second-order vertical force is of $O(\delta^2)$. Due to the presence of the forward speed, the wave field generated by the body is not anti-symmetric anymore and consequently the first-order and second-order horizontal forces become nonzero. These have been confirmed by our numerical results for the truncated vertical circular cylinder shown in Fig.8.23 – Fig.8.25. In Fig.8.23, the amplitudes of the first-order forces in x-direction and z-direction are presented for different wave numbers. Comparisons are made between Fr=0.0 and Fr=0.05. Fig.8.24 shows the comparison for the second-order vertical force of the forced surging truncated cylinder. The time histories of the second-order vertical forces on the truncated vertical circular cylinder (kR=1.0, d=R) for Fr=0.0 and Fr=0.05 are shown in Fig.8.25.

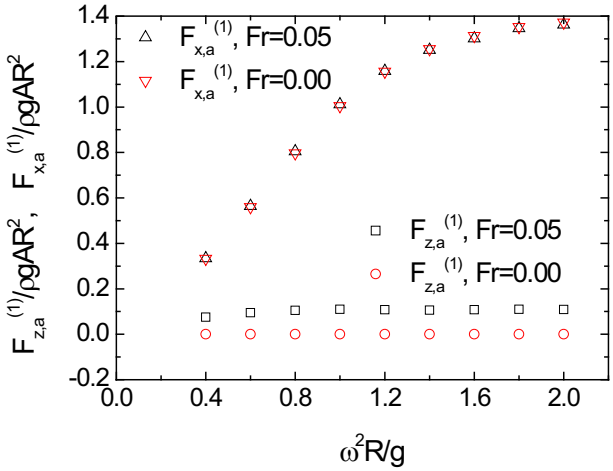

Fig.8.23. First-order forces in x- and z-directions of a forced surging truncated vertical circular cylinder with draft d=R. R is the radius. Infinite water depth is assumed. Fr=$U/\sqrt{gR}$ =0.0 and Fr=0.05 are considered.

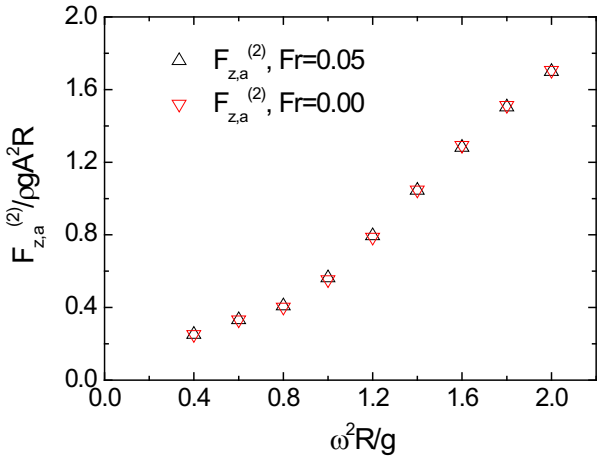

Fig.8.24. Second-order forces z-directions of a forced surging truncated vertical circular cylinder with draft d=R. R is the radius. Infinite water depth is assumed. Fr=$U/\sqrt{gR}$ =0.0 and Fr=0.05 are considered.

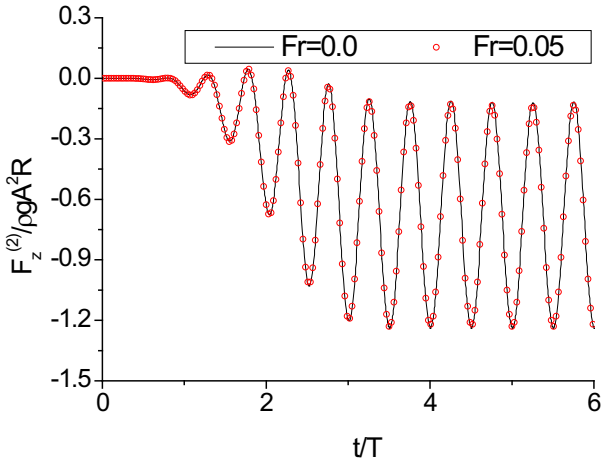

Fig.8.25. Time histories of second-order vertical force of a forced surging truncated vertical circular cylinder with draft d=R and $\omega^2 R/g$ =1.0. R is the radius. Infinite water depth is assumed. Fr=$U/\sqrt{gR}$ =0.0 and Fr=0.05 are considered. $T=2\pi/\omega$. ω is the frequency of forced heaving.

8.3 Freely-floating body in regular waves

In the previous sections of this chapter, we have studied the nonlinear wave diffraction and forced oscillation problems by considering a small constant forward speed. In this section, the bodies studied will be free to response to the incident waves.

A vertical circular cylinder studied by Malenica et al. (1995)

In order to demonstrate the robustness and accuracy of the numerical method, we firstly consider a vertical circular cylinder with d=h=R in waves. Here h is the water depth. d and R are the draft and radius of the cylinder, respectively. A small forward speed will be considered. Only the surge motion is allowed in the numerical studies, with the other five degrees of freedom restrained.

The linear solution of this problem was obtained by Malenica et al. (1995) by a semi-analytical approach in the frequency domain. Difficulties arise in order for the time-domain method to get consistent results with the frequency-domain approaches. One of the difficulties is the existence of the homogeneous solution of the motion equations. Due to the damping effects, the homogeneous solution will die out with time. However, in the case we are considering, because there is no restoring in the horizontal motion, the cylinder may experience drifting away from its original position due to the transient effects. The frequency-domain solution contains only the steady-state inhomogeneous solutions. One may use the so-called shooting technique to eliminate the effect of homogeneous solution. That is, one chooses a special phase between the incident wave and the body motions in the initial conditions so that the homogeneous solution of the body motion is zero. In the present study, a ramp function is applied over a long period for the gentle start of the flow. This is also expected to minimize the influence of the homogeneous solution of the motion equations. In the present study, a sinusoidal ramp function is applied in the first 6 linear wave periods.

The surge motion amplitudes for different Froude numbers Fr=$U/\sqrt{gR}$ =0.05, 0.0 and -0.05 are shown in Fig.8.26. Comparisons are made with Malenica et al.'s (1995) semi-analytical results in the frequency domain. U is the forward speed in x-direction. g is gravitational acceleration. The incident wave propagates in positive x-direction. The 'present' results shown in the Fig.8.26 were obtained by Fourier analysis of the time history of the surge motion of the cylinder. The present time-domain numerical results agree well with Malenica et al.'s (1995) results. The domain decomposition based method is adopted in the numerical analysis. A cylindrical surface is used as the control surface. The body motion equation is solved based on the method presented in Section 4.4. The key point of the method is that one has to move all the terms explicitly depending on the accelerations of the body to the left-hand side of the motion equations. Numerical tests show that this scheme is very stable. For a vertical circular cylinder free to surge in waves, the scheme even works when the mass of the cylinder is set to be zero. Zero mass may not be physical for the typical marine structures. But it is relevant to the dynamics of the air bubbles in the fluid. The indication is that the scheme may work even well for cases where the added mass terms are much larger than the corresponding mass terms, e.g. water entry and exit of high-speed objects.

Fig.8.27 shows the time history of the surge motion with kR=1.0 and Fr=0.05. k is the incident wave number. It is seen that, as the response to the incident waves, the cylinder oscillates about its initial position, i.e. $\xi_1^{(1)}(t=0)=0$. This also demonstrates that using the ramp function was able to minimize the effect of the homogeneous solutions of the first-order body motion equations.

The time history of the second-order surge motion of a cylinder with kR=1.0 and Fr=-0.05 is shown in Fig.8.28a. It is seen that the cylinder is drifting away from its initial position at t=0. This can be partly understood from the surge velocity in Fig.8.28b and surge acceleration in Fig.8.28c. Due to the mean drift force and the sum-frequency forces effects, the second-order surge acceleration contains a positive mean value as well as an unsteady contribution with sum-frequency. Therefore, the surge

velocity will on one hand oscillate with the sum-frequency, and on the other hand increase linearly with time. The consequence is the drifting of the cylinder. In the reality of marine structures, this would not happen because of the presence of mooring system or dynamic positioning (DP) system. However, for a moored ship in irregular waves, the difference-frequency effects may cause large second-order horizontal motions of the ship, i.e. slow-drift motions, which may be of the same order of the first-order motions. In this case, the assumption behind Stokes expansion that higher-order terms should be much smaller than the lower-order quantities is violated. Actually, the large slow-drift motions may give feedbacks to the first-order solution and thus modify the second-order results. However, this is not the end of the world for the second-order theory. We will in Chapter 9 briefly discuss how to extend the domain decomposition based method in Chapter 5 to handle this problem by considering all the horizontal motions as O(1) instead of O(ε) or O(ε^2).

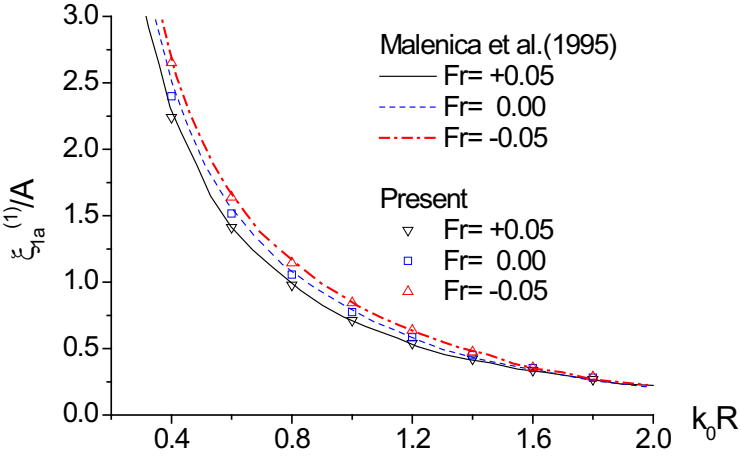

Fig.8.26. First-order surge motion amplitudes of a vertical circular cylinder with d=h=R. The cylinder is free to respond only in surge direction. Different Froude numbers Fr=$U/\sqrt{gR}$ =0.05, 0.0 and -0.05 are studied. U is the forward speed in X-direction. The incident wave propagates in positive X-direction. R and d are the radius and draft of the cylinder, respectively. h is the water depth. g is the gravitational acceleration. k is the incident wave number. A is the linear wave amplitude.

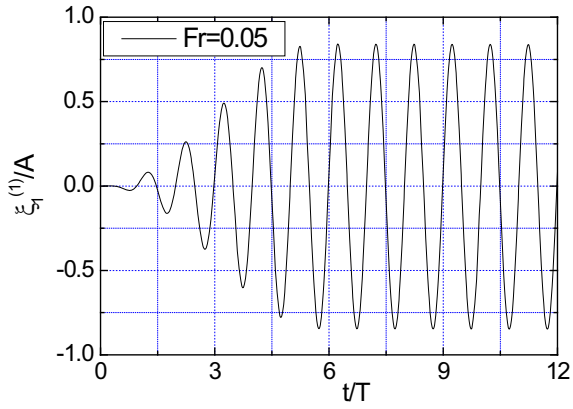

Fig.8.27. Time history of first-order surge motion of a vertical circular cylinder with d=h=R. Fr=$U/\sqrt{gR}$ =0.05. The notations are the same as that in Fig.8.26. kR=1.0.

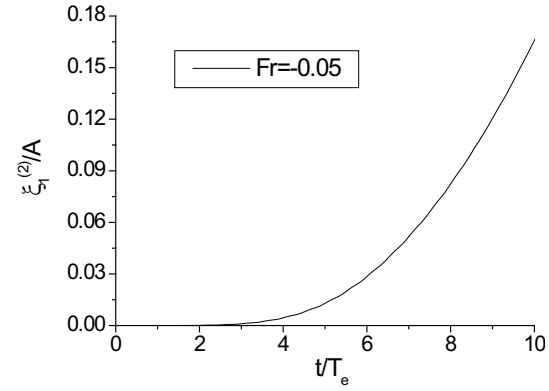

(a)

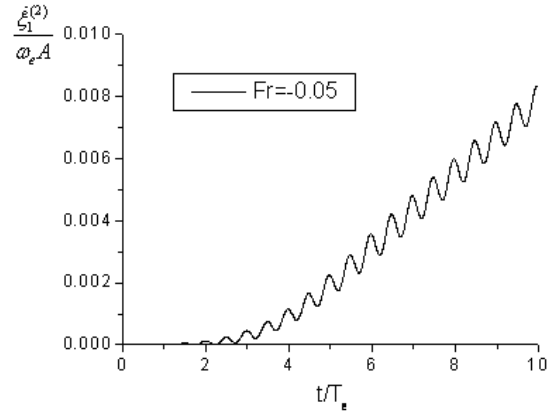

(b)

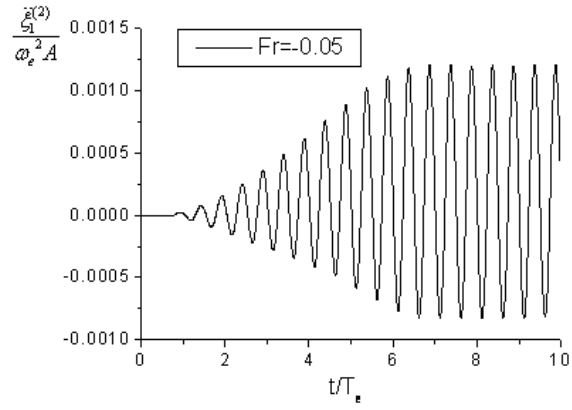

(c)

Fig.8.28. Time histories of the second-order surge response of a vertical circular cylinder with d=h=R. kR=1.0. Fr=$U/\sqrt{\mathrm{gR}}$ =-0.05. $T_e = 2\pi/\omega_e$. ω_e is the frequency of encounter. (a) Surge motion. (b) Surge velocity. (c) Surge acceleration.

Truncated vertical circular cylinder studied by Zhao & Faltinsen (1989b)

Zhao & Faltinsen (1989b) studied a truncated vertical circular cylinder that is free to oscillate in surge and heave and restrained from oscillating in pitch. A constant panel method (CPM) in the frequency domain was adopted. For zero forward speed case, they obtained the mean wave forces by using both the near-field approach based on direct pressure integration on the body surface and the far-field approach based on momentum relationship. A large discrepancy was found between these methods, which Zhao & Faltinen (1989b) attributed to the effect of CPM applied to the edge between the bottom and cylinder surface. In theory, the far-field result is much less sensitive to the meshing details on the body surface and is in general more reliable. Liu et al. (1993) computed the same problem employing a frequency-domain HOBEM based on the near-field approach which resulted in uniform convergence giving an unique result. However, Liu et al.'s (1993) results confirmed neither the far-field result nor the near-field results of Zhao & Faltinsen (1989b). In fact, their results were in between the two results of Zhao & Faltinsen (1989b). See also the text book of Kim (2008, pp.369-370).

The same problem is revisited in this thesis by using the domain decomposition based method proposed in Chapter 5. The force is obtained by the pressure integration on the body surface, i.e. the near-field approach, except that the quadratic force due to the velocity square is re-formulated based on a formula given in Newman (1977). See Appendix F for details. This re-formulation improves very much the convergence rate of the quadratic force. The cylinder has a draft equal to the radius, i.e. d=R. The water depth is 1.2 times the linear incident wave length.

The time-domain numerical results almost perfectly confirmed the far-field results of Zhao & Faltinsen (1989b). See the comparison in Fig.8.29. In the numerical calculations, uniform meshes are used on the cylindrical surface of the cylinder. 6 cubic elements are used in the vertical direction. 30 elements per linear wave length are distributed azimuthally. The elements on the bottom of the cylinder in the vicinity of the corner are of the same size of the elements on the cylinder wall. The mean wave forces shown in Fig.8.29 are obtained by time-averaging the quadratic forces acting on the body, without solving the second-order problem.

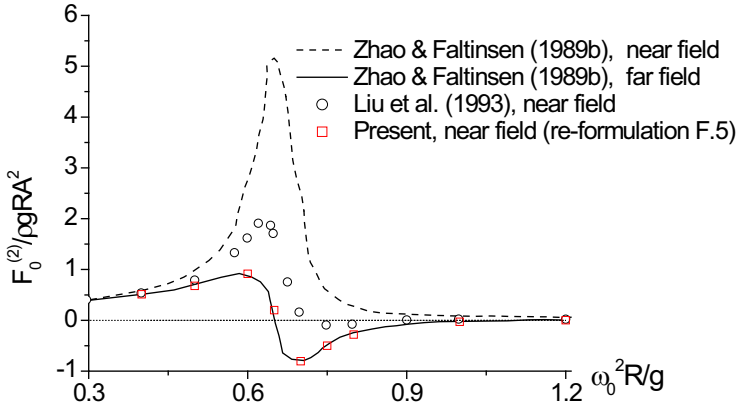

Fig.8.29. The numerical results of vertical mean wave force. The quadratic part of the second-order force is calculated by the re-formulation in Eq.(F.5). Comparisons with the near-field and far-field results of Zhao & Fatltinsen (1989b) are made. ω_0 is the frequency of the incident wave. R is the radius of the cylinder. g is gravitational acceleration.

The influence of the small forward speed effect on the horizontal and vertical mean wave forces acting on the truncated vertical circular cylinder is also investigated. The cylinder is free to oscillate in surge and heave and restrained from oscillating in pitch. Fig.8.30 shows the comparison for the horizontal mean drift forces for Fr=-0.05 and Fr=0.05. The vertical mean forces for Fr=-0.05 and Fr=0.05 are presented in Fig.8.31. The far-field results by Zhao & Faltinsen (1989b) for Fr=0.0 are also plotted in the figure. It is seen that the small forward speeds have significant effect on both the horizontal and vertical mean forces, especially in the resonant region of the heave motions.

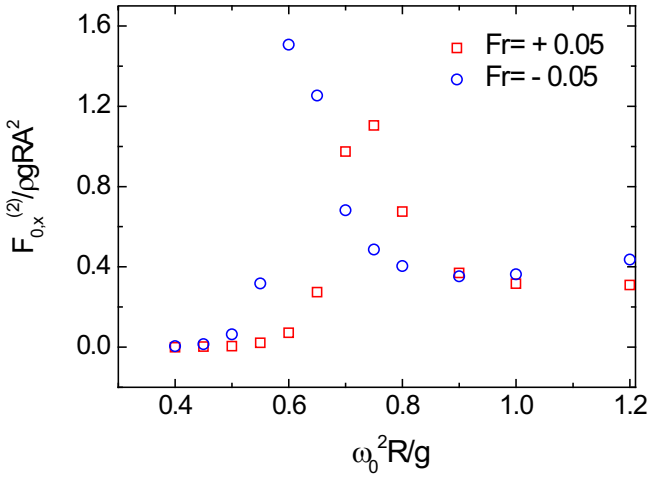

Fig.8.30. Comparison of the horizontal mean drift force for Fr=-0.05 and Fr=0.05. ω_0 is the fundamental frequency of the incident wave.

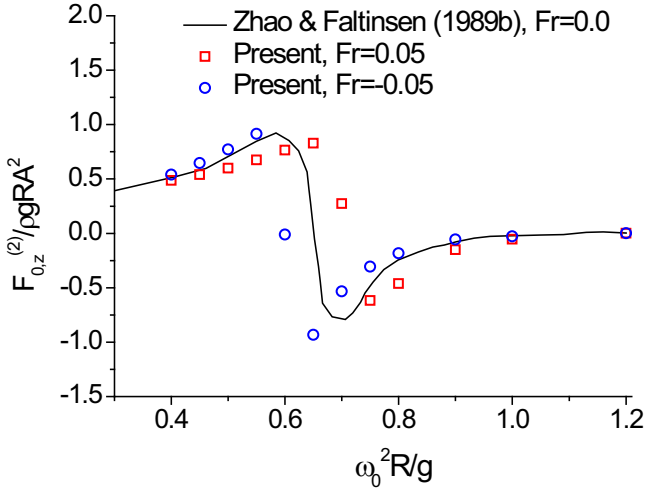

Fig.8.31. Comparison of the vertical mean force for Fr=-0.05 and Fr=0.05. The far-field results by Zhao & Faltinsen (1989b) for Fr=0.0 are also plotted in the figure. ω_0 is the fundamental frequency of the incident wave.

CHAPTER 9

Summary and Future Perspectives

9.1 Summary

A two-dimensional Quadratic Boundary Element Method (QBEM) and a three-dimensional cubic Higher-order Boundary Element Method (HOBEM) are developed to study respectively the two-dimensional and three-dimensional weakly-nonlinear wave-body interactions with/without forward speed within potential flow theory of an incompressible liquid. The basis of the 2D QBEM and 3D cubic HOBEM in the time domain are given. The necessary numerical issues are addressed.

A direct method for the evaluation of the Cauchy Principal Value (CPV) integral of the influence coefficients is proposed, which is based on a triangular-polar coordinate transformation. The numerical schemes for the time marching of the free-surface conditions are presented. In the 2D time-domain analysis, the fourth-order Runge-Kutta method is used, while the fourth-order Adams-Bashforth-Moulton method is adopted in the 3D analysis. A numerical damping zone is used to enforce the radiation conditions for the scattered waves. The mechanism of the combination of the piston wave absorber and the numerical damping zone is explained in the two-dimensional numerical wave tank.

In the 3D analysis, suggestions on the selection of the types of the grid on the free surface are given. In order to investigate to what extent the accelerated methods, e.g. the Fast Multipole Method (FMM), can speed up the calculation and to see if the accelerated method is applicable to the weakly-nonlinear wave-body analysis based on perturbation scheme, a numerical module based on the FMM has been developed to accelerate the cubic HOBEM. Guidelines on how to select a proper matrix solver for a particular 3D problem are provided.

Different methods for the direct calculation of the higher-order derivatives on the boundaries, e.g. the body surface and free surface, are given. In the 2D studies, a curve-fitting technique based on the arc-length is used. In the 3D problems, the first-order and second-order derivatives on the boundaries can be obtained accurately with the assistance of the cubic shape functions of the cubic HOBEM. For smooth and simple geometries, the desingularied BEM (DBEM) or the raised panel method (RPM)

can also be used. However, the DBEM and RPM cannot be used for bodies with sharp corners.

In the time-domain wave-body analysis without forward speed, no short wave instabilities were observed. The short wave instabilities occur in the cases with forward speed. The reason for the instability has not been completely understood. The low-pass filter is applied to the wave elevation on the free surface to suppress the short wave instabilities. Another possible numerical instability reported in the literature is associated with the time integration of the body motion equations. The motion equations are rewritten by moving all the terms explicitly dependent on the rigid-body accelerations to the left-hand sides. This results in a stable form of the rigid-body motion equation system.

A perturbation scheme is used in the studies. Stokes expansion of the velocity potential, wave elevation, translatory and rotational body motions are adopted. The formulations of the weakly-nonlinear Boundary Value Problem (BVP) in both the inertial coordinate system and the body-fixed reference frame are presented. The consequence of the perturbation scheme is that the computational domain does not change with time.

The body boundary conditions formulated in the inertial coordinate system contains higher-order derivatives, which are difficult to calculate for bodies with high surface-curvature. Because of the higher-order derivatives in the body boundary conditions, the resulting Boundary Integral Equations (BIEs) are not integrable for bodies with sharp corners. A new method based on domain decomposition is proposed to avoid derivatives on the right-hand side of the body boundary conditions. In order to demonstrate that the formulations in the body-fixed coordinate system and the inertial coordinate system shall give consistent results, we have derived the analytical (semi-analytical) second-order results for a two simple cases, i.e. the forced oscillation of a circle in infinite fluid and the forced oscillation of a 2D rectangular tank with a free surface. The analytical (semi-analytical) results obtained in the body-fixed coordinate system and the inertial coordinate system are consistent. The consistency of the formulations in the body-fixed coordinate system and the inertial frame has later been confirmed in our three-dimensional time-domain studies for a smooth body without sharp corners.

Another difficulty associated with wave-body interaction analysis of the sharp corner, which is numerical, is how to get convergent result of the quadratic forces/moments. A re-formulation of the integral of the quadratic forces/moments based on a formula (see Appendix F) given in Newman (1977) and another similar equality is proposed to achieve faster convergence of the second-order forces on bodies with sharp corners.

The numerical methods developed during this study have been applied to several 2D and 3D weakly nonlinear wave-body interaction problems with/without a small forward speed (or current) effect. Comparisons between the present numerical results and the other existing theoretical and experimental results showed very good agreement.

Two-dimensional studies

The accuracy of the 2D QBEM solver is verified by the following two-dimensional cases:

- ✓ The steady-state third-order solution of a sloshing tank

- ✓ Free oscillations and forced oscillations in a rectangular tank
- ✓ Numerical simulation of the Stokes second-order waves
- ✓ Numerical simulation of the Stokes third-order waves
- ✓ Second-order diffraction of a horizontal semi-submerged circular cylinder
- ✓ Second-order radiation of a horizontal semi-submerged circular cylinder

The sloshing in a two-dimensional rectangular tank is studied up to third order by using a combined numerical and analytical approach. The numerical part is based on the QBEM developed in this study. The comparison between the numerical results and the analytical results demonstrated the accuracy of our 2D QBEM solver and that the higher-order derivatives in the free-surface conditions can be obtained accurately by standard numerical methods.

The free oscillations and forced oscillations in a rectangular tank are studied in the time domain. The numerical results are verified by the first-order and second-order analytical results. The mass conservations of the first-order and second-order solutions are checked.

The Stokes second-order and third-order waves are reproduced in a 2D numerical wave tank (NWT) by feeding the velocity profile based on Stokes wave theory on a control surface. It was found that the Stokes drift causes the mass increase in the NWT, and a numerical damping zone which is able to 'drain' water out of the tank was used to minimize the effect of the second-order mass transport. The third-order solution in a NWT without secularity (solvability) conditions shows that the third-order component of the wave amplitude increases linearly with the horizontal distance to the wave maker. A two-time scale approach was proposed to eliminate the secular terms in the free-surface conditions.

Second-order diffraction and radiation of a horizontal semi-submerged circular cylinder are studied numerically in the time domain. The results are verified with other theoretical results and are validated by some existing experimental results. An indirect method based on Green's 2nd identity was used to check the accuracy of the second-order forces due to the second-order scattered velocity potential. The indirect method does not need a second-order solution.

Three-dimensional studies

The three-dimensional time-domain HOBEM was carefully verified by studying the nonlinear diffraction, nonlinear radiation and freely floating bodies in waves. Both the traditional method using the formulation in the inertial coordinate system and the new method with body-fixed frame near the body are used. The present study considered either a small forward speed or zero forward speed.

- ✓ **Nonlinear diffraction with Fr=0.0**

For zero Froude number, the second-order and third-order wave diffraction are studied. The second-order sum-frequency forces on a stationary hemisphere obtained by the present numerical results agree favorably with the other numerical results. For a bottom-mounted vertical circular cylinder in monochromatic waves, the first-order, second-order and third-order wave forces are calculated and compared with the analytical or semi-analytical results. The comparisons for the first-order and second-order results showed very good agreement. The third-order forces contributed on the bottom-mounted vertical circular cylinder by the first-order and second-order are consistent with the semi-analytical results, while differences were observed for the component due to the

third-order velocity potential. Sensitivity studies on the discretization, the time increment of time stepping of the free-surface conditions, the empirical damping coefficients in the numerical damping zone, the location and length of the damping zone suggested that our numerical results are convergent. An indirect method based on Green's 2nd identity has also been used as an alternative to calculate the forces. The results obtained by the direct method and the indirect method are consistent. Second-order diffraction of a bottom-mounted vertical circular cylinder in bichromatic waves has been studied. The Quadratic Transfer Functions (QTFs) of the sum-frequency forces and difference-frequency forces are recovered from the present time-domain results. The comparison of the QTFs with the other numerical and semi-analytical results showed the potential of the present method in the analysis of the second-order wave loads on floating bodies in irregular waves.

✓ **Nonlinear radiation with Fr=0.0**

The forced oscillations of free surface piercing bodies have been investigated. The hydrodynamic coefficients, i.e. the added mass and damping, for a vertical circular cylinder with draft equal to the radius and a hemisphere, have been obtained by Fourier analyzing the time-domain results. Good agreements were obtained when compared with the semi-analytical results.

For an axisymmetric body without sharp corner, we have shown that the first-order and second-order results obtained by the domain-decomposition based method are consistent with that of the traditional method with a formulation in the inertial coordinate system.

For a truncated vertical circular cylinder with sharp corners, the second-order forces obtained by the domain-decomposition based method agree fairly well with two of three existing numerical results. Those numerical results were obtained by a formulation in inertial reference frame, with the second-order derivatives in the second-order body boundary condition treated by a Stokes-like theorem. For a body with sharp corner, we also pointed out that, with a formulation in inertial reference frame, it is wrong to calculate the second-order derivatives in the second-order body boundary condition directly. This is associated with the fact that the second-order derivatives of the velocity potential at the sharp corner are not integrable. This may explain why Isaacson & Ng's (1993b) results show relatively large differences.

✓ **Nonlinear diffraction with Fr≠0.0**

For a vertical circular cylinder with draft equal to the radius with a small forward speed, the first-order and second-order in-line forces are calculated and verified by comparing with the other numerical results. Short-wave instabilities have been observed in both the first-order and second-order solutions. A low-pass filter was used to suppress the instabilities. Sensitivities on the strength of the filter and the frequency of the application of the filter have been investigated.

✓ **Nonlinear radiation with Fr≠0.0**

By studying the forced oscillations of a vertical circular cylinder with draft equal to the radius with a small forward speed, the hydrodynamic coefficients, i.e. added mass and damping, were obtained. The results were in good agreement with the frequency-domain results. The second-order forces on the same cylinder are calculated by both the traditional method and the new method based on domain decomposition. Consistent results were achieved. The consistency between the traditional method and the new method was further demonstrated by the study of a forced-oscillating axisymmetric body without sharp corner.

The forced oscillating of a truncated vertical circular cylinder is studied up to second order in wave steepness and unsteady body motions by using the new method in Chapter 5. A formulation in the inertial coordinate system is not valid for this case. It was found that the forward speed has negligible effect on the first-order and second-order vertical forces, whereas its influences on the first-order and second-order horizontal forces have linear dependence on the Froude number and are not negligible. Those observations are based on the analysis with small Froude numbers. Similarly, for a forced surging truncated circular cylinder, the forward speed effects on the first-order horizontal force and the second-order vertical force are negligible.

✓ **Freely floating bodies with Fr=0.0 or Fr≠0.0**

A freely floating vertical circular cylinder in waves was studied. The cylinder was free to response in only the surge motion. The Response Amplitude Operators (RAOs) of the first-order responses for different Froude numbers agree well with the semi-analytical results in the frequency domain. Drifting of the cylinder was observed in the second-order response of the cylinder. This is partly due to the fact that the cylinder has no restoring mechanism in the horizontal plane and that the second-order force contains a mean drift force.

The vertical mean wave force on a truncated vertical circular cylinder free to response in surge and heave was calculated. Near-field method was used in the force calculation except that the quadratic forces are re-formulated based on an equality (see Appendix F) given in Newman (1977). The present results for the zero forward speed case confirmed the far-field results by Zhao & Faltinsen (1989b), while the near-field results of Zhao & Faltinsen (1989b) and Liu et al.(1993) showed large difference. The forward speed effects on the horizontal and vertical mean drift forces are discussed.

9.2 Future perspectives

The numerical methods have been shown to be robust and able to handle a lot of weakly nonlinear wave-body interaction problems with or without a small forward speed. The numerical schemes adopted in study are workable but may not be the optimum choices.

Possible improvement of the present methods in the future

- The combination of the damping zone with, for instance the Sommerfeld-Orlanski condition would allow us to use a relatively smaller damping zone length. As a consequence, it will result in fewer unknowns and smaller matrices in the final matrix equation.

- For cases with forward speed, the low-pass filter was applied in this study. The strength of the filter was determined empirically. When the forward speed increases, the strength of the instabilities increases and one has to increase the strength of the low-pass filter. More work should be done on the understanding of the short wave instabilities. A question is: Can we come up with a numerical scheme that is free of the short wave instabilities without introducing any numerical damping or smoothing effects?

- A proper B-Spline based HOBEM is believed to have faster convergence than the present HOBEMs based on shape functions. Therefore, it is suggested to apply the B-Spline based

HOBEM on the free surface and the control surface in the domain decomposition based method in Chapter 5. The author of this thesis does not prefer to use the B-Spline based HOBEM on the body surface. One reason is that the boundary elements based on shape functions can be shared in the Finite Element Analysis (FEA) of the structural responses.

- The second-order horizontal and yaw motions of, for instance a moored ship, can be very large and it may be wrong to consider them as small. However, it is possible to extend the decomposition based method in Chapter 5 to handle this problem by re-ordering the horizontal and yaw motions as O(1) instead of O(ε) or O(ε^2). The idea is that one use a 'body-fixed' coordinate system in the outer domain as well. It is called 'body-fixed' coordinate system, because it has the same horizontal translatory and angular velocities as the body. However, it does not have any vertical motions. The coordinate system in the inner domain remains the same body-fixed coordinate system as used in this thesis. The derivation of the free-surface conditions in the outer domain is similar to what we have done in the inner domain (see Section 2.6.4). The difference is that the horizontal motions will be order of O(1). The incident wave field in the outer domain has to be described in the 'body-fixed' coordinate system as well. This is straightforward by considering the vector $\vec{U}$ in Eq.(2.144) as the total horizontal velocity of the body. On the other hand, one has to solve the body motion equations in the body-fixed coordinate system. The description of the rigid-body motion equations in the body-fixed coordinate system can be found in Section 2.7.2.

- The present work includes only small forward effects. In practice, it may be appropriate for Fr<~0.2.When the forward speed increases and cannot be considered as a small parameter, i.e. U~O(1), the steady wave elevation is not negligible. Therefore, in theory one cannot use the double-body flow as the basis flow for large forward speeds. One may need to solve the fully-nonlinear steady wave (see e.g. Raven, 1996). Furthermore, if one still wants to use the perturbation scheme, the free-surface conditions should be approximated by Taylor expansion about the steady wave elevation. The steady wave elevation also changes the mean wetted body surface that has been used in this thesis.

Future work and possible applications

In the literature, there are very limited theoretical second-order results with the presence of a forward speed. This may be associated with the difficulties that we have discussed in the formulation in the inertial coordinate system. In order to further validate the present numerical methods and to see to what extent we can apply a second-order or third-order theory, more comparisons should be made with the experimental results (if any).

Because we are solving a general second-order (or third-order for zero forward speed) problem, the possible applications of the present methods would be, for instance, the higher-harmonic wave loads, the difference-frequency wave loads and the mean drift forces on ships and offshore structures.

The sum-frequency loads are relevant for the nonlinear springing of ships and TLPs. The third-harmonic forces may also be an important source of the ringing of the TLPs and deep-water gravity based platforms. Difference-frequency and mean drift wave loads are important in the stationkeeping analysis of moored ships or platforms. The mean drift force is also responsible for the added wave resistance of a ship traveling in the seaway. A byproduct of the numerical analysis

presented in this thesis is the nonlinear run-up along the offshore structures. The nonlinear run-up is not the focus of this thesis. However, it does not mean it is not important. When the domain decomposition based method (in Chapter 5) is extended by considering all the horizontal and yaw motions as O(1), the method can also be applied to the combined problem of seakeeping and maneuvering.

Appendix

Appendix A. The double-body basis flow

A.1 The classical double-body basis flow in the inertial coordinate system

The classical basis double-body flow velocity potential $\phi^{(0)}$ satisfies the following boundary value problem defined in the inertial coordinate system OXYZ:

$$\begin{cases} \nabla^2\phi^{(0)} = 0 \quad \text{in the whole mean fluid domain} \\ \dfrac{\partial\phi^{(0)}}{\partial n} = \vec{U}\cdot\vec{n}^{(0)} \quad \text{on } SB_0 \\ \dfrac{\partial\phi^{(0)}}{\partial Z} = 0 \quad \text{on } Z = 0 \\ \phi^{(0)} \to 0 \quad \text{at infinity} \end{cases} \tag{A.1}$$

Here SB_0 is the mean wetted body surface. $\vec{U}$ is the forward speed vector described in the inertial coordinate system.

In the formulation of the free-surface and body boundary conditions in the inertial coordinate system (see Section 2.4), we have used the velocity potential $\phi^{(0)}$ described in Eq.(A.1) as the basis flow.

The rigid-wall free-surface condition at the mean free surface, i.e. OXY-plane, means that we have ignored the steady wave system due to the steady motion of the body. The body boundary condition satisfied at the mean position of the body surface indicates that the basis flow described in Eq.(A.1) cannot be used for large body motions.

When the body boundary condition is formulated in the inertial coordinate system, and in order to approximately satisfy the body boundary condition at the instantaneous body position, one has to Taylor expand the basis flow $\phi^{(0)}$ about the mean body position. See for instance Timman & Newman (1962) for the linear boundary conditions and Section 2.4 for the linear and second-order boundary conditions. When the body has sharp corners, the solution of $\phi^{(0)}$ is singular and it is not valid to make Taylor expansions.

A.2 The 'double-body' basis flow used in the domain decomposition based method

Let's now explain how we can find the zeroth-order velocity potential $\phi^{(0)}$ used in the domain decomposition based method using a body-fixed coordinate system in the near field. See Chapter 5. Physically, it can not be interpreted as exactly the same as the classical double-body basis flow defined in the inertial coordinate system (see Appendix A.1). However, it can be shown that the solution of $\phi_{\mathrm{I}}^{(0)}$ and $\phi_{\mathrm{II}}^{(0)}$ to zeroth order are the same as the inner and outer part of $\phi^{(0)}$ (defined in Eq.(A.1)) respectively.

We introduce another zeroth-order velocity potential ϕ_0 satisfying all the conditions in Eq.(A.1) except that the body boundary condition is satisfied on the instantaneous position, i.e.

$$\begin{cases} \nabla^2\phi_0 = 0 \quad \text{in the whole fluid domain} \\ \dfrac{\partial\phi_0}{\partial n} = \vec{U}\cdot\vec{n} \quad \text{on } \widehat{SB} \\ \dfrac{\partial\phi_0}{\partial Z} = 0 \quad \text{on } Z = 0 \\ \phi_0 \to 0 \quad \text{at infinity} \end{cases} \tag{A.2}$$

Here $\widehat{SB}$ is the instantaneous wetted body surface under the calm water surface Z=0, i.e. the shaded area in Fig.(A.2).

Taylor expanding the free-surface condition about the oxy-plane of the body-fixed coordinate system in the inner domain, and keeping only the leading order terms, we have that

$$\begin{cases} \nabla^2\phi_{\mathrm{I}}^{(0)} = 0 \quad \textit{in the inner fluid domain} \\ \dfrac{\partial\phi_{\mathrm{I}}^{(0)}}{\partial n} = \vec{U}'^{(0)}\cdot\vec{n}' \quad \textit{on SB} \\ \dfrac{\partial\phi_{\mathrm{I}}^{(0)}}{\partial z} = 0 \quad \textit{on } z = 0 \end{cases} \tag{A.3}$$

with

$$\phi_0 = \phi_{\mathrm{I}}^{(0)} + O(\varepsilon) \tag{A.4}$$

$\phi_{\mathrm{I}}^{(0)}$ is the leading order approximation of ϕ_0 in the inner domain. ε is the small parameter as the measurement of the unsteady rigid-body motions. $\vec{U}'^{(0)}$ is the zeroth-order component of the forward speed vector in the body-fixed coordinate system. In this study, we have assumed the forward speed to be always in the X-direction of the inertial coordinate system. The definition of $\vec{U}'^{(0)}$ was given in Eq.(2.41). $\vec{n}'$ is the normal vector of the body surface defined in the body-fixed coordinate system.

Note that the Taylor expansion of the free-surface conditions about oxy-plane is only valid in the inner domain. This reason has been explained in the text associated with Eq.(2.101). In the outer domain, the following free-surface condition holds

$$\frac{\partial\phi_{\mathrm{II}}^{(0)}}{\partial Z} = 0 \quad \textit{on } Z = 0 \tag{A.5}$$

$\phi_{\mathrm{II}}^{(0)}$ is the zeroth-order velocity potential in the outer domain.

The difference between the $\phi_{\mathrm{I}}^{(0)}$ (or $\partial\phi_{\mathrm{I}}^{(0)}/\partial n$) at the control surface SC and $\phi_{\mathrm{II}}^{(0)}$ (or $\partial\phi_{\mathrm{II}}^{(0)}/\partial n$) on SC_0 is of $O(\varepsilon)$, and thus can be ignored if only the zeroth-order quantities are of interest. That is

$$\phi_{\mathrm{I}}^{(0)}\Big|_{SC} = \phi_{\mathrm{II}}^{(0)}\Big|_{SC_0} + O(\varepsilon), \quad \frac{\partial\phi_{\mathrm{I}}^{(0)}}{\partial n}\bigg|_{SC} = \frac{\partial\phi_{\mathrm{II}}^{(0)}}{\partial n}\bigg|_{SC_0} + O(\varepsilon) \tag{A.6}$$

The definition of control surface SC and its mean position SC_0 can be found in Fig.5.1 - Fig.5.3.

Considering Eq.(A.6), Eq.(A.1), Eq.(A.3) and noticing that $\vec{U}'^{(0)} = \vec{U}$, $\vec{n}' = \vec{n}^{(0)}$, we find that, the solution of $\phi_{\mathrm{I}}^{(0)}$ and $\phi_{\mathrm{II}}^{(0)}$ to zeroth order are the same as the inner and outer part of $\phi^{(0)}$ (defined in Eq.(A.1)), respectively. Therefore, we can use $\phi^{(0)}$ as the solutions of $\phi_{\mathrm{I}}^{(0)}$ and $\phi_{\mathrm{II}}^{(0)}$.

For a double-body flow, when $\phi^{(0)}$ is being solved, the domain decomposition solver is switched off and no source/dipole distribution is distributed on the control surface. Since the control surface is enclosed by the computational boundaries of the water domain, the velocity potential $\phi^{(0)}$ and its high-order derivatives there can be calculated very accurately by using the boundary integral equation (BIE) and the spatial derivatives of the BIE.

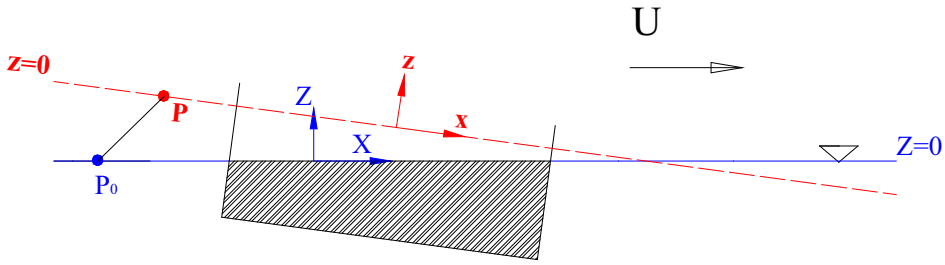

Fig.A.1. Definition of the scenario of ϕ_0 problem in Eq.(A.2). The shaded area is the wetted surface $\widehat{SB}$ in Eq.(A.2).

Appendix B. The second-order analytical solution of a circle under forced surging in an infinite fluid

B.1. Solution in the Earth-fixed coordinate system

The surge motion of the circle is assumed to be

$$\xi_1 = \xi_{1a} \sin(\omega t) \tag{B.1}$$

with the velocity expressed as

$$\dot{\xi}_1 = \xi_{1a} \omega \cos(\omega t). \tag{B.2}$$

Here ξ_{1a} is the amplitude of the surge motion. ω is the frequency of the oscillation.

We will assume that the body motion is small compared with the radius of the circle R_0. Therefore the velocity potential ϕ can be written as the series expansion

$$\phi = \phi^{(1)} + \phi^{(2)} + \cdots. \tag{B.3}$$

Taylor expanding the body boundary condition about the mean oscillatory body position, we can get the first-order and second-order body boundary conditions, which can be written respectively as

$$\frac{\partial \phi^{(1)}}{\partial n} = \frac{\partial \phi^{(1)}}{\partial r} = \dot{\xi}_1 n_1 = \xi_{1a} \omega \cos(\omega t) n_1 \qquad \text{on } SB_0, \tag{B.4}$$

$$\frac{\partial \phi^{(2)}}{\partial n} = \frac{\partial \phi^{(2)}}{\partial r} = -\xi_1 \vec{n} \cdot \nabla \phi_X^{(1)} \qquad \text{on } SB_0. \tag{B.5}$$

Here $\vec{n} = (n_1, n_2, n_3)$ is the normal vector on the mean position of the body surface SB_0. $\vec{n}$ is defined as positive pointing into the fluid domain. The subscript X in Eq.(B.5) indicates the partial differentiation with respect to the X-coordinate. $\vec{r}$ means the radial direction.

The first-order solution is known as a 2D dipole with its normal in the X-direction

$$\phi^{(1)} = -\dot{\xi}_1 \frac{R_0^2}{R} \cos\theta \tag{B.6}$$

where (R, θ) is a point in the fluid domain expressed in the polar coordinate system. We can rewrite Eq.(B.5) by putting Eq.(B.6), Eq.(B.1) and Eq.(B.2) into Eq.(B.5) as

$$\frac{\partial \phi^{(2)}}{\partial n} = \xi_1 \dot{\xi}_1 \frac{2}{R_0} \cos(2\theta) = \frac{1}{R_0} \xi_{1a}^2 \omega \sin(2\omega t) \cos(2\theta). \tag{B.7}$$

The elementary solutions of the Laplace equation in the polar coordinate system can be found in for instance Newman (1977, Eq.(70), page 125). We can formally write the solution of $\phi^{(2)}$ as the combination of the elementary solutions, i.e.

$$\phi^{(2)}\left(R,\theta,t\right)=\left\{B_0+A_0\ln(R)+\sum_{n=1}^{\infty}\cos\left(n\theta\right)\left[B_nR^n+A_n/R^n\right]\right\}\sin\left(2\omega t\right). \tag{B.8}$$

Here A_0, B_0, A_n, B_n are constants. The reason we have used sin(2ωt) as the time-dependence of the solution is that the body boundary condition in Eq.(B.7).is sin(2ωt)-dependent.

The coefficients A_0, B_0, and B_n should be all zero in order to satisfy the radiation condition, which requires that $\phi^{(2)}\to 0$ at infinity. Furthermore, the body boundary condition Eq.(B.7) suggests that

$$A_n=\begin{cases}0, & n\neq 2\\ -\dfrac{1}{2}R_0^2\xi_{1a}^2\omega, & n=2\end{cases} \tag{B.9}$$

Therefore, the solution of $\phi^{(2)}$ is found as

$$\phi^{(2)}\left(R,\theta,t\right)=-\frac{1}{2}\xi_{1a}^2\omega\left(\frac{R_0}{R}\right)^2\sin\left(2\omega t\right)\cos\left(2\theta\right). \tag{B.10}$$

The second-order approximation of the hydrodynamic pressure on the body ($R=R_0$) can be expressed as

$$\begin{aligned}p=p^{(1)}+p^{(2)}&=-\rho\frac{\partial\phi^{(1)}}{\partial t}-\rho\frac{\partial\phi^{(2)}}{\partial t}-\rho\nabla\phi^{(1)}\cdot\nabla\phi^{(1)}-\xi_1\frac{\partial^2\phi^{(1)}}{\partial t\partial X}\\ &=\frac{1}{2}\rho\xi_{1a}^2\omega^2\left[1+\cos\left(2\omega t\right)\right]\left[\cos\left(2\theta\right)-\frac{1}{2}\right]\end{aligned} \tag{B.11}$$

B.2. Solution in the body-fixed coordinate system

In the solution in the body-fixed coordinate system, we do not assume that the body motion is small. Instead the solution derived here is valid also for large-amplitude motions.

The body boundary condition satisfied on the instantaneous position of the body is

$$\frac{\partial\phi}{\partial n}=\frac{\partial\phi}{\partial r}=\dot{\xi}_1n_1=\xi_{1a}\omega\cos\left(\omega t\right)n_1 \qquad \text{on SB.} \tag{B.12}$$

The solution of ϕ is the same as $\phi^{(1)}$ given in Eq.(B.6), i.e.

$$\phi=-\dot{\xi}_1\frac{R_0^2}{R}\cos\theta. \tag{B.13}$$

Applying the Bernoulli's equation in the body-fixed coordinate system, the hydrodynamic pressure on the instantaneous body surface can be expressed as

$$\begin{aligned}p&=-\rho\frac{\partial\phi}{\partial t}-\rho\nabla\phi^{(1)}\cdot\nabla\phi^{(1)}+\dot{\xi}_1\frac{\partial\phi^{(1)}}{\partial x}\\ &=\frac{1}{2}\rho\xi_{1a}^2\omega^2\left[1+\cos\left(2\omega t\right)\right]\left[\cos\left(2\theta\right)-\frac{1}{2}\right]\end{aligned} \tag{B.14}$$

Appendix C. The second-order analytical solution for sloshing in a two-dimensional rectangular tank under forced surging

C.1 Solution in the Earth-fixed coordinate system

A 2D rectangular tank under forced sinusoidal surge motion is considered. We will show how we can find the second-order analytical solution of this problem in the Earth-fixed coordinate system by assuming a steady-state condition. By steady-state condition, it is meant that we will neglect the transient effects in the tank. Rognebakke & Faltinsen (1999) has obtained a transient solution up to second order for the same problem. The solution was also analytically based. However, in the second-order solution, Rognebakke & Faltinsen (1999) simplified their analysis by only including the contribution of the first mode in the second-order forcing terms. In the present solution, we have included the contribution from all the modes. In practice, we have to truncate the series since the high modes are highly-damped.

The surge motion of the rectangular tank is assumed to be

$$\xi_1 = \xi_{1a} \sin(\omega t), \tag{C.1}$$

with the velocity as

$$u = \dot{\xi}_1 = \xi_{1a} \omega \cos(\omega t). \tag{C.2}$$

Here ξ_{1a} is the amplitude of the surge motion. ω is the frequency of the oscillation. The over dot means time derivative.

When the tank motion and the fluid motion in the tank are small compared with the characteristic dimension of the tank, the velocity potential ϕ can be expressed by the series expansion

$$\phi = \phi^{(1)} + \phi^{(2)} + \cdots. \tag{C.3}$$

The first-order and second-order free-surface conditions can be expressed respectively as

$$\frac{\partial^2 \phi^{(1)}}{\partial t^2} + g \frac{\partial \phi^{(1)}}{\partial Z} = 0 \quad \text{on Z = 0}, \tag{C.4}$$

$$\begin{aligned} &\frac{\partial^2 \phi^{(2)}}{\partial t^2} + g \frac{\partial \phi^{(2)}}{\partial Z} = -\frac{\partial}{\partial t}\left[\left(\frac{\partial \phi^{(1)}}{\partial X}\right)^2 + \left(\frac{\partial \phi^{(1)}}{\partial Z}\right)^2\right] + \frac{1}{g}\frac{\partial \phi^{(1)}}{\partial t}\frac{\partial}{\partial Z}\left[\frac{\partial^2 \phi^{(1)}}{\partial t^2} + g\frac{\partial \phi^{(1)}}{\partial Z}\right] \\ &= -2\frac{\partial \phi^{(1)}}{\partial X}\frac{\partial^2 \phi^{(1)}}{\partial X \partial t} - 2\frac{\partial \phi^{(1)}}{\partial Z}\frac{\partial^2 \phi^{(1)}}{\partial Z \partial t} + \frac{1}{g}\frac{\partial \phi^{(1)}}{\partial t}\frac{\partial^3 \phi^{(1)}}{\partial Z \partial t^2} + \frac{\partial \phi^{(1)}}{\partial t}\frac{\partial^3 \phi^{(1)}}{\partial Z^2 \partial t} \quad \text{on Z = 0}, \end{aligned} \tag{C.5}$$

The corresponding first-order and second-order body boundary conditions are

$$\left.\frac{\partial \phi^{(1)}}{\partial X}\right|_{X=\pm a} = \xi_{1a}\omega\cos(\omega t) \tag{C.6}$$

$$\left.\frac{\partial \phi^{(2)}}{\partial X}\right|_{X=\pm a} = -\left[\xi_{1a}\sin(\omega t)\right]\left.\frac{\partial^2 \phi^{(1)}}{\partial X^2}\right|_{X=\pm a} \tag{C.7}$$

Here a is half of the breath of the tank. See the definition in Fig.5.8.

The time-domain solution for $\phi^{(1)}$ was given by Faltinsen (1978). The steady-state solution can be obtained by neglecting the transient terms in Faltinsen's (1978) solution and can be written as

$$\phi^{(1)} = \dot{\xi}_1 X + \sum_{n=1}^{\infty} A_n \cos(\omega t)\frac{\cosh\left[k_n(Z+h)\right]}{\cosh k_n h}\cos\left[k_n(X+a)\right], \tag{C.8}$$

where

$$A_n = \frac{1}{-\omega^2+\omega_n^2}\frac{(-1)^n-1}{k_n^2\cdot a}\xi_{1a}\omega^3, \tag{C.9}$$

$$k_n = \frac{n\pi}{2a}. \tag{C.10}$$

Here h is the water depth.

We define

$$B_n(Z,t) = A_n\cos(\omega t)\frac{\cosh\left[k_n(Z+h)\right]}{\cosh k_n h} \tag{C.11}$$

and rewrite Eq. (C.8) becomes

$$\phi^{(1)} = \dot{\xi}_1 X + \sum_{n=1}^{\infty} B_n(Z,t)\cos\left[k_n(X+a)\right]. \tag{C.12}$$

We will evaluate the forcing term on the right-hand side of Eq. (C.5) term by term by using Eq.(C.12).

$$\begin{aligned}\left.-2\frac{\partial \phi^{(1)}}{\partial X}\frac{\partial^2 \phi^{(1)}}{\partial X\partial t}\right|_{Z=0} &= -\sum_{m=1}^{\infty}\sum_{n=1}^{\infty} A_m C_{1,n} k_m k_n \sin\left[k_m(X+a)\right]\sin\left[k_n(X+a)\right]\sin(2\omega t)\\ &+\sum_{n=1}^{\infty}\left(C_{1,n}-\omega A_n\right)\xi_{1a}\omega k_n \sin\left[k_n(X+a)\right]\sin(2\omega t)\\ &+\xi_{1a}^2\omega^3\sin(2\omega t)\end{aligned} \tag{C.13}$$

$$\left.-2\frac{\partial \phi^{(1)}}{\partial X}\frac{\partial^2 \phi^{(1)}}{\partial X\partial t}\right|_{Z=0} = -\sum_{m=1}^{\infty}\sum_{n=1}^{\infty} C_{2,m}C_{4,n}\cos\left[k_m(X+a)\right]\cos\left[k_n(X+a)\right]\sin(2\omega t) \tag{C.14}$$

$$\frac{1}{g}\frac{\partial\phi^{(1)}}{\partial t}\frac{\partial^3\phi^{(1)}}{\partial Z\partial t^2}\bigg|_{Z=0}=\frac{1}{g}\sum_{m=1}^{\infty}\sum_{n=1}^{\infty}C_{1,m}C_{5n}\cos\left[k_m\left(X+a\right)\right]\cos\left[k_n\left(X+a\right)\right]\frac{\sin\left(2\omega t\right)}{2}+\frac{1}{g}\sum_{n=1}^{\infty}\ddot{\xi}_1C_{5,n}X\cos\left[k_n\left(X+a\right)\right]\cos\left(\omega t\right) \tag{C.15}$$

$$\frac{\partial\phi^{(1)}}{\partial t}\frac{\partial^3\phi^{(1)}}{\partial Z^2\partial t}=\sum_{m=1}^{\infty}\sum_{n=1}^{\infty}C_{1,m}C_{3,n}\cos\left[k_m\left(X+a\right)\right]\cos\left[k_n\left(X+a\right)\right]\frac{\sin\left(2\omega t\right)}{2}+\sum_{n=1}^{\infty}\ddot{\xi}_1C_{3,n}X\cos\left[k_n\left(X+a\right)\right]\cos\left(\omega t\right) \tag{C.16}$$

where $C_{1,n}$, $C_{2,n}$, $C_{3,n}$, $C_{4,n}$ and $C_{5,n}$ are defined respectively as

$$C_{1,n}=-\omega A_n, \tag{C.17}$$

$$C_{2,n}=A_nk_n\tanh\left(k_nh\right)=A_n\frac{\omega_n^2}{g}, \tag{C.18}$$

$$C_{3,n}=A_nk_n^2, \tag{C.19}$$

$$C_{4,n}=-\omega A_n\frac{\omega_n^2}{g}, \tag{C.20}$$

$$C_{5,n}=-\omega^2A_n\frac{\omega_n^2}{g}. \tag{C.21}$$

Noticing that $C_{3,n}$=0 and $C_{5,n}$=0 when n is an even number, we can rewrite the single summation in Eq. (C.15) and Eq. (C.16) respectively as

$$\frac{1}{g}\sum_{n=1}^{\infty}\ddot{\xi}_1C_{5,n}X\cos\left[k_n\left(X+a\right)\right]\cos\left(\omega t\right)=-\frac{1}{2g}\sum_{n=1}^{\infty}\xi_{1a}\omega^2C_{5,n}D_{n0}\sin\left(2\omega t\right)-\frac{1}{2g}\sum_{n=1}^{\infty}\sum_{m=1}^{\infty}\xi_{1a}\omega^2C_{5,n}D_{nm}\cos\left[k_m\left(X+a\right)\right]\sin\left(2\omega t\right), \tag{C.22}$$

and

$$\sum_{n=1}^{\infty}\ddot{\xi}_1C_{3,n}X\cos\left[k_n\left(X+a\right)\right]\cos\left(\omega t\right)=-\frac{1}{2}\sum_{n=1}^{\infty}\xi_{1a}\omega^2C_{3,n}D_{n0}\sin\left(2\omega t\right)-\frac{1}{2}\sum_{n=1}^{\infty}\sum_{m=1}^{\infty}\xi_{1a}\omega^2C_{3,n}D_{nm}\cos\left[k_m\left(X+a\right)\right]\sin\left(2\omega t\right), \tag{C.23}$$

where

$$D_{n0}=\frac{2a\left[-1+\left(-1\right)^n\right]}{n^2\pi^2}, \tag{C.24}$$

$$D_{nm}=\begin{cases}0; & m\ is\ odd\\ \dfrac{4a^2\left(n^2+m^2\right)\left[-1+\left(-1\right)^n\right]}{\pi^2\left(n^2-m^2\right)^2}; & n\neq m\ \&\ m\ is\ even\end{cases}. \tag{C.25}$$

Plugging (C.13) - (C.16) and (C.22) - (C.23) into Eq. (C.5), we have that

$$\left[\frac{\partial^2\phi^{(2)}}{\partial t^2}+g\frac{\partial\phi^{(2)}}{\partial Z}\right]_{Z=0}$$

$$=-\sum_{m=1}^{\infty}\sum_{n=1}^{\infty}A_mC_{1,n}k_mk_n\sin\left[k_m\left(X+a\right)\right]\sin\left[k_n\left(X+a\right)\right]\sin\left(2\omega t\right)$$

$$+\sum_{n=1}^{\infty}\left(C_{1,n}-\omega A_n\right)\xi_{1a}\omega k_n\sin\left[k_n\left(X+a\right)\right]\sin\left(2\omega t\right)+\xi_{1a}^2\omega^3\sin\left(2\omega t\right)$$

$$-\sum_{m=1}^{\infty}\sum_{n=1}^{\infty}C_{2,m}C_{4,n}\cos\left[k_m\left(X+a\right)\right]\cos\left[k_n\left(X+a\right)\right]\sin\left(2\omega t\right)$$

$$\frac{1}{g}\sum_{m=1}^{\infty}\sum_{n=1}^{\infty}C_{1,m}C_{5,n}\cos\left[k_m\left(X+a\right)\right]\cos\left[k_n\left(X+a\right)\right]\frac{\sin\left(2\omega t\right)}{2}$$

$$-\frac{1}{2g}\sum_{n=1}^{\infty}\xi_{1a}\omega^2C_{5,n}D_{n0}\sin\left(2\omega t\right)-\frac{1}{2g}\sum_{n=1}^{\infty}\sum_{m=1}^{\infty}\xi_{1a}\omega^2C_{5,n}D_{nm}\cos\left[k_m\left(X+a\right)\right]\sin\left(2\omega t\right)$$

$$+\sum_{m=1}^{\infty}\sum_{n=1}^{\infty}C_{1,m}C_{3,n}\cos\left[k_m\left(X+a\right)\right]\cos\left[k_n\left(X+a\right)\right]\frac{\sin\left(2\omega t\right)}{2}$$

$$-\frac{1}{2}\sum_{n=1}^{\infty}\xi_{1a}\omega^2C_{3,n}D_{n0}\sin\left(2\omega t\right)-\frac{1}{2}\sum_{n=1}^{\infty}\sum_{m=1}^{\infty}\xi_{1a}\omega^2C_{3,n}D_{nm}\cos\left[k_m\left(X+a\right)\right]\sin\left(2\omega t\right) \tag{C.26}$$

One should note that in Rognebakke & Faltinsen's (1999) analysis, there is no summation in the second-order forcing term, i.e. on the right-hand side of Eq. (C.26). The reason is that only the first mode has been used by Rognebakke & Faltinsen (1999) in the second-order forcing term. The presence of the double-summations in Eq.(C.26) makes the analytical solution very complicated. Fortunately, these double-summations can be transferred to single summations, which will result in a much simpler analytical solution. Eq. (C.26) can be rewritten in the following form

$$\left[\frac{\partial^2\phi^{(2)}}{\partial t^2}+g\frac{\partial\phi^{(2)}}{\partial Z}\right]_{Z=0}=\left\{q_0+\sum_{n=1}^{\infty}q_n\cos\left[k_n\left(X+a\right)\right]+\sum_{n=1}^{\infty}p_n\sin\left[k_n\left(X+a\right)\right]\right\}\sin\left(2\omega t\right). \tag{C.27}$$

The derivation of q_0, q_n and p_n is lengthy and we only give the final results as

$$q_0=\frac{1}{2}\sum_{n=1}^{\infty}\left\{-A_nC_{1,n}k_n^2-C_{2,n}C_{4n}+\frac{1}{2g}C_{1,n}C_{5,n}+\frac{1}{2}C_{1,n}C_{3,n}\right\}+\xi_{1a}^2\omega^3 \tag{C.28}$$

$$\begin{aligned}q_n=&\frac{1}{2}\sum_{m=n+1}^{\infty}\left\{-A_{m-n}C_{1,m}k_{m-n}k_m-C_{2,m-n}C_{4,m}+\frac{1}{2g}C_{1,m-n}C_{5,m}+\frac{1}{2}C_{1,m-n}C_{3,m}\right\}\\&+\frac{1}{2}\sum_{m=1}^{\infty}\left\{-A_{m+n}C_{1,m}k_{m+n}k_m-C_{2,m+n}C_{4,m}+\frac{1}{2g}C_{1,m+n}C_{5,m}+\frac{1}{2}C_{1,m+n}C_{3,m}\right\}\\&+\frac{H\left(n-2\right)}{4}\sum_{m=1}^{n-1}\left\{A_{n-m}C_{1,m}k_{n-m}k_m-C_{2,n-m}C_{4,m}+\frac{1}{2g}C_{1,n-m}C_{5,m}+\frac{1}{2}C_{1,n-m}C_{3,m}\right\}\\&+\sum_{m=1}^{\infty}\left\{-\frac{1}{2}\xi_{1a}\omega^2D_{mn}\left[\frac{C_{5,m}}{g}+C_{3,m}\right]\right\},\end{aligned} \tag{C.29}$$

$$p_n = \left[C_{1,n} - \omega A_n \right] \xi_{1a} \omega k_n \,. \tag{C.30}$$

In order to find the solution to $\phi^{(2)}$, we will divide it into two parts

$$\phi^{(2)} = \phi_2^* + \phi_2 \,. \tag{C.31}$$

ϕ_2 satisfies Laplace equation and the following boundary conditions

$$\begin{cases} \dfrac{\partial \phi_2}{\partial X} = 0, \quad X = \pm a; \\ \dfrac{\partial \phi_2}{\partial Z} = 0, \quad Z = -h; \\ \dfrac{\partial^2 \phi_2}{\partial t^2} + g \dfrac{\partial \phi_2}{\partial Z} = \left\{ q_0 + \sum_{n=1}^{\infty} q_n \cos\left[k_n \left(X + a \right) \right] + \sum_{n=1}^{\infty} p_n \sin\left[k_n \left(X + a \right) \right] \right\} \sin\left(2\omega t \right), \quad o \quad Z = 0. \end{cases} \tag{C.32}$$

The boundary conditions for ϕ_2^* are

$$\begin{cases} \dfrac{\partial \phi_2^*}{\partial X} = -\left[\xi_{1a} \sin\left(\omega t \right) \right] \dfrac{\partial^2 \phi^{(1)}}{\partial X^2} = \xi_{1a} \sum_{n=1}^{\infty} A_n k_n^2 \dfrac{\cosh\left[k_n \left(Z + h \right) \right]}{\cosh k_n h} \sin\left[k_n \left(X + a \right) \right] \dfrac{\sin\left(\omega t \right)}{2}, \quad X = \pm a; \\ \dfrac{\partial \phi_2^*}{\partial Z} = 0, \quad Z = -h; \\ \dfrac{\partial^2 \phi_2^*}{\partial t^2} + g \dfrac{\partial \phi_2^*}{\partial Z} = \left\{ q_0 + \sum_{n=1}^{\infty} q_n \cos\left[k_n \left(X + a \right) \right] + \sum_{n=1}^{\infty} p_n \sin\left[k_n \left(X + a \right) \right] \right\} \sin\left(2\omega t \right), \quad o \quad Z = 0. \end{cases} \tag{C.33}$$

Thus the sum of ϕ_2^* and ϕ_2, i.e. $\phi^{(2)}$ satisfies the second-order body boundary condition at the tank walls Eq (C.7), the zero-Neumann bottom condition and the second-order free-surface condition Eq.(C.27).

Solution for ϕ_2

We assume

$$\phi_2 = E_0\left(t \right) + \sum_{n=1}^{\infty} E_n\left(t \right) \frac{\cosh\left[k_n \left(Z + h \right) \right]}{\cosh k_n h} \cos\left[k_n \left(X + a \right) \right], \tag{C.34}$$

which automatically satisfies the homogeneous Neumann condition at the walls and the bottom of the tank. $E_0\left(t \right)$ and $E_n\left(t \right)$ are determined by putting Eq.(C.34) into the free-surface condition in Eq.(C.33) as

$$E_0\left(t \right) = \left\{ \frac{q_0}{-4\omega^2} - \frac{1}{8\omega^2 a} \sum_{n=1}^{\infty} p_n \frac{1 - \left(-1 \right)^n}{k_n} \right\} \sin\left(2\omega t \right), \tag{C.35}$$

$$E_n\left(t \right) = \frac{1}{-4\omega^2 + \omega_n^2} \left\{ q_n + \sum_{m=1, m \neq n}^{\infty} p_m \frac{2m\left[\left(-1 \right)^n \left(-1 \right)^m - 1 \right]}{\pi\left(n^2 - m^2 \right)} \right\} \sin\left(2\omega t \right). \tag{C.36}$$

Solution for ϕ_2^*

The body boundary condition in (C.33) for ϕ_2^* suggests the following part of the solution

$$\phi_{21}^* = \xi_{1a}\sum_{n=1}^{\infty} A_n k_n \frac{\cosh\left[k_n\left(Z+h\right)\right]}{\cosh k_n h}\sin\left[k_n\left(X+a\right)\right]\frac{\sin\left(\omega t\right)}{2}, \tag{C.37}$$

which satisfies the body boundary conditions.

However, ϕ_{21}^* does not satisfy the free-surface condition in Eq.(C.33), thus we need another part of the solution ϕ_{22}^* satisfying the following free-surface condition

$$\left[\frac{\partial^2\phi_{22}^*}{\partial t^2}+g\frac{\partial\phi_{22}^*}{\partial Z}\right]_{Z=0} = -\left[\frac{\partial^2\phi_{21}^*}{\partial t^2}+g\frac{\partial\phi_{21}^*}{\partial Z}\right]_{Z=0} = \sum_{n=1}^{\infty} F_n \sin\left[k_n\left(X+a\right)\right]\sin\left(\omega t\right) \tag{C.38}$$

with

$$F_n = -\frac{1}{2}\xi_{1a}k_n A_n\left[-4\omega^2+\omega_n^2\right]. \tag{C.39}$$

The solution to ϕ_{22}^* can be assumed as

$$\phi_{22}^* = G_0\sin\left(2\omega t\right)+\sum_{n=1}^{\infty} G_n\sin\left(2\omega t\right)\frac{\cosh\left[k_n\left(Z+h\right)\right]}{\cosh\left(k_n h\right)}\cos\left[k_n\left(X+a\right)\right], \tag{C.40}$$

which satisfies the homogeneous Neumann condition on the tank surface.

It follows by plugging Eq.(C.40) into Eq.(C.38) and using the orthogonality of the natural sloshing modes that

$$G_0\left(t\right) = \frac{-1}{8\omega^2 a}\sum_{n=1}^{\infty} F_n\frac{1-\left(-1\right)^n}{k_n}, \tag{C.41}$$

$$G_n\left(t\right) = \frac{1}{-4\omega^2+\omega_n^2}\sum_{m=1,m\neq n}^{\infty} F_m\frac{2m\left[\left(-1\right)^m\left(-1\right)^n-1\right]}{\pi\left(n^2-m^2\right)}. \tag{C.42}$$

When the velocity potential is obtained, the hydrodynamic pressure in the fluid can be obtained from the Bernoulli's equation expressed in the inertial coordinate system. The first-order and second-order hydrodynamic pressure can respectively be written as

$$p^{(1)} = -\rho\phi_t^{(1)}, \tag{C.43}$$

$$p^{(2)} = -\rho\frac{\partial\phi^{(2)}}{\partial t}-\frac{1}{2}\rho\nabla\phi^{(1)}\cdot\nabla\phi^{(1)}-\rho\xi_1\frac{\partial^2\phi^{(1)}}{\partial X\partial t}. \tag{C.44}$$

C.2 Solution in the tank-fixed coordinate system

The first-order free-surface condition is the same as (C.4) with Z replaced by z in the body-fixed coordinate system, i.e.

$$\frac{\partial^2 \phi^{(1)}}{\partial t^2} + g\frac{\partial \phi^{(1)}}{\partial z} = 0 \quad \text{on z=0.} \tag{C.45}$$

The first-order body boundary condition

$$\left.\frac{\partial \phi^{(1)}}{\partial x}\right|_{x=\pm a} = \xi_{1a}\omega\cos(\omega t) \tag{C.46}$$

is the same as Eq.(C.6) with X replaced by x. Here $\phi^{(1)}$ is the first-order absolute velocity potential.

Thus the solution to $\phi^{(1)}$ in the body-fixed coordinate system can be obtained by simply replacing X and Z in (C.12) by x and z respectively, i.e.

$$\phi^{(1)} = \dot{\xi}_1 x + \sum_{n=1}^{\infty} B_n(z,t)\cos\left[k_n(z+a)\right]. \tag{C.47}$$

with $B_n(z,t)$ and k_n defined in section Eq.(C.11) and Eq.(C.10), respectively.

The second-order body boundary condition can be expressed as

$$\begin{cases} \dfrac{\partial \phi^{(2)}}{\partial x} = 0, & x = \pm a; \\ \dfrac{\partial \phi^{(2)}}{\partial x} = 0, & z = -h; \end{cases} \tag{C.48}$$

The second-order kinematic and dynamic free-surface condition can be written respectively as

$$\frac{\partial \phi^{(2)}}{\partial z} - \frac{\partial \eta^{(2)}}{\partial t} = -\dot{\xi}_1\frac{\partial \eta^{(1)}}{\partial t} + \frac{\partial \phi^{(1)}}{\partial x}\frac{\partial \eta^{(1)}}{\partial x} - \eta^{(1)}\frac{\partial^2 \phi^{(1)}}{\partial z^2}, \tag{C.49}$$

$$\frac{\partial \phi^{(2)}}{\partial t} + g\eta^{(2)} = -\eta^{(1)}\frac{\partial^2 \phi^{(1)}}{\partial z \partial t} + \dot{\xi}_1\frac{\partial \phi^{(1)}}{\partial x} - \frac{1}{2}\nabla\phi^{(1)}\cdot\nabla\phi^{(1)}. \tag{C.50}$$

The combined second-order free surface can be expressed as

$$\begin{aligned} \frac{\partial^2 \phi^{(2)}}{\partial t^2} + g\frac{\partial \phi^{(2)}}{\partial z} = &-\frac{\partial}{\partial t}\left[\left(\frac{\partial \phi^{(1)}}{\partial x}\right)^2 + \left(\frac{\partial \phi^{(1)}}{\partial z}\right)^2\right] + \frac{1}{g}\frac{\partial \phi^{(1)}}{\partial t}\frac{\partial}{\partial z}\left[\frac{\partial^2 \phi^{(1)}}{\partial t^2} + g\frac{\partial \phi^{(1)}}{\partial z}\right] \\ &+ g\left(-\dot{\xi}_1\frac{\partial \eta^{(1)}}{\partial t}\right) + \frac{\partial}{\partial t}\left(\dot{\xi}_1\frac{\partial \phi^{(1)}}{\partial x}\right) \quad on\ z = 0. \end{aligned} \tag{C.51}$$

We notice that the last two terms are additional terms compared with the second-order free-surface condition Eq.(C.5) in the Earth-fixed coordinate system. Therefore, we will divide the solution to $\phi^{(2)}$ into two parts, i.e.

$$\phi^{(2)} = \phi_2 + \phi_2^{**}. \tag{C.52}$$

ϕ_2 satisfies the homogeneous Neumann condition on the tank surface and part of the free-surface condition

$$\frac{\partial^2 \phi^{(2)}}{\partial t^2} + g\frac{\partial \phi^{(2)}}{\partial z} = -\frac{\partial}{\partial t}\left[\left(\frac{\partial \phi^{(1)}}{\partial x}\right)^2 + \left(\frac{\partial \phi^{(1)}}{\partial z}\right)^2\right] + \frac{1}{g}\frac{\partial \phi^{(1)}}{\partial t}\frac{\partial}{\partial z}\left[\frac{\partial^2 \phi^{(1)}}{\partial t^2} + g\frac{\partial \phi^{(1)}}{\partial z}\right] \quad on\ z = 0. \tag{C.53}$$

Thus the solution for ϕ_2 is the same as ϕ_2 in Eq.(C.34) expect that we have replace X and Z by x and z respectively, i.e.

$$\phi_2 = E_0(t) + \sum_{n=1}^{\infty} E_n(t)\frac{\cosh\left[k_n(z+h)\right]}{\cosh k_n h}\cos\left[k_n(x+a)\right]. \tag{C.54}$$

with $E_0(t)$ and $E_n(t)$ given in Eq. (C.35) and Eq. (C.36) respectively.

ϕ_2^{**} satisfies the following boundary conditions

$$\begin{cases} \dfrac{\partial \phi_2^{**}}{\partial x} = 0, \quad x = \pm a; \\ \dfrac{\partial \phi_2^{**}}{\partial x} = 0, \quad z = -h; \\ \dfrac{\partial^2 \phi_2^{**}}{\partial t^2} + g\dfrac{\partial \phi_2^{**}}{\partial z} = g\left(-\dot{\xi}_1\dfrac{\partial \eta^{(1)}}{\partial t}\right) + \dfrac{\partial}{\partial t}\left(\dot{\xi}_1\dfrac{\partial \phi^{(1)}}{\partial x}\right) \\ \qquad\qquad = \left\{q_0' + \sum_{n=1}^{\infty} p_n' \sin\left[k_n(x+a)\right]\right\}\sin(2\omega t) \quad on\ z = 0 \end{cases} \tag{C.55}$$

where q_0' and p_n' are defined respectively as

$$q_0' = -\frac{3}{2}\xi_{1a}^2\omega^3, \tag{C.56}$$

$$p_n' = \left[-C_{1,n} + \frac{1}{2}\omega A_n\right]\xi_{1a}\omega k_n. \tag{C.57}$$

Here the coefficients $C_{1,n}$ and A_n have been defined in the last section.

The solution to ϕ_2^{**} is found to be

$$\phi_2^{**} = \left\{E_0' + \sum_{n=1} E_n' \frac{\cosh\left[k_n(z+h)\right]}{\cosh k_n h}\cos\left[k_n(x+a)\right]\right\}\sin(2\omega t) \tag{C.58}$$

with

$$E_0' = -\frac{q_0'}{4\omega^2} - \frac{1}{8\omega^2 a}\sum_{n=1}^{\infty} p_n' \frac{1-(-1)^n}{k_n} \tag{C.59}$$

$$E_n' = \frac{q_0'}{-4\omega^2 + \omega_n^2} \sum_{m=1, m\neq n}^{\infty} p_m' \frac{2m\left[(-1)^m (-1)^n - 1\right]}{\pi\left(n^2 - m^2\right)}. \tag{C.60}$$

According to the Bernoulli's equation in the body-fixed coordinate system, the first-order and second-order hydrodynamic pressure can be written respectively as

$$p^{(1)} = -\rho\phi_t^{(1)} \tag{C.61}$$

$$p^{(2)} = -\rho\frac{\partial\phi^{(2)}}{\partial t} - \frac{1}{2}\rho\nabla\phi^{(1)}\cdot\nabla\phi^{(1)} + \rho\dot{\xi}_1\frac{\partial\phi^{(1)}}{\partial X} \tag{C.62}$$

Appendix D. Elimination of the secular terms in the third-order free-surface conditions

The third-order kinematic and dynamic free-surface conditions can according to Eq.(2.73) and Eq.(2.74) be written respectively as

$$\frac{\partial \eta^{(3)}}{\partial t} = \frac{\partial \phi^{(3)}}{\partial z} + f_1^{(3)}(x,z,t) \quad \text{on z=0,} \tag{D.1}$$

and

$$\frac{\partial \phi^{(3)}}{\partial t} = -g\eta^{(3)} + f_2^{(3)}(x,z,t) \quad \text{on z=0,} \tag{D.2}$$

where the forcing terms are defined as

$$f_1^{(3)} = \left(\eta^{(1)}\frac{\partial^2\phi^{(2)}}{\partial z^2} + \eta^{(2)}\frac{\partial^2\phi^{(1)}}{\partial z^2}\right) + \frac{1}{2}(\eta^{(1)})^2\frac{\partial^3\phi^{(1)}}{\partial z^3} - \left(\frac{\partial\phi^{(1)}}{\partial x}\cdot\frac{\partial\eta^{(2)}}{\partial x} + \frac{\partial\phi^{(2)}}{\partial x}\cdot\frac{\partial\eta^{(1)}}{\partial x}\right) - \eta^{(1)}\frac{\partial\eta^{(1)}}{\partial x}\frac{\partial^2\phi^{(1)}}{\partial x\partial z}, \tag{D.3}$$

$$f_2^{(3)} = -\nabla\phi^{(1)}\cdot\nabla\phi^{(2)} - \eta^{(1)}\nabla\left(\frac{\partial\phi^{(1)}}{\partial z}\right)\cdot\nabla\phi^{(1)} - \left(\eta^{(1)}\frac{\partial^2\phi^{(2)}}{\partial z\partial t} + \eta^{(2)}\frac{\partial^2\phi^{(1)}}{\partial z\partial t}\right) - \frac{1}{2}\left(\eta^{(1)}\right)^2\frac{\partial^3\phi^{(1)}}{\partial z^2\partial t}. \tag{D.4}$$

The combination of the kinematic and dynamic free-surface condition can be obtained as

$$\frac{\partial^2\phi^{(3)}}{\partial t^2} + g\frac{\partial\phi^{(3)}}{\partial z} = q^{(3)}(x,z,t) \quad \text{on z=0,} \tag{D.5}$$

with

$$q^{(3)} = \frac{\partial f_2^{(3)}}{\partial t} - gf_1^{(3)}. \tag{D.6}$$

Taking the deepwater wave as an example, we have

$$\begin{cases} \phi^{(1)} = \dfrac{gA}{\omega}\dfrac{\cosh\left[k(z+h)\right]}{\cosh(kh)}\sin(kx-\omega t) \\ \phi^{(2)} = 0 \end{cases} \tag{D.7}$$

and

$$\begin{cases} \eta^{(1)} = A\cos(kx-\omega t) \\ \eta^{(2)} = \dfrac{1}{2}kA^2\cos 2(kx-\omega t) \end{cases}. \tag{D.8}$$

Applying Eq.(D.3), Eq.(D.4) and Eq.(D.6) - Eq.(D.8) in Eq.(D.5) and evaluating the forcing term on z=0, we obtain

$$\frac{\partial^2\phi^{(3)}}{\partial t^2} + g\frac{\partial\phi^{(3)}}{\partial z} = A_1\sin(kx-\omega t) + A_3\sin 3(kx-\omega t), \tag{D.9}$$

where

$$A_1 = k^2 A^3 g\omega\,, \quad A_3 = 0\,. \tag{D.10}$$

For deepwater case, we have that A_3=0. This explains $\phi^{(3)} = 0$ for the Stokes third-order wave in deep water. The forcing term associated with A_1 on the right-hand side of Eq.(D.9) is the source of secularity. In the frequency-domain analysis of Stokes third-order wave, this term is eliminated by enforcing a nonlinear dispersion relationship (see e.g. Eq.(6.21)). However, in the time-domain analysis where the problem is treated as an initial value problem, there is no rational way to modify the dispersion relationship.

Let's show how the two timescale approach described in Section 6.4 eliminate the secular term. Replacing $\partial/\partial t$ by $\left(1+0.5Ck^2A^2\right)\partial/\partial t$ in Eq.(D.1) and Eq.(D.2) and keeping terms of $O\left(\varepsilon^3\right)$, we have

$$\frac{\partial \eta^{(3)}}{\partial t} = \frac{\partial \phi^{(3)}}{\partial z} + f_1^{(3)} - \frac{1}{2}k^2A^2\frac{\partial \eta^{(1)}}{\partial t} \quad \text{on z=0} \tag{D.11}$$

and

$$\frac{\partial \phi^{(3)}}{\partial t} = -g\eta^{(3)} + f_2^{(3)} - \frac{1}{2}k^2A^2\frac{\partial \phi^{(1)}}{\partial t} \quad \text{on z=0.} \tag{D.12}$$

Combination of Eq.(D.11) and Eq.(D.12) gives

$$\frac{\partial^2 \phi^{(3)}}{\partial t^2} + g\frac{\partial \phi^{(3)}}{\partial z} = q^{(3)} - \frac{1}{2}k^2A^2\left(\frac{\partial^2 \phi^{(1)}}{\partial t^2} - g\frac{\partial \eta^{(1)}}{\partial t}\right) \quad \text{on z=0,} \tag{D.13}$$

where $q^{(3)}$ is defined in Eq.(D.6). Substituting $q^{(3)}$, $\phi^{(1)}$ and $\eta^{(1)}$ into Eq.(D.13) leads us to a homogenous third-order free-surface condition, i.e.

$$\frac{\partial^2 \phi^{(3)}}{\partial t^2} + g\frac{\partial \phi^{(3)}}{\partial z} = 0\,. \tag{D.14}$$

This means the two additional terms in Eq.(D.11) and Eq.(D.12) give a contribution that cancels out the secular term in Eq.(D.9), which explains why the two-time scale model succeeds in the reproducing of Stokes third-order waves. It can also be shown that the two-time scale model works for cases with finite water depth by following a similar procedure presented in this appendix. It will not be elaborated here.

Appendix E. Indirect method for the evaluation of forces and moments due to the ϕ_t-term

In this appendix, we will show how to calculate the forces/moments due to the ϕ_t term, i.e.

$$F_i = -\rho \int_{SB} \frac{\partial \phi}{\partial t} n_i dS \,. \tag{E.1}$$

Here F_i (i=1…6) is the component of the force or moment. SB is the body surface. It can be the mean body surface or the instantaneous body surface. This means the method presented here is applicable for both the fully-nonlinear analysis and the weakly-nonlinear analysis based on perturbation scheme. In the weakly-nonlinear problem, ϕ will be replaced by $\phi^{(m)}$ (m=1, 2, 3) in the corresponding order of problems. n_i is the i-th component of the generalized normal vector on the body surface with

$$\left(n_4, n_5, n_6\right) = \left(\vec{r} - \vec{r}_c\right) \times \left(n_1, n_2, n_3\right). \tag{E.2}$$

$\vec{r}$ is the position vector of a point on the body surface. $\vec{r}_c$ is the position vector of the center to which the moments are defined with respect.

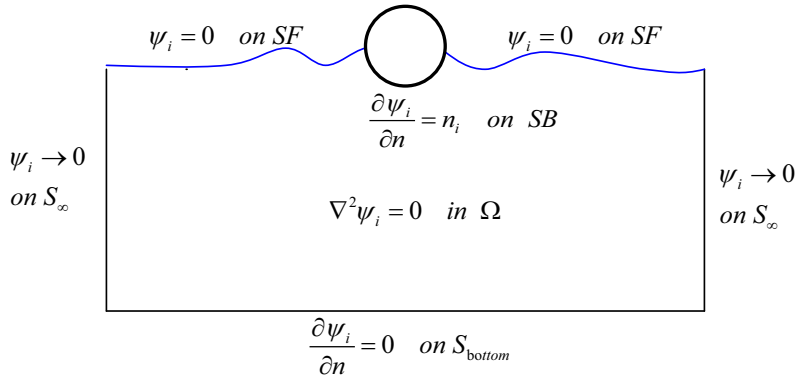

Fig.E.1. Definition of the boundary value problem for the artificial velocity potential ψ_i, i=,1,..,6.

A direct evaluation of Eq.(E.1) requires the solution of $\partial\phi/\partial t$ on the body surface, which needs a solution by solving the Laplace equation. Alternatively, one can use Green's 2nd identity. An artificial velocity potential ψ_i is introduced which satisfies the Laplace equation in the fluid domain, $\psi_i = 0$ on the free surface, $\partial\psi_i/\partial n = n_i$ on the body surface, $\partial\psi_i/\partial n = 0$ on the sea bottom and $\psi_i \to 0$ on a control surface at infinity. See Fig.E.1 for the definitions.

The Green's 2nd identity leads to

$$\int_{SB+SF+S_{bottom}+S_\infty} (\phi_t \frac{\partial \psi_i}{\partial n} - \psi_i \frac{\partial \phi_t}{\partial n}) dS = 0 \,. \tag{E.3}$$

Using the boundary conditions for ϕ_t and ψ_i and Eq.(E.3), we obtain

$$F_i = -\rho \int_{SB} \phi_t n_i dS = -\rho \int_{SB} \phi_t \frac{\partial \psi_i}{\partial n} dS = -\rho \left[\int_{SB} \psi_i \frac{\partial \phi_t}{\partial n} dS - \int_{SF} \phi_t \frac{\partial \psi_i}{\partial n} dS \right] \tag{E.4}$$

It is seen from Eq.(E.4) that the indirect method for the forces/moments evaluation does not require the solution for ϕ_t on the body surface. The ϕ_t needed on the free surface can be obtained from the free-surface condition. For a freely floating body, the $\partial \phi_t / \partial n$ term on the body surface are associated with the acceleration of the body and must be moved to the left-hand side of the body motion equations, otherwise one needs an iterative loop to take into account the coupling between the body motions and the fluid motion. In the forced oscillation or the diffraction problems, this term is known in prior from the body boundary condition. The ψ_i term on the body surface and $\partial \psi_i / \partial n$ on the free surface are obtained from the solution of the ψ_i problem defined in Fig.E.1.

Appendix F. Alternative formulas for the quadratic forces and moments

We consider the term

$$\vec{F} = -\rho \iint_{SB} \frac{1}{2} \nabla\phi \cdot \nabla\phi \, \vec{n}' dS \tag{F.1}$$

$$\vec{M} = -\rho \iint_{SB} \frac{1}{2} \nabla\phi \cdot \nabla\phi \left(\vec{r} \times \vec{n}' \right) dS \tag{F.2}$$

Here $\vec{n}'$ is the normal vector on the body surface defined with respect to the body-fixed reference frame oxyz. $\vec{r}$ is the position vector of a point relative to the center of moment.

By using the following formula given by Newman (1977)

$$\oiint \left[\frac{\partial\phi}{\partial n} \nabla\phi - \frac{1}{2} \nabla\phi \cdot \nabla\phi \, \vec{n} \right] dS = 0 , \tag{F.3}$$

we can rewrite Eq. (F.1) as

$$\vec{F} = -\rho \iint_{SB} \frac{\partial\phi}{\partial n} \nabla\phi \, dS - \iint_{SF1+SC} \left[\frac{\partial\phi}{\partial n} \nabla\phi - \frac{1}{2} \nabla\phi \cdot \nabla\phi \, \vec{n}' \right] dS . \tag{F.4}$$

Here SF1 is the plane with z=0 in the inner domain. SC is the control surface in the inner domain. See Fig.5.1 and Fig.5.2 for the illustration.

Introducing the Stokes expansion of ϕ, e.g. Eq.(2.2), into Eq.(F.4), we have the first-order and the second-order forces described in the body-fixed coordinate system respectively as

$$\begin{aligned} \vec{F}^{(1)} = & -\rho \iint_{SB} \left[\frac{\partial\phi^{(1)}}{\partial n} \nabla\phi^{(0)} + \frac{\partial\phi^{(0)}}{\partial n} \nabla\phi^{(1)} \right] dS \\ & - \iint_{SF1+SC} \left[\frac{\partial\phi^{(1)}}{\partial n} \nabla\phi^{(0)} + \frac{\partial\phi^{(0)}}{\partial n} \nabla\phi^{(1)} - \nabla\phi^{(0)} \cdot \nabla\phi^{(1)} \, \vec{n}' \right] dS \end{aligned} \tag{F.5}$$

$$\begin{aligned} \vec{F}^{(2)} = & -\rho \iint_{SB} \left[\frac{\partial\phi^{(2)}}{\partial n} \nabla\phi^{(0)} + \frac{\partial\phi^{(1)}}{\partial n} \nabla\phi^{(1)} + \frac{\partial\phi^{(0)}}{\partial n} \nabla\phi^{(2)} \right] dS \\ & - \iint_{SF1+SC} \left[\frac{\partial\phi^{(2)}}{\partial n} \nabla\phi^{(0)} + \frac{\partial\phi^{(1)}}{\partial n} \nabla\phi^{(1)} + \frac{\partial\phi^{(0)}}{\partial n} \nabla\phi^{(2)} - \left(\nabla\phi^{(0)} \cdot \nabla\phi^{(2)} + \frac{1}{2} \nabla\phi^{(1)} \cdot \nabla\phi^{(1)} \right) \vec{n}' \right] dS \end{aligned} \tag{F.6}$$

Similarly, if we apply the following equality

$$\oiint \vec{r} \times \left[\frac{\partial\phi}{\partial n} \nabla\phi - \frac{1}{2} \nabla\phi \cdot \nabla\phi \, \vec{n} \right] dS = 0 , \tag{F.7}$$

in Eq.(F.2) and introduce the Stokes expansion for the velocity potential, the first-order and second-order moments can be obtained respectively as

$$\begin{aligned}\vec{M}^{(1)} &= -\rho\iint_{SB}\left[\frac{\partial\phi^{(1)}}{\partial n}\left(\vec{r}\times\nabla\phi^{(0)}\right)+\frac{\partial\phi^{(0)}}{\partial n}\left(\vec{r}\times\nabla\phi^{(1)}\right)\right]dS \\ &\quad -\iint_{SF1+SC}\left[\frac{\partial\phi^{(1)}}{\partial n}\left(\vec{r}\times\nabla\phi^{(0)}\right)+\frac{\partial\phi^{(0)}}{\partial n}\left(\vec{r}\times\nabla\phi^{(1)}\right)-\nabla\phi^{(0)}\cdot\nabla\phi^{(1)}\left(\vec{r}\times\vec{n}'\right)\right]dS\end{aligned}, \tag{F.8}$$

$$\begin{aligned}\vec{M}^{(2)} &= -\rho\iint_{SB}\left[\frac{\partial\phi^{(2)}}{\partial n}\left(\vec{r}\times\nabla\phi^{(0)}\right)+\frac{\partial\phi^{(1)}}{\partial n}\left(\vec{r}\times\nabla\phi^{(1)}\right)+\frac{\partial\phi^{(0)}}{\partial n}\left(\vec{r}\times\nabla\phi^{(2)}\right)\right]d \\ &\quad -\oiint_{SF1+SC}\left[\frac{\partial\phi^{(2)}}{\partial n}\left(\vec{r}\times\nabla\phi^{(0)}\right)+\frac{\partial\phi^{(1)}}{\partial n}\left(\vec{r}\times\nabla\phi^{(1)}\right)+\frac{\partial\phi^{(0)}}{\partial n}\left(\vec{r}\times\nabla\phi^{(2)}\right)\right. \\ &\qquad \left.-\left(\nabla\phi^{(0)}\cdot\nabla\phi^{(2)}+\frac{1}{2}\nabla\phi^{(1)}\cdot\nabla\phi^{(1)}\right)\left(\vec{r}\times\vec{n}'\right)\right]dS\end{aligned}. \tag{F.9}$$

Note that the forces and moments in Eq.(F.5), Eq.(F.6), Eq.(F.8) and Eq.(F.9) are defined with respect to the body-fixed coordinate system. One can always use the transformation matrices defined in Section 2.3 to obtain the corresponding expressions of forces and moments in the inertial coordinate system.

Let's briefly show the derivation of Eq.(F.7) according to Faltinsen (2010). By using the following two equalities

$$\vec{r}\times\left(\frac{\nabla\phi\cdot\nabla\phi}{2}\right)\vec{n}' = -\vec{n}'\times\vec{r}\left(\frac{\nabla\phi\cdot\nabla\phi}{2}\right), \tag{F.10}$$

$$\vec{r}\times\frac{\partial\phi}{\partial n}\nabla\phi = \vec{n}'\cdot\nabla\phi\left(\vec{r}\times\nabla\phi\right), \tag{F.11}$$

and the generalized Gauss theorem, the we can rewrite on the left-hand side of Eq.(F.7) as

$$\begin{aligned}&\oiint\vec{r}\times\left[\frac{\partial\phi}{\partial n}\nabla\phi-\frac{1}{2}\nabla\phi\cdot\nabla\phi\,\vec{n}\right]dS \\ &=\oiint\vec{n}'\cdot\nabla\phi\left(\vec{r}\times\nabla\phi\right)dS+\oiint\vec{n}'\times\vec{r}\left(\frac{\nabla\phi\cdot\nabla\phi}{2}\right)dS \\ &=\underbrace{\iiint\nabla\cdot\left[\nabla\phi\left(\vec{r}\times\nabla\phi\right)\right]d\tau}_{=I_1}+\underbrace{\iiint\nabla\times\left[\vec{r}\left(\frac{\nabla\phi\cdot\nabla\phi}{2}\right)\right]d\tau}_{=I_2}\end{aligned}. \tag{F.12}$$

The integrand of the integral of I_1 in Eq.(F.12) can be rewritten as

$$\begin{aligned}&\nabla\cdot\left[\nabla\phi\left(\vec{r}\times\nabla\phi\right)\right] \\ &=\vec{e}_i\frac{\partial}{\partial x_i}\left[V_j\vec{e}_j\left(x_k\vec{e}_k\times V_m\vec{e}_m\right)\right]\end{aligned}$$

$$= \frac{\partial}{\partial x_j}\left[V_j\left(x_k\vec{e}_k \times V_m\vec{e}_m\right)\right]$$

$$= \underbrace{\frac{\partial V_j}{\partial x_j}}_{=\nabla\cdot(\nabla\phi)=0}\left(x_k\vec{e}_k \times V_m\vec{e}_m\right) + V_j\frac{\partial}{\partial x_j}\left(x_k\vec{e}_k \times V_m\vec{e}_m\right)$$

$$= \underbrace{V_j\left(\frac{\partial x_k}{\partial x_j}\vec{e}_k \times V_m\vec{e}_m\right)}_{=\nabla\phi\times\nabla\phi=0} + V_j\left(x_k\vec{e}_k \times \frac{\partial V_m}{\partial x_j}\vec{e}_m\right)$$

$$= \vec{r}\times\left[\nabla\phi\cdot\nabla\left(\nabla\phi\right)\right]. \tag{F.13}$$

Here $\vec{e}_i$, $\vec{e}_j$, $\vec{e}_k$ and $\vec{e}_m$ (*i, k, m* =1, 2, 3) are unit vectors along the *i*-th, *j*-th, *k*-th and *m*-th axis, respectively. V_i, V_j, V_k and V_m are the *i*-th, *j*-th, *k*-th and *m*-th components of $\nabla\phi$. x_i, x_j, x_k and x_m are the *i*-th, *j*-th, *k*-th and *m*-th components of $\vec{r}$.

The integrand of the integral of I_2 in Eq.(F.12) can be rewritten as

$$\begin{aligned}
\nabla\times\left[\vec{r}\left(\frac{\nabla\phi\cdot\nabla\phi}{2}\right)\right] &= \vec{e}_i\frac{\partial}{\partial x_i}\times\left(x_j\vec{e}_j\frac{\left|\nabla\phi\right|^2}{2}\right)\\
&= \vec{e}_i\times\vec{e}_j\left[\frac{\partial x_j}{\partial x_i}\frac{\left|\nabla\phi\right|^2}{2} + x_j\frac{\partial}{\partial x_i}\frac{\left|\nabla\phi\right|^2}{2}\right]\\
&= \vec{e}_i\frac{\partial}{\partial x_i}\left(\frac{\left|\nabla\phi\right|^2}{2}\right)\times\left(\vec{e}_j x_j\right)\\
&= -\vec{r}\times\nabla\left(\frac{\left|\nabla\phi\right|^2}{2}\right)
\end{aligned} \tag{F.14}$$

Considering Eq.(F.13) and Eq.(F.14) in Eq.(F.12), it is immediately apparent to us that the equality of Eq.(E.7) holds.

References

Aanesland, V., Faltinsen, O.M. and Zhao, R. (1990). Wave-drift damping of a TLP. *Advances in Underwater Technology and Offshore Engineering*. Environmental Forces on Offshore Structures and Their Predictions, 26, 383-400.

Arfken, G. and Weber, H.J. (2001). *Mathematical methods for physicists*. Academic Press, SanDiego.

Bai, W. (2001), Non-linear wave interaction with arbitary 3-D bodies. Ph.D Thesis. Dalian University of Technology, (in Chinese).

Bai, W. and Eatock Taylor, R. (2007). Numerical simulation of fully nonlinear regular and focused wave diffraction around a vertical cylinder using domain decomposition. *Appl. Ocean Res.*, 29, 55-71.

Bai, W. and Eatock Taylor, R. (2009). Fully nonlinear simulation of wave interaction with fixed and floating flared structures. *Ocean Eng.*, 36, 223-236.

Bertram, V. (2000). *Practical ship hydrodynamics.* Butterworth-Heinemann.

Bingham, H.B. and Maniar, H.D. (1996). Computing the double-body m-terms using a B-spline based panel method. *11th Int. Workshop on Water Waves and Floating Bodies*.

Board, J.A and Schulten, L. (2000). The fast multipole algorithm. *Comput. Sci. Eng.*, 2, 1, 76-9.

Board, J.A., Causey, J.W., Leathrum, J.F., Windemuth, A. and Schulten, K. (1992). Accelerated molecular dynamics simulation with the parallel fast multipole algorithm. *Chem. Phys. Lett.,* 89-94.

Brebbia, C.A, and Dominguez, J. (1992). *Boundary elements: an introductory course*. Computational mechanics publications (McGraw-Hill),London.

Brebbia, C.A. (1978). *The boundary element method for engineers*. Pentech Press, London, Halstead Press, New York.

Brorsen, M. and Larsen, J. (1987). Source generation of nonlinear gravity waves in the boundary integral method. *Coastal Eng*, 11, 2, 93-113.

Büchmann, B. (1995). A 2-D Numerical Wave Flume Based on a Third Order Boundary Element Model. M.Sc. Thesis. Department of Hydrodynamics and Water Resources, Technical University of Denmark.

Büchmann, B. (2000a). Time-domain modeling of run-up on offshore structures in waves and currents. Ph.D. thesis, Department of Hydrodynamics and Water Resources, Technical University of Denmark, Series Paper No. 71.

Büchmann, B. (2000b). Accuracy and stability of a set of free-surface time-domain boundary element models based on B-splines. *Int. J. Numer. Methods Fluids*. 33, 1, 125-55.

Büchmann, B., Skourup, J, and Cheung, F.C. (1998). Run-up on a structure due to second-order waves and a current in a numerical wave tank. *Appl. Ocean Res.*, 20, 5, 297-308.

Bunnik, T.H.J. (1999). Seakeeping Calculations for Ships, Taking into Account the Non-Linear Steady Waves, PhD thesis, Delft University of Technology, The Netherlands.

Cao, Y., Beck, R. and Schultz, W.W. (1994), Nonlinear motions of floatingb odies in incident waves, *9th Int. Workshop on Water Waves and Floating Bodies*, 33-37.

Cao, Y., Schultz, W. and Beck, R.F. (1991). A three-dimensional desingularized boundary integral method for potential problems. *Int. J. Numer. Methods Fluids* , 12, 785-803.

Chatjigeorgiou, I.K. and Mavrakos, S.A. (2007). Second-order sum-frequency wave diffraction by a truncated surface-piercing cylinder in bichromatic waves. *J. Marine Sci. Technol.*, 12, 218-231.

Chatjigeorgiou, I.K. and Mavrakos S.A. (2009). An analytical approach for the solution of the hydrodynamic diffraction by arrays of elliptical cylinders. *Appl. Ocean Res.*, doi:10.1016/j.apor.2009.11.004.

Chau, F.P. (1989). The second order velocity potential for diffraction of waves by fixed offshore structures. Ph.D. Thesis, Department of Mechanical Engineering, University College London.

Chau, F.P. and Taylor, R.E. (1988). Second-order velocity potential for arbitrary bodies in waves. 3rd *Int. Workshop on Water Waves and Floating Bodies*.

Chau, F.P. and Taylor, R.E. (1992). Second-order wave diffraction by a vertical cylinder. *J. Fluid Mech.*, 240, 571-99.

Chen, X. B., Diebold, L., and Doutreleau, Y. (2000). New green function method to predict wave-induced ship motions and loads, *Proc. of 23rd Symposium on Naval Hydrodynamics*, Val DE Reuil, France, 18-33.

Chen, X.B. (2004) New formulations of the second-order wave loads. Rapp. Technique, NT2840/DR/XC, Bureau Veritas, Paris (France).

Chen, X.B. (2007). Middle-field formulation for the computation of wave-drift loads. *J. Eng. Math.*, 59, 61-82.

Chen, X.B. and Malenica, S. (1998). Interaction effects of local steady flow on wave diffraction-radiation at low forward Speed. *Int. J. Offshore Polar Eng.,* Vol.8, 2, 102-109.

Chen, X.B., Molin, B. and Petitjean, F. (1995). Numerical evaluation of the springing loads on tension leg platforms. *Mar. Struct.*, 8, 501-524.

Cheng, H., Greengard, L.F. and Rokhlin, V. (1999). A fast adaptive multipole algorithm in three dimensions. *J. Comput. Phys.* 155, 2, 468-98.

Cheung, K.F. and Isaacson, M. (1993). Time-domain solution for second-order wave radiation. *Mar Struct*, 6, 241-258.

Cheung, K.F., Isaacson, M., and Lee, J.W. (1996). Wave diffraction around a three-dimensional body in a current. *J. Offshore Mech. Arct*. Eng., 118, 4, 247–252.

Choi, Y.R., Hong S.Y. and Choi, H.S. (2001). An analysis of second-order wave forces on floating bodies by using a higher-order boundary element method. *Ocean Eng.,* 28, 117-138.

Chung, T.J.(2002). *Computational fluid dynamics*. Cambridge University Press.

Clement, A. (1996). Coupling of two absorbing boundary conditions for 2D time-domain simulations of free surface gravity waves. *J. Comp. Phys.* 126, 139–151.

Cointe, R., Molin, B. and Nays, P. (1988). Nonlinear and second-order transient waves in a rectangular tank. In: *Proc. behavior of offshore structural systems conf.*

Cointe,R., Geyer,P., King, B., Molin,B. and Tramoni, M. (1990). Nonlinear and linear motions of a rectangular barge in perfect fluid, *Proc. of the 18th Symp. On Naval Hydro.*, AnnArbor, Michigan, 85-98.

Cummins, W.E. (1962). The impulse response function and ship motions, *Schiffstechnik*, 9, 47, 101-9.

Dai, Y.S. (1998). *Potential flow theory of ship motions in waves in frequency and time domain (in Chinese)*. Press of the National Defense Industries, Beijing, China.

Dai, Y.S., Chen, X.B. and Duan, W.Y. (2005). Computation of low-frequency loads by the middle-field formulation. *20th Int. Workshop on Water Waves and Floating Bodies.*

Dalzell, J.F. (1999). A note on finite depth second-order wave-wave interactions. *Appl. Ocean Res.*, 21, 3, 105-111.

Dean, R.G. and Dalrymple, R.A. (1991). *Water wave mechanics for engineers & scientists,* World Scientific Publishing Company.

Delves, L.M. and Walsh, J. (eds.). *Numerical Solution of Integral Equations*, Oxford University Press.

Duan, W.Y. and Price, W.G. (2002). A numerical method to solve the mj-terms of a submerged body with forward speed. *Int J Numer Methods Eng*, 40, 655-667, 2002.

Eatock Taylor, R. and Chau, F.P. (1992). Wave diffraction theory - some developments in linear and nonlinear theory. *J Offshore Mech Arct Eng*. 114, 3, 185-194.

Eatock Taylor, R. and Huang J.B. (1997). Semi-analytical formulation for second-order waves diffracted by a vertical cylinder in bichromatic waves, *J. Fluids and Structures*, 11, 465-484.

Eatock Taylor, R. and Hung S.M. (1987). Second order diffraction forces on a vertical cylinder in regular waves, *Appl. Ocean Res.,* 9, 19-30.

Eatock Taylor, R. and Teng, B. (1993). Effect of corners on diffraction/radiation forces and wave drift damping. *Proc Annu Offshore Technol Conf,* 2, 571-578.

Engsig-Karup, A. P. and Bingham, H. B. (2009). Boundary-Fitted Solutions for 3D Nonlinear Water Wave-Structure Interaction, *24th Int. Workshop on Water Waves and Floating Bodies.*

Etekin, B. and Reid L.D. (1996). *Dynamic of flight stability and control,* 3rd edition. John Wiley & Sons, Inc.

Faltinsen, O.M. (1974a). A numerical investigation of the Ogilvie-Tuck formulas for added-mass and damping coefficients. *J. Ship Res.,* 18, 73–84.

Faltinsen, O M. (1974b). A nonlinear theory of sloshing in rectangular tanks. *J. Ship Res.,* 18, 224–241.

Faltinsen, O.M. (1990). *Sea loads on ships and offshore structures.* Cambridge University Press, 1990.

Faltinsen, O.M. (1976). Slow-drift excitation of a ship in irregular beam sea waves. DNV Report, No.76-083.

Faltinsen, O.M. (1977). Numerical solutions of transient nonlinear freesurface motion outside or inside moving bodies, *Second International Conference on Numerical Ship Hydrodynamics*, University of California, Berkeley.

Faltinsen, O.M. (1978). A numerical nonlinear method of sloshing in tanks with two dimensional flow. *J Ship Res*, 22(3), 193-202

Faltinsen, O.M. (1994). Wave and current induced motions of floating production systems. *Appl. Ocean Res.*, 15, 351-370.

Faltinsen, O.M. (2005). *Hydrodynamics of high-speed marine vehicles*, Cambridge University Press.

Faltinsen, O.M. (2010). Hydrodynamic force and moment on maneuvering ship in interaction with other ships at low Froude number. Unpublished Technical Notes.

Faltinsen, O.M. and Loken, A.(1978). Drift forces and slowly-varying horizontal forces on a ship in waves, *Symposium on Applied Mathematics dedicated to the late Prof.Dr.R.Timman*. Delft The Netherlands, January, 1978.

Faltinsen, O.M. and Timokha, A.N. (2009). *Sloshing*, Cambridge University Press.

Faltinsen, O.M. and Timokha, A.N. (2010a). Multimodal method for 2D sloshing in a circular tank. *25th Int. Workshop on Water Waves and Floating Bodies*.

Faltinsen, O.M. and Timokha, A.N. (2010b). A multimodal method for liquid sloshing in a two-dimensional circular tank. *J. Fluid Mech*. To appear.

Faltinsen, O.M., Minsaas, K., Liapis, N. and Skjordal, S.O. (1981). Prediction of resistance and propulsion of a ship in a seaway. In *Proc. 13th Symposium on Naval Hydrodynamics: Impact of Hydrodynamics Theory Upon Design Practice, with Emphasis on High Performance and/or Energy Saving Ships*. 505-529.

Faltinsen, O.M., Newman, J.N., and Vinje, T. (1995). Nonlinear wave loads on a slender vertical cylinder, *J. Fluid Mech.*, 289, 179-198.

Ferrant, P.(1998). Fully nonlinear interactions of long-crested wave packets with a three dimensional body. In: *Proc. of the 22nd ONR symposium on naval hydrodynamics*, 403–15.

Ferrant, P.(2001). Runup on a cylinder due to waves and current: Potential flow solution with fully nonlinear boundary conditions. *Int. J. Offshore Polar Eng.* 33-41.

Fochesato, C. and Dias, F. (2006). A fast method for nonlinear three-dimensional free-surface waves. *Proc. R. Soc. Lond. A, Math. Phys. Eng. Sci.*, 465, 2715-35.

Gradshteyn, I.S. and Ryzhik, I.M. (2007). *Tables of integrals, series and products,* 7th Edition. Translated from Russian by Scripta Technica, Inc.

Greco, M. (2001). A two-dimensional study of green-water loading. PhD thesis, Dept of Marine. Hydrodynamics, NTNU, Trondheim, Norway.

Greengard, L.F. (1988). Rapid evaluation of potential fields in particle systems. Ph.D thesis, Yale Univ., New Haven, CT. Dept. of Computer Science.

Grilli, S.T. and Svendsen, I.A. (1990). Corner problems and global accuracy in the boundary element solution of nonlinear wave flows. *Eng. Anal. Bound. Elem.,* 7 (4), 178-195.

Huang Y.F. (1996). Nonlinear ship motions by a rankine panel method. PhD Thesis, MIT, Cambridge, MA.

Huang, J.B. and Eatock Taylor, R. (1996). Semi-analytical solution for second-order wave diffraction by a truncated circular cylinder in monochromatic waves. *J. Fluid Mech.,* 319, 171-96.

Huang, J.B. and Eatock Taylor, R. (1997). Second-order interaction of irregular waves with a truncated column. *Acta Mech. Sin.,* 13, 130-42.

Hulme, A. (1982). The wave forces acting on a floating hemisphere undergoing forced periodic oscillations. *J. Fluid Mech.,* 121, 443-63.

Hunt, J.N. and Baddour, R.E. (1980). Nonlinear standing waves bounded by cylinders. *Quart. J. Mech. Appl. Math*., 33, Part 3, 357-371.

Inglis, R..B. and Price, W.G. (1981). The Influence of Speed Dependent Boundary Condition in Three-dimensional Ship Motion Problems. *Int Shipbuilding Progress,* 28, 318, 22-29.

Isaacson, M. (1977). Nonlinear wave forces on large offshore structures. *J. WatWay, Port, Coastal Ocean Engng, ASCE*, 103, 166-170.

Isaacson, M. and Cheung, K.F. (1990). Time-domain solution for second-order wave diffraction. *J. Waterw. Port Coastal Ocean Eng.* 16, 2, 191-210.

Isaacson, M. and Cheung, K.F. (1991). Second order wave diffraction around two-dimensional bodies by time-domain method. *Appl. Ocean Res.,* 13, 175-86.

Isaacson, M. and Cheung, K.F. (1992). Time-domain second-order wave diffraction in three dimensions. *J Waterw Port Coastal Ocean Eng,* 118, 496-516.

Isaacson, M. and Ng, J.Y.T. (1993a). Time-domain second-order wave radiation in two dimensions. *J Ship Res.* 37, 1, 25-33.

Isaacson, M. and Ng, J.Y.T. (1993b). Second-order wave radiation of three-dimensional bodies by time-domain method, *Int. J. Offshore of Polar Eng.,* 13, 4, 264-272, 1993.

Iwashita, H. and Bertram, V. (1997). Numerical study on the influence of the steady flow in seakeeping. *12th Int. Workshop on Water Waves and Floating Bodies.*

Iwashita, H. and Ito, A. (1998). Seakeeping computations of a blunt ship capturing the influence of the steady flow. *Ship Technol Res,* 45, 4, 159-171.

Iwashita, H. and Ohkusu, M. (1989). Hydrodynamic forces on a ship moving at forward speed in waves. *Journal of the Society of Naval Architects of Japan,* 166, 87-109.

Jensen, J.J. et al. (2000). *Report of ISSC Committee VI.1. Extreme Hull Girder Loading.* ISSC, Nagasaki, Japan, Proc. published by Elsevier, Amsterdam.

Kashiwagi, M. (1998). Nonlinear simulations of wave-induced motions of a floatingb ody by means of MEL method, *Proc. of 3rd Int. Conf. on Hydrodynamics*, Seoul.

Kim et al. (2008). Comparative study on time-domain analysis of ship motions and structural loads in waves. *Proc Int Offshore Polar Eng Conf.* 335-340.

Kim, B. (2005). Some considerations on forward-speed seakeeping calculations in frequency domain. *Int. J. Offshore Polar Eng.,* 15, 189-197.

Kim, C.H., Clement, A. and Tanizawa, K., (1999). Recent research and development of numerical wave tanks—a review. *Int. J. Offshore Polar Eng.,* 9, 241–256.

Kim, D.J., and Kim, M.H. (1997). Wave-Current-Body interaction by a time-domain high-order boundary element method. *Proc Int Offshore Polar Eng Conf,* 3, 107-115.

Kim, K.H. and Kim, Y.H. (2008). On technical issues in the analysis of nonlinear ship motion and structural loads in waves by a time-domain rankine panel method. *23rd Int. Workshop on Water Waves and Floating Bodies.*

Kim, M.H. and Yue, D.K.P. (1989). The complete second-order diffraction solution for an axisymmetric body. Part 1. Monochromatic incident waves, *J. Fluid Mech.,* 200, 235-264.

Kim, M.H. and Yue, D.K.P. (1990). The complete second-order diffraction solution for an axisymmetric body. II. Bichromatic incident waves and body motions. *J. Fluid Mech.,* 211, 557-93.

Kim, Y., Kring. D.C. and Sclavounos, P.D. (1997). Linear and nonlinear interactions of surface waves with bodies by a three-dimensional rankine panel method. *Appl. Ocean Res.,* 19, 235-249.

Kinoshita, T. and Bao, W. (1996). Hydrodynamic forces acting on a circular cylinder oscillating in waves and a small current. *J Mar Sci Technol*, 1, 155-173.

Kinoshita, T. and Bao, W. (2000). Third-order wave diffraction by a truncated circular cylinder. *Proc. Inst. Mech. Eng. Part C J. Mech. Eng.*, 214, 789-800.

Kinoshita, T., Bao, W. and Zhu. R. (1997). Higher-order boundary element method for the interaction of a floating body with both waves and slow current. *J Mar Sci Technol,* 2, 268-279.

Kong, X.J. (2009). A numerical study of a damaged ship in beam sea waves. PhD thesis, Dept of Marine. Hydrodynamics, NTNU, Trondheim, Norway.

Koo, W.C. and Kim, M.H. (2004). Freely floating-body simulation by a 2D fully nonlinear numerical wave tank, *Ocean Eng.* 31, 2011–2046.

Kravtchenko (1954). Remarques sur le Calcul des Amplitudes de la Houle Linéaire Engendrée par un Batteur, *Proceedings of the Fifth Conference on Coastal Engineering*. 50-61.

Kring, D.C. (1994). Time domain ship motions by a three-dimensional rankine panel method . PhD Thesis, MIT, Cambridge, MA.

Kring, D.C. and Sclavounos, P.D. (1995). Numerical stability analysis for time-domain ship motion simulations. *J Ship Res.* 39, 4, 313-320.

Kring, D.C., Korsmeyer, T., Singer, J. and White, J. (2000). Analyzing mobile offshore bases using accelerated boundary-element methods. *Mar. Struct.* 13, 301-313.

Kudou, K. (1977). The drifting force acting on a three-dimensional body in waves. *J. Soc. Naval Arch. of Japan,* 141.

Kyozuka, Y. (1980). Non-linear hydrodynamic forces acting on two-dimensional bodies (1st report, diffraction problem), in Japanese, *J. Soc. Naval Arch. of Japan,* 148, 49-57.

Kyozuka, Y. (1982). Experimental study on Second order forces acting on cylinder body in waves. *Proc. 14th Symposim on Naval Hydrodynamics*, Ann Arbor, Mich., 319-382.

Lee, C.H. (2007). On the evaluation of quadratic forces on stationary bodies. *J. Eng. Math.*, 58, 141-148.

Lee, C.H. et al. (2002). Integration of geometry definition and wave analysis software. *Proc Int Conf Offshore Mech Arct Eng - OMAE*, 1, 721-733.

Lee, C.M. (1966). The second-order theory of heaving cylinders oscillating vertically in a free surface, Report No.NA-66-7., Univ. of California, Berkely.

Li, H.B., Han, G.M, and Mang, H.A. (1985). A new method for evaluating singular integrals in stress analysis of solids by the direct boundary element method. *Int J Numer Methods Eng. 21*, 2071-2098.

Lighthill, M.J.(1979). Waves and hydrodynamic loading. *Proc. of second International Conference on the Behaviour of Offshore Structures*, London, 1-40.

Liu, Y.H., Kim, C.H. and Kim, M.H. (1993). Computation of mean drift forces and wave run-up by higher-order boundary element method. *Int J Offshore Polar Eng,* 3, 2, 101-106.

Liu, Y.H., Kim, C.H., and Lu, S.X. (1991). Comparison of higher-order boundary element and constant panel method for hydrodynamic loadings, *J. Offshore Mech. Arct. Eng.,* 1, 1, 8-17.

Liu, Y.H., Kim, M.H., and Kim, C.H. (1995). The computation of second-order mean and double-frequency wave loads on a compliant TLP by HOBEM. *Int J Offshore Polar Eng,* 5, 2.

Liu, Y.H., Kim, M.H., and Kim, C.H. (1995). The computation of second-order mean and double-frequency wave loads on a compliant TLP by HOBEM. *J. Offshore Mech. Arct. Eng.,* 5, 2, 111-119.

Liu, Y.J. (2009). *Fast multipole boundary element method - theory and applications in engineering*, Cambridge University Press, Cambridge.

Loken, A.(1986). Three dimensional second order hydrodynamic effects on ocean structures in waves, Ph.D. Thesis, Dept. Marine Technology, NTNU.

Longuet-Higgins, M.S. and Cokelet, E.D. (1976). The deformation of steep surface waves on water: I. a numerical method of computation, *Proc. R. Soc. Lond. A, Math. Phys. Sci.* , 350, 1-26.

Ma, Q.W., Wu, G.X. and Eatock Taylor, R. (2001a). Finite element simulation of fully non-linear interaction between vertical cylinders and steep waves. 1. Methodology and numerical procedure. *Int. J. Numer. Methods Fluids. 3*6, 3, 265-85.

Ma, Q.W., Wu, G.X. and Eatock Taylor, R. (2001b). Finite element simulations of fully non-linear interaction between vertical cylinders and steep waves. 2. Numerical results and validation. *Int. J. Numer. Methods Fluids.* 36, 3, 287-308.

MacCamy, R. C. and Fuchs, R. A. (1954). Wave forces on piles: a diffraction theory. Report No. TM-69. Corps of Engineers Washington D C Beach Erosion Board.

Madsen, O.S. (1971). On the generation of long waves. *J. Geophys. Res.*, 76, 36, 8672-83.

Malenica, S. and Molinm B. (1995). Third harmonic wave diffraction by a vertical cylinder. *J. Fluid Mech*, 302, 203-229, 1995.

Malenica, S., Clark, P.J. and Molin, B. (1995). Wave and current forces on a vertical cylinder free to surge and sway. *Appl. Ocean Res.*, 17, 79-90.

Malenica, S., Eatock Taylor, R. and Huang, J.B. (1999). Second-order water wave diffraction by an array of vertical cylinders. *J. Fluid Mech.,* 390, 349-73.

Maniar, H.D. (1995). A three dimensional higher order panel method based on B-splines. Ph.D thesis, MIT, 1995.

Markiewicz, M., Letkowski, P. and Mahrenholtz, O. (1999). Third-order hydrodynamic loads on an oscillating vertical cylinder in water. *J. Offshore Mech. Arct. Eng,* 121, 16-21.

Maruo, H. (1960). The drift of a body floating in waves. *J. Ship. Res.,* 4, 3, 1-10.

McIver, M. (1994). Second-order wave diffraction in two dimensions, *Appl. Ocean Res.* 16, 19–25.

Miao, G.P. and Liu, Y.Z. (1989). A theoretical study on second-order wave forces for twodimensional bodies, *J. Offshore Mechanics and Arctic Engineering*, 111, 37–42.

Miloh, T. (1980). Irregularities in Solutions of Nonlinear Wave Diffraction Problem by Vertical Cylinder. *J. WatWay, Port, Coastal Ocean Engng, ASCE*, 106, 279-284.

Moiseev., N.N. (1958). To the theroy of nonlinear oscillations of a limited liquid volume of a liquid. *Applied Mathematics and Mechanics (PMM)* 22, 612-621, (in Russian).

Molin, B.(1979). Second-order diffraction loads upon three-dimensional bodies, *Appl. Ocean Res.,* 1, 197-202.

Molin, B., and Stassen, Y. (1998). A procedure to remove secularity in third-order numerical wave tanks, *13th Int. Workshop on Water Waves and Floating Bodies.*

Montic, V. (1993). A new formula for the C-matrix in the Somigliana identity, *J. Elast.,33*, 191–201.

Mouhayed, W. I. and Williams, A.N. (1995). Second-Order hydrodynamic interactions in an array of vertical cylinders in bichromatic waves,*J. Fluid and Structures,* 9, 61-98.

Newman, J. N. (1977). *Marine hydrodynamics*. Cambridge, MA: MIT Press.

Newman, J. N., and Lee, C.-H. (1992). Sensitivity of wave loads to the discretization of bodies. Proc. of 6th Int. Conf. on Behavior of Offshore Structures (BOSS '92), 1, 50–64.

Newman, J.N. and Lee, C.H. (2002). Boundary-element methods in offshore structure analysis. *J. Offshore Mech. Arct. Eng.*, 124, 81-89.

Ng, J.Y.T. and Isaacson, M. (1993). Second-order wave interaction with two-dimensional floating bodies by a time-domain method. *Appl. Ocean Res.*, 15, 95-105.

Ning D.Z., Teng B., Zhao H.T. and Hao C.L. (2010). A comparison of two methods for calculating solid angle coefficients in a BIEM numerical wave tank. *Eng. Anal. Bound. Elem.* 34, 1, 92-6.

Nishida, T. and Hayami, K. (1997). Application of the fast multipole method to the 3D BEM analysis of electron guns. In: Marchettia M, Brebbia CA, Aliabadi MH editor. *Boundary Elements XIX*, Computational Mechanics Publications, 613–22.

Nishimura, N. (2002). Fast multipole accelerated boundary integral equation methods. *Appl Mech Rev*, 55, 4, 299-324.

Ogilvie, T.F. (1963). First- and second-order forces on a cylinder submerged under a free surface. *J. Fluid Mech.*, 16, 451-72.

Ogilvie, T.F. (1964). Recent progress towards the understanding and prediction of ship motions. In *Proc. Fifth Symp. On Naval Hydrodynamics*. 3-128.

Ogilvie, T.F. (1983). Second-order hydrodynamic effects on ocean platforms. *International* Workshop *on Ship and Platform Motions*. Univ. Calif. Berkeley.

Ogilvie, T.F. and Tuck, E.O. (1969). A rational strip theory of ship motions: Part I, Report No.013, Michigan Univ. Ann Arbor, Dept. of Naval Architecture and Marine Engineering, 1969.

Orlanski, I.(1976). A simple boundary condition for unbounded hyperbolic flows. *J. Comput. Phys.*, 21, 251-69.

Papanicolaou, A. and Nowacki, A. (1980). Second-order theory of oscillating cylinders in a regular steep wave, Proc. 13th Symp. on Naval Hydrod., 303-333.

Parissis, G.C. (1966). Second-order potentials and forces for oscillating cylinders on a free surface, MIT-Rept. No. 66-10, Dept. of Ocean Eng., MIT.

Phillips, J.R. and White, J.K. (1997). A precorrected FET method for electrostatic analysis of complicated 3-d structures. *IEEE Trans. Comput-Aided Des*, 16(10), 1059–72.

Pinkster, J.A. (1980), Low frequency second order wave exciting forces on floating structures PhD. Thesis. TU Delft.

Potash, R.L. (1971). Second-order theory of oscillating cylinders, *J. Ship Res.,* 15, 295-324.

Prins, H. J. (1995). Time-domain calculations of drift forces and moments, Doctor Thesis, TU-Delft.

Raven, H.C. (1996). A solution method for the nonlinear ship wave resistance problem. Doctor's Thesis, Delft Univ. Techn., Delft, Netherlands.

Riley, K.F., Hobson, M.P. and Bence, S.J. (2006). *Mathematical methods for physics and engineering. 3rd Edition.* Cambridge University Press.

Rognebakke O.F. and Faltinsen O.M. (1999). A second-order initial value solution of two-dimensional sloshing in rectangular tanks. *14th Int. Workshop on Water Waves and Floating Bodies.*

Rokhlin, V. (1985). Rapid solution of integral equations of classical potential theory. *J. Comput. Phys.,* 60, 2, 187-207.

Romate, J.E. (1992). Absorbing boundary conditions for free surface waves. *J. Comput. Phys.,* 1, 135-45.

Saad, Y. and Schultz, M.H. (1986). GMRES: a generalized minimal residual algorithm for solving nonsymmetric linear systems. *SIAM J. Sci. Stat. Comput.,* 7, 3, 856-69.

Salmon, J.K., Warren, M.S. and Winckelmans, G.S. (1994). Fast parallel tree codes for gravitational and fluid dynamical N-body problems. *Int. J. Supercomput. Appl.,* 8, 2, 129-42.

Salvesen, N., Tuck, E.O. and Faltinsen, O.M. (1970). Ship motions and sea loads. In *Transactions of the Society of Naval Architects and Marine Engineers*, 78, 250–287.

Schaffer, H.A. (1996). Second-order wavemaker theory for irregular waves. *Ocean Eng. 23*, 1, 47-88.

Sclavounos, P.D. (1988). Radiation and diffraction of second-order surface waves by floating bodies. *J. Fluid Mech*. ,196, 65-91.

Sclavounos, P.D. and Kim, Y.H. (1995). Third-order diffraction of surface waves by a time-domain rankine panel method. *10th Int. Workshop on Water Waves and Floating Bodies.*

Scolan, Y. M. (1989). Contribution fi l'6tude des non-lin6arit6s de surface libre, deux cas d'application"" clapitos dans un bassin rectangulaire, diffraction au second ordre sur un groupe de cylindres verticaux. Th6se de Doctorat de l'Universit6 de Paris VI, France.

Sen, D. (1993), Numerical simulation of motions of two-dimensional floatingb odies, *J Ship Res*, 37, 307-330.

Shao, Y.L. (2009). Suggested solutions to the exercises in the book 'Sloshing' by Faltinsen O.M. and Timokha A., 2009. Center for Ships and Ocean Structures, NTNU, Trondheim, Norway. Available online: http://www.cambridge.org/catalogue.

Shao, Y.L. and Faltinsen, O.M. (2008). Towards development of a nonlinear perturbation method for analysis of springing of ships. *23rd Int. Workshop on Water Waves and Floating Bodies.*

Shao, Y.L. and Faltinsen, O.M. (2010a). Use of body-fixed coordinate system in analysis of weakly-nonlinear wave-body problems. *Appl. Ocean Res.*, 32, 1, 20-33.

Shao, Y.L. and Faltinsen, O.M. (2010b). Second-order diffraction and radiation of a floating body with small forward speed. In: *Proc. of the 29th international conference on ocean, offshore and arctic engineering,* OMAE2010-20073. 2010.

Shao, Y.L. and Faltinsen, O.M. (2010c). Numerical Study on the Second-Order Radiation/Diffraction of Floating Bodies with/without Forward Speed. *25th Int. Workshop on Water Waves and Floating Bodies.*

Shen, L. and Liu, Y.J. (2007). An adaptive fast multipole boundary element method for three-dimensional acoustic wave problems based on the Burton-Miller formulation. *Comput Mech,* 40, 3, 461-472.

Skourup, J., Cheung, K.F., Bingham, H.B. and Büchmann B. (2000), Loads on a 3D body due to second-order waves and a current. *Ocean Eng.*, 27, 7, 707-727.

Soding, H. (1993). A method for accurate force calculation in potential flows, *Ship Techn. Research,* 40, 176-186, 1993.

Solaas, F. (1995). Analytical and numerical studies of sloshing in Tanks. PhD thesis, Dept of Marine. Hydrodynamics, NTNU, Trondheim, Norway.

Solaas, F. and Faltinsen, O.M. (1997). Combined numerical and analytical solution for sloshing in two-dimensional tanks of general shape. *J Ship Res.,* 41, 2, 118-129.

Standing, R.G., Dacunha, N.M.C. and Matten, R.B.(1981). Slowly varying second order wave forces: theory and experiments. Report No. R138, National Maritime. Institute.

Stassen, Y., Le Boulluec, M. and Molin, B. (1998). High order boundary element model for 2D wave tank simulation. Proc *Int Offshore Polar Eng Conf,* 3, 348-355.

Stokka, T. (1994). A third-order wave model. DNV Report No. 93-2071.

Storhaug, G. (2007). Experimental investigation of wave induced vibrations and their effect on the fatigue loading of ships, Ph.D Thesis, Dept. Marine Technology, NTNU.

Tanizawa, K. (2000). The state of the art on numerical wave tank. In *Proc. Of 4th Osaka Colloquium on Seakeeping Performance of Ships*, Osaka, Japan, 95-114.

Tanizawa,K. (1995). A nonlinear simulation method of 3-D body motions in waves (1st Report), *J. Soc. Nav. Arch. Japan*, 178, 179-191.

Tanizawa,K. and Sawada,H. (1990). A numerical method for nonlinear simulation of 2-D body motions in waves by means of BEM, *J. Soc. Nav. Arch. Japan*, 168, 223-228.

Teng, B. (1995). Second order wave action on 3D floating body, *J. Hydrodynamics*, Ser. A, 10, 3, 316-327.

Teng, B., and Kato, S. (1997). Third-harmonic diffraction force on axisymmetric bodies. *12th Int. Workshop on Water Waves and Floating Bodies.*

Teng, B., Bai, W. and Dong, G. (2002). Simulation of second-order radiation of 3D bodies in time domain by a B-spline method. Proc *Int Offshore Polar Eng Conf*, 12, 487-493.

Teng, B., Gou, Y. and Ning, D.Z. (2006). Higher order BEM for wave-current action on structures direct computation of free-term coefficient and CPV integrals. *China Ocean Eng. 20*, 395-410.

Teng, B., Liu, Z. and Ning D.Z. (2008). Time-domain Simulation of Wave-Current-Body Interaction. In: *Proc. of the Eighth ISOPE Pacific/Asia Offshore Mechanics Symposium.*

Teng, B., Ning, D.Z. and Gou, Y. (2004). A fast multipole boundary element method for three-dimensional potential flow problems. *Acta Oceanol. Sin.*, 23, 4, 747-756.

Utsunomiya, T. and Okafuji, T. (2007). Wave response analysis of a VLFS by accelerated green's function method in infinite water depth. *Int. J. Offshore Polar Eng.,* 17, 1, 30-38.

Utsunomiya, T. and Watanabe, E. (2003). wave response analysis of hybrid type vlfs by accelerated BEM. *Proc. 3rd Int Conf Hydroelasticity in Marine Tech*, 297-303.

Utsunomiya, T., Watanabe, E. andNishimura, N. (2001). Fast multipole algorithm for wave diffraction/radiation problems and its application to VLFS in variable water depth and topography. *Proc Int Conf Offshore Mech Arct Eng - OMAE*, 5, 321-327.

Vada, T. and Nakos, D. (1993). Time-marching schemes for ship motion simulations. *8th Int. Workshop on Water Waves and Floating Bodies.*

Vinje, T., and Brevig, P. (1981a), Nonlinear ship motions. *Proc. of the 3rd. Int. Conf. on Num. Ship Hydro.,* pp.IV3-1-IV3-10.

Vinje, T., and Brevig, P. (1981b), Nonlinear, two dimensional ship motions, Norwegian Hydrodynamic Laboratories, Report R- 112.81,Trondheim, Norway, 1-97.

Wang, C.Z. and Wu, G.X. (2006). An unstructured mesh based finite element simulation of wave interactions with non-wall-sided bodies, *J. Fluids Struct.*, 22, 441-461.

Wang, C.Z. and Wu, G.X. (2007). Time domain analysis of second-order wave diffraction by an array of vertical cylinders. *J. Fluids Struct.,* 23, 605-631.

Wang, C.Z. and Wu, G.X. (2008). Analysis of second-order resonance in wave interactions with floating bodies through a finite-element method. *Ocean Eng.,* 35, 717-726.

Wang, H.T., Yao, Z.H. and Wang, P.B. (2005). On the preconditioners for fast multipole boundary element methods for 2D multi-domain elastostatics. *Eng. Anal. Bound. Elem.*, 29, 7, 673-88.

Warren, M.S. and Salmon, J.K. (1992). *Proceedings. Supercomputing '92.* 570-6.

Wehausen, J.V. (1980). Perturbation methods in diffraction. *Proc. ASCE,* 106, 290-291.

Wehausen, J.V. and Laitone, E.V.(1960). *Surface Waves*. Handbuch der Physik, 9, pp. 446-778. (Available for download from www.coe.berkeley.edu/SurfaceWaves)

Whitham, G.B. (1999). *Linear and nonlinear waves*. Wiley-Interscience.

Wu, G. X. (1998). Hydrodynamic force on a rigid body during impact with liquid. *J. Fluids Struct.,* 12, 549–559.

Wu, G.X. (1991). A numerical scheme for calculating the mj-terms in wave-current-body interaction problem. *Appl. Ocean Res.*, 13, 6, 317-319.

Wu, G.X. (2007). Second-order resonance of sloshing in a tank. *Ocean Eng.,* 34, 2345-2349.

Wu, G.X. and Eatock Taylor, R. (1995). Time stepping solutions of the two dimensional non- linear wave radiation problem. *Ocean Eng.*, 22, 785-798.

Wu, G.X. and Eatock Taylor, R. (1996), Transient motion of a floatingb ody in steep water waves, *11th Int. Workshop on Water Waves and Floating Bodies.*

Wu, G.X. and Eatock Taylor, R. (2003). The coupled finite element and boundary element analysis of nonlinear interactions between waves and bodies. *Ocean Eng., 30*, 387-400.

Wu, G.X. and Eatock Taylor, R.(1989). Second-order diffraction forces on horizontal cylinders. *J. Hydrodynamics 2 ,* 55–65.

Xiang, X. and Faltinsen, O.M. (2010). Maneuvering of two interacting ships in calm water. To appear in Proc. of the PRADS 2010 (Paper no. 2010-2019), Rio de Janeiro, Brazil.

Yamashita, S. (1977). Calculations of the hydrodynamic forces acting upon thin cylinders oscillating vertically with large amplitude. *Journal of the Society of Naval Architects of Japan*, 141, 61-69.

Yoshida, K. I. (2001). Application of fast multipole method to boundary integral equation method. PhD thesis, Kyoto University.

Zhang, S. and Williams, A.N. (1996). Time-domain simulation of the generation and propagation of second-order Stokes waves in a two-dimensional wave flume. Part I: monochromatic wavemaker motions, *J. Fluids Struct.* 10, 319-335.

Zhang, S. and Williams, A.N. (1999). Simulation of bichromatic second-order Stokes waves in a numerical wave flume. *Int. J. Offshore Polar Eng.*, 9, 175-181.

Zhao, R. and Faltinsen, O.M. (1988). Interaction between waves and current on a two-dimensional body in the free surface. *Appl. Ocean Res.*, 10, 2, 87-99.

Zhao, R. and Faltinsen, O.M. (1989a). A discussion of the mj-terms in the wave-current-body interaction problem. *3rd Int. Workshop on Water Waves and Floating Bodies.*

Zhao, R. and Faltinsen, O.M. (1989b). Interaction between current, waves and marine structures, *5th Int. Conf. on Num. Ship Hydrodyn* Hiroshima, National Academy Press, Washington D.C.

Zhao, R. and Faltinsen, O.M. (1993). Water entry of two-dimensional bodies. *J. Fluid Mech. 246*, 593-612.

Zhao, R., Faltinsen, O.M. and Aarsnes, J.V. (1996). Water entry of arbitary two-dimensional sections with and without flow separation. In: *Proc. Fourth International Conference on Fast Sea Transportation (FAST'97),* Sydney, Australia, July 1997.

Zhu, W. and Faltinsen, O.M. (2007). Towards numerical dynamic stability predictions of semi-displacement vessels. *Proc. of the 9th International Conference on Fast Sea Transport, FAST 2007,* September 23-27, Shanghai, China, 2007

Zhu, X. (1997). A higher-order panel method for third-harmonic diffraction problem. Ph.D. Thesis, Dept. of Ocean Engineering, MIT, 1997.

Zienkiewiza, O.C. (1971). *The finite element method in engineering science*, 2nd ed. New York: McGraw-Hill.

R A P P O R T E R
UTGITT VED
INSTITUTT FOR MARIN TEKNIKK
(tidligere: FAKULTET FOR MARIN TEKNIKK)
NORGES TEKNISK-NATURVITENSKAPELIGE UNIVERSITET

Report No.	Author	Title
	Kavlie, Dag	Optimization of Plane Elastic Grillages, 1967
	Hansen, Hans R.	Man-Machine Communication and Data-Storage Methods in Ship Structural Design, 1971
	Gisvold, Kaare M.	A Method for non-linear mixed -integer programming and its Application to Design Problems, 1971
	Lund, Sverre	Tanker Frame Optimalization by means of SUMT-Transformation and Behaviour Models, 1971
	Vinje, Tor	On Vibration of Spherical Shells Interacting with Fluid, 1972
	Lorentz, Jan D.	Tank Arrangement for Crude Oil Carriers in Accordance with the new Anti-Pollution Regulations, 1975
	Carlsen, Carl A.	Computer-Aided Design of Tanker Structures, 1975
	Larsen, Carl M.	Static and Dynamic Analysis of Offshore Pipelines during Installation, 1976
UR-79-01	Brigt Hatlestad, MK	The finite element method used in a fatigue evaluation of fixed offshore platforms. (Dr.Ing. Thesis)
UR-79-02	Erik Pettersen, MK	Analysis and design of cellular structures. (Dr.Ing. Thesis)
UR-79-03	Sverre Valsgård, MK	Finite difference and finite element methods applied to nonlinear analysis of plated structures. (Dr.Ing. Thesis)
UR-79-04	Nils T. Nordsve, MK	Finite element collapse analysis of structural members considering imperfections and stresses due to fabrication. (Dr.Ing. Thesis)
UR-79-05	Ivar J. Fylling, MK	Analysis of towline forces in ocean towing systems. (Dr.Ing. Thesis)
UR-80-06	Nils Sandsmark, MM	Analysis of Stationary and Transient Heat Conduction by the Use of the Finite Element Method. (Dr.Ing. Thesis)
UR-80-09	Sverre Haver, MK	Analysis of uncertainties related to the stochastic modeling of ocean waves. (Dr.Ing. Thesis)
UR-81-15	Odland, Jonas	On the Strength of welded Ring stiffened cylindrical Shells primarily subjected to axial Compression

UR-82-17	Engesvik, Knut	Analysis of Uncertainties in the fatigue Capacity of Welded Joints
UR-82-18	Rye, Henrik	Ocean wave groups
UR-83-30	Eide, Oddvar Inge	On Cumulative Fatigue Damage in Steel Welded Joints
UR-83-33	Mo, Olav	Stochastic Time Domain Analysis of Slender Offshore Structures
UR-83-34	Amdahl, Jørgen	Energy absorption in Ship-platform impacts
UR-84-37	Mørch, Morten	Motions and mooring forces of semi submersibles as determined by full-scale measurements and theoretical analysis
UR-84-38	Soares, C. Guedes	Probabilistic models for load effects in ship structures
UR-84-39	Aarsnes, Jan V.	Current forces on ships
UR-84-40	Czujko, Jerzy	Collapse Analysis of Plates subjected to Biaxial Compression and Lateral Load
UR-85-46	Alf G. Engseth, MK	Finite element collapse analysis of tubular steel offshore structures. (Dr.Ing. Thesis)
UR-86-47	Dengody Sheshappa, MP	A Computer Design Model for Optimizing Fishing Vessel Designs Based on Techno-Economic Analysis. (Dr.Ing. Thesis)
UR-86-48	Vidar Aanesland, MH	A Theoretical and Numerical Study of Ship Wave Resistance. (Dr.Ing. Thesis)
UR-86-49	Heinz-Joachim Wessel, MK	Fracture Mechanics Analysis of Crack Growth in Plate Girders. (Dr.Ing. Thesis)
UR-86-50	Jon Taby, MK	Ultimate and Post-ultimate Strength of Dented Tubular Members. (Dr.Ing. Thesis)
UR-86-51	Walter Lian, MH	A Numerical Study of Two-Dimensional Separated Flow Past Bluff Bodies at Moderate KC-Numbers. (Dr.Ing. Thesis)
UR-86-52	Bjørn Sortland, MH	Force Measurements in Oscillating Flow on Ship Sections and Circular Cylinders in a U-Tube Water Tank. (Dr.Ing. Thesis)
UR-86-53	Kurt Strand, MM	A System Dynamic Approach to One-dimensional Fluid Flow. (Dr.Ing. Thesis)
UR-86-54	Arne Edvin Løken, MH	Three Dimensional Second Order Hydrodynamic Effects on Ocean Structures in Waves. (Dr.Ing. Thesis)
UR-86-55	Sigurd Falch, MH	A Numerical Study of Slamming of Two-Dimensional Bodies. (Dr.Ing. Thesis)
UR-87-56	Arne Braathen, MH	Application of a Vortex Tracking Method to the Prediction of Roll Damping of a Two-Dimension

		Floating Body. (Dr.Ing. Thesis)
UR-87-57	Bernt Leira, MK	Gaussian Vector Processes for Reliability Analysis involving Wave-Induced Load Effects. (Dr.Ing. Thesis)
UR-87-58	Magnus Småvik, MM	Thermal Load and Process Characteristics in a Two-Stroke Diesel Engine with Thermal Barriers (in Norwegian). (Dr.Ing. Thesis)
MTA-88-59	Bernt Arild Bremdal, MP	An Investigation of Marine Installation Processes – A Knowledge - Based Planning Approach. (Dr.Ing. Thesis)
MTA-88-60	Xu Jun, MK	Non-linear Dynamic Analysis of Space-framed Offshore Structures. (Dr.Ing. Thesis)
MTA-89-61	Gang Miao, MH	Hydrodynamic Forces and Dynamic Responses of Circular Cylinders in Wave Zones. (Dr.Ing. Thesis)
MTA-89-62	Martin Greenhow, MH	Linear and Non-Linear Studies of Waves and Floating Bodies. Part I and Part II. (Dr.Techn. Thesis)
MTA-89-63	Chang Li, MH	Force Coefficients of Spheres and Cubes in Oscillatory Flow with and without Current. (Dr.Ing. Thesis
MTA-89-64	Hu Ying, MP	A Study of Marketing and Design in Development of Marine Transport Systems. (Dr.Ing. Thesis)
MTA-89-65	Arild Jæger, MH	Seakeeping, Dynamic Stability and Performance of a Wedge Shaped Planing Hull. (Dr.Ing. Thesis)
MTA-89-66	Chan Siu Hung, MM	The dynamic characteristics of tilting-pad bearings
MTA-89-67	Kim Wikstrøm, MP	Analysis av projekteringen for ett offshore projekt. (Licenciat-avhandling)
MTA-89-68	Jiao Guoyang, MK	Reliability Analysis of Crack Growth under Random Loading, considering Model Updating. (Dr.Ing. Thesis)
MTA-89-69	Arnt Olufsen, MK	Uncertainty and Reliability Analysis of Fixed Offshore Structures. (Dr.Ing. Thesis)
MTA-89-70	Wu Yu-Lin, MR	System Reliability Analyses of Offshore Structures using improved Truss and Beam Models. (Dr.Ing. Thesis)
MTA-90-71	Jan Roger Hoff, MH	Three-dimensional Green function of a vessel with forward speed in waves. (Dr.Ing. Thesis)
MTA-90-72	Rong Zhao, MH	Slow-Drift Motions of a Moored Two-Dimensional Body in Irregular Waves. (Dr.Ing. Thesis)
MTA-90-73	Atle Minsaas, MP	Economical Risk Analysis. (Dr.Ing. Thesis)
MTA-90-74	Knut-Aril Farnes, MK	Long-term Statistics of Response in Non-linear Marine Structures. (Dr.Ing. Thesis)
MTA-90-	Torbjørn Sotberg, MK	Application of Reliability Methods for Safety

75		Assessment of Submarine Pipelines. (Dr.Ing. Thesis)
MTA-90-76	Zeuthen, Steffen, MP	SEAMAID. A computational model of the design process in a constraint-based logic programming environment. An example from the offshore domain. (Dr.Ing. Thesis)
MTA-91-77	Haagensen, Sven, MM	Fuel Dependant Cyclic Variability in a Spark Ignition Engine - An Optical Approach. (Dr.Ing. Thesis)
MTA-91-78	Løland, Geir, MH	Current forces on and flow through fish farms. (Dr.Ing. Thesis)
MTA-91-79	Hoen, Christopher, MK	System Identification of Structures Excited by Stochastic Load Processes. (Dr.Ing. Thesis)
MTA-91-80	Haugen, Stein, MK	Probabilistic Evaluation of Frequency of Collision between Ships and Offshore Platforms. (Dr.Ing. Thesis)
MTA-91-81	Sødahl, Nils, MK	Methods for Design and Analysis of Flexible Risers. (Dr.Ing. Thesis)
MTA-91-82	Ormberg, Harald, MK	Non-linear Response Analysis of Floating Fish Farm Systems. (Dr.Ing. Thesis)
MTA-91-83	Marley, Mark J., MK	Time Variant Reliability under Fatigue Degradation. (Dr.Ing. Thesis)
MTA-91-84	Krokstad, Jørgen R., MH	Second-order Loads in Multidirectional Seas. (Dr.Ing. Thesis)
MTA-91-85	Molteberg, Gunnar A., MM	The Application of System Identification Techniques to Performance Monitoring of Four Stroke Turbocharged Diesel Engines. (Dr.Ing. Thesis)
MTA-92-86	Mørch, Hans Jørgen Bjelke, MH	Aspects of Hydrofoil Design: with Emphasis on Hydrofoil Interaction in Calm Water. (Dr.Ing. Thesis)
MTA-92-87	Chan Siu Hung, MM	Nonlinear Analysis of Rotordynamic Instabilities in Highspeed Turbomachinery. (Dr.Ing. Thesis)
MTA-92-88	Bessason, Bjarni, MK	Assessment of Earthquake Loading and Response of Seismically Isolated Bridges. (Dr.Ing. Thesis)
MTA-92-89	Langli, Geir, MP	Improving Operational Safety through exploitation of Design Knowledge - an investigation of offshore platform safety. (Dr.Ing. Thesis)
MTA-92-90	Sævik, Svein, MK	On Stresses and Fatigue in Flexible Pipes. (Dr.Ing. Thesis)
MTA-92-91	Ask, Tor Ø., MM	Ignition and Flame Growth in Lean Gas-Air Mixtures. An Experimental Study with a Schlieren System. (Dr.Ing. Thesis)
MTA-86-92	Hessen, Gunnar, MK	Fracture Mechanics Analysis of Stiffened Tubular

		Members. (Dr.Ing. Thesis)
MTA-93-93	Steinebach, Christian, MM	Knowledge Based Systems for Diagnosis of Rotating Machinery. (Dr.Ing. Thesis)
MTA-93-94	Dalane, Jan Inge, MK	System Reliability in Design and Maintenance of Fixed Offshore Structures. (Dr.Ing. Thesis)
MTA-93-95	Steen, Sverre, MH	Cobblestone Effect on SES. (Dr.Ing. Thesis)
MTA-93-96	Karunakaran, Daniel, MK	Nonlinear Dynamic Response and Reliability Analysis of Drag-dominated Offshore Platforms. (Dr.Ing. Thesis)
MTA-93-97	Hagen, Arnulf, MP	The Framework of a Design Process Language. (Dr.Ing. Thesis)
MTA-93-98	Nordrik, Rune, MM	Investigation of Spark Ignition and Autoignition in Methane and Air Using Computational Fluid Dynamics and Chemical Reaction Kinetics. A Numerical Study of Ignition Processes in Internal Combustion Engines. (Dr.Ing. Thesis)
MTA-94-99	Passano, Elizabeth, MK	Efficient Analysis of Nonlinear Slender Marine Structures. (Dr.Ing. Thesis)
MTA-94-100	Kvålsvold, Jan, MH	Hydroelastic Modelling of Wetdeck Slamming on Multihull Vessels. (Dr.Ing. Thesis)
MTA-94-102	Bech, Sidsel M., MK	Experimental and Numerical Determination of Stiffness and Strength of GRP/PVC Sandwich Structures. (Dr.Ing. Thesis)
MTA-95-103	Paulsen, Hallvard, MM	A Study of Transient Jet and Spray using a Schlieren Method and Digital Image Processing. (Dr.Ing. Thesis)
MTA-95-104	Hovde, Geir Olav, MK	Fatigue and Overload Reliability of Offshore Structural Systems, Considering the Effect of Inspection and Repair. (Dr.Ing. Thesis)
MTA-95-105	Wang, Xiaozhi, MK	Reliability Analysis of Production Ships with Emphasis on Load Combination and Ultimate Strength. (Dr.Ing. Thesis)
MTA-95-106	Ulstein, Tore, MH	Nonlinear Effects of a Flexible Stern Seal Bag on Cobblestone Oscillations of an SES. (Dr.Ing. Thesis)
MTA-95-107	Solaas, Frøydis, MH	Analytical and Numerical Studies of Sloshing in Tanks. (Dr.Ing. Thesis)
MTA-95-108	Hellan, Øyvind, MK	Nonlinear Pushover and Cyclic Analyses in Ultimate Limit State Design and Reassessment of Tubular Steel Offshore Structures. (Dr.Ing. Thesis)
MTA-95-109	Hermundstad, Ole A., MK	Theoretical and Experimental Hydroelastic Analysis of High Speed Vessels. (Dr.Ing. Thesis)
MTA-96-110	Bratland, Anne K., MH	Wave-Current Interaction Effects on Large-Volume Bodies in Water of Finite Depth. (Dr.Ing. Thesis)

MTA-96-111	Herfjord, Kjell, MH	A Study of Two-dimensional Separated Flow by a Combination of the Finite Element Method and Navier-Stokes Equations. (Dr.Ing. Thesis)
MTA-96-112	Æsøy, Vilmar, MM	Hot Surface Assisted Compression Ignition in a Direct Injection Natural Gas Engine. (Dr.Ing. Thesis)
MTA-96-113	Eknes, Monika L., MK	Escalation Scenarios Initiated by Gas Explosions on Offshore Installations. (Dr.Ing. Thesis)
MTA-96-114	Erikstad, Stein O., MP	A Decision Support Model for Preliminary Ship Design. (Dr.Ing. Thesis)
MTA-96-115	Pedersen, Egil, MH	A Nautical Study of Towed Marine Seismic Streamer Cable Configurations. (Dr.Ing. Thesis)
MTA-97-116	Moksnes, Paul O., MM	Modelling Two-Phase Thermo-Fluid Systems Using Bond Graphs. (Dr.Ing. Thesis)
MTA-97-117	Halse, Karl H., MK	On Vortex Shedding and Prediction of Vortex-Induced Vibrations of Circular Cylinders. (Dr.Ing. Thesis)
MTA-97-118	Igland, Ragnar T., MK	Reliability Analysis of Pipelines during Laying, considering Ultimate Strength under Combined Loads. (Dr.Ing. Thesis)
MTA-97-119	Pedersen, Hans-P., MP	Levendefiskteknologi for fiskefartøy. (Dr.Ing. Thesis)
MTA-98-120	Vikestad, Kyrre, MK	Multi-Frequency Response of a Cylinder Subjected to Vortex Shedding and Support Motions. (Dr.Ing. Thesis)
MTA-98-121	Azadi, Mohammad R. E., MK	Analysis of Static and Dynamic Pile-Soil-Jacket Behaviour. (Dr.Ing. Thesis)
MTA-98-122	Ulltang, Terje, MP	A Communication Model for Product Information. (Dr.Ing. Thesis)
MTA-98-123	Torbergsen, Erik, MM	Impeller/Diffuser Interaction Forces in Centrifugal Pumps. (Dr.Ing. Thesis)
MTA-98-124	Hansen, Edmond, MH	A Discrete Element Model to Study Marginal Ice Zone Dynamics and the Behaviour of Vessels Moored in Broken Ice. (Dr.Ing. Thesis)
MTA-98-125	Videiro, Paulo M., MK	Reliability Based Design of Marine Structures. (Dr.Ing. Thesis)
MTA-99-126	Mainçon, Philippe, MK	Fatigue Reliability of Long Welds Application to Titanium Risers. (Dr.Ing. Thesis)
MTA-99-127	Haugen, Elin M., MH	Hydroelastic Analysis of Slamming on Stiffened Plates with Application to Catamaran Wetdecks. (Dr.Ing. Thesis)
MTA-99-128	Langhelle, Nina K., MK	Experimental Validation and Calibration of Nonlinear Finite Element Models for Use in Design of Aluminium Structures Exposed to Fire. (Dr.Ing.

		Thesis)
MTA-99-129	Berstad, Are J., MK	Calculation of Fatigue Damage in Ship Structures. (Dr.Ing. Thesis)
MTA-99-130	Andersen, Trond M., MM	Short Term Maintenance Planning. (Dr.Ing. Thesis)
MTA-99-131	Tveiten, Bård Wathne, MK	Fatigue Assessment of Welded Aluminium Ship Details. (Dr.Ing. Thesis)
MTA-99-132	Søreide, Fredrik, MP	Applications of underwater technology in deep water archaeology. Principles and practice. (Dr.Ing. Thesis)
MTA-99-133	Tønnessen, Rune, MH	A Finite Element Method Applied to Unsteady Viscous Flow Around 2D Blunt Bodies With Sharp Corners. (Dr.Ing. Thesis)
MTA-99-134	Elvekrok, Dag R., MP	Engineering Integration in Field Development Projects in the Norwegian Oil and Gas Industry. The Supplier Management of Norne. (Dr.Ing. Thesis)
MTA-99-135	Fagerholt, Kjetil, MP	Optimeringsbaserte Metoder for Ruteplanlegging innen skipsfart. (Dr.Ing. Thesis)
MTA-99-136	Bysveen, Marie, MM	Visualization in Two Directions on a Dynamic Combustion Rig for Studies of Fuel Quality. (Dr.Ing. Thesis)
MTA-2000-137	Storteig, Eskild, MM	Dynamic characteristics and leakage performance of liquid annular seals in centrifugal pumps. (Dr.Ing. Thesis)
MTA-2000-138	Sagli, Gro, MK	Model uncertainty and simplified estimates of long term extremes of hull girder loads in ships. (Dr.Ing. Thesis)
MTA-2000-139	Tronstad, Harald, MK	Nonlinear analysis and design of cable net structures like fishing gear based on the finite element method. (Dr.Ing. Thesis)
MTA-2000-140	Kroneberg, André, MP	Innovation in shipping by using scenarios. (Dr.Ing. Thesis)
MTA-2000-141	Haslum, Herbjørn Alf, MH	Simplified methods applied to nonlinear motion of spar platforms. (Dr.Ing. Thesis)
MTA-2001-142	Samdal, Ole Johan, MM	Modelling of Degradation Mechanisms and Stressor Interaction on Static Mechanical Equipment Residual Lifetime. (Dr.Ing. Thesis)
MTA-2001-143	Baarholm, Rolf Jarle, MH	Theoretical and experimental studies of wave impact underneath decks of offshore platforms. (Dr.Ing. Thesis)
MTA-2001-144	Wang, Lihua, MK	Probabilistic Analysis of Nonlinear Wave-induced Loads on Ships. (Dr.Ing. Thesis)
MTA-2001-145	Kristensen, Odd H. Holt, MK	Ultimate Capacity of Aluminium Plates under Multiple Loads, Considering HAZ Properties. (Dr.Ing. Thesis)

MTA-2001-146	Greco, Marilena, MH	A Two-Dimensional Study of Green-Water Loading. (Dr.Ing. Thesis)
MTA-2001-147	Heggelund, Svein E., MK	Calculation of Global Design Loads and Load Effects in Large High Speed Catamarans. (Dr.Ing. Thesis)
MTA-2001-148	Babalola, Olusegun T., MK	Fatigue Strength of Titanium Risers – Defect Sensitivity. (Dr.Ing. Thesis)
MTA-2001-149	Mohammed, Abuu K., MK	Nonlinear Shell Finite Elements for Ultimate Strength and Collapse Analysis of Ship Structures. (Dr.Ing. Thesis)
MTA-2002-150	Holmedal, Lars E., MH	Wave-current interactions in the vicinity of the sea bed. (Dr.Ing. Thesis)
MTA-2002-151	Rognebakke, Olav F., MH	Sloshing in rectangular tanks and interaction with ship motions. (Dr.Ing. Thesis)
MTA-2002-152	Lader, Pål Furset, MH	Geometry and Kinematics of Breaking Waves. (Dr.Ing. Thesis)
MTA-2002-153	Yang, Qinzheng, MH	Wash and wave resistance of ships in finite water depth. (Dr.Ing. Thesis)
MTA-2002-154	Melhus, Øyvin, MM	Utilization of VOC in Diesel Engines. Ignition and combustion of VOC released by crude oil tankers. (Dr.Ing. Thesis)
MTA-2002-155	Ronæss, Marit, MH	Wave Induced Motions of Two Ships Advancing on Parallel Course. (Dr.Ing. Thesis)
MTA-2002-156	Økland, Ole D., MK	Numerical and experimental investigation of whipping in twin hull vessels exposed to severe wet deck slamming. (Dr.Ing. Thesis)
MTA-2002-157	Ge, Chunhua, MK	Global Hydroelastic Response of Catamarans due to Wet Deck Slamming. (Dr.Ing. Thesis)
MTA-2002-158	Byklum, Eirik, MK	Nonlinear Shell Finite Elements for Ultimate Strength and Collapse Analysis of Ship Structures. (Dr.Ing. Thesis)
IMT-2003-1	Chen, Haibo, MK	Probabilistic Evaluation of FPSO-Tanker Collision in Tandem Offloading Operation. (Dr.Ing. Thesis)
IMT-2003-2	Skaugset, Kjetil Bjørn, MK	On the Suppression of Vortex Induced Vibrations of Circular Cylinders by Radial Water Jets. (Dr.Ing. Thesis)
IMT-2003-3	Chezhian, Muthu	Three-Dimensional Analysis of Slamming. (Dr.Ing. Thesis)
IMT-2003-4	Buhaug, Øyvind	Deposit Formation on Cylinder Liner Surfaces in Medium Speed Engines. (Dr.Ing. Thesis)
IMT-2003-5	Tregde, Vidar	Aspects of Ship Design: Optimization of Aft Hull with Inverse Geometry Design. (Dr.Ing. Thesis)
IMT-2003-6	Wist, Hanne Therese	Statistical Properties of Successive Ocean Wave

		Parameters. (Dr.Ing. Thesis)
IMT-2004-7	Ransau, Samuel	Numerical Methods for Flows with Evolving Interfaces. (Dr.Ing. Thesis)
IMT-2004-8	Soma, Torkel	Blue-Chip or Sub-Standard. A data interrogation approach of identity safety characteristics of shipping organization. (Dr.Ing. Thesis)
IMT-2004-9	Ersdal, Svein	An experimental study of hydrodynamic forces on cylinders and cables in near axial flow. (Dr.Ing. Thesis)
IMT-2005-10	Brodtkorb, Per Andreas	The Probability of Occurrence of Dangerous Wave Situations at Sea. (Dr.Ing. Thesis)
IMT-2005-11	Yttervik, Rune	Ocean current variability in relation to offshore engineering. (Dr.Ing. Thesis)
IMT-2005-12	Fredheim, Arne	Current Forces on Net-Structures. (Dr.Ing. Thesis)
IMT-2005-13	Heggernes, Kjetil	Flow around marine structures. (Dr.Ing. Thesis
IMT-2005-14	Fouques, Sebastien	Lagrangian Modelling of Ocean Surface Waves and Synthetic Aperture Radar Wave Measurements. (Dr.Ing. Thesis)
IMT-2006-15	Holm, Håvard	Numerical calculation of viscous free surface flow around marine structures. (Dr.Ing. Thesis)
IMT-2006-16	Bjørheim, Lars G.	Failure Assessment of Long Through Thickness Fatigue Cracks in Ship Hulls. (Dr.Ing. Thesis)
IMT-2006-17	Hansson, Lisbeth	Safety Management for Prevention of Occupational Accidents. (Dr.Ing. Thesis)
IMT-2006-18	Zhu, Xinying	Application of the CIP Method to Strongly Nonlinear Wave-Body Interaction Problems. (Dr.Ing. Thesis)
IMT-2006-19	Reite, Karl Johan	Modelling and Control of Trawl Systems. (Dr.Ing. Thesis)
IMT-2006-20	Smogeli, Øyvind Notland	Control of Marine Propellers. From Normal to Extreme Conditions. (Dr.Ing. Thesis)
IMT-2007-21	Storhaug, Gaute	Experimental Investigation of Wave Induced Vibrations and Their Effect on the Fatigue Loading of Ships. (Dr.Ing. Thesis)
IMT-2007-22	Sun, Hui	A Boundary Element Method Applied to Strongly Nonlinear Wave-Body Interaction Problems. (PhD Thesis, CeSOS)
IMT-2007-23	Rustad, Anne Marthine	Modelling and Control of Top Tensioned Risers. (PhD Thesis, CeSOS)
IMT-2007-24	Johansen, Vegar	Modelling flexible slender system for real-time simulations and control applications
IMT-2007-25	Wroldsen, Anders Sunde	Modelling and control of tensegrity structures. (PhD

		Thesis, CeSOS)
IMT-2007-26	Aronsen, Kristoffer Høye	An experimental investigation of in-line and combined inline and cross flow vortex induced vibrations. (Dr. avhandling, IMT)
IMT-2007-27	Gao, Zhen	Stochastic Response Analysis of Mooring Systems with Emphasis on Frequency-domain Analysis of Fatigue due to Wide-band Response Processes (PhD Thesis, CeSOS)
IMT-2007-28	Thorstensen, Tom Anders	Lifetime Profit Modelling of Ageing Systems Utilizing Information about Technical Condition. (Dr.ing. thesis, IMT)
IMT-2008-29	Berntsen, Per Ivar B.	Structural Reliability Based Position Mooring. (PhD-Thesis, IMT)
IMT-2008-30	Ye, Naiquan	Fatigue Assessment of Aluminium Welded Box-stiffener Joints in Ships (Dr.ing. thesis, IMT)
IMT-2008-31	Radan, Damir	Integrated Control of Marine Electrical Power Systems. (PhD-Thesis, IMT)
IMT-2008-32	Thomassen, Paul	Methods for Dynamic Response Analysis and Fatigue Life Estimation of Floating Fish Cages. (Dr.ing. thesis, IMT)
IMT-2008-33	Pákozdi, Csaba	A Smoothed Particle Hydrodynamics Study of Two-dimensional Nonlinear Sloshing in Rectangular Tanks. (Dr.ing.thesis, IMT)
IMT-2007-34	Grytøyr, Guttorm	A Higher-Order Boundary Element Method and Applications to Marine Hydrodynamics. (Dr.ing.thesis, IMT)
IMT-2008-35	Drummen, Ingo	Experimental and Numerical Investigation of Nonlinear Wave-Induced Load Effects in Containerships considering Hydroelasticity. (PhD thesis, CeSOS)
IMT-2008-36	Skejic, Renato	Maneuvering and Seakeeping of a Singel Ship and of Two Ships in Interaction. (PhD-Thesis, CeSOS)
IMT-2008-37	Harlem, Alf	An Age-Based Replacement Model for Repairable Systems with Attention to High-Speed Marine Diesel Engines. (PhD-Thesis, IMT)
IMT-2008-38	Alsos, Hagbart S.	Ship Grounding. Analysis of Ductile Fracture, Bottom Damage and Hull Girder Response. (PhD-thesis, IMT)
IMT-2008-39	Graczyk, Mateusz	Experimental Investigation of Sloshing Loading and Load Effects in Membrane LNG Tanks Subjected to Random Excitation. (PhD-thesis, CeSOS)
IMT-2008-40	Taghipour, Reza	Efficient Prediction of Dynamic Response for Flexible amd Multi-body Marine Structures. (PhD-thesis, CeSOS)
IMT-2008-41	Ruth, Eivind	Propulsion control and thrust allocation on marine vessels. (PhD thesis, CeSOS)

IMT-2008-42	Nystad, Bent Helge	Technical Condition Indexes and Remaining Useful Life of Aggregated Systems. PhD thesis, IMT
IMT-2008-43	Soni, Prashant Kumar	Hydrodynamic Coefficients for Vortex Induced Vibrations of Flexible Beams, PhD thesis, CeSOS
IMT-2009-43	Amlashi, Hadi K.K.	Ultimate Strength and Reliability-based Design of Ship Hulls with Emphasis on Combined Global and Local Loads. PhD Thesis, IMT
IMT-2009-44	Pedersen, Tom Arne	Bond Graph Modelling of Marine Power Systems. PhD Thesis, IMT
IMT-2009-45	Kristiansen, Trygve	Two-Dimensional Numerical and Experimental Studies of Piston-Mode Resonance. PhD-Thesis, CeSOS
IMT-2009-46	Ong, Muk Chen	Applications of a Standard High Reynolds Number Model and a Stochastic Scour Prediction Model for Marine Structures. PhD-thesis, IMT
IMT-2009-47	Hong, Lin	Simplified Analysis and Design of Ships subjected to Collision and Grounding. PhD-thesis, IMT
IMT-2009-48	Koushan, Kamran	Vortex Induced Vibrations of Free Span Pipelines, PhD thesis, IMT
IMT-2009-49	Korsvik, Jarl Eirik	Heuristic Methods for Ship Routing and Scheduling. PhD-thesis, IMT
IMT-2009-50	Lee, Jihoon	Experimental Investigation and Numerical in Analyzing the Ocean Current Displacement of Longlines. Ph.d.-Thesis, IMT.
IMT-2009-51	Vestbøstad, Tone Gran	A Numerical Study of Wave-in-Deck Impact usin a Two-Dimensional Constrained Interpolation Profile Method, Ph.d.thesis, CeSOS.
IMT-2009-52	Bruun, Kristine	Bond Graph Modelling of Fuel Cells for Marine Power Plants. Ph.d.-thesis, IMT
IMT 2009-53	Holstad, Anders	Numerical Investigation of Turbulence in a Sekwed Three-Dimensional Channel Flow, Ph.d.-thesis, IMT.
IMT 2009-54	Ayala-Uraga, Efren	Reliability-Based Assessment of Deteriorating Ship-shaped Offshore Structures, Ph.d.-thesis, IMT
IMT 2009-55	Kong, Xiangjun	A Numerical Study of a Damaged Ship in Beam Sea Waves. Ph.d.-thesis, IMT/CeSOS.
IMT 2010-56	Kristiansen, David	Wave Induced Effects on Floaters of Aquaculture Plants, Ph.d.-thesis, IMT/CeSOS.
IMT 2010-57	Ludvigsen, Martin	An ROV-Toolbox for Optical and Acoustic Scientific Seabed Investigation. Ph.d.-thesis IMT.
IMT 2010-58	Hals, Jørgen	Modelling and Phase Control of Wave-Energy Converters Ph.d.thesis, CeSOS.

IMT 2010-59	Shu, Zhi	Uncertainty Assesment of Wave Loads and Ultimate Strength of Tankers and Bulk Carriers in a Reliability Framework, Ph.d.-thesis, IMT.
IMT 2010-60	Jakobsen, Ken-Robert G.	Turbulence Modeling of Transverse Flow on Ship Hulls in Shallow Water. Ph.d.thesis, IMT.